Energetic particle precipitation into the middle atmosphere - optimization and applications of the NOAA POES MEPED data

Linn-Kristine Glesnes Ødegaard

Dissertation for the degree of Philosophiae Doctor (PhD)

Department of Physics and Technology
University of Bergen

June 2016

Preface

This synthesis and a collection of papers are submitted for the degree of philosophiae doctor (PhD) in physics at the Department of Physics and Technology, University of Bergen.

The thesis is divided into an introductory part and a part consisting of four papers already published or submitted to international peer reviewed journals.

Paper I Sandanger, M. I , L.-K. G. Ødegaard, H. Nesse Tyssøy, J. Stadsnes, F. Søraas, K. Oksavik, and K. Aarsnes (2015), In-flight calibration of NOAA POES proton detectors - Derivation of the MEPED correction factors, *J. Geophys. Res. Space Physics*, *120*, doi:10.1002/2015JA021388.

Paper II Ødegaard, L.-K. G., H. Nesse Tyssøy, M. I. Sandanger, J. Stadsnes, and F. Søraas (2016), Space weather impact on the degradation of NOAA POES MEPED proton detectors, *Journal of Space Weather and Space Climate*, *6* doi: 10.1051/swsc/201620.

Paper III Nesse Tyssøy, H., M. I. Sandanger, L.-K. G. Ødegaard, J. Stadsnes, A. Aasnes, and A. E. Zawedde (2016), Energetic electron precipitation into the middle atmosphere - Constructing the loss cone fluxes from MEPED POES. *J. Geophys. Res. Space Physics*, *21*, doi: 1002/2016JA022752.

Paper IV Ødegaard, L.-K. G., H. Nesse Tyssøy, F. Søraas, J. Stadsnes, and M. I. Sandanger (2017), Energetic Electron Precipitation in Weak to Moderate Corotating Interaction Region-driven Storms. *Journal of Geophysical Research: Space Physics*, *122*, 2900–2921, doi:10.1002/2016JA023096.

Contents

Abstract

This thesis has been a part of the research in the Q3 group of the Birkeland Centre for Space Science, which focus on the larger question "What are the effects of particle precipitation on the atmosphere?". An important step towards achieving an answer has been to optimize the NOAA POES MEPED data, which contain measurements of protons and electrons in the medium to high energy range. The particles measured by MEPED can penetrate deep into the atmosphere and create ionization, which ultimately can affect chemistry, temperature and dynamics. There have, unfortunately, been some challenges with the MEPED detectors. The proton detectors of the MEPED instrument are known to degrade with time. In addition, the proton measurements can be contaminated by relativistic electrons. Adding to this, the electron measurements have also been reported to suffer from low-energy proton contamination. Finally, the detectors only cover a limited part of the particle pitch angle distribution being lost to the atmosphere.

In paper I (*Sandanger et al.*, 2015) we present a robust method for correcting the MEPED proton detector degradation. We show that when the correction is applied to the degraded SEM-2 detectors, the long time flux series measured by the different satellites agree extremely well. Without correction, the data from a detector could not be used after only a few years in operation. For the very first time, we present correction factors for the MEPED proton channels with highest energy.

In paper II (*Ødegaard et al.*, 2016a), we use the correction factors for the MEPED proton detectors derived in paper I and show that they exhibit a varying trend in degradation rate throughout the solar cycle. The degradation rate is found to be strongest in the declining phase of the solar cycle. We exploit this trait and present a model which can be used to estimate the correction factor of any of the SEM-2 MEPED detectors. This allowed for the calculation of yearly correction factors throughout all SEM-2 operational periods. It may also be used to correct the SEM-1 detectors, enabling long term studies of energetic particle precipitation.

In paper III (*Nesse Tyssøy et al.*, 2016), we tackle challenges related to the MEPED electron detector. We take advantage of the MEPED proton detectors' response to relativistic electrons and provide an additional measurement to the electron spectrum. We also correct for discrepancies between the reported geometric factors of the MEPED instrument and the modelled geometric factors. An effect of this is that the threshold of the lowest energy channel is raised from $>$ 30 keV to $>$ 50 keV. However, the most important result in this paper is that we combine measurements from the two directional telescopes of the MEPED, and use pitch angle distributions from theory of wave-particle interactions to present complete bounce loss cone fluxes for $>$ 50 keV, $>$ 100 keV, $>$ 300 keV and $>$ 1000 keV electrons. These energies cover the range of electron precipitation which will deposit energy in the middle atmosphere. The bounce

loss cone fluxes are substantiated by estimating the OH produced during a weak storm, and comparing with OH observations from the Aura satellite.

In paper IV (*Ødegaard et al.*, 2016b), we use the bounce loss cone fluxes to study precipitation during storms driven by corotating interaction regions. We find that a group of storms that give increased precipitation of > 1 MeV electrons are associated with high solar wind speeds and a higher energy input to the magnetosphere from the solar wind, as estimated by the Akasofu Epsilon parameter. These findings might offer an opportunity to the atmospheric modelling community to improve their estimates of energetic electron precipitation.

Acknowledgements

It's strange to think that I have spent the last five years of my life working with optimization of data from a space-borne particle detector. I have loved it, and I have hated it. I will never in my life forget what the energy thresholds of the MEPED proton detectors are, or in what year NOAA-15 was launched. This will probably never win me any quizzes. Nevertheless, I am proud to have made it through to the other side, and I would not have been without this experience.

I would like to thank my supervisor Hilde Nesse Tyssøy for giving me the opportunity of being a PhD candidate at the Birkeland Centre for Space Science, and for believing more in me than I have done myself. Your guidance have been invaluable. I would also like to thank Professors Emeriti Johan Stadsnes and Finn Søraas for your patience, discussions, ideas and support. And Marit Sandanger, I would probably not have finished if it were not for you cheering me on and lifting me up. I thank all four of you for your good humour. It has been a pleasure to work with you. A huge thank you also to the rest of the people at the Birkeland Centre for Space Science, for lunch every day at 11:30, for hundreds and hundreds of coffees, and generally for being a cheerful crowd.

I want to thank my mother for being an inspiration. By being who you are, you have thought me that I too can be whatever I want. And last, to Kristian. You are a wonderful person, and I am lucky to have you. To my friends and family who never understand what it is that I am actually doing - I have written the introduction chapter with you in mind.

My Master and PhD theses have both been about optimization of the NOAA POES MEPED data, and I acknowledge the NOAA National Geophysical Data Center (NGDS) for providing the data. I also acknowledge the NASA/GSFCs Space Physics Data Facility's OMNIWeb service and OMNI data for providing solar wind and geomagnetic measurements.

Bergen, June 2016
Linn-Kristine Glesnes Ødegaard

Chapter 1

Introduction

Figure 1.1: Aurora over Longyearbyen, 2013. Photo by Linn-K. G. Ødegaard.

The work performed in working on this thesis has been part of the research at the Birkeland Centre for Space Science, more specifically the group investigating the overarching question "What are the effects of particle precipitation on the atmospheric system?". The objectives of my thesis were to optimize and apply particle measurements from the polar orbiting NOAA POES[1] satellites for studies on the influence of particle precipitation on the middle atmosphere. Why these satellites? Why do the measurements need optimization? And why the middle atmosphere? These are questions you might pose. To try and answer them we have to dig into the motivation behind the objective. Let us start with the atmosphere, work our way through climate change, before we end up with why particle precipitation driven by the solar wind is important.

Our planet is surrounded by a layer of gas we call the atmosphere, held in place by Earth's gravity. The density of the atmospheric gases decreases with altitude, and 99.99997% of the mass is contained below 100 km altitude. This is the altitude where "space" begins. The temperature profile of the atmosphere is rather more complicated, oscillating between increasing and decreasing temperatures as we move upwards. The characteristics of the temperature is used to divide the atmosphere into layers. These are the Troposphere (0-12 km), Stratosphere (12-50 km), Mesosphere (50-90 km), Thermosphere (90-700 km) and Exosphere ($\sim$ 700 km $\rightarrow$ The outer edge is difficult to define). In Figure 1.2 we can see how the temperature changes as one moves up through the different layers. The two temperature profiles[2] shown here apply for latitudes close to Bergen (60° North, 5° East). The red curve is a summer profile, the blue curve a winter profile, and the approximate height regions of the atmospheric layers have been

[1] National Oceanic and Atmospheric Administration, Polar Orbiting Environmental Satellites

[2] Constructed based on data downloaded from the the OMNIweb MSIS-E-90 Atmosphere Model [http://omniweb.gsfc.nasa.gov/vitmo/msis_vitmo.html]

coloured in different shadings. As we see here, the winter mesopause (the upper boundary of the mesosphere) would be located at a higher altitude compared to summer, at around 100 km instead of 90 km. We also see here that the mesopause is cooler in summer compared to winter.

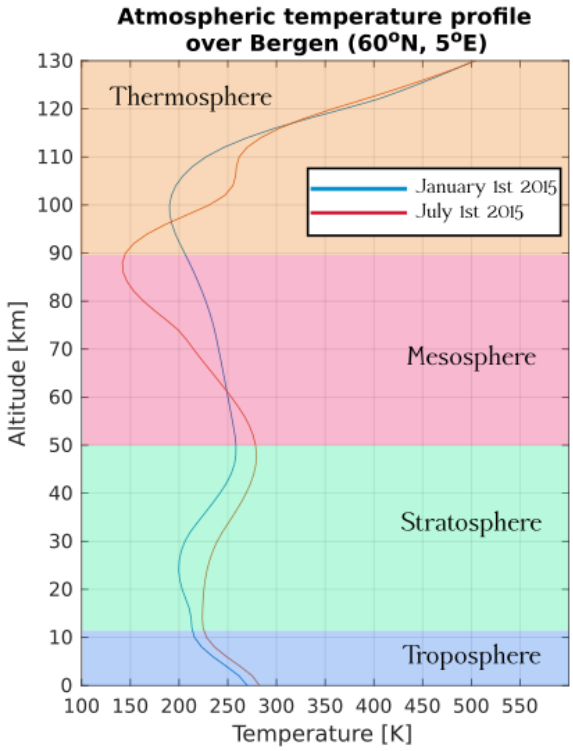

Figure 1.2: Modelled temperature profiles for a day of winter (January 1st) and summer (July 1st) over Bergen. The shaded regions show the approximate locations of the troposphere, stratosphere, mesosphere and thermosphere in summer time.

The dynamics of the atmosphere is powered by energy from the Sun. Radiation is emitted from the Sun in all directions, and the Earth absorbs a small portion of this energy. However, since the Earth is a sphere the heat will be unevenly distributed, with more heat in the equator region compared to the polar regions. This causes pressure differences which makes the air in the atmosphere move. The wind and the clouds, or the absence of these, together with temperature, is what we use to describe day-to-day weather. Climate, however, describe long-term trends in the weather, for example that the surface temperature is currently on an upward trend. To tell something about climate we have to look at average behaviour of the weather system over long time scales, for example 100 years. By clever methods, researches have ways to study how the climate has behaved over millions of years, and we know that it has changed many times before the present. So why do we make such a big deal about the change that we see happening right now? It is because there is strong evidence that *this time* anthropogenic emissions of so-called greenhouse gases (mainly CO_2) is the primary cause of the change, because the increased CO_2 concentration leads to trapping of more heat in the atmosphere.

To understand the consequences of global warming, we need to understand what will affect atmospheric dynamics, and how. We have already mentioned that the dynamics are driven by radiation from the Sun, and that greenhouse gas emissions trap more of the heat and warms the globe. This is a simple description of a very complex system. The intensity of the Sun's radiation is known to vary in an 11 year cycle, the air in the atmosphere moves in global patterns that change due to heat and pressure gradients, gasses in the atmosphere absorb and emit energy, the composition of gasses in the different atmospheric layers makes the dynamics in each layer different - but the layers are not separated by any physical boundary, and what happens in one height region will affect the dynamics above and below. Even the ocean is important, because it can store both heat and CO_2, and creates a delay in the system. The list goes on, and it is extremely hard to have a complete overview of all the pieces of the puzzle. Still, The

Intergovernmental Panel on Climate Change (IPCC) have been working since 1988 to try and do just that - construct the whole puzzle. The IPCC assess research done by different communities; oceanic, atmospheric and solar physicists.

Even though this introduction may give the impression that this is a thesis on climate change, it is not. However, our work is partly motivated by climate change, and we are working with a small but important piece of the puzzle. The Sun does not only emit electromagnetic radiation (e.g. infrared or visible light), but also charged particles. The charged particles travel through the interplanetary space, frozen together with the Sun's magnetic field. The Earth is protected from most of this particle radiation by its own magnetic field, reaching as far as $\sim 10\ R_E$ (earth radii) in the direction facing the Sun, and more than $100\ R_E$ in the opposite direction. Under certain conditions, the magnetic fields of the Sun and Earth couple together, and the charged particles are allowed to enter the Magnetosphere (which we call the region of space where the Earth's magnetic field dominates). In these cases, the charged particles can follow the magnetic field from space and down to Earth's poles, where they can collide with the atmosphere and deposit their energy. This is the phenomena called particle precipitation, which is what this thesis is about. Maybe the most fascinating effect of particle precipitation, and certainly the origin of the space physics community, is the aurora. The aurora is produced right above the altitude where space starts, at approximately 100 km. At what altitude the precipitating particles collide with the atmosphere depends on their energy. Auroral precipitation is caused by relatively low-energy particles. A photo I took of the Aurora while visiting Svalbard is shown in Figure 1.1.

Some precipitating particles have higher energy and can reach down to mesospheric and upper stratospheric altitudes. Here, the atmosphere is too dense for any currents to flow (like they can at auroral altitudes), but the energy from the precipitating particles can ionize the gas there (mostly N_2, O_2 and O). The ionized gas reacts further, and the product is so-called HO_x and NO_x gases. HO_x and NO_x can destroy ozone, which is an important gas in the atmosphere. Most of the ozone in the atmosphere is concentrated in the stratosphere, and we call this the ozone layer. The ozone layer absorbs solar UV-radiation which heats the stratosphere. This is a good thing for life, since UV-radiation can be dangerous to biology. It also acts as a cooler, emitting infrared radiation. When ozone is destroyed, the associated heating and cooling rates are changed. Not many precipitating particles have enough energy to penetrate all the way to the stratosphere, but during winter, the NO_x created by their energy deposition in the lower thermosphere and mesosphere can be transported downwards. There are a lot of unknowns regarding how important the effect from particle precipitation on the atmosphere is, and especially whether it is important for climate change. The IPCC did not include this effect in their reports. However, there is no doubt that the particle precipitation *does* lead to ozone loss, and further to heating or cooling, depending on season, which can alter the dynamics at the location. This have led to an increased, joint effort in part of the atmospheric and space physics communities to understand more so that the effects can be accounted for in atmospheric models.

We have now, hopefully, outlined some reasons for why our studies are focused on the middle atmosphere; this is the altitude region to which the highest energy precipitation driven by solar activity can penetrate and create atmospheric effects. From a space physics point of view, it is our task to tell the atmospheric modelling community how often, how much and where high-energy particle precipitation occur. We are

now closing in on the questions "why use the NOAA POES?", and "why do the satellite measurements need optimization?". We will give brief answer here, and elaborate in the following chapters. To understand more about the high-energy particle precipitation, ideally we should measure the number of particles, their energy and where they precipitate into the atmosphere. The measurements should be global and continuous. Unfortunately, such measurements do not exist. The closest thing we have are the NOAA POES, and their Medium Energy Proton and Electron Detector (MEPED). The MEPED instrument can measure a portion of the high energy protons and medium energy electrons at satellite altitude, which is about 800-850 km. By use of theory concerning charged particles in magnetic fields, we can use the measurements to calculate how many of them will reach down to the denser atmosphere and be lost there. Since there are several satellites flying simultaneously, we are lucky enough to be able to create an almost global picture when we combine the measurements, as well as covering more than 35 years together. The detectors unfortunately degrade with time, as well as having the proton measurements contaminated by electrons and vice versa. Before the data can be used reliably in studies of electron or proton precipitation, the known errors need to be accounted for.

Most studies investigating the impact of Energetic Particle Precipitation (EPP) on the atmosphere have focused on Solar Proton Events (SPE). SPEs are a well understood phenomenon. Protons are accelerated to high energies at the Sun and associated with Coronal Mass Ejections (CME) and flares, and travel with the solar wind to Earth. SPEs are rare events, but they happen more frequently around solar maximum, when the Sun is more active. When the SPEs hit the Earth, the high-energy protons precipitate more or less homogeneous over the poles, at high latitudes. Energetic Electron Precipitation (EEP) events are more complicated in nature, and less studied. The electrons are *not* accelerated at the Sun, but inside Earth's magnetic field in processes not fully understood. The high energy electrons get trapped in the magnetic field in what is known as the radiation belts. Understanding of the dynamics of the radiation belts has also been elusive. Similar geomagnetic storms have been found to both enhance and deplete the radiation belt population, and there is no strong indication as to what causes the different behaviour. This makes the effect from EEP hard to account for in atmospheric models, since the controlling parameters have not been revealed yet. In paper IV of this thesis, we apply the corrected NOAA POES electron measurements to a selection of geomagnetic storms to study the behaviour of the EEP.

In the following chapter, we will present relevant theory on the charged particle population in the magnetosphere, where it comes from, and mechanisms that precipitates particles. Chapter 3 will be devoted to the challenges related to the MEPED detectors. Chapter 4 will address how the optimization of the MEPED data can improve studies on atmospheric effects. In Chapter 5, we outline a few future prospects. Finally, the four papers will be summarized in Chapter 6, and are included in their entirety in Chapter 7. Two papers are concerned with calibration of the MEPED proton detector, and one with estimating the precipitating electrons in the atmosphere from measurements at satellite altitude, as well as dealing with the mutual contamination between the electron and proton measurements, retrieving electron flux with energies > 1 MeV from the proton detector, and correcting the electron detector geometric factors. In the final paper we apply the newly corrected electron data to study the characteristics of small, recurring geomagnetic storms known to drive high-energy electron precipitation.

Throughout the thesis, we will refer to the papers as paper I (*Sandanger et al.*, 2015), paper II (*Ødegaard et al.*, 2016a), paper III (*Nesse Tyssøy et al.*, 2016), and paper IV (*Ødegaard et al.*, 2016b).

Chapter 2

Theory

The work of this thesis has mainly been concerned with high-energy charged particles in the magnetosphere. The term used for a gas of ionized particles is plasma, and the main constituents of space plasma are the negatively charged electrons and positively charged protons. We will in Section 2.1 introduce plasma regions in near-Earth space, and also how plasma and magnetic field interact. Further, we explain how geomagnetic disturbances affect the plasma regions in Section 2.2. A more detailed description of the radiation belts will be given in Section 2.3. This is where the electrons with the highest energy are found, and their variation is the subject of paper IV.

2.1 Plasma regions in near-Earth space

The Earth is surrounded by a magnetic field generated mainly in its core (*Russell*, 1993a,b). If left undisturbed, this magnetic field would be approximately dipole shaped, as illustrated in Figure 2.1 a). A schematic view more resemblant of the real shape of the magnetic field is shown in Figure 2.1 b). Close to Earth, the shape can still be approximated to a dipole.

The Sun's magnetic field is generated by moving plasma, and has a much more complicated structure than the Earth's magnetic field. Plasma from the Sun expands into interplanetary space, and as a result of high conductivity, the magnetic field of the Sun and the plasma are frozen together. This emitted plasma is called the solar wind, and the associated magnetic field is often referred to as the Interplanetary Magnetic Field (IMF).

A characteristic of magnetic fields is that they have a direction. The Earth's magnetic field direction is fixed, with the magnetic south pole located in the geographic Northern Hemisphere, and the dipole axis slightly titled away from the rotational axis. The direction of the IMF is not fixed, and if the two fields are parallel, it is deflected by the magnetosphere. When the solar wind blows past the magnetosphere it distorts the shape from dipole towards a tear-drop shape — compressed on the side facing the Sun and stretched on the opposite side. If it was not for the magnetosphere, the solar wind would blow away the Earth's atmosphere and our planet would not be able to sustain life. This is what happened on Mars, which no longer has a significant magnetic field

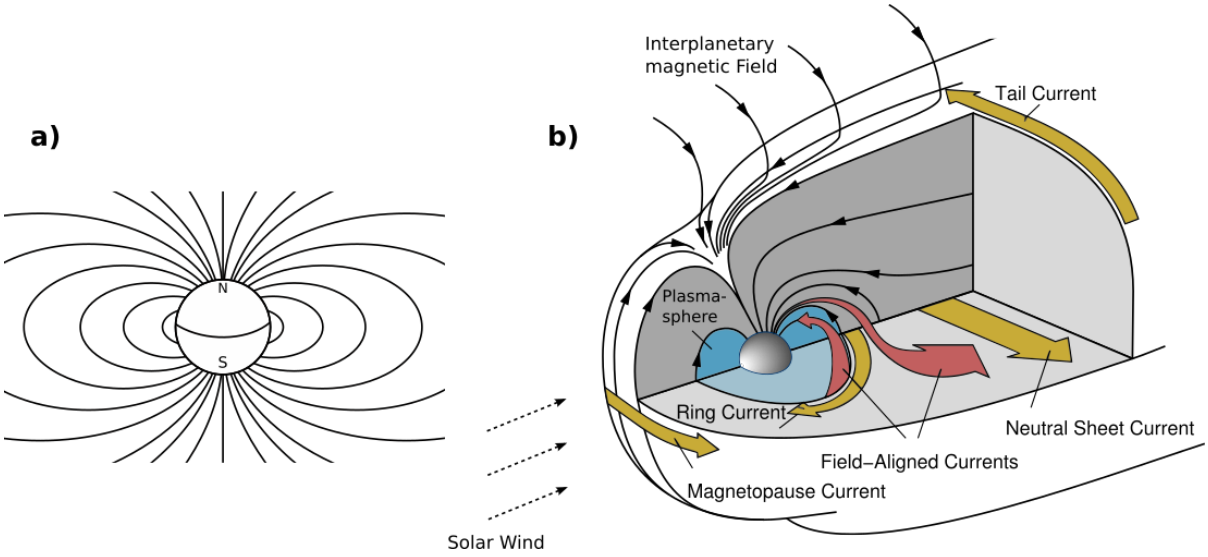

Figure 2.1: a) Illustration of the dipole magnetic field generated in the Earth's core. b) Figure adapted from *Russell* (1993a), displaying selected currents and plasma regions within the magnetosphere. The dipole magnetic field is compressed by the solar wind at the side facing the Sun, and stretched out into a long tail on the opposite side.

and only a very thin atmosphere remains[1].

When the directions of the IMF and the Earth's magnetic field are anti-parallel they can couple together, allowing plasma from the solar wind to enter the magnetosphere (*Dungey*, 1961; *Russell et al.*, 1974). In this way the solar wind acts as a source of plasma for the magnetosphere. Inside the magnetosphere the plasma is grouped into regions characterized by different densities and temperatures. Figure 2.1 b) shows some of the plasma regions and currents in the magnetosphere.

Closest to the Earth, on closed and almost dipolar magnetic field lines, we find the plasmasphere. The plasmasphere contains a high-density, low-energy plasma originating from the top of the atmosphere. The outer plasmaspheric boundary, called the plasmapause, is dependent on the level of geomagnetic activity. In quiet times it can be found at $5-6$ R_E, while during disturbed times it moves inwards to around 4 R_E (*Chapell*, 1972).

The inner radiation belt is embedded in the plasmasphere. It mainly consists of rather stably trapped high-energy protons contained inside 2 R_E. The outer radiation belt is dominated by electrons and is highly variable in location and intensity. The inner edge of the outer belt is approximately co-located with the plasmapause for reasons that will be elaborated in Section 2.3. The outer edge can be located between $6-10$ R_E, depending on geomagnetic activity (*Kievelson and Russel*, 1995; *Lyons and Williams*, 1984). Figure 2.2 (adapted from *Thorne* (1980)) displays the approximate relative locations of the inner and outer radiation belts, and also the plasmapause. The shaded region illustrates the plasma sheet, which is the source region for low-energy auroral precipitation. In the figure, one can observe how magnetic field lines close to Earth map to low latitudes, and field lines far from the Earth map to high latitudes.

A third plasma population also overlaps with parts of the plasmasphere and the

[1] more information on planetary science and how the atmosphere of a planet escapes into space can be found for example on: http://www.astronomynotes.com/solarsys/s3.htm.

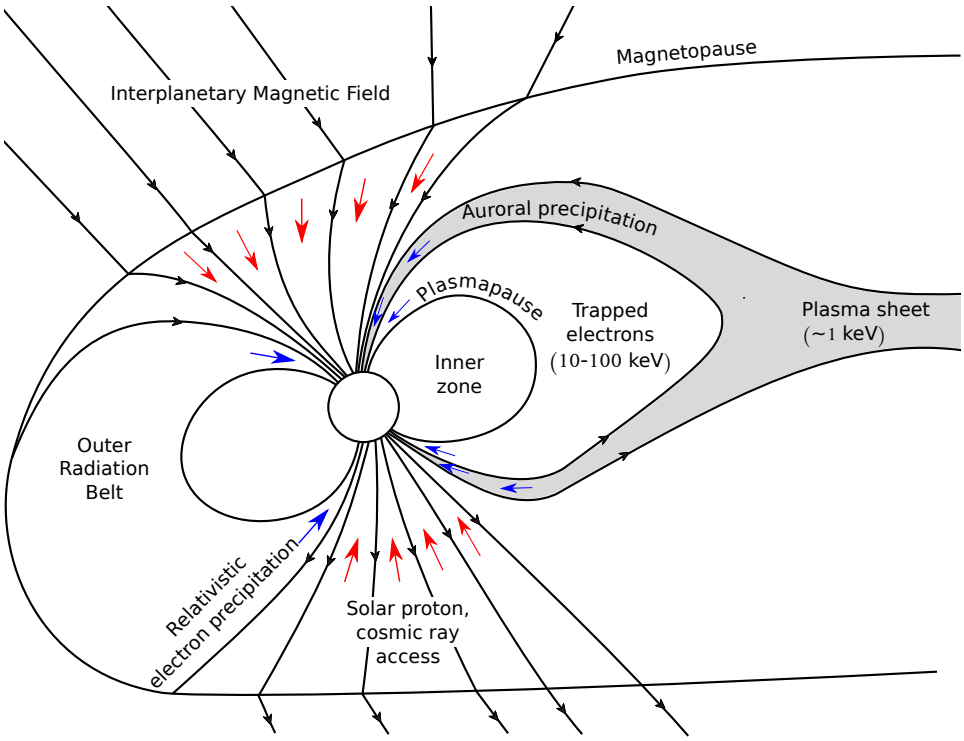

Figure 2.2: Illustration of the magnetosphere, adapted from *Thorne* (1980). The inner belt is located close to Earth, mostly contained inside 2 R_E, and overlapping with the plasmasphere. There is a slot region where particles are lost to the atmosphere between the inner and outer belt due to wave-particle interactions, approximately co-located with the plasmapause. The outer radiation belt is highly variable during geomagnetic activity, both in location and intensity. Auroral precipitation from the plasma sheet is also included in the sketch, which happen on magnetic field lines that map to higher latitudes than the outer radiation belt. The energetic solar protons can directly access the magnetosphere via field lines connected to the IMF over the Earth's polar regions.

radiation belts. This is the ring current, indicated in Figure 2.1 b) with a curved, yellow arrow. The ring current consists of positive ions flowing westward around Earth in the equatorial region, and negative electrons flowing eastward. Together they set up a westward current. The current is mainly carried by the positive ions, which have energies in the 10-300 keV range (*Gonzalez et al.*, 1994; *Koskinen*, 2005; *Stern*, 2005).

2.2 Geomagnetic storms

Geomagnetic storms often evolve when the IMF has a southward component ($B_Z < 0$), and can connect to the magnetosphere (*Russell et al.*, 1974). When the IMF is turned southward for an extended period of time, energy is transferred to the magnetosphere from the solar wind (*Akasofu*, 1981). During such times the Earth's dawn-to-dusk convection electric field is strengthened and particle injection from the magnetotail to the inner magnetosphere is increased. The freshly injected particles enhance the ring current. On Earth's surface we can measure a depression of the total magnetic field strength when the ring current grows, as the intensification of the ring current produce a magnetic field oppositely directed to the terrestrial field. An index derived based on measurements of the ring current intensity is the most common method used to quantify the magnitude of storms, the Disturbed Storm Time (Dst)-index. The quiet day level of the Dst-index is around 0 nT, and an increase in ring current intensity is seen as a negative deviation away from quiet day levels. The period of ring current growth is the main phase of the storm. The recovery phase starts when the IMF turns northward, and energy transfer is cut off. During the recovery phase, loss processes dominate in the inner magnetosphere, decreasing the intensity of the ring current until it returns to quiet-day values (*Gonzalez et al.*, 1994).

There are mainly two categories of geomagnetic storms; Corotating Interaction Region storms and Coronal Mass Ejection storms. Their main difference is the solar source driving the activity, but their signatures measured close to Earth can also distinguish them. Both types of storms can initiate magnetospheric processes which can accelerate the injected (low energy) plasma to radiation belt energies.

2.2.1 Corotation interaction region storms

A Corotating Interaction Region (CIR) is created when fast solar wind streams from coronal holes interact with upstream slow solar wind. The Sun has a rotational period of ~ 27 days, and if the coronal holes exist for longer than one solar rotational period, the high-speed stream emanating from it will corotate. In effect, the interaction region created upstream will also corotate with the Sun. CIRs are the dominating form of geomagnetic activity during the declining and minimum phases of the solar cycle. For a comprehensive review on CIR storms, see *Tsurutani et al.* (2006).

When the fast solar wind overtakes the slow solar wind, there will be a compression of the magnetic field and plasma in the interaction region. In the solar wind measured at 1 Astronomical Unit from the Sun (abbreviated AU, roughly corresponding to the distance between the Sun and the Earth), the CIR is seen to have signatures as a high-pressure/high-density region arriving with subsequent transition from slow (300-400 km/s) to fast (600-800 km/s) solar wind velocity. The IMF B_Z component is seen to

oscillate rapidly between positive and negative values at the arrival of the CIR, while the total magnetic field strength |B| displays a large increase. Solar wind parameters, AE and Dst indices are plotted for one of the storms used in paper IV in Figure 2.3 to illustrate the solar wind and geomagnetic signatures from a typical CIR at 1 AU. Simultaneous with the arrival of the increased solar wind density associated with the CIR, the Dst-index is highly positive. This is due to the compression and inward motion of the dayside magnetopause (*Tsurutani et al.* (2006) and references therein).

CIR storms typically produces moderate ring current enhancements during storm main phase, but often have long lasting recovery phases (*Tsurutani et al.*, 1995, 2006). The storm presented in Figure 2.3 only reaches a minimum Dst ≈ -40 nT, while the recovery phase of the event lasts for many days (seen in the Dst index). The AE-index is a measure of the auroral electrojets, composed of the high latitude current system which enhances during periods of auroral particle precipitation. In Figure 2.3 the AE-index shows signs of auroral activity starting after the arrival of the CIR (at zero epoch time), and staying active throughout the interval. In the recovery phase of CIR storms AE activity often persists for many days. These long-duration auroral events are sometimes called High-Intensity Long-Duration Continuous AE Activity events (HILDCAAs)[2]. The cause of the long recovery phase and HILDCAAs is associated with Alfvén waves in the solar wind, which trigger magnetic field reconnection and small plasma injections to the magnetosphere also in the recovery phase (*Sandanger et al.*, 2005; *Søraas et al.*, 2004). This is central for the theory of why CIR storms often accelerate relativistic electrons; the injected plasma causes asymmetric plasma distributions, which are unstable to wave growth. The theories of acceleration mechanisms will be discussed in more detail in Section 2.3.

There is evidence that storms caused by CIRs inject more energy into the magnetosphere in the declining phase of the solar cycle, compared to larger storms caused by coronal mass ejections during solar maximum (*Tsurutani et al.* (2006) and references therein). *Asikainen and Ruopsa* (2016) showed that both CIRs and coronal mass ejections were most effective in producing precipitation in the declining phase. The occurrence rate of coronal mass ejections is small compared to CIRs in this phase of the solar cycle, and therefore CIRs may be responsible for a larger energy input.

2.2.2 Coronal mass ejection storms

The other main source of geomagnetic activity is Coronal Mass Ejections (CME). Like the name suggests, mass is ejected from the Sun into interplanetary space. CMEs often have a leading shock created when the fast ejecta overtakes the upstream, slow solar wind (*Gonzalez et al.*, 1999; *Jian et al.*, 2006). At 1 AU, the shock manifests as a sudden impulse in the Dst-index (*Gonzalez et al.*, 1994, 1999). The positive impulse is much more abrupt than the gradual increase caused by CIR storms. If the solar wind IMF in the ejecta is southward, the sudden impulse will be followed by the storm main phase. The storm main phase typically lasts a few hours, as long as energy injection dominates. Decay of the ring current is dependent on slower processes, e.g. charge exchange and Coulomb collisions, and the recovery phase typically lasts for one to a

[2]HILDCAAs are defined as events where the AE index reaches at least 1000 nT, and does not drop below 200 nT for more than two hours at a time (e.g. *Tsurutani et al.* (2004)). CIR storms may have long duration AE activity without the criteria for HILDCAAs being fulfilled. This is the case for the event plotted in Figure 2.3.

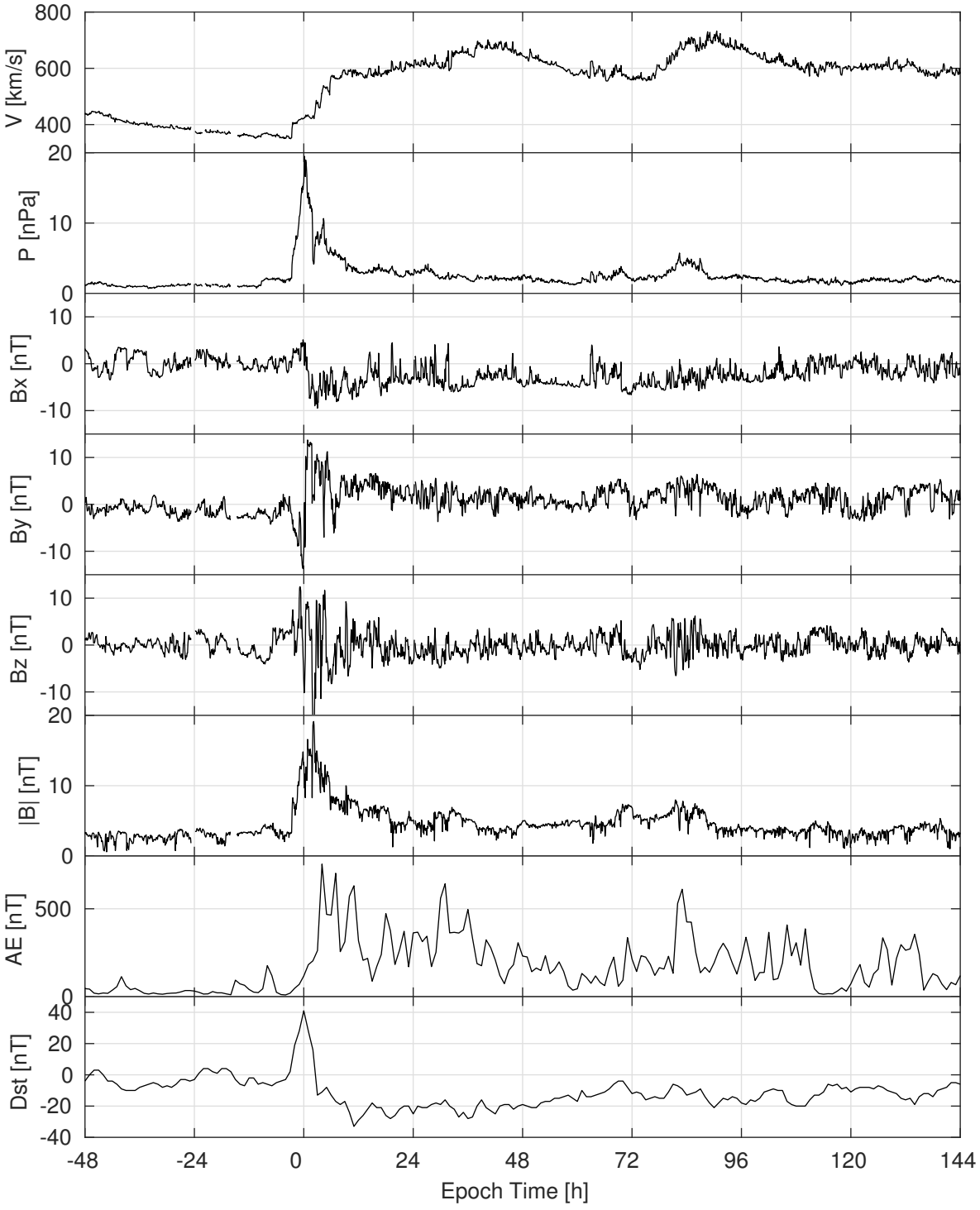

Figure 2.3: Typical CIR storm (December 2007). The arrival of the increased solar wind pressure is used as identification of CIR start (zero Epoch Time) in paper IV of this thesis. The geomagnetic activity is weak, as seen by e.g. the weak minimum Dst ≈ -40 nT, but the recovery phase lasts for many days. Fluctuating IMF B_Z allows for continuous, long-lasting energy input into the magnetosphere.

few days (*Gonzalez et al.*, 1999; *Kamide et al.*, 1997). A storm driven by a CME is presented later, in chapter 4 (Figure 4.3).

2.2.3 Solar proton events

Solar flares and CMEs can be accompanied by high fluxes of high energy ions from the Sun. These events are called by many names, both Solar Energetic Particle events (SEP) and Solar Proton Events (SPE) are common. The intensity of the relativistic ions increase with increasing CME speed (*Borovsky and Denton*, 2006). The particles are accelerated at the Sun and in the shock front of the CME, and can reach Earth in a few minutes (*Shea and Smart*, 1990). During large SPEs the peak proton flux of energy > 10 MeV can reach $10^6/\text{cm}^2/\text{s}$, and fluxes of protons up to several hundreds of MeV can be significant. These high-energy protons can harm satellite instrumentation, but also be dangerous for manned spacecraft (*Tranquille*, 1994). The protons precipitate over the polar regions, where the magnetic field of Earth is open and connected to the IMF. It will also penetrate the closed field lines as low as 60° invariant latitude (*Thorne*, 1980) (see Figure 2.2).

2.3 The radiation belts

The radiation belts are regions of the magnetosphere populated with energetic charged particles. In this section we will give an introduction to the radiation belts, and some of the theories concerning radiation belt acceleration and loss. Paper IV of this thesis is concerned with precipitation from the radiation belts, and this section is meant to give context for the understanding and motivation of paper IV. It will by no means give a complete picture of radiation belt research. The interested reader can find more information and references to important earlier works in reviews e.g. by *Friedel et al.* (2002); *Millan and Baker* (2012); *Millan and Thorne* (2007). There are also a large number of recent papers on the radiation belts using data from the Van Allen Probes. *Kessel* (2016) summarize the recent progress, and the still unresolved questions.

The energies of the electrons in the radiation belts are much higher than the solar wind plasma, and it was long considered a mystery where these high-energy electrons came from, or how they were accelerated to such high energies. On the dipolar magnetic field close to Earth, the particles have three principal ways they can move; they gyrate around the field line they are bound to; they bounce back and forth between the two hemispheres along the field line; and they can drift on paths of constant magnetic field strength around the Earth. Each motion is connected to a time scale, and an adiabatic invariant. Each invariant is proportional to a property of the magnetic field; 1 - magnetic flux through the gyro motion, 2 - integrated magnetic field along the bounce orbit, 3 - magnetic flux within the drift orbit. If the magnetic field is (close to) constant within the time scale of the motion, the invariant is conserved[3]. The combination of these motions leads to a doughnut-shaped population of trapped radiation in the inner magnetosphere.

[3] e.g. *Baumjohann and Treumann* (1996) give a theoretical introduction to motion of charged particles in magnetic fields.

The radiation belts were discovered in 1958 by James Van Allen and collaborators, using a Geiger counters on board the Explorer I satellite. The instrument saturated due to the high radiation doses observed, and it was shortly established that there were two distinct zones of radiation separated by an empty region. The radiation belts are often referred to as Van Allen Belts in honour of their discoverer (*Millan and Baker*, 2012).

The inner zone consists of an overlapping region of protons and electrons, which is stable on long time scales. The protons are observed to have energies of several hundred MeV, but the main population is between 0.1 - 40 MeV. The source of protons in the inner belt is Cosmic Ray Albedo Neutron Decay (CRAND). The proton population does not exhibit the division into two zones like the electrons, but extends outwards. However, their energy decrease drastically beyond a few R_E. The maximum flux of protons is found inside 2 R_E. The largest flux of electrons is mostly found with energy < 1 MeV in the inner region, but lower fluxes of energies upward to ~ 5 MeV also exist (*Millan and Baker*, 2012).

The dominating radiation in the outer belt is electrons, with energies ranging from some hundred keV's to more than 10 MeV. To set strict energy boundaries on what is considered a "radiation belt electron" is not straight forward, as the processes that accelerate the electrons are still debated. Often, electrons below a few hundred keV are considered the source population on which the acceleration processes work (*Millan and Baker*, 2012). As previously mentioned, the plasmasphere, ring current and radiation belts more or less occupy the same region of space, and the dynamics of the different energy ranges influence other populations of higher and lower energy particles. The outer belt fluxes are highly variable due to the competing processes of acceleration and loss.

The empty region between the outer and inner electron radiation belts is thought to be created by plasmaspheric hiss (*Lyons et al.*, 1972), and is one example of how the low-energy electron population can influence the dynamics of the high-energy population. The slot region and separation of the radiation into two belts is observed also at rather low energies of a few tens of keV, but becomes more prominent with increasing electron energy (*Reeves et al.*, 2016).

2.3.1 Acceleration in the radiation belts

Acceleration of electrons involve violation of one or more of the three adiabatic invariants connected to the particle motion. There are two main theories for radiation belt electron acceleration; global and local acceleration (or most likely, a combination of global and local processes) (*Friedel et al.*, 2002; *Millan and Baker*, 2012). The first one entails radial transport, and the second acceleration at a fixed radial location.

The timescales of the motion connected to the thee adiabatic invariants are typically separated by orders of magnitude, with frequencies on the order of kHz for the electron gyration, the order of Hz for the electron bounce period, and mHz for the electron drift frequency (*Millan and Baker*, 2012). The particular gyro, bounce and drift frequencies of an electron is dependent on its radial distance from Earth and its kinetic energy. The difference in timescales is important, as it decouples the three motions, and restricts the frequencies of waves that will affect each type of motion.

Radial diffusion involves variations in the large-scale electric and magnetic fields. The variations are too slow to break the invariant related to the gyration and bounce

motion of the electron, but fast enough to break the third, the drift invariant (*Blanc et al.*, 1999; *Millan and Baker*, 2012). Local acceleration involve interaction between the trapped particles and plasma waves which violates the first or second (or both) invariants. This can change the particle energy, pitch angle, or both (*Millan and Baker*, 2012; *Tsurutani and Lakhina*, 1997). If an electron is moved radially inward, the electron's energy perpendicular to the magnetic field will increase as it moves from weaker to stronger field strength. The energy increase follows from the conservation of the first adiabatic invariant. If the particle has an equatorial pitch angle $\alpha_{eq} = 90°$, the total energy of the particle will increase due to conservation of the second adiabatic invariant. This process is known as betatron acceleration. If the electron has a smaller pitch angle, $\alpha_{eq} < 90°$, the radial transport will lead to an increased pitch angle, and a smaller gain in the electron's total energy. The effect of radial transport is therefore to increase the pitch angles of the electron population, with distribution peak near $\alpha_{eq} = 90°$. Global waves with Ultra Low Frequency (ULF), in the mHz range, can resonate with the electron drift period (*Millan and Baker*, 2012). ULF waves can be generated e.g. by Kelvin-Helmholtz instabilities at the magnetopause boundary, or by solar wind ram pressure increases, and tend to accompany high solar wind speeds (*Friedel et al.*, 2002; *Mann et al.*, 2004; *Thorne*, 2010).

The other processes for particle energy gain is through wave-particle interactions, violating the two first adiabatic invariants. Resonance occurs when the Doppler-shifted wave frequency matches the particle cyclotron frequency (*Millan and Thorne*, 2007; *Tsurutani and Lakhina*, 1997). Whistler mode chorus waves can be excited by anisotropy in the electron temperature when plasma sheet electrons are injected in the inner magnetosphere, for example when convection is enhanced during geomagnetic storm time (*Thorne*, 2010). The injected low-energy electron population ($\sim$keV) provide energy which allows the chorus waves to grow. The waves can further interact with higher energy electrons ($\sim$ 100 keV to MeV) through cyclotron resonance, and accelerate the electrons to even higher energies.

There is evidence that acceleration by radial transport is insufficient to produce the observed radiation belt fluxes. One example is shown by *Horne et al.* (2005) where the power of ULF waves in the magnetosphere decreased simultaneously with flux increase of relativistic radiation belt electrons in the 2003 Halloween storm. They suggest that whistler mode chorus (local acceleration) was more important than large scale diffusion in this particular event. *Reeves et al.* (2013) showed a case study of a large geomagnetic storm where the most likely scenario for the observed radial profiles of phase space density is local acceleration by wave-particle interactions at $L \approx 4$, right in the heart of the outer radiation belt (L is the distance in the equator plane to a magnetic field line from Earth's center, measured in number of R_E. L-value is also often used to refer to the footpoint of the respective field lines). Others, e.g. *Mann et al.* (2004), find a strong correlation between ULF wave power, solar wind velocity, and MeV electron response. *Mann et al.* (2004) also found that the correlation is dependent on the solar cycle, with stronger correlation in the declining phase. The relative importance of local and global acceleration is still an unresolved question.

The solar wind velocity and relativistic electron flux enhancement are closely linked, this has been known for a long time (*Paulikas and Blake*, 1979). The relationship is, however, not necessarily linear (*Reeves et al.*, 2011). When examining 276 moderate to intense geomagnetic storms during 1989-2000, *Reeves et al.* (2003) found

that higher solar wind velocities increase the probability of large flux increase in the radiation belts. Despite the statistical probability of flux increase, high-speed storms were found that depleted the radiation belt flux, and low-speed storms were found that enhanced the flux. *Reeves et al.* (2003) found no correlation between pre-storm and post-storm flux.

Kilpua et al. (2015) found that the level of pre-storm flux in combination with solar wind conditions were important for how the radiation belt responded. One of their results was that high-speed solar winds trailing CMEs or CIRs were connected to acceleration and radiation belt flux increase. The events found to deplete the radiation belt fluxes had clearly higher pre-storm flux, compared to events that enhanced the radiation belt fluxes. The conflicting findings from *Reeves et al.* (2003) and *Kilpua et al.* (2015) regarding the relationship between pre-storm and post-storm radiation belt fluxes demonstrate how uncertain and elusive the understanding of the radiation belt dynamics still is.

2.3.2 Loss processes in the radiation belts

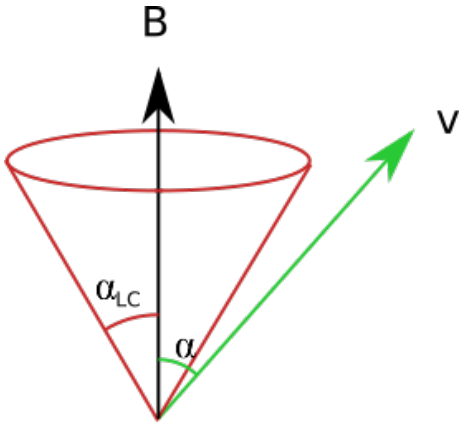

Figure 2.4: Illustration of the velocity, v, of an electron (green arrow) and its pitch angle, α, relative to the magnetic field, B (black arrow). Electrons with equatorial pitch angles contained inside the red cone will be lost to the atmosphere. Figure adapted from *Rodger et al.* (2013).

When the charged particles bounce back and forth along the magnetic field between the two hemispheres, the pitch angle between the particle's velocity vector and the magnetic field will change through the motion. The pitch angle is smallest in the equatorial plane, where the magnetic field strength is weakest. As the particle approaches the polar regions, the pitch angle grows larger. If the pitch angle reaches 90° somewhere along the field line, the particle turns around. It is in fact this feature that causes the bounce motion.

All particles can be characterized by their pitch angle, measured in the equatorial plane, α_{eq}. The set of α_{eq} corresponding to particles that will mirror at altitudes $\leq$ 100 km will be lost to the atmosphere define the loss cone. The particle's mirror point is then located below the altitude where the atmosphere is so dense that collision is highly probable, and it will lose its energy to the atmosphere. The equatorial loss cone, α_{LC}, and a particle with a larger equatorial pitch angle is illustrated in Figure 2.4. The pitch angle defining the outer edge of the loss cone is purely a function of the magnetic field strength in the equator plane, B_{eq}, and the magnetic field strength at the altitude where the particle is lost, e.g. 120 km, B_{120}. This relationship can be shown to be $sin^2\alpha_{LC} = \frac{B_{eq}}{B_{120}}$. This means that the size of the loss cone decreases when B_{eq} decreases, which is equivalent to saying that the equatorial loss cone decreases with larger L-values.

Wave-particle interactions can alter the pitch angle of an electron, moving a previously trapped electron into the loss cone. There are mainly three types of wave-particle

interactions responsible for pitch angle scattering; plasmaspheric hiss, whistler mode chorus, and electromagnetic ion cyclotron (EMIC) waves (*Millan and Thorne*, 2007). Plasmaspheric hiss is a whistler mode emission with frequencies between 100 Hz to a few kHz (extremely low frequency, ELF). Because the wave frequency is generally lower than the gyro frequency of electrons, the waves will mainly change the electron pitch angle (not accelerate it). Hiss is primarily found in high-density regions such as the plasmasphere, and is more intense in the dawn to evening sector (*Millan and Thorne*, 2007) (see Figure 2.5). As previously mentioned, plasmaspheric hiss is responsible for the so-called slot-region between the outer and inner radiation belt, scattering electrons into the loss cone at locations near the plasmapause (*Lyons et al.*, 1972). Whistler mode chorus is observed outside the plasmasphere, and grow by cyclotron resonance with unstable electron populations, for example during storm time plasma sheet injection. The waves are found in the frequency range $\sim$ 100 Hz $-$5 kHz. A $\sim$ 2 kHz wave can interact with $\sim$ 100 keV electrons in the equatorial plane, and higher energies at higher latitudes (*Millan and Thorne*, 2007). EMIC waves grow when there is a proton anisotropy in the ring current ($T_\perp > T_\parallel$), as for example during proton injection in storms and substorms. Even though EMIC waves are left-hand polarized and mainly interact with ions, they can also interact with high-energy electrons via anomalous resonance if the wave and electron travel in the same direction (*Millan and Thorne*, 2007; *Tsurutani and Lakhina*, 1997). This is why precipitation of electrons by EMIC waves can be called "parasitic", since it accompanies ion precipitation (e.g. *Søraas et al.* (1999)). Electrons from a few hundred keV to MeV energies are prone to EMIC scattering (*Millan and Thorne*, 2007). EMIC wave activity is enhanced in the local evening to midnight sector (see Figure 2.5).

In addition to being scattered into the loss cone, particles may also be lost to the magnetopause during storm main phase. As the ring current intensifies, the magnetic field is weakened. To conserve the drift invariant, particles move radially outward. If the dayside magnetopause is simultaneously compressed, the particles that were previously on closed drift paths may now be located on open drift paths, and subsequently lost (*Millan and Thorne*, 2007). This mechanism has been suggested as partly responsible for the flux drop-out seen during storm main phase.

Precipitation from the radiation belts has been of high interest in recent years, in part due to the fact that the high-energy electron can penetrate deep into the atmosphere. Studies focusing on the effect of radiation belt precipitation will be discussed in chapter 4. Others have studied how the precipitation relates to geomagnetic activity. Especially High Speed Solar Wind Streams (HSSWS) trailing CIRs have gained a lot of attention. CIR recovery phases are connected to oscillating IMF B_Z and Alfvén waves, and thus continuous small energy injections from the solar wind. *Asikainen and Ruopsa* (2016) found that the solar wind speed was the parameter affecting precipitation the most, when studying energetic electron precipitation in relation to HSSWS and CMEs over decades. *Kavanagh et al.* (2012) found that the average state of the IMF B_Z one day before the CIR arrived strongly controlled the level of precipitation. *Horne et al.* (2009) analysed storms in 9 years of MEPED data, concluding that $>$ 300 keV precipitation peaked during main phase of storms, while $>$ 1 MeV peaked during the recovery phase. Both EMIC (*Horne et al.*, 2009; *Rodger et al.*, 2015; *Sandanger et al.*, 2007) and chorus waves (*Meredith et al.*, 2011) have been suggested as mechanisms causing the observed precipitation. Also *Meredith et al.* (2011) showed the different timing of peak flux for

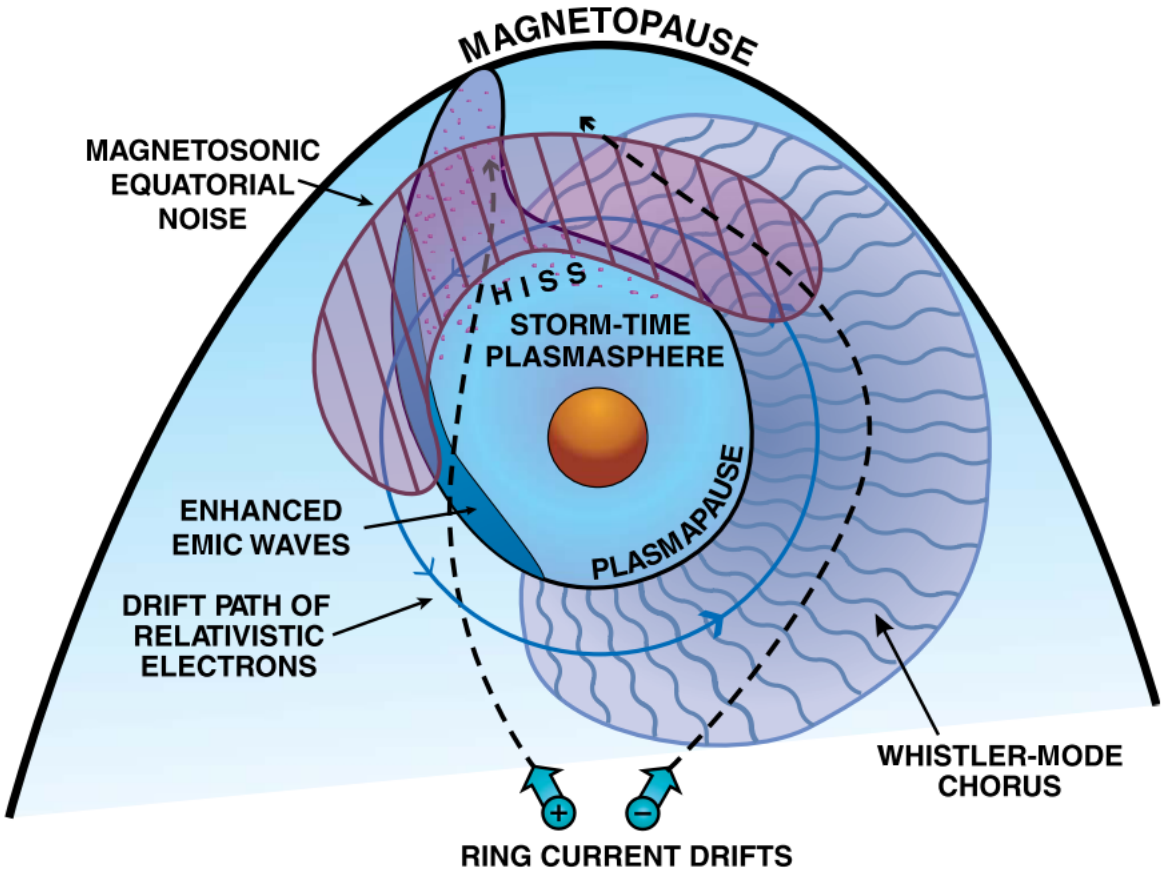

Figure 2.5: From *Thorne* (2010). An illustration of the most important waves in the inner magnetosphere, and their spatial distribution. The ring current drift paths of electrons (10-100 keV) and ions, as well as the drift path of relativistic electrons ($\geq$ 0.3 MeV) are shown.

the $>$ 300 keV and $>$ 1 MeV precipitation, as well as emphasizing the drop-out in fluxes seen during storm main phase. *Meredith et al.* (2011) did not find evidence that precipitation was increased during the flux drop-out.

The waves that have been discussed in this section and their spatial and local time distribution relative to the plasmasphere and drift paths of ring current particles and relativistic electrons are illustrated in Figure 2.5.

Chapter 3

NOAA POES and MEPED

Geomagnetic indices are often used as proxies for energetic particle precipitation. However, while the lower energy part of the electron precipitation spectrum can be closely correlated with geomagnetic indices (e.g. *Hendrickx et al.* (2015)), the higher electron energies are more ambiguous (*Turunen et al.*, 2009). The measure of currents produced in the ionosphere and magnetosphere during particle precipitation does not give any information on, for example, the energy of the precipitating particles, nor if it is electrons or protons, nor the horizontal distribution of the precipitating particles. Relativistic electrons can penetrate to altitudes below 60 km (*Turunen et al.*, 2009). In this altitude range the ionization created by the electrons will not be able to flow as a current, because the atmospheric neutral density is too large. The precipitation can therefore not be measured indirectly via induced magnetic fields. Also, the different solar wind drivers produce different geomagnetic signatures not necessarily to scale or in phase with the fluxes of energetic electrons and protons. The precipitating high-energy particles thus need to be directly measured from space, and the best option available for this is the National Oceanic and Atmospheric Administration Polar Orbiting Satellites (NOAA POES) and their Medium Energy Proton and Electron Detector (MEPED).

Accurate quantification of the effect of energetic electron precipitation still remains a challenge, as the MEPED instruments have had several issues. The MEPED proton detectors are known to degrade due to the very own particles they measure, electrons and protons causes cross-contamination in the proton and electron detectors, respectively, and the detectors do not cover all particle pitch angles which are lost to the atmosphere. Overcoming these challenges has been the main focus of my work, and is addressed in the first three papers of this thesis.

Section 3.1 will introduce some technical details concerning the MEPED detectors and the satellites they are mounted on. We will then proceed to discuss the degradation of the proton detectors in Section 3.2. Section 3.3 deals with the cross-contamination of protons and electrons in the MEPED detectors. In Section 3.4, we will discuss how to retrieve the MEPED loss cone fluxes. We will introduce what efforts have already been made in the different areas, and present our own work in this context.

3.1 The MEPED instrument

The MEPED instrument has been successfully launched on 14 satellites, 12 from the NOAA, and two from the European Organisation for the Exploitation of Meteorological

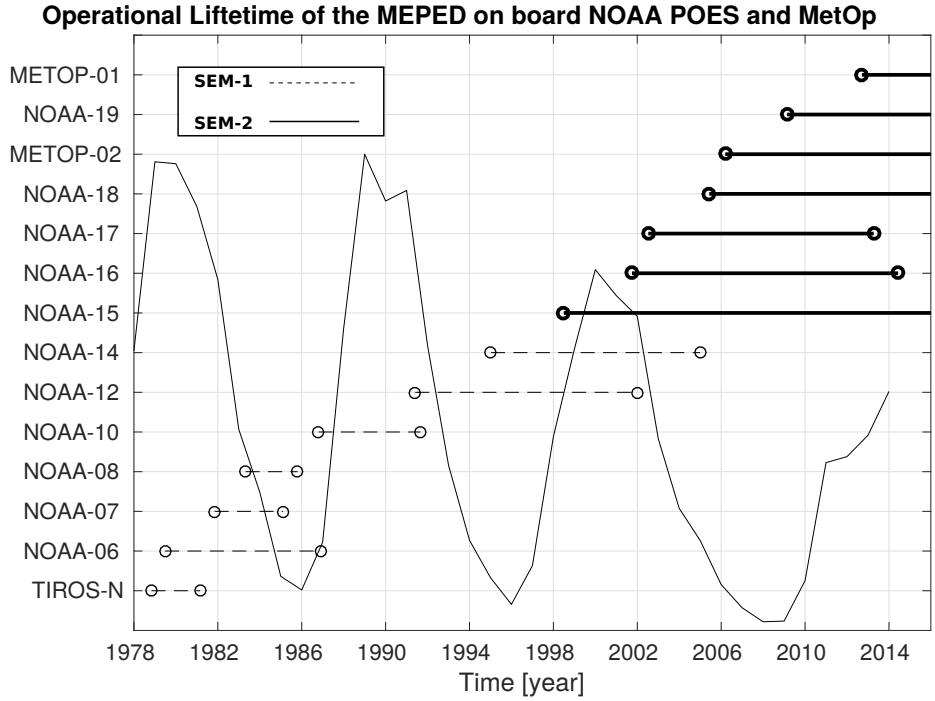

Figure 3.1: The operational lifetime of the MEPED instrument on all NOAA POES and MetOp satellites. The solar cycle is included for reference. This same plot was used in paper II.

Satellites (EUMETSAT), called MetOp satellites. There is one remaining MEPED instrument, planned to be launched on MetOp-C in 2018[1]. In June 2016, five SEM-2 satellites are still in operation.

MEPED is part of the larger instrument package called the Space Environment Monitor (SEM). SEM also contains a Total Energy Detector (TED) which measure the energy flux carried by auroral electrons and protons (0.5-20 keV), and additionally gives information on the energy spectrum and characteristic energy of the measured particles (*Evans and Greer*, 2000). Two generations of SEM exist, with some upgrades introduced when SEM-2 replaced SEM-1 in 1998 on NOAA-15. Figure 3.1 shows the operational lifetime of all SEM carrying satellites, with the two versions distinguished by dashed and solid lines (the figure was also used in paper II). The combined time series of MEPED data stretches over three solar cycles, as shown in Figure 3.1 by the yearly sunspot number. This constitutes, to our knowledge, the longest continuous measurement series of radiation belt protons and electrons. Continuous time series over multiple years is a clear advantage when performing studies of trends in precipitation. A large data base also gives an advantage for statistical studies, since it allows for more cases to fulfil your criteria for event selection.

The POES satellites fly in sun-synchronous polar orbits. Their satellite tracks stay relatively constant in Local Solar Time, except for NOAA-15 and NOAA-16, which exhibit a significant drift of their respective orbital planes through their operational time. The SEM-2 satellites were launched in alternating low-altitude morning orbits and high-altitude afternoon orbits, defined by whether the day-time equatorial crossing occurs before or after Local Solar Time 12:00, respectively. The approximate altitude of these orbits are 825 km and 865 km. The Northern hemisphere magnetic coordinates

[1] http://www.eumetsat.int/website/home/Satellites/CurrentSatellites/Metop/index.html

of all SEM-2 satellites in 2006, 2007, 2009, and 2013 are shown in Figure 3.2 (this plot was also used in paper I). The combined coverage of the high latitude polar regions is fairly good, which is also one of the advantages of using the POES satellites.

The MEPED instrument package consists of two directional electron telescopes and two directional proton telescopes, as well as an omni-detector for very energetic protons measured over a wide range of angles (*Evans and Greer*, 2000). The omni-detectors are not used in this thesis. On all satellites (regardless of SEM version) one proton and one electron directional telescope are mounted such that they point radially out from the Earth, called the 0° detector. The 0° detectors measure particles that precipitate into the high-latitude atmosphere at small pitch angles, near the center of the loss cone. The other telescopes in the proton/electron pairs are mounted such that they should measure the trapped particle population at high latitudes, with pitch angles $\approx 90°$ at satellite altitude. These are generally referred to as 90° detectors. However, both of the telescopes in reality measure a mix of trapped and precipitated particles depending on the satellite's position (*Rodger et al.*, 2010a,b), which we will return to later.

One of the main distinctions between SEM-1 and SEM-2 is the direction of the 90° telescope. In SEM-1 it is mounted perpendicular to both the 0° detector and the satellite travelling direction. In the SEM-2 version however, it is mounted perpendicular to the 0° detector and anti-parallel to the satellite travelling direction (*Evans and Greer*, 2000; *Raben et al.*, 1995). The direction of the SEM-2 MEPED telescopes and the satellite coordinate system is illustrated in Figure 3.3. There was also a change in the number of channels when the SEM package was updated, increased from five to six. The highest channel measure integral flux in both version, and the rest measure differential flux. The electron detector of both SEM versions have three integral flux channels, and the energy ranges for these have been listed together with the proton energy ranges in Table 3.1. In the work of this thesis and the associated papers, we have only used the SEM-2 satellites. A more subtle difference between SEM-1 and SEM-2 is the coating used on top of the silicon detector chip, which differs between the SEM versions and is important to acknowledge if one uses both versions in one study (*Evans and Greer*, 2000; *Raben et al.*, 1995). Since we have only used SEM-2 satellites, we will not go further into these details. From this point in the thesis, if it is not specified, all references to MEPED apply for the SEM-2 version of the instrument.

The MEPED consists of silicon surface barrier detectors. The proton directional telescope has two such detectors stacked on top of each other. Protons stopped in the front detector will be sorted according to energy into one of the five differential flux channels. Protons that penetrate all the way to the back detector is sorted into the integral flux channel (*Evans and Greer*, 2000). Over the 30° entrance of the telescope, a magnetic field is applied to prevent electrons with energies of < 1 MeV from hitting the solid-state detectors. In addition, the detector is shielded in a housing that prevents < 6 MeV electrons and < 90 MeV protons from penetrating through the walls. The electron directional telescope has only one solid-state detector, encased in the same type of housing as the proton telescope. The opening angle of the electron telescope is also 30°. Each proton/electron telescope pair (0° and 90° detectors) share electronics. One detector accumulates counts for 1 second, making a full dataset from both detectors in 2 seconds. The nominal geometric factor for both detector types is 0.01 cm^2 sr (*Evans and Greer*, 2000).

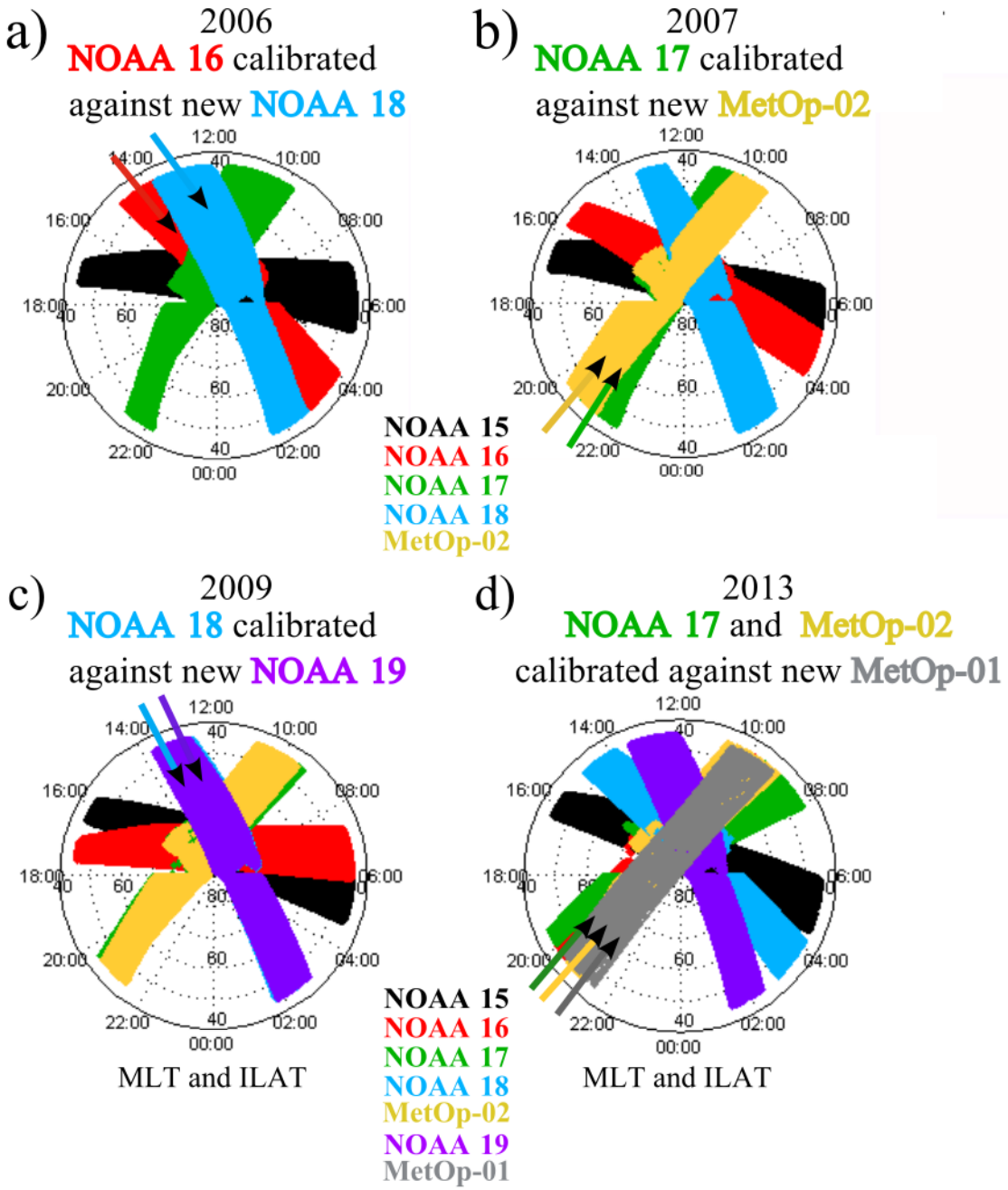

Figure 3.2: SEM-2 satellites' orbital tracks plotted in Magnetic Local Time (MLT) versus Invariant Latitude (ILAT) in four different years. The arrows indicate the satellites orbital direction across the Northern hemisphere. In each of these years, a new POES satellite was launched into orbit in the same local time as an old satellite. This allowed for calibration of the MEPED proton detector of all old satellites in the respective local time orbits. Notice the large drift in the orbital plane of NOAA-16 (red tracks) from 2006-2013. This figure was published in paper I.

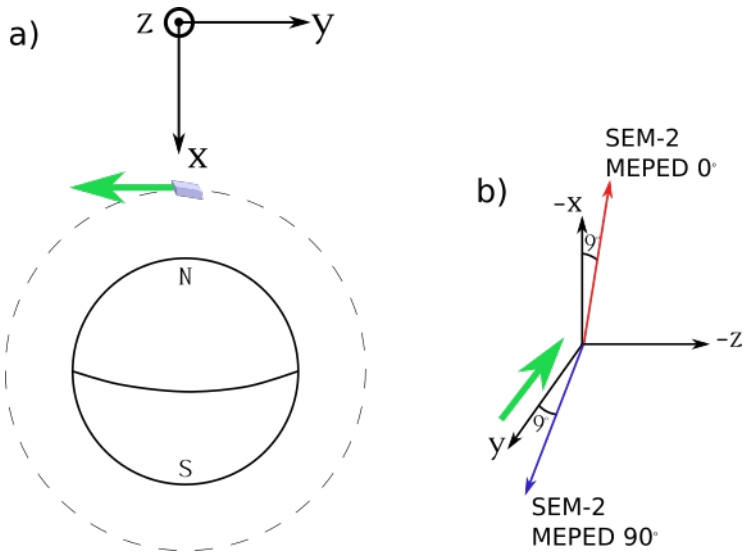

Figure 3.3: a) Illustration of a polar orbiting satellite. The satellite direction in the coordinate system of the NOAA POES is indicated with the green arrow (in the -y direction). The coordinate axes are given in the top of the figure. b) The directions of the two MEPED telescopes of SEM-2 in the same coordinate system, but with axes rotated compared to panel a). The green arrow represents the satellite's direction of travel in the -y direction. The 0° telescopes are in the XZ-plane (here marked by a red arrow), and the 90° telescopes in the YZ-plane (here marked by a blue arrow). The telescopes are rotated 9° away from the -x and +y axes, respectively, both towards the -z axis. This ensures a clear field of view for the telescopes.

Table 3.1: Nominal energy ranges of the proton and electron detectors of the MEPED SEM instruments (*Evans and Greer*, 2000; *Raben et al.*, 1995).

Energy Channel	SEM-2 (keV)	SEM-1 (keV)
P1	30-80	30-80
P2	80-240	80-250
P3	240-800	250-800
P4	800-2500	800-2500
P5	2500-6900	>2500
P6	> 6900	n/a
E1	> 30	> 30
E2	> 100	> 100
E3	> 300	> 300

3.2 The MEPED proton detector degradation

The MEPED proton data was reported by *Lyons and Evans* (1984) to have higher fluxes of precipitating than trapped particles at latitudes where isotropy was expected in the pitch angle distribution. They were not able to explain the feature at the time, but a study by *Galand and Evans* (2000) confirmed that it was due to detector degradation caused by the incoming proton flux. The higher count rate in the 90° detector caused it to degrade faster than the 0° detector. *Galand and Evans* (2000) also noted that detectors on satellites launched during solar maximum had a higher degradation rate compared to those launched at solar minimum. Protons with energy 5 keV to 5 MeV are known to damage silicon detectors (*Coleman et al.*, 1968), and *Galand and Evans* (2000) showed that the flux of protons measured by MEPED in P1-P5 (they used SEM-1 satellites) was large enough to produce a significant damage. In addition, protons in the energy range 9 keV to 30 keV can enter the detector without being counted in P1, but will still contribute to the damage (*Evans and Greer*, 2000; *Galand and Evans*, 2000).

The degradation affects the silicon detector in two ways. A dead layer forms on the surface of the detector. This renders a part of the detector useless, in that the energy deposited there by the protons is not measured. In addition, damage to the crystal structure deeper in the detector can decrease the mobility of the charge carriers released in the silicon crystal, leading to a too small charge collection and an underestimation of the energy of the detected proton. In effect, the lower boundary of the energy channels is raised with time, because a proton will need more and more energy to be counted as, e.g., having 30 to 80 keV. The consequential underestimation of the flux is true for a differential flux spectrum with the shape of a decreasing power law, which is the case for the protons over most of the NOAA POES orbits. In the South Atlantic Anomaly however, differential fluxes may be increasing across P1 and P2, leading to an overestimation of the fluxes at low energies. The two different spectral shapes are illustrated in Figure 3.4, with the respective overestimation and underestimation by a degraded satellite.

3.2.1 Previous efforts to correct for degradation

The first significant study to correct for the degradation was published by *Asikainen and Mursula* (2011). They used integral proton fluxes[2] and compared the spectra of a new satellite to that of an old when the two were found to be close in space and time. More specifically, a conjunction between an old and a new satellite was defined when;

1. It was within five months from launch of the new satellite
2. The latitudinal and longitudinal difference (in geomagnetic coordinates) of the footpoints (at 120 km altitude) of the magnetic field lines confining the two satellites were $< 1^\circ$
3. The relative difference in the L-value of the satellites was $< 10\%$

[2]The integral flux was constructed using P1-P5, excluding P6. P6 can be contaminated by relativistic electrons, which we will elaborate on later. When it is not contaminated, the flux in P6 is so low that it is safe to exclude it when calculating the integral fluxes.

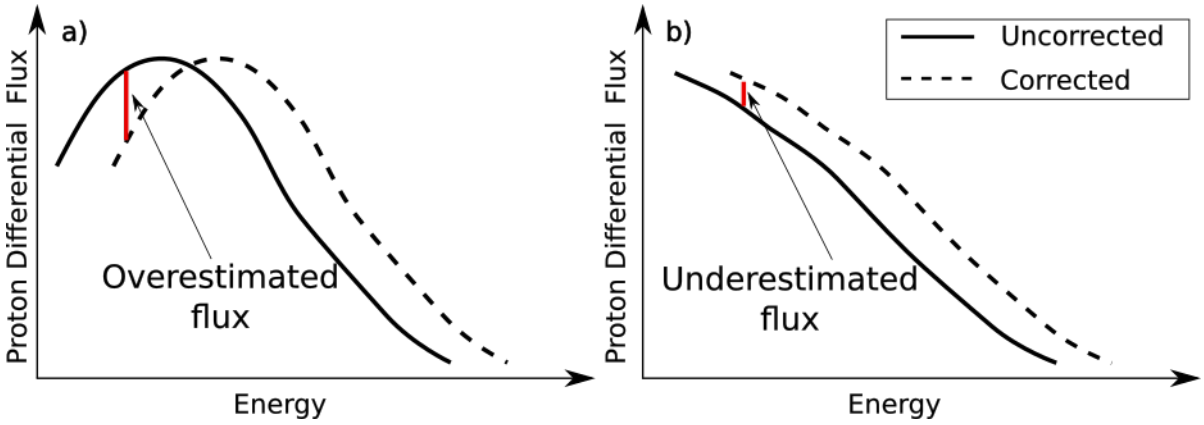

Figure 3.4: a) An illustration of a proton differential spectrum with increasing flux over the lowest energies, before it falls off towards higher energies. Such spectra may be found in the South Atlantic Anomaly. In the case where the MEPED proton detector is degraded (solid line) and the energy thresholds have been corrected (dashed line) we see that the uncorrected spectrum overestimates the flux measured at lower energies (red vertical line). b) Illustration of a spectrum where the flux decreases with increasing energy. In such a case, the uncorrected spectrum will underestimate the flux at any given energy, compared to the corrected spectrum.

4. The particle count rates at the lowest energy channels exceeded the one count level

5. The time difference between two conjugate measurements was < 30 s.

(*Asikainen and Mursula*, 2011). The criteria defining a conjunction between an old and a new satellite ensured that the two satellites were close in time and space. A comparison of spectra was performed based on the assumption that the new detector measured the real, non-degraded spectrum of protons. The two detectors should then measure the same particle population and energy spectrum during conjunctions, however, at different energies. Before the comparison, the spectra were interpolated using a Piecewise Cubic Hermite Interpolating Polynomial (PCHIP), such that the energy and flux of the spectra were resolved on much finer scales than the original five P1-P5 measurements. Comparing the two spectra, the flux level measured in the integral P1 channel of the old detector was identified in the interpolated spectrum measured by the new detector. The corresponding energy was taken to be the effective threshold of the degraded satellite at the time. The relative change in the energy threshold was expressed as the ratio of effective threshold versus nominal threshold;

$$\alpha = \frac{E_{new}}{E_{nom}} \tag{3.1}$$

where E_{nom} are the nominal, lower energy boundaries for each channel, listed in Table 3.1.

For each conjunction a few tens of 2s measurements from both satellites could be used, resulting in multiple α factors. The median of the final distribution of all α factors was taken to be representative for that year. Different fits or interpolation were used to determine the time evolution of the α factor. The integral P4 and P5 channels had too low count rates to determine the level of degradation by satellite conjunctions.

In the integral P1-P3 channels, the general temporal trend of the α factors was increasing, mostly in a non-linear way. In some cases, the factors decreased in 2006/2007, which the authors noted as unrealistic behaviour since it is unlikely that the detectors will self-heal notably. Hence, they disregarded the decrease, and assumed a constant level of degradation from 2006 onwards. *Asikainen and Mursula* (2011) finally presented yearly α factors from the fitted temporal behaviour of the degradation, as well as corrected proton data for the integral P1-P3 channels. This showed for the first time how severe the underestimated fluxes could be, and how important it is to correct for the degradation if the MEPED proton data are to be used in quantitative studies.

A follow-up study (*Asikainen et al.*, 2012) introduced some improvements to *Asikainen and Mursula* (2011). The SEM-1 satellites NOAA-12 and NOAA-08 were corrected for increased noise in the back detector chip. In addition, daily averaged spectra (from the Northern hemisphere $L > 2$) were used to improve the α factors for NOAA-12 and NOAA-06, comparing them to daily averaged spectra from new satellites in the same local time sector. This method was verified by also calculating a NOAA-10 α factor using daily average spectra, and comparing with the *Asikainen and Mursula* (2011) factor which was based on a significant number of conjunctions. The two α factors for NOAA-10, obtained by the two different methods, were found to be the same within error limits, supporting that the method using average spectra was reasonable.

The temporal evolution of the degradation in the SEM-1 satellites was very roughly approximated by linear fits by *Asikainen and Mursula* (2011) due to a limited number of α factors that could be determined by conjunctions. Most of the SEM-2 satellites demonstrated that a linear increase of α with time was unrealistic. *Asikainen et al.* (2012) therefore suggested a new method to improve the time evolution of the SEM-1 satellite α factors. The α factors were expressed as a function of cumulative Ap-index, which was assumed to represent the approximate intensity of particle fluxes in the magnetosphere.

Smaller adjustments were also made to a few of the SEM-2 α factors to make the corrected fluxes agree better between satellites overlapping in time. Finally, the α factors were used to correct the time series of fluxes, and a good linear relationship was found between the accumulated corrected fluxes with E $>$ 120 keV and the P1 and P2 channels' log(α), and fluxes with E $>$ 800 keV with the P3 channel's log(α). The relationship was, however, different for the 0° and 90° detectors, with a larger degradation rate in the 0° detector than in the 90° detector. This discrepancy was explained by the accumulation of fluxes at the energy limits of $>$ 120 keV and $>$ 800 keV which might not be representative for the degrading fluxes. Protons with energy down to 9 keV can enter the detector, and can cause damage to it (*Evans and Greer*, 2000; *Galand and Evans*, 2000). *Asikainen et al.* (2012) were limited to accumulating the fluxes of energy $>$ 120 keV because of the large $\alpha \approx 4$ of the NOAA-06 90° detector, and could not represent the α factors as a function of lower energies without extrapolation of the spectra. They finally argue that due to the average 90° detector spectrum being harder than the 0° spectrum, the actual difference in the degradation rate of the two detectors is probably smaller than the presented $>$ 120 keV and $>$ 800 keV fluxes.

3.2.2 Correction for degradation in Papers I and II

Following up on *Asikainen and Mursula* (2011) and *Asikainen et al.* (2012) I worked on different ways of calibrating the MEPED detectors in my Master thesis (*Ødegaard*, 2013). One of the methods was later developed and applied to the SEM-2 satellites in paper I of this thesis.

Similar to *Asikainen and Mursula* (2011), the method used in paper I is also based on comparing proton integral spectra from a new and an old satellite. The spectra are calculated as monthly average fluxes taken from the whole satellite orbit. Only satellites traversing the same local time were compared, as the intensity of the proton fluxes vary with local time (*Codrescu et al.*, 1997). If the two satellites being compared traverse very different local times, this will make the assumption that the two satellites measure the same particle population and spectrum invalid. Figure 3.5 is from my master thesis (*Ødegaard*, 2013), showing proton flux with energy 30-80 keV from the first year of operation for the SEM-2 satellites from NOAA-15 to NOAA-19, binned and averaged according to magnetic local time and latitude (data from the Northern and Southern hemisphere combined). The data were sorted according to geomagnetic activity as measured by the Kp index. The figure illustrates the varying intensity of proton flux with magnetic local time, and also geomagnetic activity. The data are only from the 0° detector, but an equivalent plot can be found for the 90° detector in *Ødegaard* (2013).

Since only new satellites in the same local time as an old satellite could be used for calibration, NOAA-17 was the only satellite which could be calibrated on two occasions (see Figure 3.2). On the other hand, the statistical approach led to determination of the α factors in the P4 and P5 channels for the first time. Figure 3.6 (which was presented in paper I) shows a monthly mean integral spectrum measured by NOAA-18 (which in this case is the new satellite), and NOAA-16 (the degraded satellite). When this comparison is made, NOAA-16 is approximately four years old, and one can clearly see from the figure how the flux is underestimated severely in P1-P3 channels, and to a smaller degree in the P4 and P5 channels, when compared to the new NOAA-18 satellite. Part b) of the figure demonstrates how the α factor for each channel is determined by identifying the flux measured in the integral P1-P5 channels of NOAA-16 in the interpolated spectrum of NOAA-18, and thus identifying the increased NOAA-16 thresholds.

Applying the method demonstrated in Figure 3.6 for the twelve first months of the new satellite's operational period provided a distribution of twelve α factors per detector per channel, from which the mean α factor was used as representative for the respective years. We thus assumed the new satellite to be non-degraded for the first year of operation. All distributions were found to have very small standard deviations, making the calculated mean of the distribution very robust.

Because the α factors determined by this method were few and separated by several years, an approach was proposed to determine the temporal evolution of the degradation. We assumed the α factors to be a function of the accumulated corrected flux, and calculated it an iterative process. When the calculated monthly α factors were applied for all satellites, the resulting corrected fluxes showed a remarkable agreement throughout the SEM-2 era.

Neither NOAA-15 nor NOAA-19 could be calibrated in paper I, and the α factors for the remaining satellites did not cover their full operational periods (except for

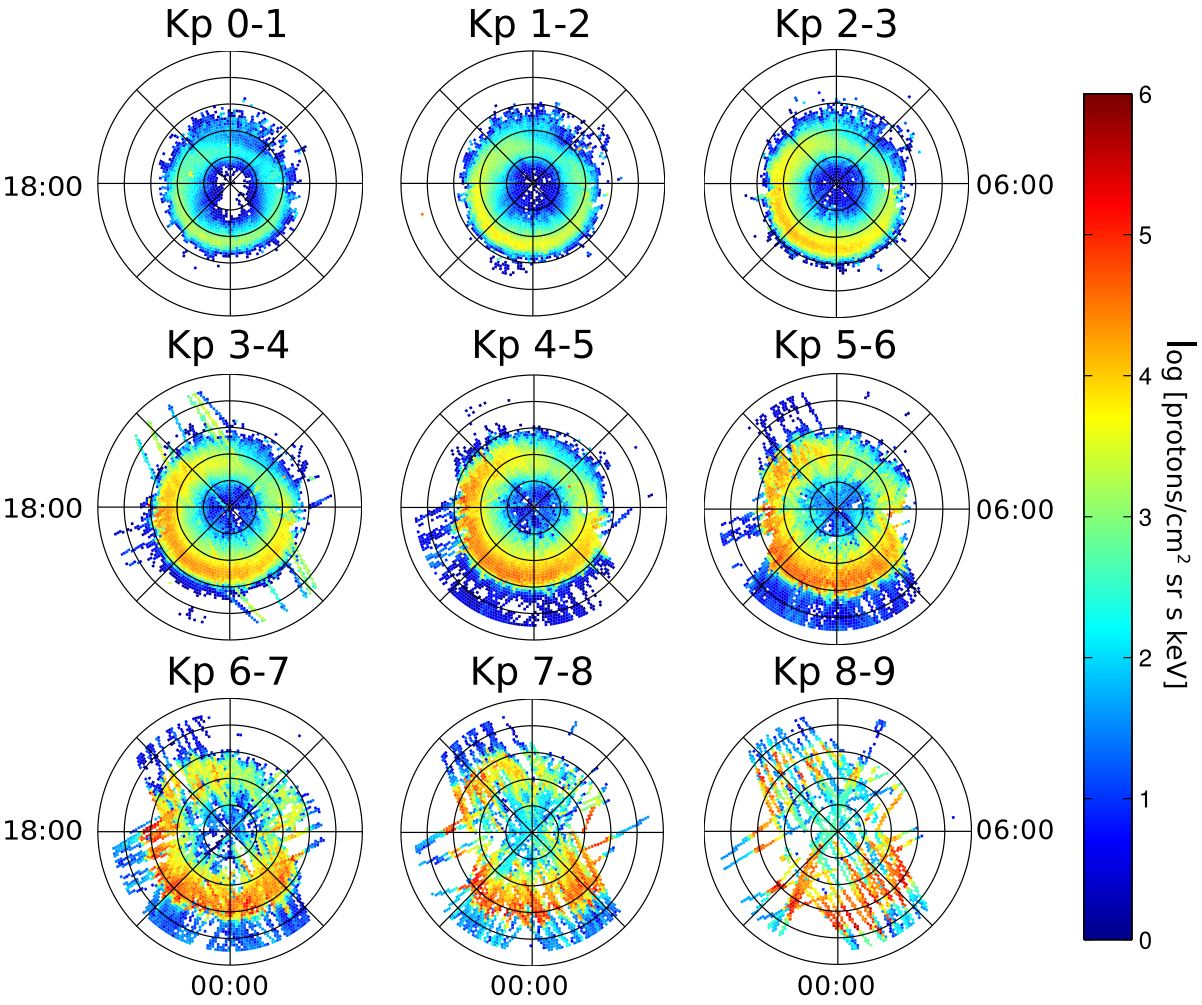

Figure 3.5: Data from the first year of operation for NOAA-15, NOAA-16, NOAA-17, NOAA-18, MetOp-02 and NOAA-19, binned and averaged according to magnetic local time and latitude, Northern and Southern hemisphere data combined. The data are sorted according to geomagnetic activity as measured by the Kp index. The P1 channel of the 0° detector is used here, and the intensity of the flux is plotted in logarithmic colour scale.

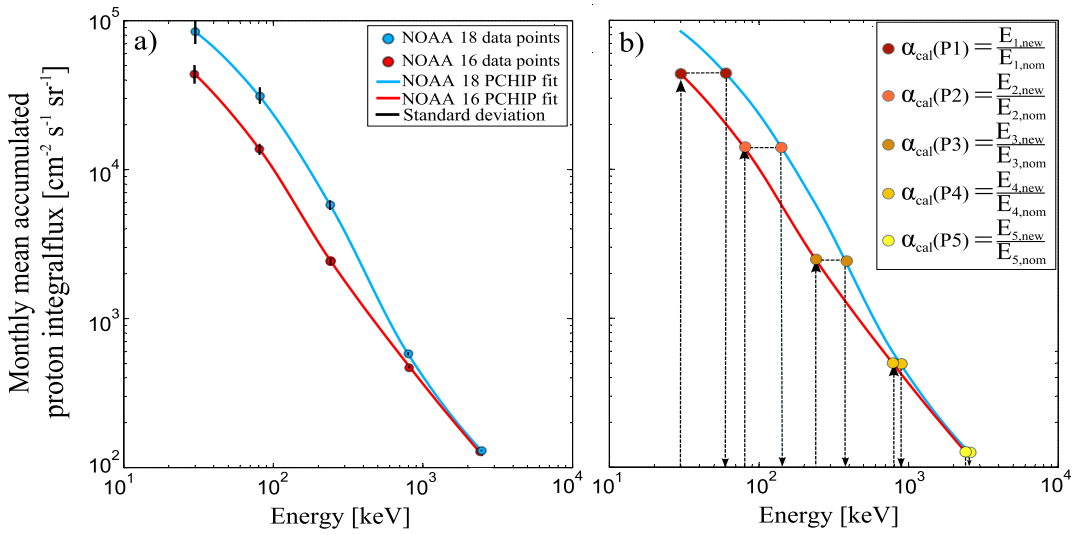

Figure 3.6: A figure from paper I, which illustrates the general process of deriving α factors. Both panels show the average integral flux measured in the P1-P5 channels of the MEPED 90° proton detectors on board NOAA-16 (red colour, degraded satellite) and NOAA-18 (blue colour, new satellite) in October 2005. Panel a) shows the actual measured average flux in filled circles, with the standard deviation as vertical lines. The interpolated spectrum is drawn as solid lines in-between the measured fluxes. Panel b) demonstrated how the α factors for each channel of NOAA-16 is derived.

NOAA-17). We were therefore motivated to find a general way of estimating the α factor of a satellite independent of comparisons with new satellites in the same local time. The result was published in paper II.

Using the α factors estimated in paper I, we found a linear response between the level of degradation and the accumulated corrected fluxes (abbreviated *acf*) with energy E $>$ 90 keV in the same phase of the solar cycle. The correlation coefficients for the P1-P5 channels were $r = [0.84, 0.91, 0.86, 0.60, 0.55]$, using the data from the 0° and 90° detectors to create one linear fit. This means that the detectors degrade in a similar manner in response to a given radiation dose, independent of satellite and the detectors' pointing direction. We showed in the paper that this is only an approximation, and that there seem to be a solar cycle dependence on the degradation rate. To account for this in the model, the $\Delta acf/\Delta t$ was weighted by the average *ap*-index. The correlation was improved for P1-P3 (and decreased slightly in P4 and P5) to $r = [0.93, 0.96, 0.95, 0.58, 0.49]$. The increased correlations in P1-P3 after weighting iare probably due to the *ap*-index representing the low-energy particles degrading the instrument. E $>$ 90 keV is a somewhat high energy to be representative for the total integral fluxes inflicting the damage. The weighting by *ap*-index increases the degradation rate in periods with high activity compared to low activity, accounting for the observed solar cycle dependence.

The α factors from the P1 channels of all satellites are plotted versus *acf* (left) and weighted $\Delta acf/\Delta t$ (right) in Figure 3.7. The equivalent plots for the other channels are shown in paper II. The red symbols are α factors from the 90° detectors, while the open, black symbols are from the 0° detector. The calibration period (Δt) is defined as starting in the month when a satellite is launched, and ending in the month when the same satellite has been calibrated by satellite comparison in paper I.

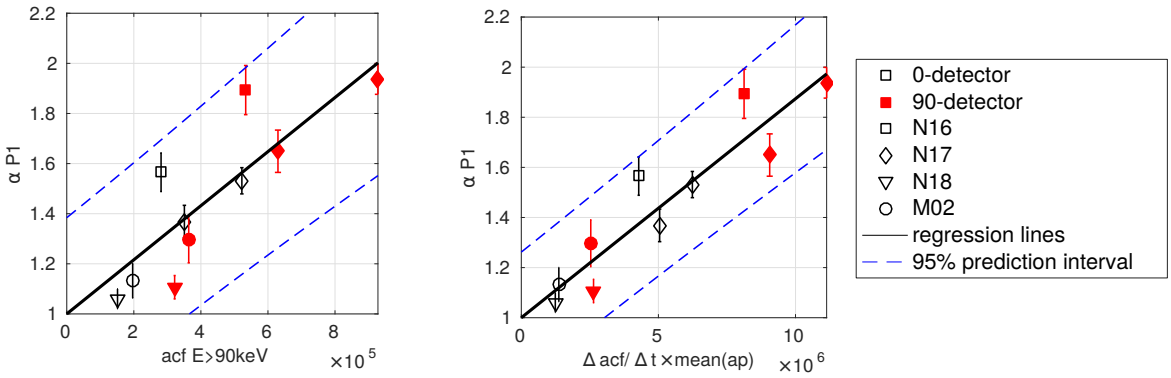

Figure 3.7: Left: α factors for the P1 channel, both detectors and all satellites, plotted versus the accumulated corrected flux (*acf*) with energy > 90 keV. The correlation coefficient is $r = 0.84$. A linear fit is also plotted with the prediction interval outlined in dashed lines. Right: The same α factors, but now the $\Delta acf/\Delta t$ belonging to each factor have been weighted with the mean *ap*-index over the calibration period. The correlation coefficient is increased to $r = 0.94$. A new linear fit is performed, which provides a smaller prediction interval. These panels were part of two figures in paper II, which show the same kind of relation for the α factors of P2-P5.

Using the relationships found between α and the *acf*, and the weighted relationships, we were able to construct two sets of general equations to calculate α factors for any of the given MEPED proton detectors. Equation set (2) in the paper can be used to calculate a detector's α factor at any given instance through its operational time. The first step is to estimate the $\Delta acf/\Delta t$ over the period using Equation set (1) in the paper. $\Delta acf/\Delta t$ is finally weighted by the mean *ap* index over the same period. The use of Equation set (1) and (2) is done iteratively to get the best approximation of *acf* until α converge in Equation set (2).

In the paper, we apply the method to calculate yearly α factors for all SEM-2 satellites. This extends the NOAA-18 and MetOp-02 α factors until 2015, and NOAA-16 to the end of its operational time. In addition NOAA-15, NOAA-19 and MetOp-01 could now be calibrated from launch and until 2015. The error estimation of α using this method is, however, quite large compared to the paper I method. We therefore recommend the α factors presented in paper I for those time periods. The reason for this is that the method presented in paper II is only a model built on the paper I results. The prediction error connected to the linear fits in the model will therefore naturally be larger than the error of the data used to make the model.

We suspected that the α factors provided for NOAA-15 might be underestimated, especially the P1 and P2 α factors. For P1, the 0° (90°) detector reached 1.6 (1.9) in 2015, while for P2 we calculated α factors of 1.7 (2.1). After 17 years in operation, including both the current and previous solar maxima, this appeared somewhat small compared to other satellites. Converting to effective energy thresholds, the factors correspond to 48 (51) keV for the P1 channel 0° (90°) detector, and 136 (168) keV for the P2 channel 0° (90°) detector. In contrast, NOAA-17 was found in paper I to reach approximately the same degradation level in P1 and P2 after only 11 years in operation.

We have therefore performed a new test to estimate the degradation in NOAA-15

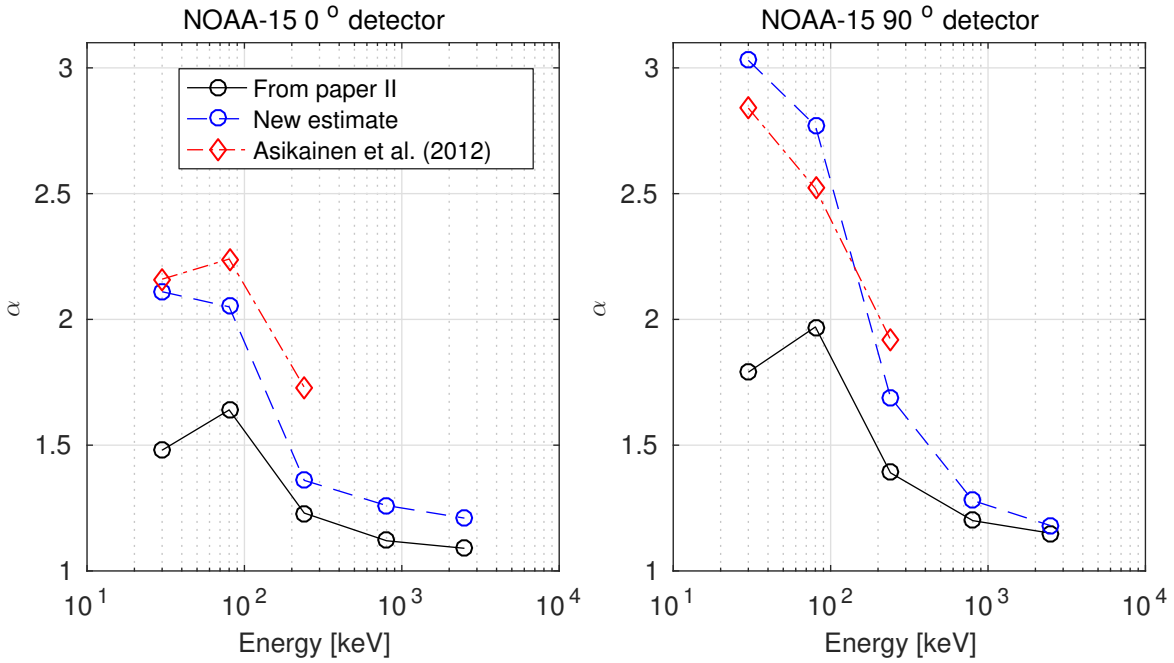

Figure 3.8: Comparison of NOAA-15 α factors from 2008 as found in paper II, with new estimates based on the corrected NOAA-16 measurements. The new estimates are more in agreement with *Asikainen et al.* (2012). The x-axis is here given in energy, representing the nominal thresholds of the P1-P5 channels.

after paper II was published. We exploit the fact that NOAA-15 and NOAA-16's orbital planes drift in local time. In 2008, they are in roughly overlapping orbits. Using the correction factors for NOAA-16 provided in paper II for 2008, we first corrected its monthly average spectra. We then applied the method in paper I. Monthly average spectra for the corrected NOAA-16 were compared against the uncorrected NOAA-15, resulting in 12 α factors. In this case the "new" satellite is the corrected NOAA-16 after it has been in operation for approximately 6 years. The mean α factors from the 12 monthly α factors was found, and was higher in all channels compared to the results presented in paper II. In Figure 3.8, the new estimations are compared to the results from the paper, and with results obtained by *Asikainen et al.* (2012). The new estimations are more similar to results obtained by *Asikainen et al.* (2012) for NOAA-15 in 2008.

In the summary of paper II, based on our concerns connected to the low NOAA-15 estimate, we speculate that the proposed model for estimating α factors cannot be extended far beyond the phases of the solar cycle that have been used to construct the model in the first place. Since NOAA-15 is launched before the previous solar maximum was reached, it may have experienced a degradation rate that is not described by our model, since the previous maximum was much stronger than the one experienced in the current cycle. A more thorough investigation of this should be performed in the future, with a potential adjustment of the model presented in paper II.

The time evolution of the new NOAA-15 α factors from 1998 to 2008 is shown in Figure 3.9 for P1-P5. The α factor from the mid-point of each year is also summarized in Table 3.2.

When using the new estimates for the NOAA-15 α factors, the corrected time se-

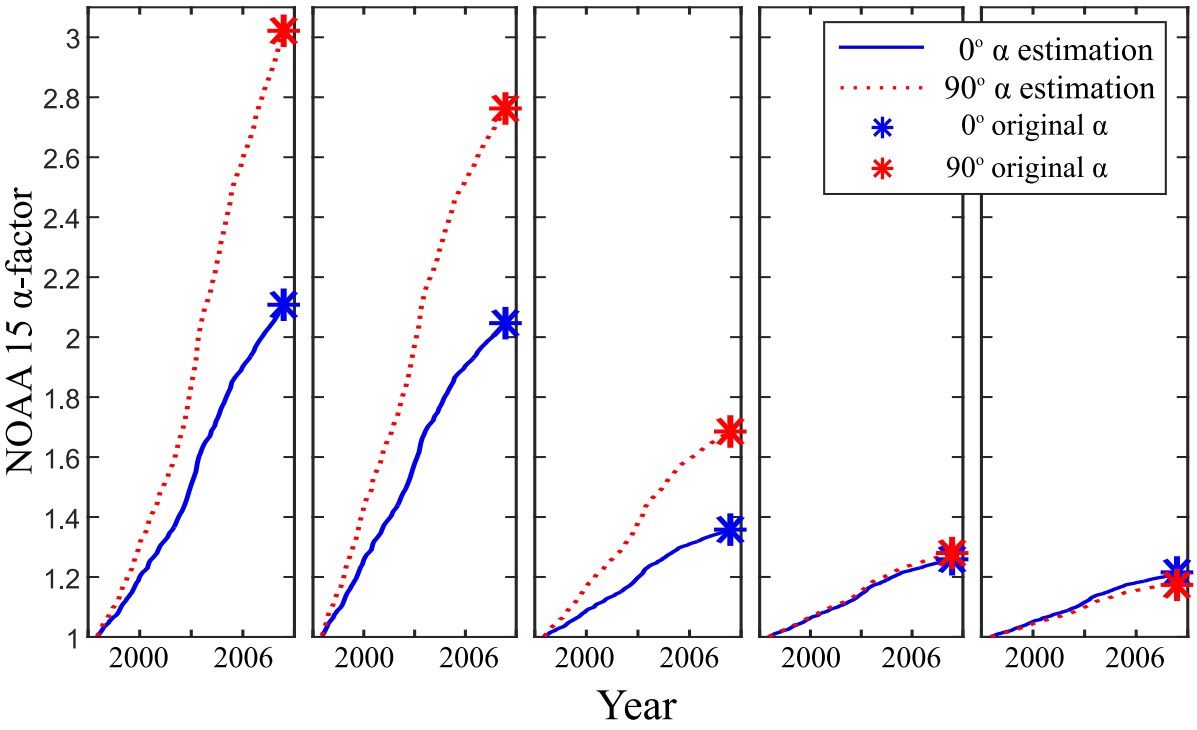

Figure 3.9: The monthly α factor versus time for NOAA 15 from year of launch (1998) and until calibration against NOAA 16 in year 2008.

Table 3.2: The yearly α factors for NOAA-15 for the 0° and the 90° detector. The α factors are from the midpoint of each year, and the subscript x in α_x indicates which channel the factor belongs to ($x = [1,2,3,4,5]$). The factors marked in **bold** are from the year where the comparison with NOAA-16 is performed.

		0° detector					**90° detector**				
Satellite	**Year**	α_1	α_2	α_3	α_4	α_5	α_1	α_2	α_3	α_4	α_5
NOAA-15	1998	1.00	1.00	1.00	1.00	1.00	1.00	1.00	1.00	1.00	1.00
NOAA-15	1999	1.07	1.10	1.03	1.02	1.02	1.11	1.17	1.06	1.03	1.02
NOAA-15	2000	1.17	1.22	1.08	1.05	1.04	1.26	1.37	1.14	1.06	1.04
NOAA-15	2001	1.27	1.33	1.11	1.08	1.07	1.42	1.56	1.22	1.09	1.06
NOAA-15	2002	1.36	1.43	1.15	1.11	1.09	1.57	1.72	1.28	1.11	1.07
NOAA-15	2003	1.51	1.58	1.20	1.14	1.12	1.84	1.97	1.38	1.15	1.10
NOAA-15	2004	1.67	1.72	1.25	1.18	1.14	2.14	2.21	1.47	1.19	1.12
NOAA-15	2005	1.82	1.84	1.29	1.21	1.17	2.43	2.42	1.55	1.22	1.14
NOAA-15	2006	1.92	1.92	1.32	1.23	1.18	2.64	2.55	1.60	1.25	1.16
NOAA-15	2007	2.02	1.99	1.34	1.24	1.20	2.84	2.67	1.65	1.26	1.17
NOAA-15	**2008**	**2.11**	**2.05**	**1.36**	**1.26**	**1.21**	**3.03**	**2.77**	**1.69**	**1.28**	**1.18**

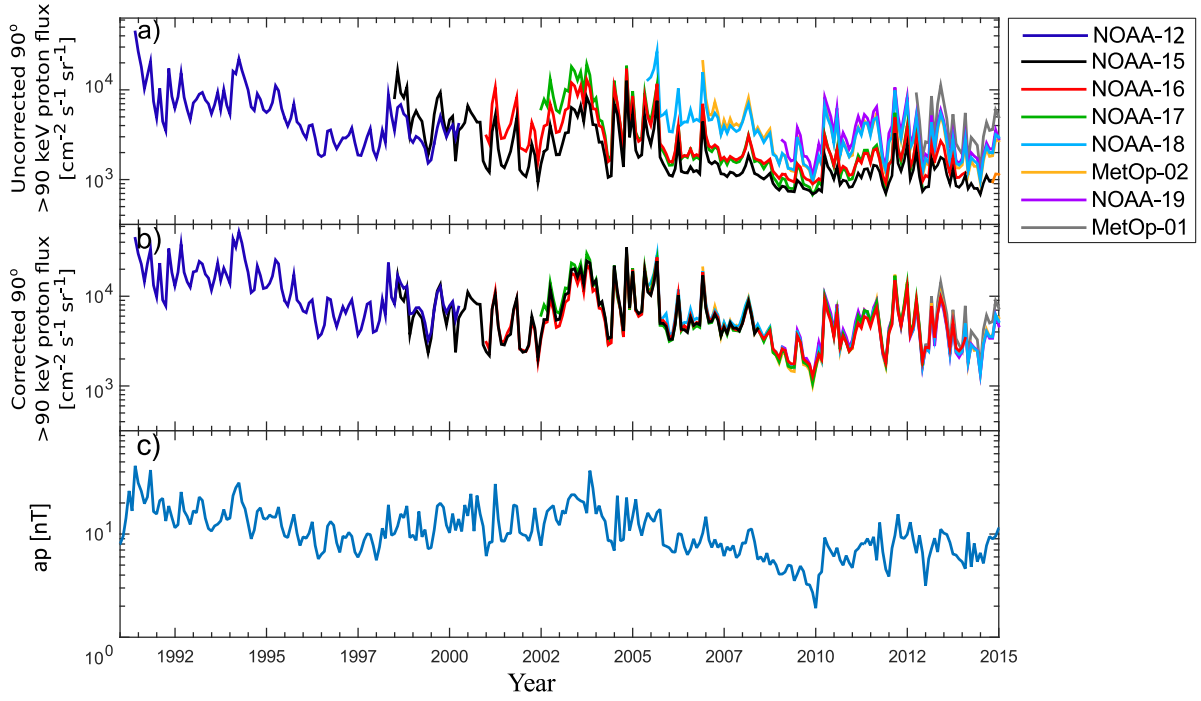

Figure 3.10: a) Monthly uncorrected 90° proton flux with energy > 90 keV, retrieved from the interpolated spectra from the original NOAA data. The different satellites have been colour coded. b) Monthly corrected 90° proton flux with energy > 90 keV. NOAA-12 is here calibrated using the method from paper II. NOAA-15 has been calibrated using the new estimated from this thesis. The rest of the satellites have been calibrated as shown in paper I and II. c) The monthly mean *ap*-index, representing the level of geomagnetic activity.

ries of flux behave in accordance with the other calibrated satellites, as shown for the 90° detector in Figure 3.10. The *ap*-index is included in the figure to demonstrate the monthly geomagnetic activity. The Figure also includes the uncalibrated and calibrated SEM-1 satellite NOAA-12, using the model from paper II. We can clearly see that the fluxes are higher in the corrected time series. The overlap period with the corrected NOAA-15 is not perfect, but improved from the uncorrected versions. This demonstrates that the method from paper II can be used to estimate the level of degradation in SEM-1 satellites, but more work is needed to validate these α factors.

3.3 MEPED cross-contamination

The P6 channel of the MEPED proton detector is an integral channel which can measure protons with energies > 6900 keV. This channel sometimes register a higher count rate than the P4 and P5 channels (800 – 6900 keV). *Sandanger et al.* (2009) reported that the flux observed in the NOAA-15 P6 channel during such conditions was in fact electrons with energies > 1 MeV. *Yando et al.* (2011) confirmed this, comparing the fluxes in the P5 and P6 channels of MEPED to electron measurements by the SAMPEX satellite in the energy range 2 – 6 MeV.

Low energy protons contaminating the electron detector has also been known for a long time (*Evans and Greer*, 2000). Since the proton detector covers the energy range of interest (210-2600 keV, see Table 3.3), it is theoretically possible to subtract the

proton flux from the contaminated electron flux. There are, however, a few challenges in practice. Firstly, the energy resolution of the proton detector is not very refined, and assumptions have to be made on the spectral shape based on the measurements available in P1-P5. Secondly, as already discussed, the proton detector degrades and cannot readily be trusted after one to a few years.

3.3.1 Previous efforts to correct for contamination

Rodger et al. (2010a) investigated MEPED data through a period of $\sim$ 10 years, and concluded that 30% of the electron measurements were contaminated by protons during quiet times, and as much as 55% during geomagnetically disturbed periods. The electron measurements were said to be good when electron and proton measurements behaved according to the relations;

$$\begin{aligned} E1 &> 2 \times P2 \\ E2 &> 2 \times P3 \\ E3 &> 2 \times P3 \end{aligned} \tag{3.2}$$

They only tested for contamination using these criteria, and did not attempt any correction.

A correction for proton contamination in the electron detector was presented by *Lam et al.* (2010), using the count rates of protons in MEPED and estimating a spectrum. They assumed that the spectrum was a series of piecewise exponential functions, one for each of the channels' energy ranges, and used a bow tie method of iteration to find the best spectral shape fitting the data. *Peck et al.* (2015) performed various fits to the spectral distribution; exponential, power law, single and double maxwellian. Neither *Lam et al.* (2010) nor *Peck et al.* (2015) took into account the proton detectors degradation with time, therefore their methods for removal of protons will consequently underestimate the contamination.

Yando et al. (2011) published a simulation of geometric factors of the contaminating fluxes of protons in the electron detector, and electrons in the proton detector. *Asikainen and Mursula* (2013) did a similar study as *Yando et al.* (2011), but included the slightly different SEM-1 MEPED instrument in their study. They took into account that the two generations of MEPED did not have the same response to proton and electron fluxes (*Evans and Greer*, 2000; *Hill et al.*, 1985; *Raben et al.*, 1995; *Seale and Bushnell*, 1987). *Asikainen and Mursula* (2013) also highlight the importance of correcting the electron channel geometric factors, which were shown both by *Yando et al.* (2011) and *Asikainen and Mursula* (2013) to deviate from 0.01 cm^2 sr within the nominal energy ranges.

3.3.2 Correction for cross-contamination in Paper III

Table 3.3 lists the energy ranges to which the proton detector channels (P1-P6) and the electron channels (E1-E3) respond for both protons and electron. The numbers are based on results from *Yando et al.* (2011), listing the contaminating energies where the geometric factor surpasses 0.005 cm^2 sr.

Table 3.3: Energy range of fluxes in the MEPED proton and electron detectors (*Evans and Greer*, 2000; *Yando et al.*, 2011)

Channel	Proton response (keV)	Electron response (keV)
P1	30-80	-
P2	80-250	>7000
P3	250-800	>7000
P4	800-2500	-
P5	2500-6900	-
P6	>6900	>1000
E1	210-2600	>50
E2	280-2600	>100
E3	440-2600	>300

Applying the results by *Yando et al.* (2011) it is possible to address the cross-contamination issues in the MEPED detectors. In paper III we have performed an intricate routine to retrieve corrected electron and proton fluxes. The focus of paper III was, however, the loss cone fluxes and the theory behind the calculations, and the contamination and geometric factor correction were not highly emphasized. We will therefore elaborate here.

Yando et al. (2011) showed that the electron detector did not smoothly respond to electrons within the nominally given energy ranges. The E1 channel, which nominally is said to measure electrons with energies >30 keV with a geometric factor of 0.01 cm^2 sr (*Evans and Greer*, 2000) was found to have a significantly lower geometric factor by *Yando et al.* (2011). The geometric factor was reported to surpass 0.01 cm^2 sr only for energies >100 keV. To account for the discrepancy, we chose to raise the energy threshold of E1 to >50 keV, where the geometric factor was reported as 0.005 cm^2 sr (*Yando et al.*, 2011). In addition, we calculated an average geometric factor for energies $50-100$ keV (E1) and $100-300$ keV (E2) based on the simulations by *Yando et al.* (2011). The flux measured in E2 was corrected by this new, average geometric factor, found to be 0.0114 cm^2 sr. The same was next applied to E1 (0.0072 cm^2 sr). E3 was reported by *Yando et al.* (2011) to have a geometric factor of 0.009 cm^2 sr for energies >300 keV, and we kept the fluxes in this channel without any geometric factor correction.

After applying the new geometric factors to the electron events, we could remove proton contamination using the MEPED proton detectors. Proton spectra were corrected using the results in paper I and paper II to the raised energy thresholds caused by degradation. The correction was done on the integral flux averaged over 16 seconds. In the PCHIP interpolated proton spectrum, the proton energies impacting E1-E3 were identified. These are listed in Table 3.3. The associated proton fluxes were subtracted from the E1-E3 fluxes.

We proceed to check the severity of the proton contamination. Only when the ratio of removed protons/remaining electrons is <1 we chose to trust the remaining electron flux. This means that we allowed for a proton contamination of up to 50%. All three channels had to fulfil the criterion for the spectrum to be kept in the dataset. We also

checked the spectrum after proton removal to see if the fluxes behaved according to $E1 > E2 > E3$. If not, the spectrum was disregarded.

The method successfully removes electron spectra which are highly contaminated by protons, for example during the solar proton events in 2003. Checking the period October 1st 2003 to December 31st 2003 on the NOAA-17 satellite (Northern hemisphere, MLT 18-24), our method only remove 4.8% of the spectra in the 0° detector, and 4,4% in the 90° detector data due to more than 50% contamination. Using criteria for proton contamination suggested by *Rodger et al.* (2010a) would remove 49.4% of the 0° detector spectra, and 45.5% of the 90° detector spectra due to a too high contamination through this period.

A much larger portion of the data is removed due to not fulfilling $E1 > E2 > E3$. This typically occurs when the electron fluxes are of the same order as the background noise in all three channels. 37,3% of the data in the 0° detector and 32,5% in the 90° detector are disregarded. The electrons fluxes, uncorrected for proton contamination, in E3 (> 300 keV) of both detectors are shown in the upper panels of Figure 3.11. The contaminating fluxes of protons with energies > 440 kev (retrieved from the MEPED proton detector) are shown in the middle panel. The corrected fluxes in E3, where contamination is removed and the spectral forms ($E1 > E2 > E3$) are checked, are presented in the bottom panels.

In addition to the E1-E3 electron fluxes, we retrieved the > 1 MeV electron fluxes contaminating the proton detector as a fourth electron integral channel in paper III. *Yando et al.* (2011) showed that the energy at which the geometric factor of the contaminating high-energy electron fluxes surpasses 0.005 cm^2 sr in the P6 channel was 1000 keV. When the fluxes in the P5 channel (2500-6900 keV) are much lower than the fluxes in the P6 channel, the flux can be assumed to be caused by electrons. In the 16 second averaged proton measurements, we perform a check of P5 versus P6. Since P6 is an integral flux channel, we use the integral P5 flux in the comparison (that is, we multiply the differential P5 flux with the energy width of P5). When the fluxes are such that P6 [cm^{-2} sr^{-1} s^{-1}] $> 10\times$ P5 $\times 4400$ keV [cm^{-2} sr^{-1} s^{-1} keV^{-1}], we assume that the fluxes are purely electrons. This threshold was based on the empirical data presented in the paper, where we found that this criterion effectively sorted protons from electrons in the large Halloween storm of 2003, as well as other solar proton events of that year (see Figure 3 in the paper).

3.4 MEPED electron loss cone fluxes

We discussed the definition of the loss cone in Section 2.3.2. Since the pitch angle restricting the loss cone (α_{LC}) is dependent on the magnetic field strength at the altitude beneath which the particle is lost (assumed to be around 120 km), α_{LC} can be different in the Northern and Southern hemispheres. Figure 3.12 shows the magnetic field strength at an altitude of 120 km, produced by the International Geomagnetic Reference Field (IGRF) model. An extreme case of different loss cone size on the two hemispheres is found in relation to the South Atlantic Anomaly (SAA), where the magnetic field exhibit a particularly weak spot. This can be seen in Figure 3.12 at longitudes $\sim 300°$ and latitudes $\sim -20°$ as a deep blue shade.

The weak magnetic field strength in the SAA results in a low mirror altitude for the

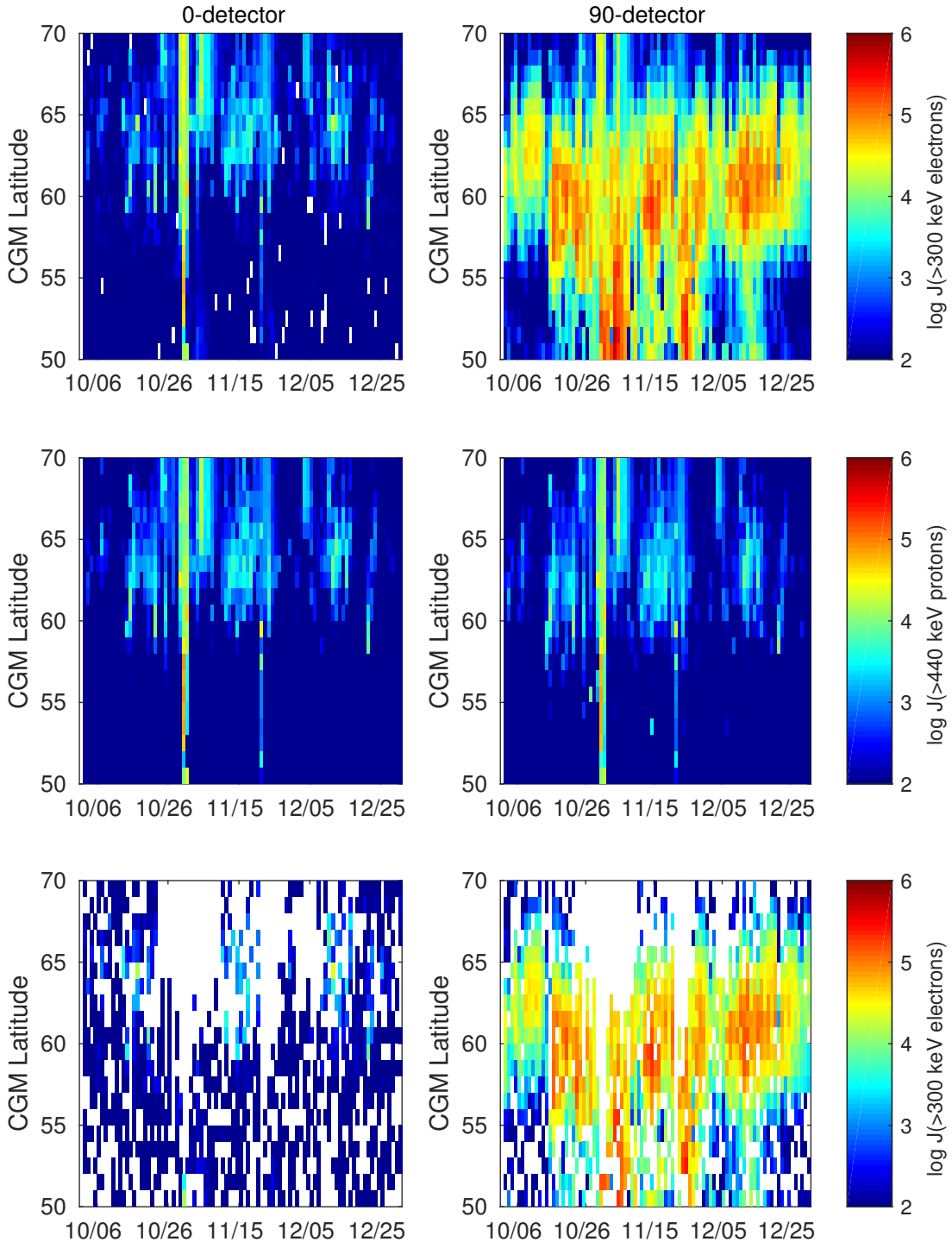

Figure 3.11: Upper panels: Electron flux in the E3 channel ($>$ 300 keV) without corrections for proton contamination applied. Middle panels: Contaminating fluxes of protons $>$ 440 keV, retrieved from the MEPED proton detectors. Bottom panel: Electron flux in the E3 channel, corrected for proton contamination and checked for the spectral shape fulfilling $E1 > E2 > E3$. All data are from NOAA-17, and from the MLT sector 18-24 in the Northern hemisphere.

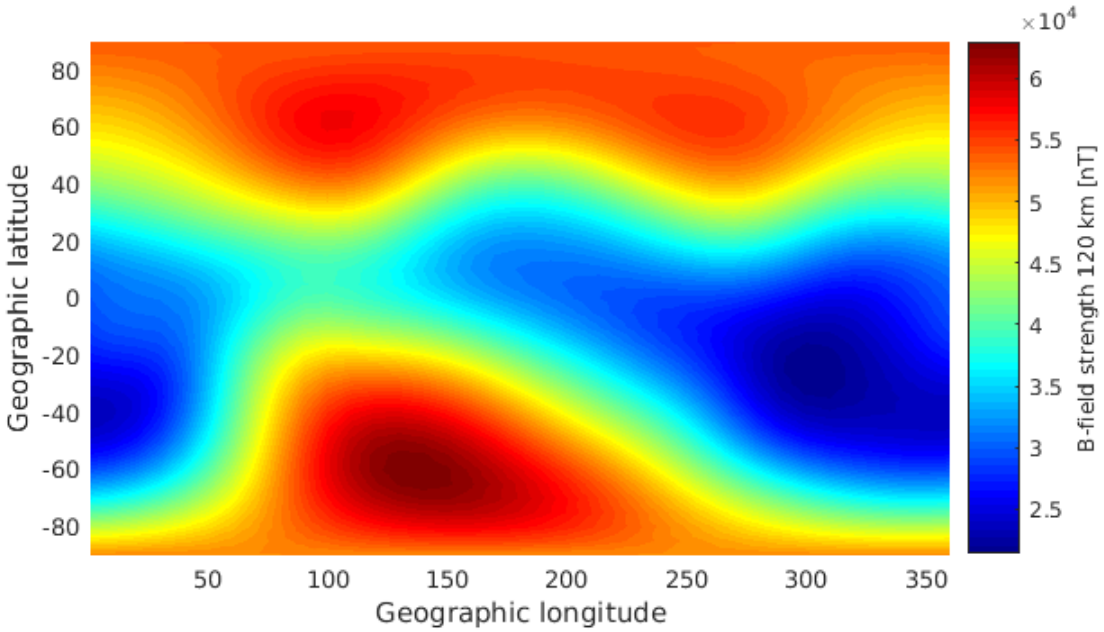

Figure 3.12: The magnetic field strength at an altitude of 120 km in 2015, according to the International Geomagnetic Reference Field (IGRF) model.

particles compared to the conjugate Northern mirroring altitude. This leads to a larger particle loss in the SAA compared to the conjugate magnetic latitude in the Northern hemisphere, but also compared to other longitudes in the Southern Hemisphere. This again means that particles that are just outside of the bounce loss cone may still be lost when the particles have drifted around the Earth and reached SAA longitudes. Due to this fact, the literature separates between the Bounce Loss Cone (BLC) and the Drift Loss Cone (DLC). To best estimate the atmospheric response of particle precipitation at a given set of coordinates, we calculate the local BLC size associated with the specific location.

The MEPED directional telescopes can only measure a subset of pitch angles, limited by the telescope opening angle of $\pm 15°$. The $0°$ detectors are directed radially outward from the satellite to measure precipitating particles, i.e. inside the bounce loss cone, at high latitudes. *Rodger et al.* (2010a,b) showed that for $L > 1.4$ the MEPED electron $0°$ detector measure, for the most part, BLC fluxes. *Rodger et al.* (2013) plotted (in their Figure 2) the fraction of the BLC radius the electron $0°$ detector observe, showing that it varies from $\sim 40 - 50\%$ at $L > 1.4$. At these same latitudes, the $90°$ detector will also measure a portion of the BLC, as well as DLC and trapped particles (see *Rodger et al.* (2010b) Figure A2). The pitch angle coverage of the $90°$ telescope systematically depends on whether the satellite is in the descending or ascending phase of the orbit.

The varying magnetic field strength, and also direction, makes it a challenge to interpret what the MEPED $0°$ and $90°$ detectors are actually measuring. The size of the loss cone varies, the direction of the telescopes in relation to the magnetic field varies, and adding to this, the flux distribution varies with pitch angle, and the efficient detector area varies with the acceptance angle over the telescope. Except for the cases when strong diffusion dominates and the electron flux is isotropic, the pitch angle distribution in the BLC generally shows higher fluxes with increasing angles, as illustrated in Figure

3.13. This means that the largest contribution of flux to the BLC comes from the population with pitch angles close to α_{BLC}. In such cases, taking the flux measured by the 0° detector as representative for the whole BLC and integrating over pitch angles $\alpha \leq \alpha_{BLC}$, would underestimate the total flux in the BLC. Similarly, the fluxes measured by the 90° detector will represent an overestimation of the precipitating particles.

3.4.1 Previous effort to account for the loss cone flux

Rodger et al. (2013) compared the MEPED electron flux with ground-based riometer observations. Riometers respond to changes in the electron density in the lower ionosphere, thus to precipitation from the whole loss cone. It does not provide information on the energy of the precipitating particles. *Rodger et al.* (2013) calculated the produced changes in electron number density from the measurements in the MEPED electron 0° detector, and compared it with riometer absorption. They found a reasonable agreement for E1 fluxes $> 10^6$ [cm^{-2} s^{-1} sr^{-1}]. Otherwise, the riometer measured higher electron densities than the MEPED calculations. *Rodger et al.* (2013) further investigated this underestimation by MEPED, and found that the probable cause is weak diffusion during low geomagnetic activity. They improved the estimation of the BLC flux by using a geometric mean of the 0° and 90° detector fluxes to calculate the produced changes in electron number density. This led to an overestimation in low active periods, but closer to the riometer observations than by using only the 0° detector.

Asikainen and Ruopsa (2016) used an average between the 0° and 90° detector electron fluxes to study the long term trend of energetic electron precipitation, assuming that this may be a closer approximation to the actual BLC content compared to using only the 0° detector.

The mathematical approach of using both the arithmetic and geometric mean may impose some systematic differences. *Rodger et al.* (2013) did his validation against a specific ground based station. However, the pitch angles for the detector will vary over the orbit of the satellites, and systematically vary with the descending or ascending phase of the satellite. Also, in view of that the comparison was made in the auroral zone where isotropy is more common compared to the subauroral latitudes where the medium energy (100-300 keV) and relativistic (>300 keV) electron precipitation usually occur, the geometric mean will not provide sufficient accuracy in determining the particle energy deposition. Applying the geometric mean to lower L-values, Craig Rodger confirmed (personal communication), that the geometric mean fluxes provided an unrealistic high BLC flux estimate.

Already from the very early age of studying the radiation belt physics, pitch angle scattering by wave-particle interaction received considerable attention. This effort resulted in the theoretical solution of the Fokker-Planck equation for particle diffusion (*Kennel and Petschek*, 1966; *Theodoridis and Paolini*, 1967). The equations apply independently of the wave-particle source causing the diffusion (*Theodoridis and Paolini*, 1967). The Fokker-Planck equation has therefore previously been used to determine the level of diffusion based on the MEPED observations (*Li et al.*, 2013, 2014a,b) with the purpose of identifying the wave-particle sources for pitch angle scattering. Although, these studies did not calculate the BLC fluxes, retrieving the level of diffusion is an important step towards a physics-based estimate. The MEPED 0° and 90° fluxes were fitted onto the solution of the Fokker-Planck equation for wave-particle diffusion

(e.g. by *Li et al.* (2013)). The Fokker-Planck equation requires steady-state conditions where the particles being lost will be replenished so that the pitch angle distribution is in diffusion equilibrium. However, *Li et al.* (2013) and multiple follow up papers have shown that without any strict criteria the diffusion coefficient estimated from the MEPED instrument was consistent with independent observations of chorus waves by the Van Allen Probes.

3.4.2 Constructing the loss cone fluxes in Paper III

Using theory on pitch angle diffusion and wave-particle interactions in the magnetosphere, we were able to propose a method in paper III calculating the BLC fluxes from the MEPED electron directional telescopes. The energy deposition in the atmosphere from the theoretically derived BLC fluxes was compared with OH measurements, and found to be a reasonable estimate of the true precipitating flux producing the changes to the atmospheric OH concentration.

After all corrections described in the previous sections had been performed, and the P6 channel was added to all spectra as > 1 MeV electrons, the MEPED directional fluxes were used to estimate the total BLC flux. Relevant theory regarding the pitch angle diffusion theory by *Kennel and Petschek* (1966) and *Theodoridis and Paolini* (1967) has been outlined in the paper. The main procedure is summarized here.

Based on the IGRF magnetic field model, we construct a library of the equatorial loss cone size given by the limiting pitch angle α_{eq}, covering geographical latitudes $40^\circ - 90^\circ$ (in both hemispheres), and latitudes $0^\circ - 360^\circ$, and assuming the particle to be lost at an altitude of 120 km. We then calculate a complete set of pitch angle distribution functions for all of the different equatorial loss cone sizes (ranging from $\alpha_{eq} = 1^\circ$ to $\alpha_{eq} = 31^\circ$). The set of pitch angle distribution functions range from weak diffusion ($\sqrt{DT} = \frac{1}{4000}$) to strong diffusion ($\sqrt{DT} = 1$). From the equatorial loss cone size, we calculate the loss cone size at satellite altitude. At satellite altitude we account for the detector response function, as well as the the detectors' viewing angles with respect to the loss cone (see Figure 1 in paper III). We can then use the measurements from the MEPED 0° and 90° detectors to find the pitch angle distribution within the loss cone at satellite altitude. We do this by first identifying the central pitch angle measured by each of the two detectors (this is given in the dataset). We then find the ratio of the $90^\circ/0^\circ$ fluxes. The pre-calculated pitch angle distribution which have the same ratio of flux at these two pitch angles (the central pitch angle in each telescope), is then the real pitch angle distribution. From the distribution at satellite altitude, the distribution in the atmospheric loss cone at 120 km follows.

One example is illustrated here in Figure 3.13. The central pitch angles measured by the 0° detector is in this case identified as $\sim 20^\circ$, and for the 90° detector it is $\sim 65^\circ$. Depending on the flux measured by the two detectors, and the ratio between the fluxes, one would choose the magenta, blue or black pitch angle distribution function. The three functions represents three different theoretical diffusion profiles. The loss cone size at satellite altitude is here slightly less than 60°, and from the chosen pitch angle distribution together with the MEPED measurements, the total loss cone flux can be constructed.

We found that it was necessary to apply a lower limit on the 0° fluxes at energies

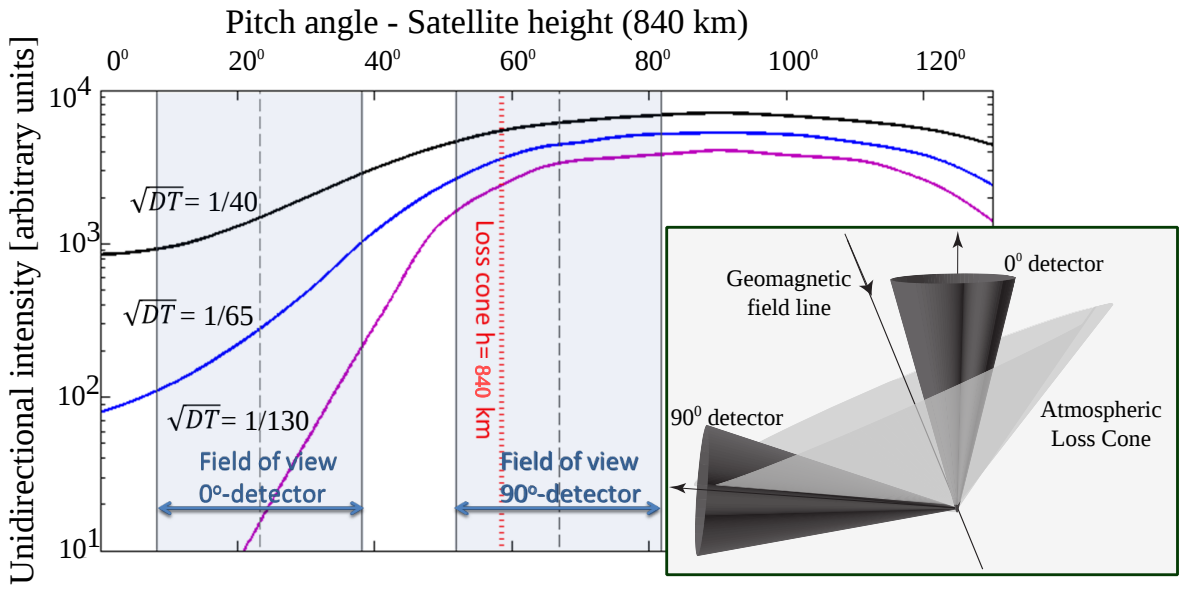

Figure 3.13: Theoretical distributions of fluxes depending on pitch angles at the altitude of the satellites (∼840 km). Three different distributions are shown with different diffusion coefficients, in black, blue and magenta curves. The detectors' field of view are shaded in pale blue, and the size of the loss cone is marked with a vertical, dashed red line. The inserted panel is a cartoon of the two detectors' field of view relative to the magnetic field. The size of the loss cone is shown enclosing the field line.

$>$ 50 keV and $>$ 100 keV of 300 [cm^{-2} s^{-1} sr^{-1}] when deriving the BLC fluxes. This was determined based on comparison with the OH measurements provided by the Aura satellite, which covers the same local time in 2008 as NOAA-18. The energy deposition calculated from the BLC fluxes, when the lower limit was applied, corresponded to a calculated OH production of the same order of magnitude as the actual OH measurements.

Chapter 4

Applications of the optimized energetic particle fluxes from MEPED

Up until now, the quantification of energetic electron precipitation (EPP) has been challenging due to the instrument related issues. Our new optimization opens the door for a more accurate estimate of the energetic particle fluxes. This is in particular interesting from the perspective of both radiation belt and atmospheric physics, as we are now able to quantify the radiation belt variation due to atmospheric loss as a result of pitch angle scattering from wave-particle interaction. Precipitating electrons and protons deposit their energy at various altitudes throughout the lower thermosphere down to the stratosphere, depending on their initial energy. It has long been recognized that EPP is an important source of NO_x (*Randall et al.*, 2005, 2009; *Sætre et al.*, 2004, 2006, 2007) and HO_x (*Andersson et al.*, 2012; *Verronen et al.*, 2011; *Zawedde et al.*, 2016). Increases in the concentrations of NO_x and HO_x can affect the atmospheric dynamics. This is because both species can catalytically destroy ozone, which in turn can alter the heating and cooling rates in the atmosphere. As ozone plays a key role in the middle atmospheric energy budget, a good estimate of the particle energy input and its altitude distribution is crucial for determining the role of EPP in affecting the middle atmosphere, as well as its potential impact on the regional surface temperatures.

In Section 4.1, we will present findings from paper IV related to storms that may cause atmospheric effects. Section 4.2 discusses some of these effects, and presents findings from *Zawedde et al.* (2016), and preliminary findings by C. Smith-Johnsen, who both use data optimized through the work of this thesis.

4.1 Precipitating electron fluxes during geomagnetic storms

In Chapter 2, theory regarding radiation belt particle acceleration and loss were presented. Storms driven by CIRs and CMEs can cause high-energy electron precipitation, since geomagnetic activity in general will enhance wave generation in the magnetosphere.

There is evidence that geomagnetic storms caused by CIRs, which produce moderate main phase ring current enhancements, can create significant atmospheric effect, e.g. in the OH production (*Zawedde et al.*, 2016). To make progress in the understanding of the EEP impact on the atmosphere, also during quite weak geomagnetic disturbances, we study CIR storms in paper IV. Our main motivation was to identify

controlling parameters which decide whether a storm will have EEP or not. This is closely related to whether the source electron population in the magnetosphere is accelerated to higher energies, or if the high-energy electrons are depleted during the storm.

We identified 41 isolated storms driven by CIRs in the period 2006-2010, during the declining and minimum phase of the solar cycle. The method of deriving BLC fluxes from paper III was applied for all operational satellites during a storm. We only used data from the Northern hemisphere, and binned the data from all satellites in a magnetic grid covering almost the entire polar region (corrected geomagnetic latitude $> 40^{\circ}$). There was unfortunately limited coverage of the 22-2 MLT sector. We use superposed epoch analysis to investigate the average behaviour of fluxes, solar wind parameters and geomagnetic indices. The zero epoch is identified in the solar wind pressure, which increase when the CIR arrive.

4.1.1 Energetic electron precipitation and its dependence on Magnetic Local Time - Paper IV

Electrons with energies 50-100 keV can penetrate to the upper mesosphere, while 300-1000 keV electrons penetrate to the middle and lower mesosphere (see Figure 4.1). It is therefore of interest to study the whole spectrum of energies provided by the MEPED electron detector. When conducting a superposed epoch analysis of the BLC fluxes, we find that $>$ 50 keV and $>$ 100 keV are unevenly distributed in MLT and magnetic latitude.

The $>$ 50 keV fluxes respond more or less immediately after zero epoch with a large increase in the precipitation, and the $>$ 100 keV fluxes are delayed by a few hours. The maximum increases in both these channels are largest in the 2-6 MLT and 6-12 MLT sectors. This is interpreted as a result of the eastward electron drift direction around the Earth, and that a large portion of the flux is lost before it can make a full drift orbit. The same asymmetry is not seen in the $>$ 300 keV and $>$ 1 MeV BLC fluxes, as these energies have a shorter drift period. This is also indicative of whistler mode chorus interacting with the lower energies ($>$ 50 keV and $>$ 100 keV) in these MLT sectors (see also Figure 2.5). In addition to the MLT asymmetry, we also observed that the precipitation was spread over a larger range of latitudes in the 6-18 MLT sector compared to 18-22 MLT and 2-6 MLT.

An interesting phenomena was observed in the 18-22 MLT sector. While the $>$ 100 keV, $>$ 300 keV and $>$ 1 MeV fluxes at 65° corrected geomagnetic latitude displayed a drop-out after zero epoch, the precipitated fluxes were increasing at latitudes of 60° in these energies. That is, while some process decrease the precipitation at radial distances of $L = 5.5$, another process increase the precipitation further in, at $L = 4$. It may be that EMIC waves act on the electrons to increase precipitation at $L = 4$, but other processes dominate further out in the magnetosphere which accounts for a net loss of particles (by other means than precipitation) at $L = 5.5$.

4.1.2 Energetic electron precipitation and its dependence on the solar wind and geomagnetic indices - Paper IV

In the second part of the paper, we divided the storms into three groups according to the change in BLC fluxes measured in the $>$ 300 keV and $>$ 1 MeV channels. We compared the pre-storm fluxes (an average over two days before zero epoch) with the post-storm fluxes (an average over day 4 and 5 after zero). The averages were taken over all MLT and cgm latitudes $55^\circ - 70^\circ$. The groups were defined as;

1. post-1 MeV flux $>$ 2$\times$ pre-1 MeV flux
2. post-300 keV flux $>$ 2$\times$ pre-300 keV flux, and post-1 MeV flux $\leq$ 2$\times$pre-1 MeV flux
3. post-300 keV flux $\leq$ 2$\times$ pre-300 keV flux, and post-1 MeV flux $\leq$ 2$\times$pre-1 MeV flux.

The criteria above ensured that each storm was only sorted into one group. We found that 22% were sorted into group 1, 44% into group 2, and the remaining 34% into group 3.

A superposed epoch analysis of the solar wind parameters and geomagnetic indices, where the data were divided into the three groups, revealed that the group 1 and group 2 storms had higher solar wind velocities sustained over a longer period compared to group 3. Group 1 was further separated by having an average IMF $B_Z < 0$ for a longer time, and with more negative values compared to groups 2 and 3. The general storm strength of the average group 1 storm was higher in all indices, although not by a large factor.

Although a correlation could be obtained between the BLC fluxes and most of the solar wind parameters and geomagnetic indices, there was little systematic behaviour that could separate a storm from group 1 and a storm from group 3. For example, storms from all groups were found for small and large Dst response. The only parameter which stood out as a method for sorting the storms were the integrated solar wind E-field from zero epoch until day 3-4. The E-field has previously been used as a proxy for solar wind energy input (*Burton et al.*, 1975), and we speculate that this is the controlling parameter separating the different groups of CIR storms. Using the *Akasofu* (1981) Epsilon (ε) parameter, we calculated the energy input in Joules. We found that the average energy input was highest for group 1 storms, and smallest for group 3. The possible mechanism coupling the energy input to the magnetosphere and the increase in precipitation, however, is somewhat unclear.

Knowledge of both the local time, latitude, timing and level of EEP is important to be able to reconstruct EEP events back in time. Their link to solar wind and geomagnetic observations might provide a key to develop an EEP parametrization to be used in model and observational studies.

4.2 Atmospheric effects from particle precipitation

The atmospheric effects from EPP has been studied for many decades, but previously with main emphasis on large solar proton events and auroral electrons (*Sinnhuber et al.*,

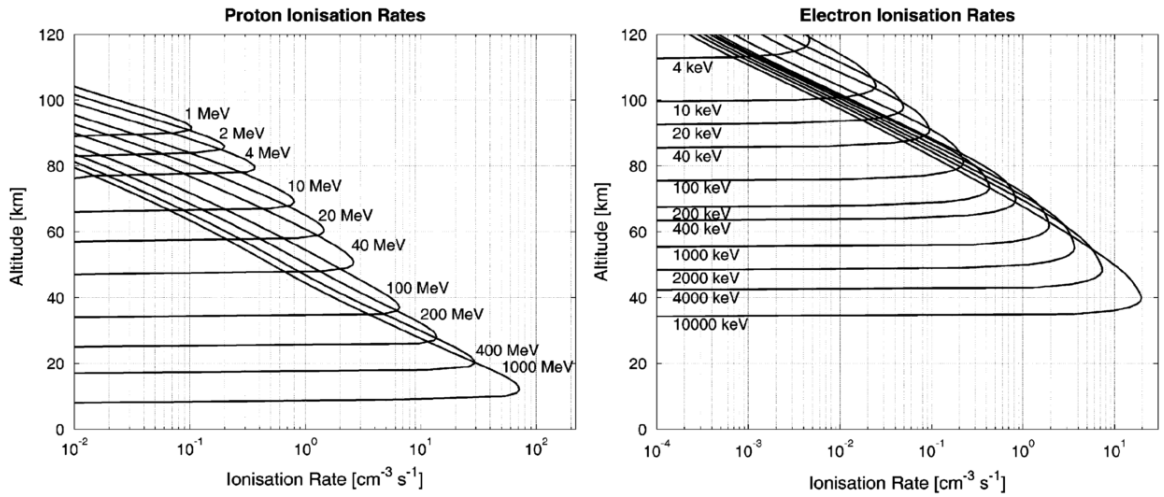

Figure 4.1: Ionization profiles for monoenergetic beams of protons (left) and electrons (right). Adapted from *Turunen et al.* (2009).

2012). The impact of the medium to high energy ($>$ 30 keV) electrons are, however, still undetermined and often poorly represented in current atmospheric models (e.g. *Rozanov et al.* (2012); *Seppälä et al.* (2014)). Figure 4.1 displays altitude versus ionisation rates for monoenergetic beams of protons to the left, and electrons to the right. A 20 MeV proton can penetrate to just below 60 km altitude, while an electron would need only 1 MeV to reach the same altitude. As previously shown (Figure 1.2) 60 km corresponds to the mesosphere region.

EPP-HO_x production is strongly altitude dependent, occurring mainly below 80 km (*Sinnhuber et al.*, 2012; *Solomon et al.*, 1981). It has a short lifetime (hours) and will impact the ozone concentration locally. The production of NO_x will on the other hand occur at all altitudes from the lower thermosphere throughout the mesosphere, but it is first at stratospheric altitudes ($>$ 50 km) that it can interact with ozone. NO_x has a long lifetime, and in the dark polar winter atmosphere even the auroral produced NO_x gasses can be transported down below 50 km. The downward transport of NO_x produced at higher altitudes is known as the "EPP indirect effect". The indirect effect may be especially strong in the Southern hemisphere, where the polar vortex is more stable than in the Northern hemisphere, leading to a stronger "trapping" of air over the south pole. However, after sudden stratospheric warming events in the Northern hemisphere, the polar vortex may reform strongly, which can lead to an EPP indirect effect of comparable size as in the Southern hemisphere (*Sinnhuber et al.*, 2012). A schematic which illustrates the pathway of how particle precipitation can be linked with changes in the atmospheric dynamics is shown in Figure 4.2.

Understanding both the strength and the altitude distribution of the particle precipitation forcing is therefore vital for understanding both the direct and indirect effect on ozone and for the assessment of its atmospheric and climate impacts. The electron bounce loss cone fluxes presented in this thesis, with all corrections applied, and with the extension of the electron spectrum up to $>$ 1 MeV in energy, is ideal to study the OH enhancements in the mesosphere and its relationship to electron precipitation. Using the NOAA-18 MEPED electron BLC fluxes, *Zawedde et al.* (2016) calculated the electrons' energy deposition as a function of altitude. The deposited energy was com-

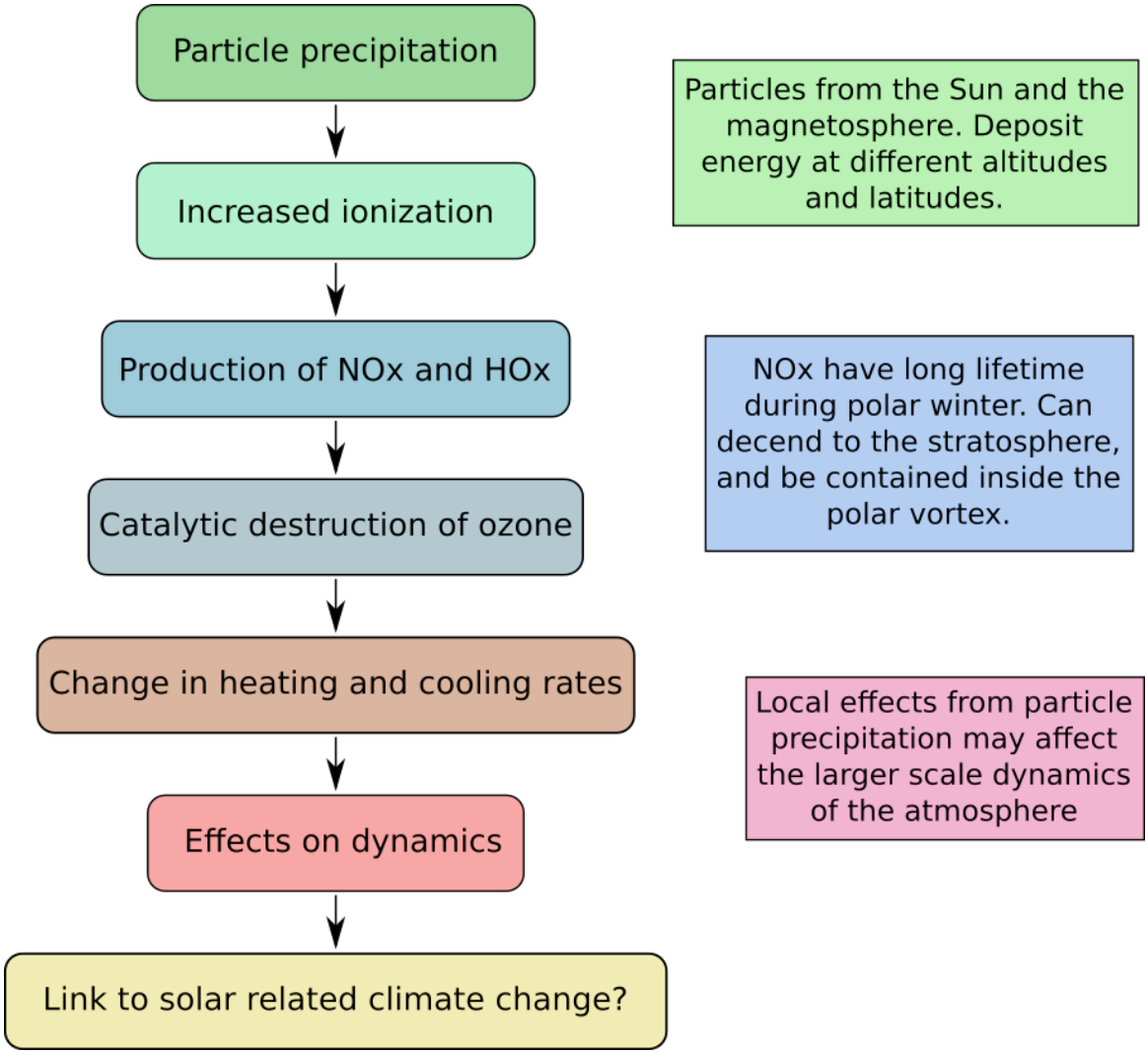

Figure 4.2: A schematic to illustrate the main link between particle precipitation and the atmospheric effects.

pared with OH measurements from the Aura satellite, which orbits the Earth in the same local time as NOAA-18. *Zawedde et al.* (2016) studied the year 2008, which had many recurrent, weak to moderate geomagnetic storms caused by two CIRs. We concluded that the energetic electron precipitation produced substantial OH, even during this solar minimum year. With detailed knowledge of where and when the EEP occured, we were for the first time able to separate the OH variability caused by EEP and by atmospheric dynamics.

No single electron energy detector covers the range impacting the NO_x production from the lower thermosphere to the stratosphere. Therefore, the relative contribution of the direct production and indirect effect of NO_x-rich air masses descending into the mesosphere is still an unresolved problem (*Funke et al.*, 2005; *Randall et al.*, 2007; *Siskind and Russell III*, 1996). To overcome this challenge, I have worked on combining the measurements from both TED and MEPED covering the energy range from 1-1000 keV. The data are applied in an ongoing study by my fellow PhD student from the University of Oslo, Christine Smith-Johnsen. The full spectrum gives us a valuable opportunity to assess the local production of NO throughout the mesosphere and lower

thermosphere, and evaluate the contribution of indirect NO enhancement at specific altitude levels. The wider goal is to improve how The Whole Atmosphere Community Climate Model (WACCM) treats electron precipitation. The parametrization of auroral electrons in WACCM uses the planetary geomagnetic Kp-index. Kp can be used to calculate the hemispheric power, which is the estimated power in Giga Watts deposited in the polar regions by energetic particles (*Zhang and Paxton*, 2008). From the hemispheric power, the energy flux is calculated as a Maxwellian spectrum with a characteristic energy of 2 keV. The total ionization rate as a function of altitude is calculated in the same way as *Roble and Ridley* (1987), which results in an ionization profile that peaks in altitude around 100 km.

The medium energy electrons are parametrised using ten activity levels based on the MEPED electron measurements (*Codrescu et al.*, 1997), with ten corresponding estimations of the hemispheric power. The method allows for the construction of statistical patterns for the electrons. Improved energy-dependent parametrization has been developed by *Fang et al.* (2008).

Based on our combined TED and MEPED measurements, Smith-Johnsen address the two main issues with WACCM electron parametrization; the fixed characteristic energy of 2 keV in the low-energy electrons, and the decoupled way of treating low and high energy electrons. This can potentially lead to large improvements in how electron precipitation effects are modelled. The two TED telescopes on board NOAA POES are mounted radially outwards (0°) and at an angle of 30° to the Earth-center-to-satellite radial vector (*Evans and Greer*, 2000). A future aspect is to look into the possibility of constructing TED bounce loss cone fluxes, but currently Smith-Johnsen is only using the TED and MEPED 0° detector measurements. All other corrections discussed through this thesis have, however, been applied to the MEPED electrons, including extending the spectrum to > 1 MeV. The combined TED and MEPED thus covers the energy range 0.8 keV to 1 MeV.

Preliminary results comparing the WACCM modelled ion production from a period of one month in 2010, to the ion production calculated from Smith-Johnsen's parametrization, are presented here. Solar wind parameters, the AE and SYM-H[1] indexes from 26th March to 25th April 2010 are shown in Figure 4.3. A storm with minimum SYM-H of -89 nT initiates on April 5th (DOY 95). This is the CME arrival. A second storm can be seen in the SYM-H index starting at the end of April 11th (DOY 101), which corresponds to a period of IMF $B_Z < 0$. Another smaller and shorter storm can be seen starting on April 14th (DOY 104) near midnight.

A run using WACCM during the time period 26th March to 25th April 2010 is shown in the left panel of Figure 4.4. The plotted parameter is daily mean polar cap average (geographic latitude $> 60°$ in the Southern Hemisphere) of ion production rate.

Smith-Johnsen used all available NOAA POES, enabling a close to global view of the precipitating electron fluxes with a 1.5 hour resolution. Either a maxwellian or an exponential spectrum were used to fit the TED measurements, and then combined with a power law spectrum covering the higher energies. The satellite coordinates were converted from geomagnetic to geographic, before energy deposition was calculated from the fluxes as a function of altitude. The result is shown in the right panel of Figure 4.4.

[1] SYM-H is almost the same as the Dst index, but given in 5 minute resolution.

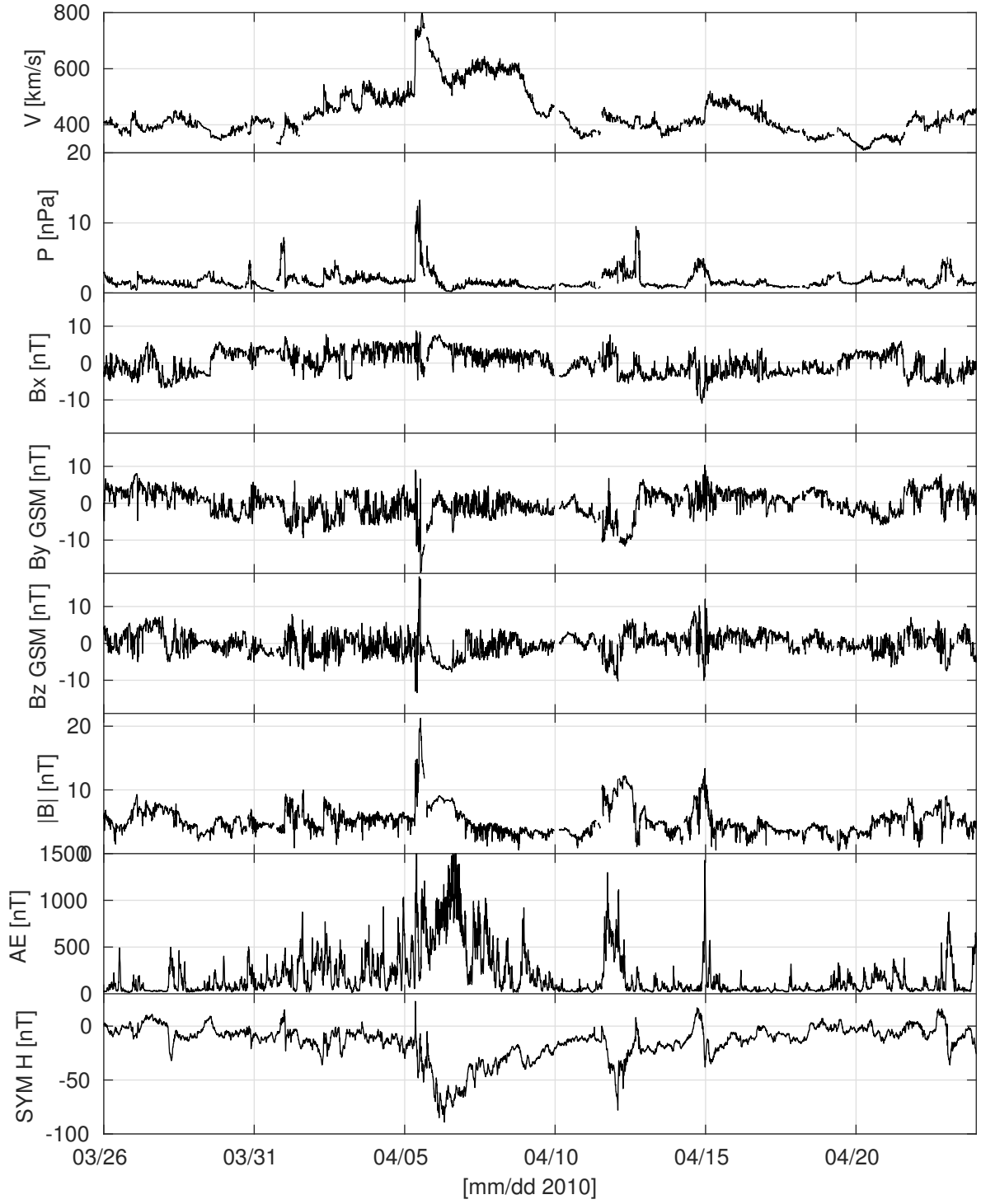

Figure 4.3: Solar wind parameters, AE and SYM-H indices for 26th March - 25th April 2010, the period studied by C. Smith-Johnsen (*private comm. 2016*).

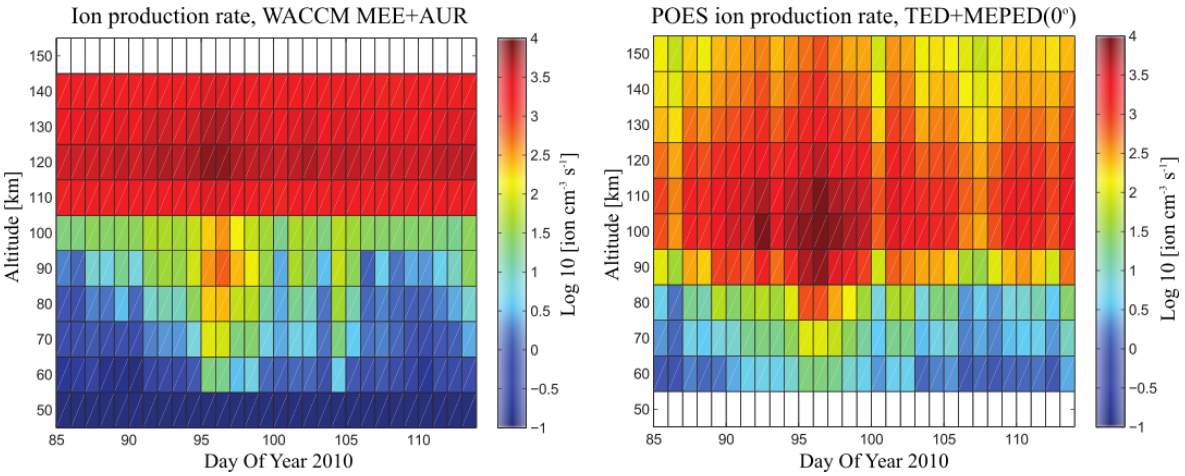

Figure 4.4: Left: Ion production rate modelled by WACCM for the Southern hemisphere with a combined parametrization; the electron spectrum has a constant characteristic energy of 2 keV above 100 km and intensity varies with Kp index, below 100 km the spectrum and energy deposition is parametrized based on statistical precipitation patterns inferred from MEPED (*Codrescu et al.*, 1997). Day of year 85 corresponds to 26th March, day of year 115 to 25th April. Right: Ion production rate modelled for the Southern hemisphere with a new parametrization based on measurements from TED and MEPED 0° detectors, which allows the characteristic energy to vary through the event (*private comm. with C. Smith-Johnsen 2016*).

The production rate predicted by WACCM displays a clear discontinuity at 100 km. This is obviously caused by the decoupled way of treating < 30 keV and > 30 keV electrons. Both above and below 100 km, we can observe three maxima in the production rates, one on DOY 95-96, one on DOY 101-102, and the last on DOY 104-105. WACCM can reproduce enhanced ion production rates at the right times, but the discontinuity at 100 km is not a natural feature of the atmospheric response.

The ion production rate calculated from the combined TED and MEPED 0° detector gives a much more realistic altitude distribution. As discussed previously in this thesis, the 0° detector underestimates the precipitating flux, and thus the production rates shown in Figure 4.4 are a lower estimate. The WACCM parametrization underestimates the energy deposition at 80-100 km in the DOY 95 storm, and overestimates the energy deposition in the height region > 100 km compared to the TED and MEPED estimates. The latter is particularly true when there is low activity, which might be due to a small dynamical range of the low-energy Kp-parametrization.

In summary, our optimization of the MEPED measurements is currently used in multiple studies investigating the EEP impact upon the atmosphere. The work of Smith-Johnsen will contribute to a more accurate modelling of electron precipitation, taking the high-energy part of the spectrum properly into account. The results by e.g. *Zawedde et al.* (2016) indicate that the impact on the atmosphere by energetic electron precipitation may be significant also during geomagnetically low-active years, and better modelling is needed to study the effects more accurately.

Chapter 5

Future prospects

The optimized MEPED data may open for many new projects. Some of these have already been mentioned in the introductory chapters. A few other ideas and ongoing projects are listed below.

Calibration of SEM-1 satellites

A future task is to calibrate the SEM-1 satellite based on the model described in Paper II. First, we need to achieve a better understanding of why NOAA-15 α factors appears to be underestimated, and potentially update our model based on the new correction coefficient presented in Section 3.2.2.

We have already done preliminary tests on the calibration of the SEM-1 satellite NOAA-12 using the method from paper II. The advantage of the method from paper II is that it can calibrate both the 0° and 90° detectors on the SEM-1 satellite, even though the pointing direction of the SEM-2 and SEM-1 90° telescopes are different. This is because the equations presented in the paper only express α as a function of accumulated corrected fluxes. Using direct comparisons between SEM-1 and SEM-2 satellites may pose a challenge, because the assumption that the two 90° detectors should measure the same spectrum can fail, unless the satellites are in the isotropy zone. The comparison of 0° detectors would still hold, because the SEM-1 and SEM-2 versions only differ slightly in pointing direction.

If successful, the outcome will be a long term dataset to be used for e.g. parametrization of the electron and proton fluxes over more than three solar cycles. From 2002, three or more satellites ensures a reasonable magnetic local time coverage supporting a fairly global coverage. Solar cycle 24 (starting in 2008) was weaker, with fewer sunspots and less geomagnetic activity, compared with the three previous cycles. A parametrization therefore needs to be verified and potentially scaled to the electron measurements from this early stage.

A statistical empirical model of EEP

In relation to working with paper IV, a great effort was put into investigating a possible parametrization of the EEP based on solar wind parameters and geomagnetic indices. The preliminary model showed promising results for the lower energies $>$ 50 keV and

$>$ 100 keV (not shown), but was unable to separate the storms that caused increase in $>$300 keV and $>$1 MeV fluxes from the ones that did not. The linear dependence between the Epsilon parameter and the high energy fluxes might offer the means to single out the strongest EEP events.

Study of EEP during CME driven storms

The newly developed BLC fluxes have been applied in a study of CIR storms. A contrasting study using a selection of CME driven storms may also be of great interest. A comparison of the two solar wind drivers will as such shed light on their relative contribution to the EEP over the solar cycle.

Implementing a full range EEP spectrum in WACCM

Combining the effort of concatenating TED and MEPED with the new physics based technique of the BLC estimates allows for a full-range coverage of the electron energy deposition for the entire altitude region from the lower thermosphere to the mesosphere (60-120 km). With a full energy range for precipitating electrons to be implemented in WACCM it will for example be possible to separate the contribution from the indirect and direct effect on the NOx composition. It will resolve the low electron energy overestimation seen in WACCM associated with the Kp-parametrization, and it will contribute to a more realistic estimate of energetic electron precipitation. The latter part is currently of particular interest for the modelling community in their effort to entangle potential EEP impact on the atmospheric temperature and dynamics.

Chapter 6

Summary of papers

6.1 Paper I: In-flight calibration of NOAA POES proton detectors - Derivation of the MEPED correction factors

In this paper, we derive the correction factors for the SEM-2 MEPED proton detectors on board NOAA-16, NOAA-17, NOAA-18 and MetOp-02. To calculate correction factors, we compare average monthly integral flux spectra from the first twelve months after a new satellite is launched into the same local time as one of the four satellites. The mean correction factor from the distribution of twelve is taken to be representative for the respective year. All distributions show a small standard deviation, supporting that the method is robust. By only comparing satellites in the same local time, we ensure that no MLT effects are introduced to the calibration.

To estimate the temporal evolution of the correction factors, we develop a method which iteratively retrieves both the corrected fluxes within each channel which the most degraded satellite is still able to measure, and the monthly correction factors.

The corrected flux agrees remarkably well after correction.

6.2 Paper II: Space weather impact on the degradation of NOAA POES MEPED proton detectors

In this paper, we use the results from paper I to show that there is a dependence of the correction factors (α factors) on the activity level. In times of high geomagnetic activity the degradation rate is higher than during less active periods.

A model is presented based on α factors from paper I, calculated by satellite comparison. It consists of two sets of equations which is used iteratively. Equation set (1) is used to calculate a first approximation of α, and simultaneously, the accumulated corrected flux, *acf*. In Equation set (2), the estimated $\Delta acf/\Delta t$ is weighted by the mean ap index over the chosen period (Δt), for example 1 year. The $\Delta acf/\Delta t \times \overline{ap}$ over the period is used in Equation set (2) to estimate the $\Delta\alpha$ over the same period.

The model can be used to extend the temporal evolutions of α factors in satellites already calibrated in paper I, as well as estimate the α factors for satellites which could not be calibrated in paper I. It does, however, have large uncertainties associated with the estimated α. In addition, it seems like the model underestimates the α factors for

NOAA-15. Some caution should therefore be taken regarding the NOAA-15 factors. The most likely cause for the underestimation is that no other satellite have been operating for an equally long time as NOAA-15, and the model is therefore not built on data representative for the oldest SEM-2 satellite. The estimated factors for the other satellites do not seem unreasonable, even though they cannot be determined with large precision.

6.3 Paper III: Energetic electron precipitation into the middle atmosphere - Constructing the loss cone fluxes from MEPED POES

We use the NOAA POES MEPED directional electron telescopes together with theory concerning pitch angle diffusion in the outer radiation belt, and derive the bounce loss cone fluxes.

The electron data are corrected for proton contamination, and the geometric factors of the E1 and E2 channels are adjusted. For this reason, the lower energy threshold of E1 is raised from the nominal > 30 keV to > 50 keV. In addition, we take advantage of the proton detector's response to > 1 MeV electrons, and provide this as a fourth energy channel on the electron spectrum

We take into account the detector response for different pitch angle distributions, and that the detector area varies with the particles angle through the collimator. In addition to this, the offset between the telescope viewing direction and the magnetic field line where the pitch angle distribution is centred is also accounted for.

The pitch angles measured by the detectors, calculated from the IGRF magnetic field model, are given in the NOAA dataset. From this we can find the telescopes viewing angle with respect to the magnetic field at satellite altitude. From the satellite geographic position, we use the IGRF to calculate the magnetic field strength at satellite altitude, and at the equator. The equatorial pitch angles of the particles measured in the two telescopes can then be calculated. We also calculate the equatorial loss cone size. Using a dense set of pre-determined diffusion profiles, information retrieved about the telescope looking direction, and the equatorial loss cone size, we determine the diffusion profile which fit the level of anisotropy observed by the two telescopes. When we know the right diffusion profile, the bounce loss cone flux at the foot of field line (120 km) can be determined.

The bounce loss cone fluxes are validated by estimating the energy deposition in the atmosphere, and estimating the OH density this would produce. This is compared with real measurements of OH, and a good agreement was found in the magnitude of estimated and measured OH.

6.4 Paper IV: Energetic electron precipitation in weak to moderate Corotating Interaction Region-Driven storms

In this paper, we analyse a group of 41 weak to moderate geomagnetic storms, with main emphasis on the high-energy precipitation they cause. We use the bounce loss cone fluxes constructed based on results in paper III.

The storms are caused by Corotating Interaction Regions (CIR) in the declining phase of the solar cycle, which we limited to the years 2006-2010. A motivation behind the study was to identify possible parameters which could be used to parametrize energetic electron precipitation, to improve upon studies that model effects from precipitation.

The selection of storms was done using the Dst-index, visually inspecting for storm signatures, without any criteria put on the size of the storm. Periods with CMEs were excluded, and the selection of storms were checked to be caused by CIRs by inspection of the solar wind signatures, as well as an online catalogue of geoeffective coronal holes. We selected only isolated storms, defined by the average Dst-index two days prior to storm start (Dst≥ -15 nT). This excluded a large number of possible events. Especially the year 2008 is known for having two CIRs causing many recurrent storms on Earth, but very few of them are isolated with quiet conditions before and after. Also, CIR storms have very long recovery phases, and we had to apply a limit on how long a storm could be. The final selection of storms were in all eight days long, with two of the days being the quiet period before storm main phase.

The main finding from this paper is that events which caused an increase in precipitation of > 1 MeV electrons were connected with a higher solar wind energy transfer, as estimated by the Akasofu Epsilon parameter. In the solar wind, these storms were mainly distinguished by having a larger period of negative IMF B_Z. Elevated solar wind velocity (~ 600 km/s) over a period of 2-3 days was connected with storms that enhanced precipitation of > 300 keV electrons.

We show that the precipitation of especially > 50 keV and > 100 keV is not evenly distributed in magnetic local time, which is important if the fluxes are to be used in studies of atmospheric effects. There is also an energy dependent delay observed in the precipitating fluxes, due to the acceleration processes to higher energies in the radiation belts.

Abbreviations

acf	Accumulated Corrected Flux
BLC	Bounce Loss Cone
CME	Coronal Mass Ejection
CGM	Corrected Geomagnetic Latitude
CIR	Corotating Interaction Region
DLC	Drift Loss Cone
EEP	Energetic Electron Precipitation
EMIC	Electromagnetic ion Cyclotron
EPP	Energetic Particle Precipitation
EUMETSAT	European Organisation for the Exploitation of Meteorological Satellites
HILDCAA	High-Intensity Long-Duration Continuous AE Activity
HOx	H, OH, HO_2, H_2O_2
HSSWS	High Speed Solar Wind Stream
IGRF	International Geomagnetic Reference Field
ILAT	Invariant Latitude
IMF	Interplanetary Magnetic Filed
IPCC	Intergovernmental Panel on Climate Change
MEPED	Medium Energy Proton and Electron Detector
MetOp	Meteorological Operational satellite programme
MLT	Magnetic Local Time
M02	MetOp-02
M01	MetOp-01
NOAA	National Oceanic and Atmospheric Administration
NOx	N, NO, NO_2
N15	NOAA-15
N16	NOAA-16
N17	NOAA-17
N18	NOAA-18
N19	NOAA-19
PCHIP	Piecewise Cubic Hermite Interpolating Polynomial
POES	Polar Orbiting Environmental Satellites
R_E	Earth Radii
SAA	South Atlantic Anomaly
SEM	Space Environment Monitor
SEP	Solar Energetic Particle
SPE	Solar Proton Event
TED	Total Energy Detector
ULF	Ultra-low frequency
VLF	Very-low frequency
WACCM	Whole Atmosphere Community Climate Model

Bibliography

Akasofu, S.-I. (1981), Energy Coupling Between the Solar Wind and the Magnetosphere, *Space Science Reviews*, *28*(1963), 121–190.

Andersson, M. E., P. T. Verronen, S. Wang, C. J. Rodger, M. A. Clilverd, and B. R. Carson (2012), Precipitating radiation belt electrons and enhancements of mesospheric hydroxyl during 2004–2009, *Journal of Geophysical Research*, *117*(D9), D09,304, doi:10.1029/2011JD017246.

Asikainen, T., and K. Mursula (2011), Recalibration of the long-term NOAA/MEPED energetic proton measurements, *Journal of Atmospheric and Solar-Terrestrial Physics*, *73*, 335–347, doi:10.1016/j.jastp.2009.12.011.

Asikainen, T., and K. Mursula (2013), Correcting the NOAA/MEPED energetic electron fluxes for detector efficiency and proton contamination, *Journal of Geophysical Research: Space Physics*, *118*(10), 6500–6510, doi:10.1002/jgra.50584.

Asikainen, T., and M. Ruopsa (2016), Solar wind drivers of energetic electron precipitation, *Journal of Geophysical Research: Space Physics*, *121*, 1–50, doi:10.1002/2015JA022215.

Asikainen, T., K. Mursula, and V. Maliniemi (2012), Correction of detector noise and recalibration of NOAA/MEPED energetic proton fluxes, *Journal of Geophysical Research*, *117*(A9), 1–16, doi:10.1029/2012JA017593.

Baumjohann, W., and R. A. Treumann (1996), *Basic Space Plasma Physics*, Imperial College Press.

Blanc, M., J. L. Horwitz, J. B. Blake, I. Daglis, J. F. Lemaire, M. B. Moldwin, O. S, T. R. M, and R. A. Wolfe (1999), Source and loss processes in the inner magnetosphere, in *Magnetospheric Plasma Sources and Losses*, edited by B. Hultqvist, M. Øieroset, G. Paschmann, and R. A. Treumann, chap. 4, Kluwer Academic Publishers.

Borovsky, J. E., and M. H. Denton (2006), Differences between CME-driven storms and CIR-driven storms, *Journal of Geophysical Research*, *111*(A7), A07S08, doi:10.1029/2005JA011447.

Burton, R. K., R. L. McPherron, and C. T. Russell (1975), An Empirical Relationship Between Interplanetary Conditions and Dst, *Journal of Geophysical Research*, *80*(31), 4204–4214.

Chapell, C. R. (1972), Recent Satellite Measurements of the Morphology and Dynamics of the Plasmasphere, *Reviews of Geophysics and Space Physics*, *10*(4), 951–979.

Codrescu, M. V., T. J. Fuller-Rowell, R. G. Roble, and D. S. Evans (1997), Medium energy particle precipitation influences on the mesosphere and lower thermosphere, *Journal of Geophysical Research*, *102*(A9), 19,977, doi:10.1029/97JA01728.

Coleman, J. A., D. P. Love, J. H. Trainor, and D. J. Williams (1968), EFFECTS OF DAMAGE BY 0.8 MeV - 5.0 MeV PROTONS IN SILICON SURFACE-BARRIER DETECTORS J. A. Coleman, *IEEE Transactions on Nuclear Science*, doi:10.1109.

Dungey, J. W. (1961), Interplanetary Magnetic Field And Auroral Zones, *Physical Review Letters*, *6*(2), 47.

Evans, D. S., and M. S. Greer (2000), Polar Orbiting Environmental Satellite Space Environment Monitor - 2 Instrument Descriptions and Archive Data Documentation, *Tech. rep.*, Natl. Atmos. and Oceanic Admin., Space Environ. Cent., Boulder, Colorado.

Fang, X., C. E. Randall, D. Lummerzheim, S. C. Solomon, M. J. Mills, D. R. Marsh, C. H. Jackman, W. Wang, and G. Lu (2008), Electron impact ionization: A new parameterization for 100 eV to 1 MeV electrons, *Journal of Geophysical Research: Space Physics*, *113*(9), 1–8, doi:10.1029/2008JA013384.

Friedel, R. H. W., E. G. D. Reeves, and T. Obara (2002), Relativistic electron dynamics in the inner magnetosphere — a review, *Journal of Atmospheric and Solar-Terrestrial Physics*, *64*(2), 265–282, doi:10.1016/S1364-6826(01)00088-8.

Funke, B., M. L??pez-Puertas, S. Gil-L??pez, T. von Clarmann, G. P. Stiller, H. Fischer, and S. Kellmann (2005), Downward transport of upper atmospheric NO<inf>x</inf> into the polar stratosphere and lower mesosphere during the Antarctic 2003 and Arctic 2002/2003 winters, *Journal of Geophysical Research Atmospheres*, *110*(24), 1–17, doi:10.1029/2005JD006463.

Galand, M., and D. S. Evans (2000), Radiation Damage of the Proton MEPED Detector on POES (TIROS/NOAA) Satellites, *Tech. Rep. 456*, Space Environment Center, Boulder, Colorado.

Gonzalez, W. D., J. a. Joselyn, Y. Kamide, H. W. Kroehl, G. Rostoker, B. T. Tsurutani, and V. M. Vasyliunas (1994), What is a geomagnetic storm?, *Journal of Geophysical Research*, *99*(A4), 5771, doi:10.1029/93JA02867.

Gonzalez, W. D., B. T. Tsurutani, and A. L. C. Gonzales (1999), INTERPLANETARY ORIGIN OF GEOMAGNETIC STORMS, *Space Science Reviews*, pp. 529–562.

Hendrickx, K., L. Megner, J. Gumbel, D. E. Siskind, Y. J. Orsolini, H. N. Tyss??y, and M. Hervig (2015), Observation of 27 day solar cycles in the production and mesospheric descent of EPP-produced NO, *Journal of Geophysical Research A: Space Physics*, *120*(10), 8978–8988, doi:10.1002/2015JA021441.

Hill, V., D. S. Evans, and H. Sauer (1985), NOAA Technical Memorandum ERL SEL-71.

Horne, R. B., R. M. Thorne, Y. Y. Shprits, N. P. Meredith, S. a. Glauert, A. J. Smith, S. G. Kanekal, D. N. Baker, M. J. Engebretson, J. L. Posch, M. Spasojevic, U. S. Inan, J. S. Pickett, and P. M. E. Decreau (2005), Wave acceleration of electrons in the Van Allen radiation belts., *Nature*, *437*(7056), 227–230, doi:10.1038/nature03939.

Horne, R. B., M. M. Lam, and J. C. Green (2009), Energetic electron precipitation from the outer radiation belt during geomagnetic storms, *Geophysical Research Letters*, *36*(19), L19,104, doi:10.1029/2009GL040236.

Jian, L., C. T. Russell, J. G. Luhmann, and R. M. Skoug (2006), Properties of Interplanetary Coronal Mass Ejections at One AU During 1995 – 2004, *Solar Physics*, *239*(1-2), 393–436, doi:10.1007/s11207-006-0133-2.

Kamide, Y., R. L. McPherron, W. D. Gonzalez, D. Hamilton, H. Hudson, J. A. Joselyn, S. W. Kahler, L. R. Lyons, H. Lundstedt, and E. Szuszczewicz (1997), Magnetic Storms: Current Understanding and Outstanding Questions, in *Magnetic Storms, Geophys. Monogr. Ser. vol. 98*, edited by B. T. Tsurutani, W. D. Gonzalez, Y. Kamide, and J. K. Arballo, pp. 1–19, American Geophysical Union, Washington D.C.

Kavanagh, A. J., F. Honary, E. F. Donovan, T. Ulich, and M. H. Denton (2012), Key features of >30 keV electron precipitation during high speed solar wind streams: A superposed epoch analysis, *Journal of Geophysical Research: Space Physics*, *117*(6), 1–13, doi:10.1029/2011JA017320.

Kennel, C. F., and H. E. Petschek (1966), Limit on stably trapped particle fluxes, *Journal of Geophysical Research*, *71*(1), 1–28.

Kessel, M. (2016), Things we don't yet understand about solar driving of the radiation belts., *Journal of Geophysical Research: Space Physics*, doi:10.1002/2016JA022472.

Kievelson, M. G., and C. Russel (Eds.) (1995), *Introduction to Space Physics*, 1 ed., Cambridge University Press, New York.

Kilpua, E., H. Hietala, D. L. Turner, H. E. J. Koskinen, T. I. Pulkkinen, J. V. Rodriguez, E. G. D. Reeves, S. G. Claudepierre, and H. E. Spence (2015), Unraveling the drivers of the storm-time radiation belt response, *Geophysical Research Letters*, *42*, doi:10.1002/2015GL063542.

Koskinen, H. E. J. (2005), Energetic Particle Losses From the Inner Magnetosphere, in *The Inner Magnetosphere - Physics and Modelling*, pp. 23–31, American Geophysical Union.

Lam, M. M., R. B. Horne, N. P. Meredith, S. a. Glauert, T. Moffat-Griffin, and J. C. Green (2010), Origin of energetic electron precipitation >30 keV into the atmosphere, *115*, 1–16, doi:10.1029/2009JA014619.

Li, W., B. Ni, R. M. Thorne, J. Bortnik, J. C. Green, C. A. Kletzing, W. S. Kurth, and G. B. Hospodarsky (2013), Constructing the global distribution of chorus wave intensity using measurements of electrons by the POES satellites and waves by the Van Allen Probes, *Geophysical Research Letters*, *40*(17), 4526–4532, doi:10.1002/grl.50920.

Li, W., R. M. Thorne, Q. Ma, B. Ni, J. Bortnik, D. N. Baker, H. E. Spence, G. D. Reeves, S. G. Kanekal, J. C. Green, C. A. Kletzing, W. S. Kurth, G. B. Hospodarsky, J. B. Blake, J. F. Fennell, and S. G. Claudepierre (2014a), Radiation belt electron acceleration by chorus waves during the 17 March 2013 storm, *Journal of Geophysical Research: Space Physics*, *119*(March 2011), 4681–4693, doi:10.1002/jgra.50578.Comment.

Li, W., B. Ni, R. M. Thorne, J. Bortnik, Y. Nishimura, J. C. Green, C. A. Kletzing, W. S. Kurth, G. B. Hospodarsky, H. E. Spence, G. D. Reeves, J. B. Blake, J. F. Fennell, S. G. Claudepierre, and X. Gu (2014b), Quantifying hiss-driven energetic electron precipitation: A detailed conjunction event analysis, *Geophysical Research Letters*, *41*(4), 1085–1092, doi:10.1002/2013GL059132.

Lyons, L., R. Thorne, and C. Kennel (1972), Pitch-angle diffusion of radiation belt electrons within the plasmasphere., *J. Geophys. Res.*, *77*(19), 3455–3474, doi:10.1029/JA077i028p05608.

Lyons, L. R., and D. S. Evans (1984), An association between discrete aurora and energetic particle boundaries, *Journal of Geophysical Research*, *89*(A4), 2395–2400.

Lyons, L. R., and D. J. Williams (1984), *Quantitative Aspects of Magnetospheric Physics*, D. Reidel Publishing Company.

Mann, I. R., T. P. O'Brien, and D. K. Milling (2004), Correlations between ULF wave power, solar wind speed, and relativistic electron flux in the magnetosphere: Solar cycle dependence, *Journal of Atmospheric and Solar-Terrestrial Physics*, *66*(2), 187–198, doi:10.1016/j.jastp.2003.10.002.

Meredith, N. P., R. B. Horne, M. M. Lam, M. H. Denton, J. E. Borovsky, and J. C. Green (2011), Energetic electron precipitation during high-speed solar wind stream driven storms, *Journal of Geophysical Research: Space Physics*, *116*(x), 1–16, doi:10.1029/2010JA016293.

Millan, R. M., and D. N. Baker (2012), Acceleration of particles to high energies in earth's radiation belts, *Space Science Reviews*, *173*(1-4), 103–131, doi:10.1007/s11214-012-9941-x.

Millan, R. M., and R. M. Thorne (2007), Review of radiation belt relativistic electron losses, *Journal of Atmospheric and Solar-Terrestrial Physics*, *69*(3), 362–377, doi:10.1016/j.jastp.2006.06.019.

Nesse Tyssøy, H., M. I. Sandanger, L.-K. G. Ødegaard, J. Stadsnes, A. Aasnes, and A. E. Zawedde (2016), Energetic Electron Precipitation into the Middle Atmosphere - Constructing the Loss Cone Fluxes from MEPED POES, *Journal of Geophysical Research: Space Physics*, *121*, doi:10.1002/2016JA022752.

Ødegaard, L.-K. G. (2013), Recalibration of the MEPED Proton Detectors Onboard NOAA POES Satellites, Masters degree, University of Bergen.

Ødegaard, L.-K. G., H. Nesse Tyssøy, M. I. Jakobsen, J. Stadsnes, and F. Søraas (2016a), Space Weather impact on the degradation of energetic proton detectors.

Ødegaard, L.-K. G., H. Nesse Tyssøy, F. Søraas, J. Stadsnes, and M. I. Sandanger (2016b), Energetic Electron Precipitation in Weak to Moderate Corotating Interaction Region Storms.

Paulikas, G. A., and J. B. Blake (1979), Effects of the solar wind on mag-netospheric dynamics: Energetic electrons at the synchronous orbit, in *Quantitative Modeling of the Magnetosphereic Processes, Geophys. Monogr. Ser.*, vol. 21, pp. 180–202, AGU, Washington D.C.

Peck, E. D., C. E. Randall, J. C. Green, J. V. Rodriguez, and C. J. Rodger (2015), POES MEPED differential flux retrievals and electron channel contamination correction, *Journal of Geophysical Research: Space Physics*, pp. 4596–4612, doi: 10.1002/2014JA020817.Received.

Raben, V. J., D. S. Evans, H. H. Sauer, S. R. Sahm, and M. Huynh (1995), TIROS/NOAA Satellite Space Environment Monitor Data Archive Documentation: 1995 Update, *Tech. Rep. February*, National Oceanic and Atmospheric Administration.

Randall, C. E., V. L. Harvey, G. L. Manney, Y. Orsolini, M. Codrescu, C. Sioris, S. Brohede, C. S. Haley, L. L. Gordley, J. M. Zawodny, and I. M. Russell (2005), Stratospheric effects of energetic particle precipitation in 2003-2004, *Geophysical Research Letters*, *32*(5), 1–4, doi:10.1029/2004GL022003.

Randall, C. E., V. L. Harvey, C. S. Singleton, S. M. Bailey, P. F. Bernath, M. Codrescu, H. Nakajima, and I. M. Russell (2007), Energetic particle precipitation effects on the Southern Hemisphere stratosphere in 1992-2005, *Journal of Geophysical Research Atmospheres*, *112*(8), 1–13, doi:10.1029/2006JD007696.

Randall, C. E., V. L. Harvey, D. E. Siskind, J. France, P. F. Bernath, C. D. Boone, and K. A. Walker (2009), NOx descent in the arctic middle atmosphere in early 2009, *Geophysical Research Letters*, *36*(18), 2007–2010, doi:10.1029/2009GL039706.

Reeves, E. G. D., K. L. McAdams, R. H. W. Friedel, and T. P. O'Brien (2003), Acceleration and loss of relativistic electrons during geomagnetic storms, *Geophysical Research Letters*, *30*(10), doi:10.1029/2002GL016513.

Reeves, E. G. D., S. K. Morley, R. H. W. Friedel, M. G. Henderson, T. E. Cayton, G. Cunningham, J. B. Blake, R. a. Christensen, and D. Thomsen (2011), On the relationship between relativistic electron flux and solar wind velocity: Paulikas and Blake revisited, *Journal of Geophysical Research*, *116*(A2), A02,213, doi:10.1029/2010JA015735.

Reeves, E. G. D., H. E. Spence, M. G. Henderson, S. K. Morley, R. H. W. Friedel, H. O. Funsten, D. N. Baker, S. G. Kanekal, J. B. Blake, J. F. Fennell, S. G. Claudepierre, R. M. Thorne, D. L. Turner, C. A. Kletzing, W. S. Kurth, B. A. Larsen, and J. T. Niehof (2013), Electron Acceleration in the Heart of the Van Allen Radiation Belts, *Science*, *341*.

Reeves, G. D., R. H. W. Friedel, B. A. Larsen, R. M. Skoug, H. O. Funsten, S. G. Claudepierre, J. F. Fennell, D. L. Turner, M. H. Denton, H. E. Spence, J. B. Blake, and D. N. Baker (2016), Energy dependent dynamics of keV to MeV electrons in the inner zone, outer zone, and slot regions., *Journal of Geophysical Research: Space Physics*, doi:10.1002/2015JA021569.

Roble, R. G., and E. C. Ridley (1987), An auroral model for the NCAR thermosphere general-circulation model (TGCM), *Annales Geophysicae*, *5*(6), 369–382.

Rodger, C. J., M. A. Clilverd, J. C. Green, and M. M. Lam (2010a), Use of POES SEM-2 observations to examine radiation belt dynamics and energetic electron precipitation into the atmosphere, *Journal of Geophysical Research*, *115*(A4), A04,202, doi:10.1029/2008JA014023.

Rodger, C. J., B. R. Carson, S. A. Cummer, R. J. Gamble, M. A. Clilverd, J. C. Green, J. A. Sauvaud, M. Parrot, and J. J. Berthelier (2010b), Contrasting the efficiency of radiation belt losses caused by ducted and nonducted whistler-mode waves from ground-based transmitters, *Journal of Geophysical Research: Space Physics*, *115*(12), 1–13, doi:10.1029/2010JA015880.

Rodger, C. J., A. J. Kavanagh, M. A. Clilverd, and S. R. Marple (2013), Comparison between POES energetic electron precipitation observations and riometer absorptions: Implications for determining true precipitation fluxes, *Journal of Geophysical Research: Space Physics*, *118*(12), 7810–7821, doi:10.1002/2013JA019439.

Rodger, C. J., A. T. Hendry, M. A. Clilverd, C. A. Kletzing, J. B. Brundell, and E. G. D. Reeves (2015), High-resolution in situ observations of electron precipitation-causing EMIC waves, *Geophysical Research Letters*, pp. 9633–9641, doi:10.1002/2015GL066581.Received.

Rozanov, E., M. Calisto, T. Egorova, T. Peter, and W. Schmutz (2012), Influence of the Precipitating Energetic Particles on Atmospheric Chemistry and Climate, *Surveys in Geophysics*, *33*(3-4), 483–501, doi:10.1007/s10712-012-9192-0.

Russell, C. T. (1993a), Magnetic Fields of the Terrestrial Planets, *Journal of Geophysical Research*, *98*, 18,681–18,695.

Russell, C. T. (1993b), Planetary magnetospheres, *Rep. Prog. Phys*, *56*, 687–732.

Russell, C. T., McPherro.Rl, and R. K. Burton (1974), Cause of Geomagnetic Storms, *Journal of Geophysical Research*, *79*(7), 1105–1109, doi:10.1029/JA079i007p01105.

Sætre, C., J. Stadsnes, H. Nesse, A. Aksnes, S. M. Petrinec, C. A. Barth, D. N. Baker, R. R. Vondrak, and N. ??stgaard (2004), Energetic electron precipitation and the NO abundance in the upper atmosphere: A direct comparison during a geomagnetic storm, *Journal of Geophysical Research: Space Physics*, *109*(A9), 1–9, doi:10.1029/2004JA010485.

Sætre, C., C. A. Barth, J. Stadsnes, N. Østgaard, S. M. Bailey, D. N. Baker, and J. W. Gjerloev (2006), Comparisons of electron energy deposition derived from observations of lower thermospheric nitric oxide and from X-ray bremsstrahlung measurements, *Journal of Geophysical Research: Space Physics*, *111*(4), 1–10, doi:10.1029/2005JA011391.

Sætre, C., C. A. Barth, J. Stadsnes, N. Østgaard, S. M. Bailey, D. N. Baker, G. A. Germany, and J. W. Gjerloev (2007), Thermospheric nitric oxide at higher latitudes: Model calculations with auroral energy input, *Journal of Geophysical Research: Space Physics*, *112*(8), 1–11, doi:10.1029/2006JA012203.

Sandanger, M. I., F. Søraas, K. Aarsnes, K. Oksavik, D. S. Evans, and M. S. Greer (2005), Proton Injections Into the Ring Current Associated with Bz Variations During HILDCAA Events, in *The Inner Magnetosphere - Physics and Modelling*, pp. 249–256, American Geophysical Union, doi:10.1029/155GM26.

Sandanger, M. I., F. Søraas, K. Aarsnes, K. Oksavik, and D. S. Evans (2007), Loss of relativistic electrons: Evidence for pitch angle scattering by electromagnetic ion cyclotron waves excited by unstable ring current protons, *Journal of Geophysical Research*, *112*(A12), A12,213, doi:10.1029/2006JA012138.

Sandanger, M. I., F. Søraas, M. Sørbø, K. Aarsnes, K. Oksavik, and D. S. Evans (2009), Relativistic electron losses related to EMIC waves during CIR and CME storms, *Journal of Atmospheric and Solar-Terrestrial Physics*, *71*(10-11), 1126–1144, doi:10.1016/j.jastp.2008.07.006.

Sandanger, M. I., L.-K. G. Ødegaard, H. Nesse Tyssøy, J. Stadsnes, F. Søraas, K. Oksavik, and K. Aarsnes (2015), In-flight calibration of NOAA POES proton detectors - Derivation of the MEPED correction factors, *Journal of Geophysical Research: Space Physics*, *120*, 9578–9593, doi:10.1002/2015JA021388.

Seale, R., and R.-H. Bushnell (1987), NOAA Technical Memorandum ERL SEL-75.

Seppälä, A., K. Matthes, C. E. Randall, and I. A. Mironova (2014), What is the solar influence on climate? Overview of activities during CAWSES-II, *Progress in Earth and Planetary Science*, *1*, 1–12, doi:10.1186/s40645-014-0024-3.

Shea, M., and D. F. Smart (1990), A Summary of Major Solar Proton Events, *Solar Physics*, *127*, 297–320.

Sinnhuber, M., H. Nieder, and N. Wieters (2012), Energetic Particle Precipitation and the Chemistry of the Mesosphere/Lower Thermosphere, *Surveys in Geophysics*, *33*(6), 1281–1334, doi:10.1007/s10712-012-9201-3.

Siskind, D., and J. Russell III (1996), Coupling between middle and upper atmospheric NO: Constraints from HALOE observations, *Geophysical Research Letters*, *23*(2), 137–140.

Solomon, S., D. W. Rusch, J. C. Gérard, G. C. Reid, and P. J. Crutzen (1981), The effect of particle precipitation events on the neutral and ion chemistry of the middle atmosphere: II. Odd hydrogen, *Planetary and Space Science*, *29*(8), 885–893, doi: 10.1016/0032-0633(81)90078-7.

Søraas, F., K. Aarsnes, J. Å. Lundblad, and D. S. Evans (1999), Enhanced Pitch Angle Scattering of Protons at Mid-Latitudes During Geomagnetic Storms, *Phys. Chem. Earth*, *24*(1), 287–292.

Søraas, F., K. Aarsnes, K. Oksavik, M. I. Sandanger, D. S. Evans, and M. S. Greer (2004), Evidence for particle injection as the cause of Dst reduction during HILDCAA events, *Journal of Atmospheric and Solar-Terrestrial Physics*, *66*(2), 177–186, doi:10.1016/j.jastp.2003.05.001.

Stern, D. P. (2005), A Historical Introduction to the Ring Current, in *The Inner Magnetosphere - Physics and Modelling*, pp. 1–8, American Geophysical Union.

Theodoridis, G. C., and F. R. Paolini (1967), Pitch angle diffusion of relativistic outer belt electrons, *Annales Geophysicae*, *23*, 375–380.

Thorne, R. M. (1980), The importance of energetic particle precipitation on the chemical composition of the middle atmosphere, *Pure and Applied Geophysics PAGEOPH*, *118*(1), 128–151, doi:10.1007/BF01586448.

Thorne, R. M. (2010), Radiation belt dynamics: The importance of wave-particle interactions, *Geophysical Research Letters*, *37*(September), 1–7, doi:10.1029/2010GL044990.

Tranquille, C. (1994), Solar proton events and their effect on space systems, *Radiation Physics and Chemistry*, *43*(1-2), 35–45, doi:10.1016/0969-806X(94)90200-3.

Tsurutani, B. T., and G. S. Lakhina (1997), Some basic concepts of wave-particle interactions in collisionless plasmas, *Reviews of Geophysics*, *35*(4), 491–502.

Tsurutani, B. T., W. D. Gonzalez, A. L. C. Gonzalez, F. Tang, J. K. Arballo, and M. Okada (1995), Interplanetary origin of geomagnetic activity in the declining phase of the solar cycle, *Journal of Geophysical Research*, *100*, 21,717, doi: 10.1029/95JA01476.

Tsurutani, B. T., W. D. Gonzalez, F. Guarnieri, Y. Kamide, X. Zhou, and J. K. Arballo (2004), Are high-intensity long-duration continuous AE activity (HILDCAA) events substorm expansion events?, *Journal of Atmospheric and Solar-Terrestrial Physics*, *66*(2), 167–176, doi:10.1016/j.jastp.2003.08.015.

Tsurutani, B. T., W. D. Gonzalez, A. L. C. Gonzales, F. L. Guarnieri, N. Gopalswamy, M. Grande, Y. Kamide, Y. Kasahara, G. Lu, I. Mann, R. L. McPherron, F. Søraas,

and V. M. Vasyliunas (2006), Corotating solar wind streams and recurrent geomagnetic activity: A review, *Journal of Geophysical Research*, *111*(A7), A07S01, doi: 10.1029/2005JA011273.

Turunen, E., P. T. Verronen, A. Seppälä, C. J. Rodger, M. A. Clilverd, J. Tamminen, C.-F. Enell, and T. Ulich (2009), Impact of different energies of precipitating particles on NOx generation in the middle and upper atmosphere during geomagnetic storms, *Journal of Atmospheric and Solar-Terrestrial Physics*, *71*(10-11), 1176–1189, doi: 10.1016/j.jastp.2008.07.005.

Verronen, P. T., C. J. Rodger, M. A. Clilverd, and S. Wang (2011), First evidence of mesospheric hydroxyl response to electron precipitation from the radiation belts, *Journal of Geophysical Research*, *116*, doi:10.1029/2010JD014965.

Yando, K. B., R. M. Millan, J. C. Green, and D. S. Evans (2011), A Monte Carlo simulation of the NOAA POES Medium Energy Proton and Electron Detector instrument, *Journal of Geophysical Research*, *116*(A10231), 1–13, doi:10.1029/2011JA016671.

Zawedde, A. E., H. N. Tyssøy, J. Stadsnes, L.-K. Ødegaard, M. I. Sandanger, P. J. Espy, and R. Hibbins (2016), The impact of energetic electron precipitation on mesospheric hydroxyl during a year of solar minimum.

Zhang, Y., and L. J. Paxton (2008), An empirical Kp-dependent global auroral model based on TIMED/GUVI FUV data, *Journal of Atmospheric and Solar-Terrestrial Physics*, *70*(8-9), 1231–1242, doi:10.1016/j.jastp.2008.03.008.

Chapter 7

Papers

Paper I

In-flight calibration of NOAA POES proton detectors - Derivation of the MEPED correction factors

Sandanger, M. I , L.-K. G. Ødegaard, H. Nesse Tyssøy, J. Stadsnes, F. Søraas, K. Oksavik, and K. Aarsnes

Journal of Geophysical Research: Space Physics, *120*, (2015). doi: 10.1002/2015JA021388

AGU PUBLICATIONS

JGR

Journal of Geophysical Research: Space Physics

RESEARCH ARTICLE
10.1002/2015JA021388

Key Points:
- MEPED proton detectors degrade and must be corrected before used quantitatively
- The degradation imposes great challenges for long-term studies
- A new set of correction factors to prolong the validity of the data is presented

Correspondence to:
M. I. Sandanger,
marit.sandanger@ift.uib.no

Citation:
Sandanger, M. I., L.-K. G. Ødegaard, H. Nesse Tyssøy, J. Stadsnes, F. Søraas, K. Oksavik, and K. Aarsnes (2015), In-flight calibration of NOAA POES proton detectors—Derivation of the MEPED correction factors, *J. Geophys. Res. Space Physics*, *120*, doi:10.1002/2015JA021388.

Received 28 APR 2015
Accepted 30 OCT 2015
Accepted article online 3 NOV 2015

In-flight calibration of NOAA POES proton detectors—Derivation of the MEPED correction factors

Marit Irene Sandanger[1], Linn-Kristine Glesnes Ødegaard[1], Hilde Nesse Tyssøy[1], Johan Stadsnes[1], Finn Søraas[1], Kjellmar Oksavik[1,2], and Kjell Aarsnes[1]

[1]Birkeland Centre for Space Science, Department of Physics and Technology, University of Bergen, Bergen, Norway, [2]Department of Arctic Geophysics, University Centre in Svalbard, Longyearbyen, Norway

Abstract The MEPED instruments on board the NOAA POES and MetOp satellites have been continuously measuring energetic particles in the magnetosphere since 1978. However, degradation of the proton detectors over time leads to an increase in the energy thresholds of the instrument and imposes great challenges to studies of long-term variability in the near-Earth space environment as well as a general quantification of the proton fluxes. By comparing monthly mean accumulated integral flux from a new and an old satellite at the same magnetic local time (MLT) and time period, we estimate the change in energy thresholds. The first 12 monthly energy spectra of the new satellite are used as a reference, and the derived monthly correction factors over a year for an old satellite show a small spread, indicating a robust calibration procedure. The method enables us to determine for the first time the correction factors also for the highest-energy channels of the proton detector. In addition, we make use of the newest satellite in orbit (MetOp-01) to find correction factors for 2013 for the NOAA 17 and MetOp-02 satellites. Without taking into account the level of degradation, the proton data from one satellite cannot be used quantitatively for more than 2 to 3 years after launch. As the electron detectors are vulnerable to contamination from energetic protons, the corrected proton measurements will be of value for electron flux measurements too. Thus, the correction factors ensure the correctness of both the proton and electron measurements.

1. Introduction

The NOAA (National Oceanic and Atmospheric Administration) POES (Polar Orbiting Environment Satellites), and MetOp (Meteorological Operational) satellites have continuously been orbiting the Earth since 1978. During this time period, 14 satellites with nearly the same instrumentation have been used to monitor the near-Earth space particle environment as well as predict the weather and climate pattern. Each satellite has a nominal lifespan of 3 years, but most satellites have been in operation much longer. NOAA 15, which was launched in 1998, is the oldest spacecraft in operation.

The protons in the inner radiation belt were first detected at low altitude by the second Soviet satellite [*Vernov et al.*, 1962]. Since then, the space age has provided us important in situ measurements of the near-Earth space environment including the ring current as well as the radiation belts. The extensive POES and MetOp series, covering more than three solar cycles (as shown in Figure 1), are currently providing the longest running estimates of the particle flux being deposited into the upper and middle atmosphere, where it can affect the chemical composition [*Jackman et al.*, 2001; *Seppälä et al.*, 2006]. However, the proton detectors on board POES and MetOp will degrade with time due to radiation damage [*Galand and Evans*, 2000] making them less sensitive to energetic particles.

It has been known for some time that solid state detectors may degrade due to radiation damage [*Coleman et al.*, 1968]. *Lyons and Evans* [1984] were the first to report nonphysical features in the MEPED (Medium Energy Proton and Electron Detector) data set that was attributed to degradation. In areas where the pitch angle distribution was expected to be isotropic or near isotropic, the proton intensities at small pitch angles often exceeded those near 90°, which is highly unlikely for energies above 30 keV. *Galand and Evans* [2000] studied the degradation of the MEPED proton detectors, and they suggested not using the data after 2–3 years for quantitative studies due to reduced sensitivity. Even though their report left no doubt that the proton detectors degrade with time, there were no immediate follow up studies. It is a complex and time-consuming

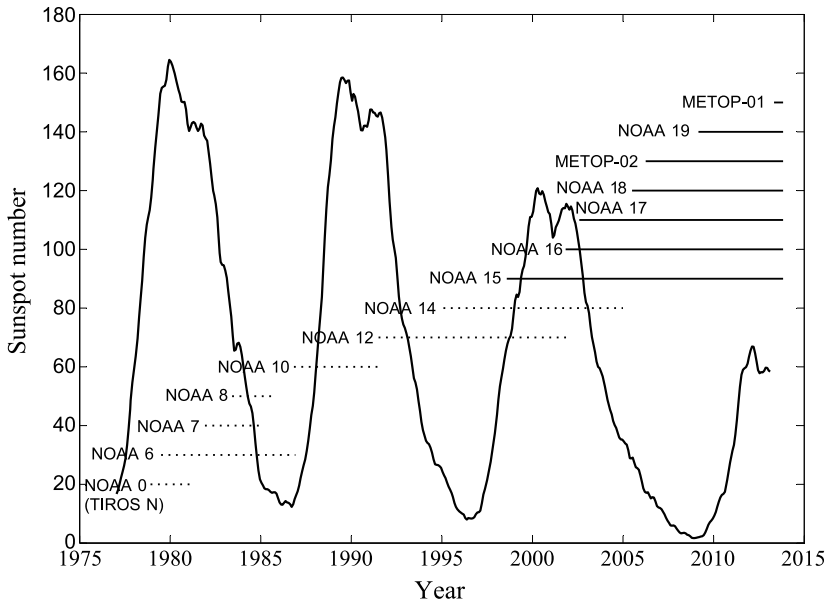

Figure 1. NOAA POES and MetOp satellites cover more than three solar cycles. Satellites with the SEM-1 and SEM-2 instrument package are displayed using dotted and solid lines, respectively.

task to determine the exact amount of degradation during the lifetime of each MEPED detector. It took a decade before the first study, which derived correction factors for the degradation, was done by *Asikainen and Mursula* [2011] and followed up by *Asikainen et al.* [2012] and *Ødegaard* [2013]. The studies by *Asikainen and Mursula* [2011] and *Asikainen et al.* [2012] derived correction factors for the three lowest energy channels, while *Ødegaard* [2013] derived correction factors for the two lowest energy channels. In this study, correction factors for all five energy channels are provided.

In order to move from qualitative studies [e.g., *Codrescu et al.*, 1997; *Oksavik et al.*, 2000; *Søraas et al.*, 2003; *Sandanger et al.*, 2007; *Miyoshi and Kataoka*, 2008; *Horne et al.*, 2009; *Sandanger et al.*, 2009; *Rodger et al.*, 2010] to quantitative studies of protons and their effect on the environment, it is of major importance to know the MEPED detector degradation for each satellite.

The MEPED electron detectors are protected from protons below 135 keV, but higher energy protons will be able to contaminate the electron measurements. Energetic protons above 200 keV are efficiently detected by the electron detector. This is known and well understood [*Evans and Greer*, 2000; *Yando et al.*, 2011]. The contribution of protons to the electron detector response can be determined from the corrected proton observations. In order to use the MEPED electron data in quantitative studies, one has to know the flux of the energetic protons [*Evans and Greer*, 2000; *Yando et al.*, 2011; *Whittaker et al.*, 2014]. The MEPED proton correction factors are thus also needed for the quantitative use of the electron data. The main purpose of this paper is to enable the use of proton and electron data from POES MEPED detectors even after the proton detectors start to degrade.

We start in section 2 with an orbital overview of the POES and MetOp satellites where we focus on the satellites NOAA 15 and above, with the SEM-2, a newer and modified SEM (Space Environment Monitor) instrument package, followed by section 3 describing the degradation and radiation damage of the MEPED proton detectors. Section 4 explains our method for deriving the correction factors. We use all available data throughout the whole orbit. Only satellites in the same MLT are compared. The monthly mean integral flux spectrum from an old satellite is compared with that from a new satellite for the same month. By comparing monthly mean spectra, it is expected that rapid fluctuations in the data are leveled out and that the two satellites are subjected to the same average particle environment. The 12 monthly energy spectra from the first year of a new satellite are used as a reference. Section 5 gives an overview of the correction factors, while section 6 explains how to obtain the monthly correction factors for times when direct calibration is not available. We show how the temporal evolution of our correction factors compares with results from earlier studies [*Asikainen and Mursula*, 2011; *Asikainen et al.*, 2012]. In section 7 the corrected proton flux at fixed energies from satellites of

Table 1. Overview of the Different Energy Channels (Differential and Integral) of the SEM-2 MEPED Proton Detectors for Both the 0° and the 90° Detector[a]

	Proton Energy (keV)	
Channel Identification	Differential Channel	Integral Channel
0°/90° P1	30 to 80	>30
0°/90° P2	80 to 250	>80
0°/90° P3	250 to 800	>250
0°/90° P4	800 to 2500	>800
0°/90° P5	2500 to 6900	>2500
0°/90° P6	>6900	

[a]The flux in the integral channels is derived from the differential channels. The flux in the P6 differential channel is not used to derive integral flux, due to possible contamination by relativistic electrons [*Yando et al.*, 2011].

different operation times are compared. The fluxes overlap close to perfectly, verifying of the quality of the derived correction factors. We also demonstrate examples of uncorrected and corrected data for a ten year old satellite to visualize the importance of correcting the data. Finally, we discuss reliability and limitation of our method and results.

2. NOAA POES and MetOp Satellites

The NOAA POES and MetOp satellites are Sun-synchronous low-altitude polar orbiting spacecraft. Their orbital period is about 103 min, resulting in 14–15 orbits each day. The NOAA POES and the MetOp satellites together cover more than three solar cycles, with the first spacecraft NOAA 0 (TIROS-N) launched in 1978. The satellites from NOAA 0 up to NOAA 14 carried the first version of the instrument package, SEM-1, which varies slightly in energy bands from the SEM-2. In the current paper we focus on the newer SEM-2 instrument package used on NOAA 15 launched in 1998, and up until MetOp-01 launched in late 2012. The satellite MetOp-03 is planned to be launched in 2017 and will be the last one in this series carrying the instrument package SEM-2.

Figure 1 displays the operational period of the satellites with the SEM-1 (dotted lines) and SEM-2 (solid lines) instrument packages. The SEM MEPED instrument consists of two identical proton detectors, one viewing nearly radially outward from Earth and the other viewing nearly antiparallel to the satellite's velocity vector; for details, see *Evans and Greer* [2000]. These two detectors will be referred to as the 0° and the 90° detectors. At high latitudes this is approximately the pitch angle of the particles being measured by the respective detectors. The detectors have an opening angle of 30° full width half maximum. Table 1 gives an overview of the nominal energy thresholds of the SEM-2 MEPED proton detectors. The P6 channel (>6900 keV) sometimes experiences contamination from relativistic electrons. Except for these periods, this channel has very low count rates compared to the other channels. Based on this fact, we have dropped the P6 channel from our analysis. We then treat the P5 channel (2500–6900 keV) as an integral channel for >2500 keV protons.

The satellite orbits are located at different magnetic local time sectors, as visualized in Figure 2. The orbital planes show a variable drift in local time, and as shown in Figure 2, NOAA 15 and NOAA 16 have an especially large drift in local time. This drift has been previously shown by *Asikainen et al.* [2012]. Table 2 gives an overview of the satellites' operation time, mean altitude, ascending node at launch, and which satellites are intercalibrated. The satellites are launched alternately in low-altitude (~825 km) morning orbits, and high-altitude (~865 km) afternoon orbits. In the calibration we are comparing satellites which have the same local time orbits and, therefore, due to the launch procedure, also fly in the same orbit height. NOAA 16 is an exception, as the orbit is drifting into new local time sectors during its lifetime. Due to possible biases in several of its monthly spectra in 2013 we do not compare it with MetOp-01.

The MEPED instrument measures both protons and electrons, but we will focus on the proton detector which is more affected by radiation damage compared to the electron detector, as the electron detector has a nickel foil protecting it from protons below 135 keV [*Galand and Evans*, 2000]. The proton detectors are equipped with broom magnets excluding electrons with energies below 1.5 MeV to be detected. MEPED cannot

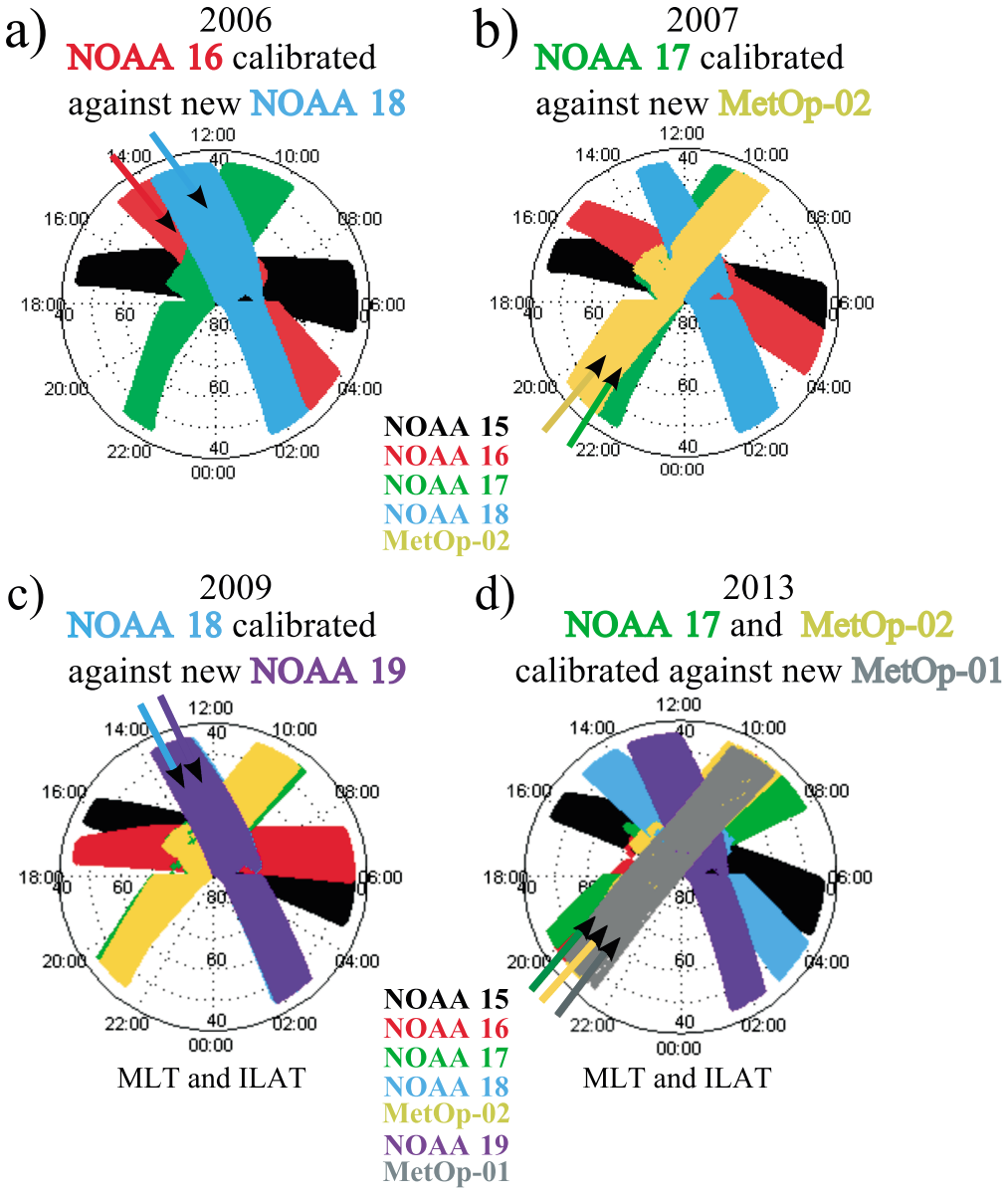

Figure 2. Footprints of the NOAA/POES and MetOp spacecrafts given as invariant latitude and magnetic local time in the Northern Hemisphere. (a) February 2006 when NOAA 18 is newly launched and have overlapping footprints with NOAA 16. (b) July 2007 when MetOp-02 is newly launched and calibrates NOAA 17. (c) September 2009 when NOAA 19 is newly launched and calibrates NOAA 18. (d) Data from 2013 when the footprint of NOAA 16, NOAA 17, and MetOp-02 are underneath the footprint of MetOp-01. MetOp-01 calibrates only NOAA 17 and MetOp-02 due to possible biases in several of the NOAA 16 monthly spectra in 2013.

distinguish between different ion species, but we will use the term protons to represent all ions measured by MEPED. A full description of the SEM-2 instrument package is given by *Evans and Greer* [2000], while the older SEM-1 instrument package is described by *Raben et al.* [1995].

3. Radiation Damage

Protons of energies between 50 keV and 5 MeV can generate significant radiation damage in silicon surface-barrier detectors [*Coleman et al.*, 1968]. The MEPED instrument measures protons in this energy range. *Galand and Evans* [2000] showed that the amount of proton flux measured by the MEPED detector is large enough to induce serious damage to the instrument.

Table 2. List of NOAA POES and MetOp Satellites Operation Time, Mean Altitude, Ascending Nodes at Launch, and Which Satellites They Calibrate[a]

Spacecraft	Operation	Altitude	Ascending Node	Calibrates	Figure 2 Panel
NOAA 15	1998–present	821	19:30		
NOAA 16	2001–2014	862	14:00		
NOAA 17	2002–2013	823	22:00		
NOAA 18	2005–present	866	14:00	NOAA 16	(a)
MetOp-02	2006–present	832	21:30	NOAA 17	(b)
NOAA 19	2009–present	868	14:00	NOAA 18	(c)
MetOp-01	2012–present	832	21:30	NOAA 17	(d)
MetOp-01	2012–present	832	21:30	MetOp-02	(d)

[a]The given mean altitude is for the year 2009. The ascending node is the local time when the spacecraft cross the equator in a northerly direction. Last column refers to the panel in Figure 2 that visualizes the satellites overlapping orbits in MLT which gives grounds for calibration. Section 4 will focus on the last column in the table (which shows the satellite that can be calibrated).

The NOAA Technical Report [*Galand and Evans*, 2000] gives a thorough evaluation of the MEPED proton instrument's radiation damage. The MEPED electron detector, on the other hand, did not suffer as badly from radiation damage. This can be explained by the electron detector's nickel foil, which prevents any protons of energy below 135 keV from reaching the detector and also considerably reduces the energy flux of protons of higher energies [*Galand and Evans*, 2000; *Yando et al.*, 2011].

During its lifetime, the 90° detector accumulates more counts than the 0° detector due to the pitch angle distribution (PAD) of the particles. One therefore expects that the 90° detector deteriorates faster than the 0° detector [*Galand and Evans*, 2000]. To determine the rate of degradation, *Galand and Evans* [2000] examined the ratio of the 0° response versus 90° response at geomagnetic latitudes above 60°. This ratio reflects the level of anisotropy of the radiation. Since anisotropic conditions during an orbit are more common than isotropic conditions, this ratio is usually low. Nevertheless, *Galand and Evans* [2000] found that the number of cases with the ratio >1 increased with time for all four NOAA satellites investigated (NOAA 0, NOAA 6, NOAA 10, and NOAA 12), confirming that the 90° proton detector degrades faster than the 0° detector, consistent with a pancake-shaped PAD of the protons. This comparison was performed using all SEM-1 instruments and for different levels of solar activity.

Galand and Evans [2000] plotted the occurrence rate of higher responses in the 0° detector than in the 90° detector, and they found that the slope and shape of the increase varied from one satellite to the next, implying different degradation rates. For NOAA 6, launched during solar maximum, the occurrence rate reached higher values for a much smaller total accumulated counts compared to NOAA 10, which was launched during solar minimum. They suggested that the radiation damage may not be a linear function of the total number of accumulated counts; the count rate may also play a role. It is also possible that the protons measured by the MEPED are not the only particles responsible for the radiation damage. Protons of lower energies, as well as electrons, relativistic protons with energies >100 MeV (from solar proton events), and heavy ions can also participate in the deterioration of the instruments.

Galand and Evans [2000] highlighted two types of possible damage:

1. Dead layer. The formation of a dead layer in which the incident particle is slowed down and where part of its energy is absorbed without contributing to the charge collection (not measured).
2. Partial charge collection. A decrease in the mobility of the free electrons/holes created in the crystal by the incident proton. The free electrons/holes recombine before they have contributed fully to the charge collection.

Due to the two effects, the charge collection is reduced and the energy of the incident proton will thereby be underestimated. As the detector degrades, the energy of the protons must increase in order to trigger a fixed energy threshold, and a new and an old detector will be sensitive to different parts of the particle population. A new detector measures protons with energies as low as 30 keV (see Table 1), whereas the most degraded detector in our study (see NOAA 17 in Table 4), cannot detect protons with energy lower than 60 keV.

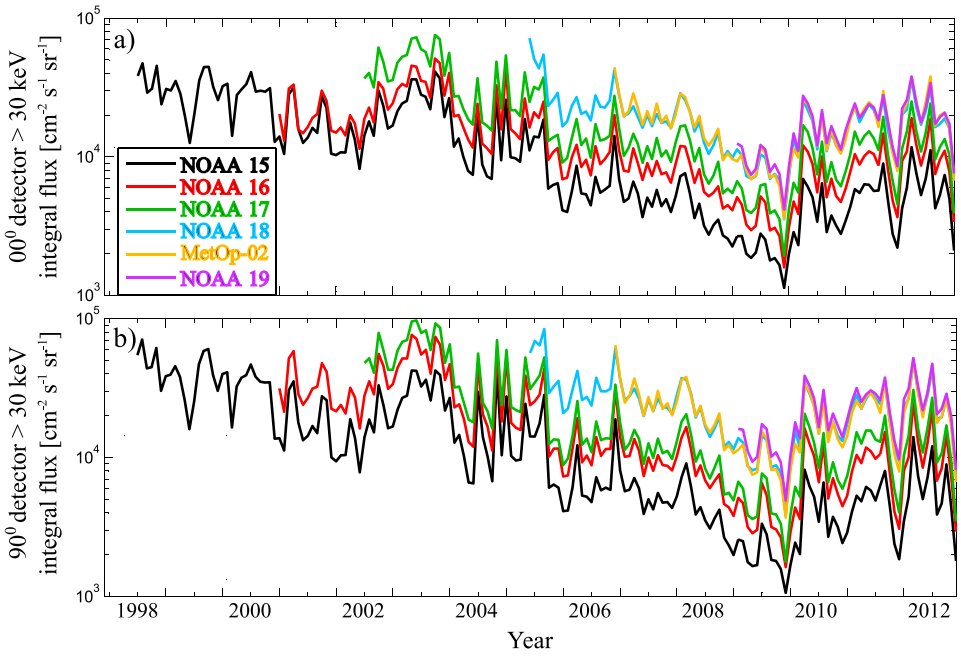

Figure 3. The monthly accumulated proton integral flux for the satellites NOAA 15, 16, 17, 18, and 19 and MetOp-02 with nominal energy greater than 30 keV. (a) Data from the 0° detector. (b) Data from the 90° detector.

Figure 3 shows the monthly mean proton integral flux (for the uncorrected nominal energy threshold E > 30 keV) from 1998 to the end of 2013 for the NOAA 15, NOAA 16, NOAA 17, NOAA 18, MetOp-02, and NOAA 19 satellites. The data from the 0° detector are displayed in Figure 3a, and data from the 90° detector is displayed in Figure 3b. Satellites in similar orbits with identical instruments should measure the same particle flux variations when monthly averages are compared. Figure 3 clearly shows indications of detector degradation, as an old satellite measures lower fluxes than a new satellite in the same time period at nominal energies. The discrepancy between the flux measured by an old and a new satellite can be nearly an order of magnitude. It is worth noticing how the 90° detector (Figure 3b) shows higher fluxes than the 0° detector (Figure 3a), even though the 90° detector suffers more damage than the 0° detector. The 90° detector measures up to 50% more than the 0° detector and on an average 25% more, due to the pancake shaped PAD.

4. Method to Determine the Correction Factors

We want to estimate the current energy thresholds of the MEPED proton detector. The In-Flight-Calibration files for all the satellites have been examined, and the noise level in all of them, in the time intervals when the α factors have been estimated, is nominal. The ratio of the current energy thresholds to the nominal energy thresholds is called the correction factor, α. The α factors give the energy changes of the degraded detector. In that way we can establish corrected integral spectra. To achieve this, we compare particle spectra from a degraded detector with a new and nondegraded detector.

A magnetic storm will increase the proton fluxes more in the MLT evening and nightside sector than in the morning and noon sector [*Codrescu et al.*, 1997], on timescales ranging from a few hours to a few days. Due to such magnetic local time effects, an old satellite is only compared to a satellite in the same MLT sector. NOAA 15, NOAA 17, MetOp-02, and MetOp-01 have ascending nodes in the evening MLT region, while NOAA 16, NOAA 18, and NOAA 19 have ascending nodes in the afternoon sector. It is important to account for this systematic behavior, and therefore, we only compare a new satellite with an old satellite at the same MLT. The NOAA 15 and NOAA 16 drift in their orbits, making them hard to compare with newer satellites (see last column of Table 2 for an overview of comparable satellites).

In our method the data from all latitudes and longitudes are used. For each satellite, the monthly mean of the proton flux is calculated for each energy channel. If data for a whole day is missing for one satellite, then the same day is removed from all comparable satellite's data sets in order for the satellites to measure in the same

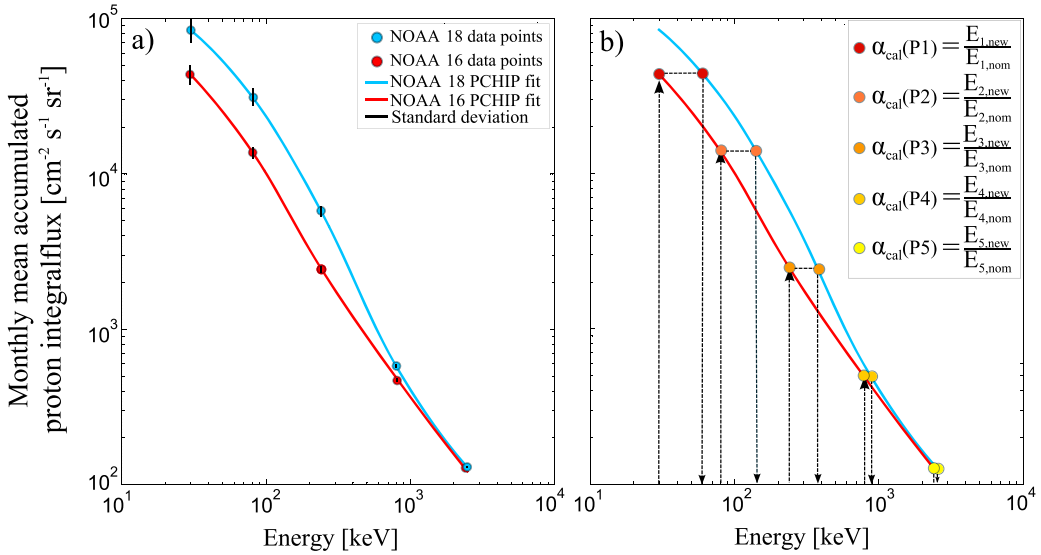

Figure 4. Illustration of how the α_{cal} factors are derived. The monthly mean accumulated proton energy spectra from a new (NOAA 18) and 4.5 years old (NOAA 16) satellite are shown in the panels. The data are from the 90° detectors during October 2005. (a) The integral flux from NOAA 18 and from NOAA 16 with a PCHIP fit to the data plotted on a logarithmic scale. (b) The procedure of determining the new energy thresholds of the older NOAA 16 satellite from the NOAA 18 energy spectrum. The standard deviations are shown as error bars in panel (a).

time intervals. The monthly mean differential flux is then converted to a monthly mean integral flux. Figure 4 illustrates how the α factors are derived based on the monthly mean accumulated integral flux energy spectra from a new satellite (NOAA 18) and a 4.5 year old satellite (NOAA 16). Henceforth, the α factors derived from this calibration method will be referred to as the α_{cal} factor.

We have chosen to use the mean and include zero count rate values within this calculation. This inclusion is due to low fluxes, which might not trigger a count in the instrument. It should be noted that there is a potential for error by including zero counts. Hence, our use of the mean is essential with a large number of zero values and again this could be a source of error in a skewed distribution. The final results are discussed in section 7, which show a good correlation between an old satellite with an alpha correction and a new satellite and indicate that this method of analysis is justified and the errors are assumed to be minimal.

In order to numerically represent the integral spectrum, we have fitted a monotonic Piecewise Cubic Hermite Interpolating Polynomial (PCHIP) to the measurements, illustrated in Figure 4a. A PCHIP fit is guaranteed to go through all your data points, as well as producing a monotone function that is physically consistent with an integral spectrum. Figure 4b demonstrates the method and the basic idea behind correcting for the degradation of a detector. The new detector measures the observed energy spectrum at the nominal energy thresholds, while the degraded detector measures the same energy spectrum, with the important difference that the energy thresholds are unknown. With the assumption that the old satellite's integral flux level is correct, and the energy threshold is the unknown, the procedure is as follows: The integral flux at the nominal energy threshold for the old satellite is found (follow the arrows in Figure 4b), and for that specific integral flux the corresponding energy threshold of the new satellite is found. This is done for all five nominal energy thresholds.

The respective flux and the associated energy give us the increased energy threshold for the particles detected:

$$\alpha_{cal} = \frac{E_{new}}{E_{nom}} \tag{1}$$

Each comparison between the energy spectrum from a new and an old satellite generates a set of α_{cal} factors

$$\text{Correction factors} = [\alpha_{cal}(P1), \alpha_{cal}(P2), \alpha_{cal}(P3), \alpha_{cal}(P4), \alpha_{cal}(P5)] \tag{2}$$

that corresponds to the five integral channels P1–P5 (as shown in Figure 4b). The nominal energy of the integral channels P1–P5 is given in the last column in Table 1.

Table 3. The α_{cal} Factors for All Four Satellites and for Both the 0° and 90° Detectors[a]

Satellite	Year (Month)	Mean α_{cal}(Standard Deviation)				
		α_1	α_2	α_3	α_4	α_5
				0° Detector		
NOAA 16	2005 (Feb)	1.57 (0.08)	1.65 (0.08)	1.22 (0.05)	1.12 (0.06)	1.08 (0.08)
NOAA 17	2007 (Jul)	1.37 (0.06)	1.59 (0.07)	1.19 (0.02)	1.07 (0.01)	1.03 (0.01)
NOAA 17	2013 (Apr)	1.53 (0.05)	1.82 (0.10)	1.32 (0.07)	1.27 (0.09)	1.16 (0.08)
NOAA 18	2009 (Sep)	1.06 (0.04)	1.14 (0.05)	1.07 (0.01)	1.16 (0.01)	1.17 (0.01)
MetOp-02	2013 (Apr)	1.13 (0.07)	1.27 (0.10)	1.09 (0.07)	1.04 (0.06)	1.05 (0.06)
				90° Detector		
NOAA 16	2005 (Feb)	1.89 (0.10)	1.86 (0.07)	1.31 (0.02)	1.08 (0.03)	1.03 (0.03)
NOAA 17	2007 (Jul)	1.65 (0.08)	1.94 (0.07)	1.46 (0.02)	1.25 (0.01)	1.21 (0.01)
NOAA 17	2013 (Apr)	1.94 (0.06)	2.10 (0.10)	1.39 (0.09)	1.22 (0.06)	1.21 (0.05)
NOAA 18	2009 (Sep)	1.11 (0.05)	1.28 (0.06)	1.12 (0.01)	1.05 (0.01)	1.03 (0.01)
MetOp-02	2013 (Apr)	1.30 (0.09)	1.47 (0.10)	1.10 (0.06)	0.92 (0.05)	0.92 (0.05)

[a]Columns 3–7 show the mean α_{cal} factors with the standard deviation value in parentheses.

The α_{cal} factors are derived for each month throughout the first year after launch of a new satellite in the same MLT range as that of the old satellites. The sets of 12 monthly α_{cal} factors are used to determine the mean α_{cal} factors for the respective years, and the standard deviation is used as a measure of the spread in the data.

5. Resulting α_{cal} Factors

With our method we retrieve two sets of α_{cal} factors for NOAA 17 at the age of 4 and 10 years. For NOAA 16, NOAA 18, and MetOp-02 we retrieve only one set of α_{cal} factors, the NOAA 16 and 18 at the age of 4 and for MetOp-02 at 6 years. NOAA 15, NOAA 19, and MetOp-01 are without any α_{cal} factor at present time. In 2016/2017, the MetOp-03 satellite will be launched. This new MetOp satellite will orbit the Earth in the same MLT range as the MetOp-01 and 02 satellites, giving us the opportunity to derive α_{cal} factors for NOAA 17, MetOp-02, and MetOp-01 (all in the same MLT sector).

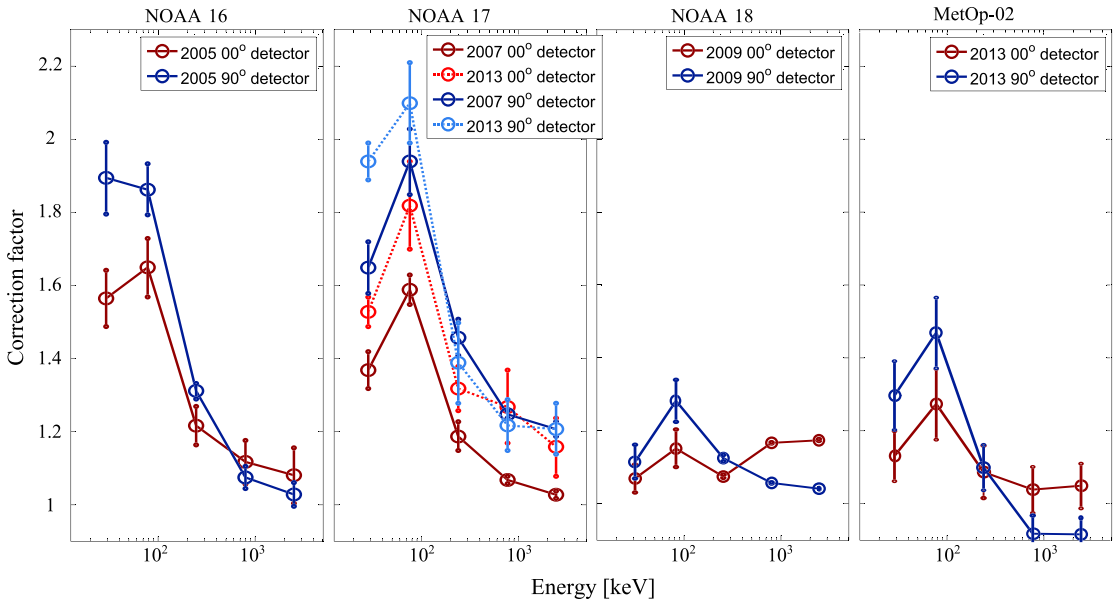

Figure 5. The different α_{cal} factors as a function of energy for NOAA 16, NOAA 17, NOAA 18, and MetOp-02. The blue lines display the α_{cal} factors for the 90° detector, while the red lines display the 0° detector. In the second panel, the dotted lines display the α_{cal} factors for 2013. The mean standard deviation is marked as a vertical error bar in each point.

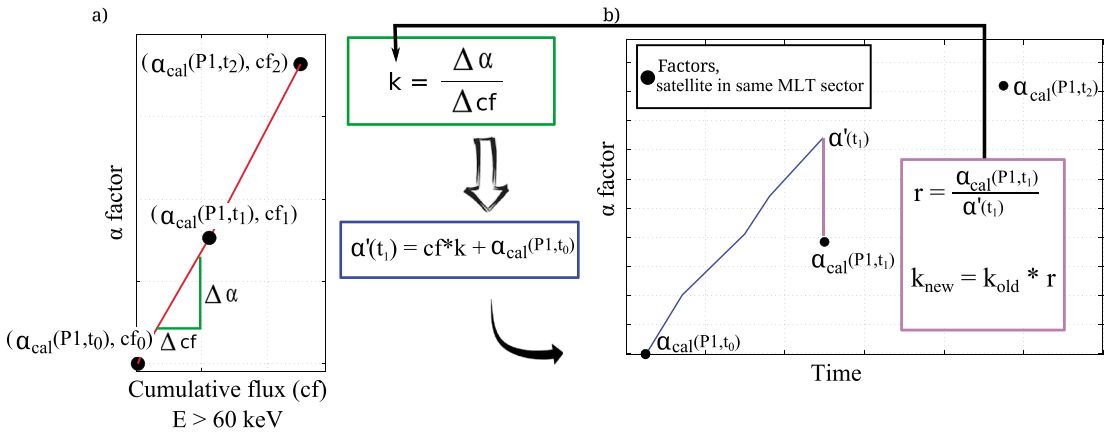

Figure 6. A visualization of the iteration process that is used to find the monthly α_{month} factors in between two α_{cal} factors. (a) The α_{cal} factors versus the calculated accumulated integral flux at the time when we have determined the α_{cal} factors. The linear slope k is calculated and used in the calculation of an α' describing the α factor after the first month. (b) The α factors versus time, showing the same three α_{cal} points as in Figure 6a, but also the new point α'. Figure 6b shows how we need an iterative process to find the right constant k in the linear equation.

Our mean α_{cal} factors together with the associated standard deviation values are shown in Table 3.

Figure 5 displays the α_{cal} factors versus energy for the four NOAA POES and MetOp satellites. It illustrates how the 90° detector (blue color scale) degrades faster than the 0° detector (red color scale). It is also evident from Figure 5 and Table 3 that the lowest energy channel (P1) degrades slower than the second energy channel (P2). This feature is somewhat unexpected and is commented further in relation to other studies at the end of section 6.1.

6. Temporal Evolution of the Degradation

The α factor is calculated at points separated by several years, and it is thus important to find a method of interpolation in between the calibration points. In this section we show a procedure for finding the monthly correction factors, α_{month}, throughout a satellites's lifetime. Assuming that it is the number of particles that hit the detector that is the main cause of the degradation, we use the method of accumulative flux to achieve the temporal evolution of the degradation.

To get an estimation of α_{month} based on the flux in the period between two α_{cal} factors, we go through an iterative process illustrated in Figure 6. This process is done for both detectors and all channels separately.

The first step is to apply the uncorrected integral flux, accumulated from the satellite was new and until the time of our α_{cal} factors. The uncorrected accumulative integral flux at these points is denoted cf_t, where the time is given by t. The α_{cal} factor for energy channel P1 is denoted $\alpha_{cal}(P1)$, and for time $t = 0$ the factor is denoted $\alpha_{cal}(P1, t_0)$. The α_{cal} factor and cf at $t = 0$, when the satellite is new, is respectively 1 and 0 for all energy channels. In Figure 6a $\{\alpha_{cal}(P1, t_0), cf_0\}$, $\{\alpha_{cal}(P1, t_1), cf_1\}$ and $\{\alpha_{cal}(P1, t_2), cf_2\}$ are plotted as black points.

The second step of the process is to calculate the linear slope k between the two first points in Figure 6a.

$$k = \frac{\Delta\alpha}{\Delta cf} = \frac{\alpha_{cal}(P1, t_1) - \alpha_{cal}(P1, t_0)}{cf_1 - cf_0} \tag{3}$$

The third step is to find the accumulated flux 1 month after the launch of the satellite. The flux is not accumulated $> E_{nom}$ thresholds, but rather the $> E_{new}$ thresholds. In that way, we ensure to accumulate the correct particle population. Lower energy protons can still degrade the detectors, but the E_{new} thresholds are set at the energies where even the most degraded satellite is still able to measure:

$$E_{new} = [60, 167, 360, 1050, 2300] \text{ (keV)} \tag{4}$$

in contrary to the nominal energy thresholds:

$$E_{nom} = [30, 80, 250, 800, 2500] \text{ (keV)} \tag{5}$$

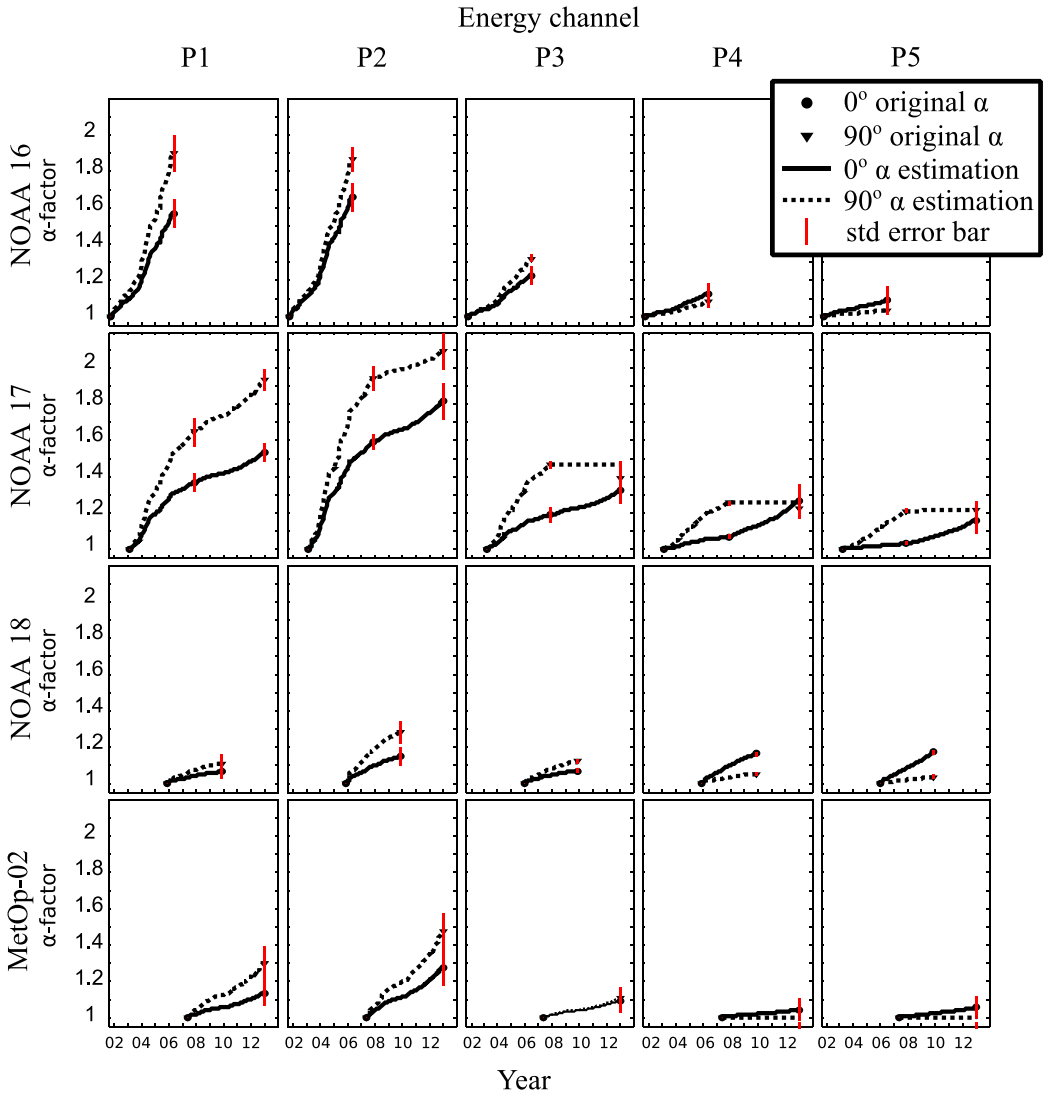

Figure 7. Each of the subplots display the α_{month} factor versus time for all four NOAA POES and MetOp satellites. The circles and triangles mark the α_{cal} factors from the 0° and the 90° detectors, respectively. The line in between these points is found through flux estimation, the dotted lines exhibit the 90° detector, and the solid lines exhibit the 0° detector. The MAD error bar is shown as red vertical lines.

The fourth step is to use the accumulated flux 1 month after the launch of a new satellite, together with the calculated slope k found in equation (3) in order to find the α_{month} factor after 1 month, α':

$$\alpha' = cf \times k + \alpha_{cal}(P1, t_0) = cf \times k + 1 \tag{6}$$

The calculated α' factor for the first month is used to correct the energy threshold and thus the accumulated flux of the second month in the satellite's lifetime, before an α' factor is calculated for the second month. This process is repeated until we reach the month at time t_1 corresponding to the month where we have our $\alpha_{cal}(P1, t_1)$. By this point, we have reached an $\alpha'(t_1)$ factor that is larger or smaller than the $\alpha_{cal}(P1, t_1)$. We find the ratio:

$$r = \frac{\alpha_{cal}(P1, t_1)}{\alpha'(t_1)} \tag{7}$$

and adjust the slope k by this factor, i.e.,

$$k_{new} = k_{old} \times r \tag{8}$$

Table 4. The α_{year} Factors for NOAA 16, NOAA 17, NOAA 18, and MetOp-02 Satellites for the 0° and the 90° Detectors[a]

		0° Detector					90° Detector				
Satellite	Year	α_1	α_2	α_3	α_4	α_5	α_1	α_2	α_3	α_4	α_5
NOAA 16	2001	1.03	1.04	1.01	1.01	1.01	1.05	1.05	1.02	1.01	1.00
NOAA 16	2002	1.09	1.11	1.04	1.02	1.03	1.13	1.13	1.05	1.01	1.01
NOAA 16	2003	1.21	1.24	1.08	1.04	1.04	1.30	1.29	1.11	1.03	1.02
NOAA 16	2004	1.37	1.43	1.14	1.08	1.06	1.53	1.51	1.19	1.03	1.02
NOAA 16	**2005**	**1.51**	**1.59**	**1.20**	**1.11**	**1.08**	**1.79**	**1.76**	**1.28**	**1.07**	**1.03**
NOAA 17	2002	1.00	1.00	1.00	1.00	1.00	1.00	1.00	1.00	1.00	1.00
NOAA 17	2003	1.08	1.13	1.04	1.01	1.00	1.13	1.19	1.10	1.04	1.02
NOAA 17	2004	1.19	1.31	1.10	1.03	1.01	1.31	1.44	1.22	1.11	1.06
NOAA 17	2005	1.27	1.44	1.14	1.05	1.02	1.47	1.68	1.33	1.17	1.12
NOAA 17	2006	1.33	1.52	1.17	1.06	1.02	1.57	1.83	1.41	1.22	1.16
NOAA 17	**2007**	**1.37**	**1.59**	**1.19**	**1.07**	**1.03**	**1.64**	**1.94**	**1.46**	**1.25**	**1.21**
NOAA 17	2008	1.40	1.63	1.21	1.10	1.04	1.70	1.97	1.46	1.25	1.21
NOAA 17	2009	1.41	1.66	1.22	1.12	1.06	1.73	1.99	1.46	1.25	1.21
NOAA 17	2010	1.44	1.69	1.24	1.15	1.09	1.77	2.01	1.46	1.25	1.21
NOAA 17	2011	1.47	1.73	1.27	1.19	1.11	1.83	2.04	1.46	1.25	1.21
NOAA 17	2012	1.51	1.79	1.30	1.24	1.14	1.90	2.08	1.46	1.25	1.21
NOAA 17	**2013**	**1.53**	**1.82**	**1.32**	**1.27**	**1.16**	**1.94**	**2.10**	**1.46**	**1.25**	**1.21**
NOAA 18	2005	1.00	1.00	1.00	1.00	1.00	1.00	1.00	1.00	1.00	1.00
NOAA 18	2006	1.02	1.05	1.02	1.05	1.04	1.04	1.10	1.04	1.02	1.01
NOAA 18	2007	1.04	1.09	1.04	1.09	1.08	1.07	1.18	1.08	1.03	1.02
NOAA 18	2008	1.05	1.12	1.06	1.13	1.12	1.09	1.24	1.10	1.04	1.02
NOAA 18	**2009**	**1.06**	**1.14**	**1.07**	**1.15**	**1.16**	**1.10**	**1.27**	**1.11**	**1.05**	**1.03**
MetOp-02	2007	1.01	1.03	1.01	1.00	1.00	1.03	1.05	1.01	1.00	1.00
MetOp-02	2008	1.04	1.08	1.03	1.01	1.01	1.09	1.14	1.03	1.00	1.00
MetOp-02	2009	1.05	1.10	1.03	1.02	1.02	1.12	1.18	1.04	1.00	1.00
MetOp-02	2010	1.07	1.14	1.04	1.02	1.03	1.15	1.24	1.05	1.00	1.00
MetOp-02	2011	1.09	1.18	1.06	1.03	1.04	1.20	1.31	1.07	1.00	1.00
MetOp-02	2012	1.12	1.25	1.08	1.04	1.05	1.26	1.42	1.09	1.00	1.00
MetOp-02	**2013**	**1.13**	**1.27**	**1.09**	**1.04**	**1.05**	**1.30**	**1.47**	**1.10**	**1.00**	**1.00**

[a]The α_{year} factors are from the midpoint of each year. The α_{year} factors given in bold text are from the same years when we have α_{cal} factors.

The process starts again from the first month after launch with the slope k_{new} as input in equation (6), that is:

$$\alpha' = cf \times k_{new} + \alpha_{cal}(P1, t_0) = cf \times k_{new} + 1 \tag{9}$$

The process is then repeated until $\alpha'(t_1) = \alpha_{cal}(P1, t_1)$. The same process is also applied between factors $\alpha_{cal}(P1, t_1)$ and $\alpha_{cal}(P1, t_2)$.

The α_{month} factors based on the accumulated flux method is shown with a monthly resolution in Figure 7 for NOAA 16, NOAA 17, NOAA 18, and MetOp-02.

The resulting yearly α factors, for NOAA 16, NOAA 17, NOAA 18, and MetOp-02 are given in Table 4. Henceforth, these yearly α factors will be referred to as the α_{year} factors and are taken from the month in the middle of each year. The α_{year} factors given in bold text in Table 4 are from the same years when we have α_{cal} factors. But the α_{year} factor with bold text may not be identical to the values in Table 3 since the α_{cal} factors in Table 3 are placed at the midpoint of the first 12 months after launch of a new satellite, while the α_{year} factors are from the middle of the calender year. Also, the accumulative flux method does not allow the α_{month} factors and α_{year} factors to decrease. This can lead to a constant α factor as shown in Figure 7 (third panel, NOAA 17). The 90° detector's $\alpha_{cal}(P3, t_2)$ value is slightly less than the $\alpha_{cal}(P3, t_1)$ value but can be kept constant within the error bars.

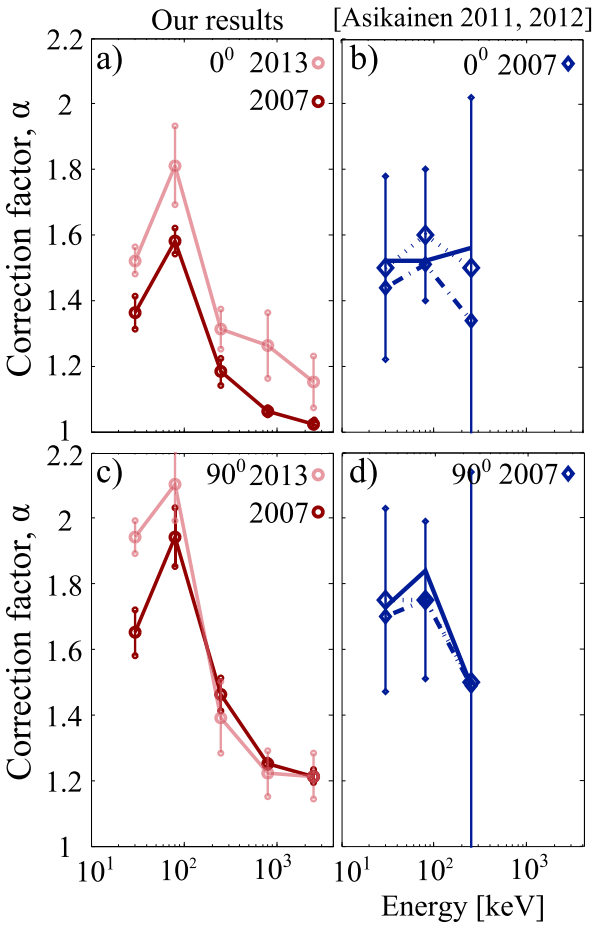

Figure 8. A comparison between the α_{cal} factors of the (a and b) 0° and (c and d) 90° detector of the two different studies. Our α factors for NOAA 17, year 2007 and 2013 are shown in, respectively, solid and dotted lines (Figures 8a and 8c). The α_{cal} factor for the same satellite in 2007 retrieved by *Asikainen and Mursula* [2011] is shown in dotted and dashed blue lines in Figures 8b and 8d, while *Asikainen et al.* [2012]'s corresponding results are shown in solid lines. The standard deviation (Figures 8a and 8c) and MAD (Figures 8b and 8d) are shown as vertical error bars in all α points.

6.1. Comparison With Earlier Studies

The first effort to quantify the α factors was done by *Asikainen and Mursula* [2011]. They identified cases where one old and one new satellites were close in time and space and assumed that the two satellites were observing the same particle population. The integral energy spectra from the two satellites were compared and the α factors for the old satellite were established. A challenge for the method is the lack of cases with new and old satellites being close in both time and space. Due to few cases, they did not derive α factors for the higher-energy channels. Different from our method is also the temporal evolution. *Asikainen and Mursula* [2011] fitted not only linear curves to the derived α factors but also second-, third-order polynomials, and PCHIP and presented α_{year} factors from the curve fitting. The follow-up paper, *Asikainen et al.* [2012], made use of the accumulated *Ap* index to refine the estimate for the temporal evolution of the yearly α factor.

Ødegaard [2013] is a prestudy for our work here as it sorted the first year of SEM-2 MEPED proton data according to the *Kp* index in a MLT/ILAT grid. The statistical maps gave the average proton flux as a function of MLT and ILAT. *Ødegaard* [2013] then compared measurements from the old satellite with a new satellite using these statistical maps. In that way, *Ødegaard* [2013] obtained α factors for P1 and P2. Like *Asikainen and Mursula* [2011] and *Asikainen et al.* [2012], this method also struggled regarding determination of the higher-energy α factors due to few cases.

Our study, as well as *Ødegaard* [2013] use average measurements to construct energy spectra for comparisons and mean or median to find the final α factor. But *Asikainen and Mursula* [2011] calculated numerous α factors for a limited number of conjunctions, whereas the final α factor was median of these.

Our study differs from *Asikainen and Mursula* [2011], *Asikainen et al.* [2012], and *Ødegaard* [2013] with a larger statistical database that makes us able to derive the α_{cal} factor also for the highest-energy channels of the proton MEPED detector. In addition, we make use of the newest satellite in orbit (MetOp-01) to find α_{cal} factors for the year 2013, and thereby α_{year} factors for the years 2011–2013.

In Figure 8 we focus on the NOAA 17 α_{cal} factors from a year that both *Asikainen and Mursula* [2011] and *Asikainen et al.* [2012] and our current study cover. Figure 8 shows α_{cal} factors as a function of nominal energy for our study (Figures 8a and 8c), *Asikainen and Mursula* [2011] and *Asikainen et al.* [2012] (Figures 8b and 8d). Solid lines with dark color visualize α_{cal} factors from 2007, while dotted lines with lighter colors in Figures 8a and 8c visualize α_{cal} factors from 2013. Figures 8b and 8d) show the α_{cal} factors both before (dotted lines)

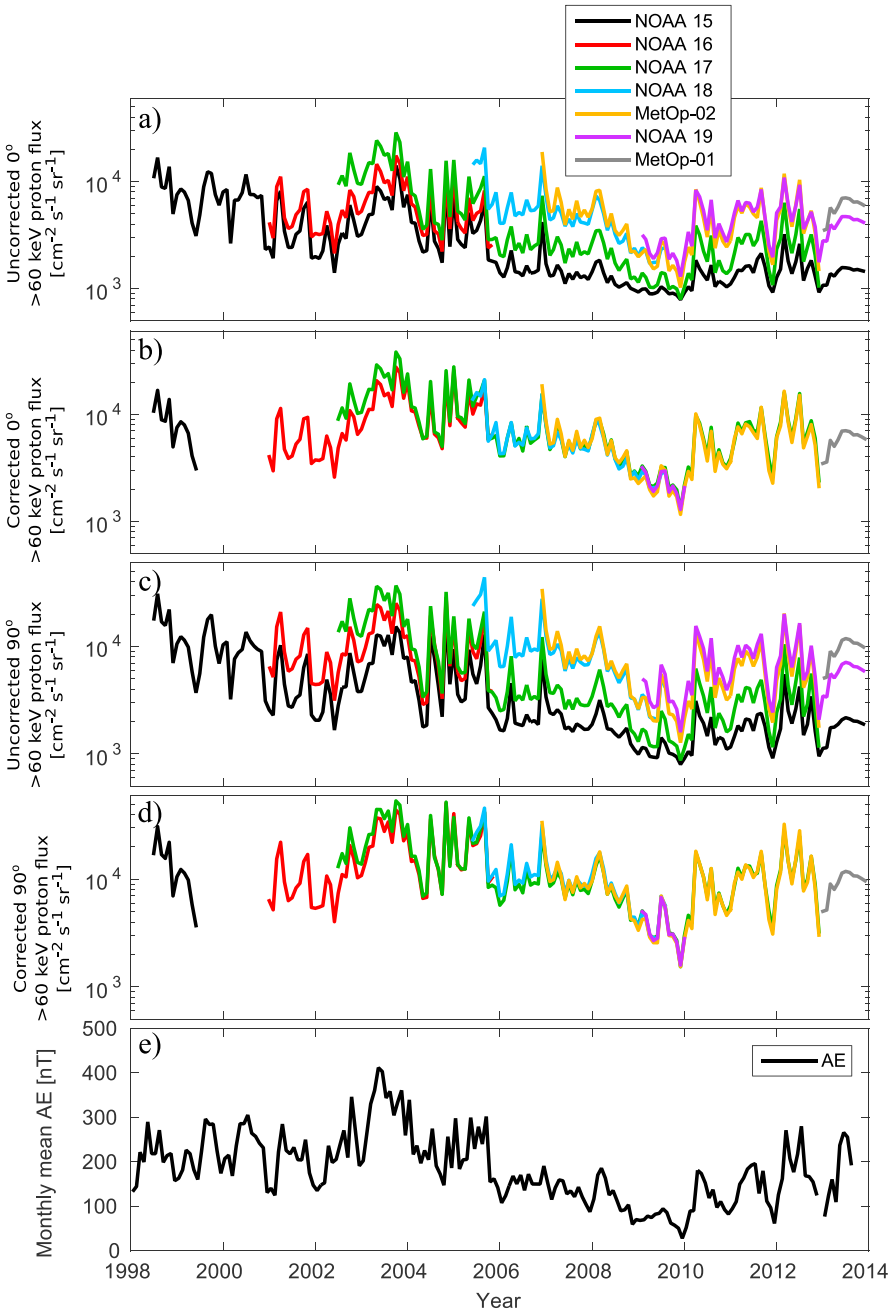

Figure 9. The monthly mean accumulated proton flux >60 keV measured by NOAA 15 (black line), NOAA 16 (red line), NOAA 17 (green line), NOAA 18 (light blue line), MetOp-02 (yellow line), NOAA 19 (purple line), and MetOp-01 (grey line). (a and b) Data from the 0° detector. (c and d) Data from the 90° detector. The uncorrected flux is shown in Figures 9a and 9c, and the alpha-corrected flux is shown in Figures 9b and 9d. Data from NOAA 15, NOAA 19 and MetOp-01 are added to the alpha-corrected (Figures 9b and 9d) but only for the first year of the satellite's operation. Data from NOAA 16 and NOAA 18 are displayed in the alpha-corrected panels (Figures 9b and 9d) until 1 year beyond their last α factor. (e) The monthly mean *AE* index.

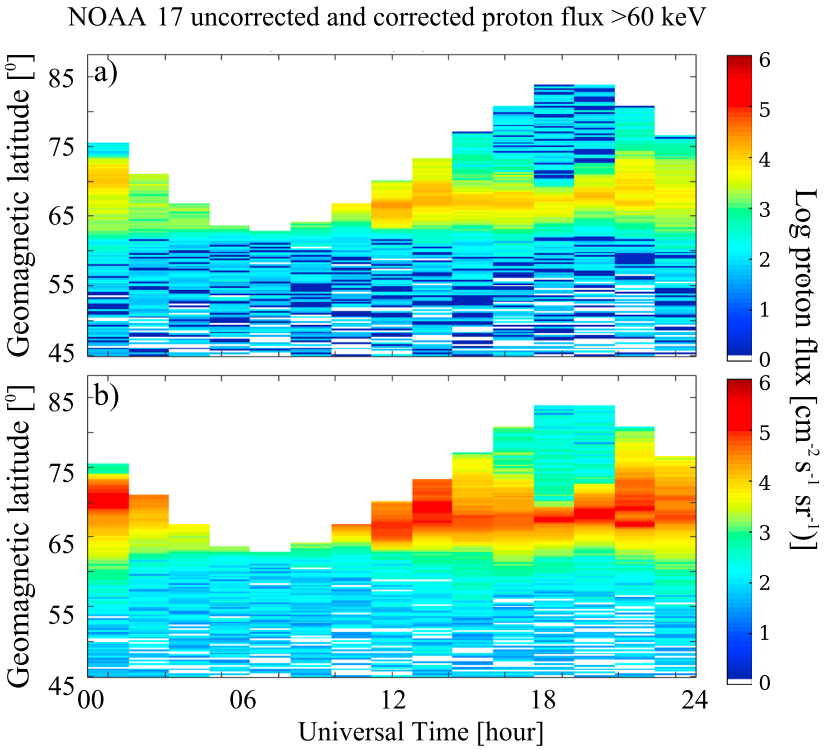

Figure 10. (a) Uncorrected and (b) corrected proton flux > 60 keV on a logarithmic color scale. The NOAA 17 proton flux are from the 90° detector. The data are from the evening side Northern Hemisphere on 5 January 2012.

and after this curve-fitting routine (dashed lines). Some of the α factors from *Asikainen and Mursula* [2011] are adjusted by *Asikainen et al.* [2012] due to the *Ap* activity index in order to get a better agreement between the satellites. The α factors resulting from the curve fit of *Asikainen et al.* [2012] are shown in solid lines in Figures 8b and 8d and are at times significantly different from the α factors achieved directly from their method shown as dotted and dashed lines. Our α factors are not adjusted due to curve fitting, and only one set of α factors are therefore shown in Figures 8a and 8c).

Comparing our α_{cal} factors from NOAA 16 in 2005, NOAA 17 in 2007, and NOAA 18 in 2009 with *Asikainen et al.* [2012], we find that their new energy thresholds show about 10% discrepancies from ours for the two lowest-energy channels. Their energy threshold for channel P3 is generally elevated by 5%–40% compared to ours.

Figure 8 shows that P2 degrades faster than P1, as visualized by the α_1 and α_2 factors. The degradation factors of all satellites examined in this study reveal the same quite puzzling feature regarding the temporal evolution between the α_1 and α_2 factors. The studies by *Asikainen and Mursula* [2011], *Asikainen et al.* [2012], and *Ødegaard* [2013] (not shown) all display the same trend, implying that this is a real feature of the detector degradation. Although a physical understanding of this artifact would be interesting, it is not essential for establishing a set of α factors that can be applied to the NOAA POES data.

7. Application of the α Factors

The importance of having high and reliable accuracy in the α factors is best illustrated by an example. The α factors are given as a set $[\alpha_{P1}, \alpha_{P2}, \alpha_{P3}, \alpha_{P4}, \alpha_{P5}]$ as shown in equation (2). For each of the nominal energies given in Table 1, one has to multiply by the α factor to achieve the corrected energy threshold:

$$E_{\text{corrected}}(n) = E_{\text{nominal}}(n) \times \alpha(Pn) \tag{10}$$

where $n \in [1, 2, 3, 4, 5]$ is the energy channel. The shape of the spectrum is essential for the level of correction at a specific energy.

Figures 9a and 9c show the uncorrected monthly mean integral fluxes for all satellites interpolated to >60 keV. This is done in order to compare at the same energy ranges, as 60 keV corresponds to the most degraded satellite in the period considered. The fluxes for all satellites in Figures 9a and 9c exhibit roughly the same short-term variations, but the measured flux is significantly lower when measured by an old satellite compared with a new one. Figures 9b and 9d show the mean integral fluxes for each month and satellite after the fluxes are corrected using the corresponding α_{month} factor. There is now a close to perfect overlap between the fluxes measured by the different satellites. Over the years 1998 to 2013 it is evident that there is a steady decline in the radiation measured at low altitude by a factor of 2 roughly linked to the solar cycle shown in Figure 1. The short time variation in the data is due to geophysical activity with injection of protons into the magnetosphere, as evident from the close similarities between these variations and the monthly mean *AE* index shown in Figure 9e.

Finally, to further illustrate the importance of applying the corrections, Figure 10 shows data from the 90° detector on board NOAA 17, from the evening side Northern Hemisphere on 5 January 2012, after the detector has experienced 10 years of radiation and subsequent degradation. For each of the pixels, the integral flux from all energy channels are used to construct a PCHIP-fitted spectrum. The spectrum is then corrected using the specific α_{month} factors. The uncorrected and the corrected spectra are used to determine the integral flux of $E > 60$ keV shown in Figures 10a and 10b, respectively. The corrected flux is often nearly 1 order of magnitude larger than the uncorrected flux.

8. Conclusion

For the first time the level of degradation of the MEPED proton detectors is revealed for all five energy channels. Our α_{cal} factors are based on a larger database than earlier studies. We also separate the satellites according to MLT sectors, and the new MetOp-01 satellite gives us new α_{cal} factors for 2013 for the satellites in the same MLT sector. Figure 9 shows that the corrected fluxes overlap close to perfectly, verifying the quality of the derived correction factors.

It is important in quantitative studies to correct for changes in energy levels in the proton detector as the detectors experience radiation damage throughout their lifetime. In the future, there will be no new satellite to compare against. It would therefore be valuable to establish a method to predict the degradation in order to have a continuous set of correction factors throughout the lifetime of all NOAA and MetOp satellites.

Acknowledgments

This study was supported by the Research Council of Norway under contracts 184701, 212014, and 223252. The authors especially thank David S. Evans for all help and comments. The authors thank Janet C. Green, Daniel C. Wilkinson, and the NOAA's National Geophysical Data Center (NGDS) for providing NOAA data. We thank the SIDC-team, World Data Center for the Sunspot Index, Royal Observatory of Belgium, Monthly Report on the International Sunspot Number, online catalog of the sunspot index: http://www.sidc.be/sunspot-data/. We thank NOAA and European Space Agency (ESA) for providing information regarding ascending node of the satellites (http://www.ngdc.noaa.gov/ and http://www.esa.int/esaLP/).

References

Asikainen, T., and K. Mursula (2011), Recalibration of the long-term NOAA/MEPED energetic proton measurements, *J. Atmos. Sol. Terr. Phys.*, *73*, 335–347.

Asikainen, T., K. Mursula, and V. Maliniemi (2012), Correction of detector noise and recalibration of NOAA/MEPED energetic proton fluxes, *J. Geophys. Res.*, *117*, A09204, doi:10.1029/2012JA017593.

Codrescu, M. V., T. J. Fuller-Rowell, R. G. Roble, and D. S. Evans (1997), Medium energy particle precipitation influences on the mesosphere and lower thermosphere, *J. Geophys. Res.*, *102*(A9), 19,977–19,987.

Coleman, J. A., D. P. Love, J. H. Trainor, and D. J. Williams (1968), Effects of damage by 0.8 MeV–5.0 MeV protons in silicon surface-barrier detectors, *IEEE Trans. Nucl. Sci.*, *NS-15*, 363–372.

Evans, D. S., and M. S. Greer (2000), Polar orbiting environmental satellite space environment monitor-2: Instrument descriptions and archive data documentation, *NOAA Technical Memorandum, Boulder, Colorado OAR SEC 93, 93, version 1.4, January 2004*.

Galand, M., and D. S. Evans (2000), Radiation damage of the proton MEPED detector on POES (TIROS/NOAA) satellites, *NOAA Technical Memorandum, Boulder, Colorado OAR 456-SEC. 42*.

Horne, R. B., M. M. Lam, and J. C. Green (2009), Energetic electron precipitation from the outer radiation belt during geomagnetic storms, *Geophys. Res. Lett.*, *36*, L19104, doi:10.1029/2009GL040236.

Jackman, C. H., R. D. McPeters, G. J. Labow, E. L. Fleming, C. J. Praderas, and J. M. Russel (2001), Northern Hemisphere atmospheric effects due to the July 2000 solar proton events, *Geophys. Res. Lett.*, *28*, 2883–2886.

Lyons, L. R., and D. S. Evans (1984), An association between discrete aurora and energetic particle boundaries, *J. Geophys. Res.*, *89*(A4), 2395–2400.

Miyoshi, Y., and R. Kataoka (2008), Flux enhancement of the outer radiation belt electrons after the arrival of stream interaction regions, *J. Geophys. Res.*, *113*, A03S09, doi:10.1029/2007JA012506.

Ødegaard, L.-K. G. (2013), Recalibration of the MEPED proton detectors onboard NOAA POES satellites, Master thesis in Space Physics, Department of Physics and Technology, University of Bergen, Norway.

Oksavik, K., F. Søraas, J. Moen, and W. J. Burke (2000), Optical and particle signatures of magnetospheric boundary layers near magnetic noon: Satellite and ground-based observations, *J. Geophys. Res.*, *105*(A12), 27,555–27,568.

Raben, V. J., D. S. Evans, H. H. Sauer, S. R. Sahm, and M. Huynh (1995), Difference of scattering geometrical optics components and line integrals of currents in modified edge representation, *NOAA Technical Memorandum, Boulder, Colorado ERL SEL-86*.

Rodger, C. J., M. A. Clilverd, J. C. Green, and M. M. Lam (2010), Use of POES SEM-2 observations to examine radiation belt dynamics and energetic electron precipitation into the atmosphere, *J. Geophys. Res.*, *115*, A04202, doi:10.1029/2008JA014023.

Sandanger, M., F. Søraas, K. Aarsnes, K. Oksavik, and D. S. Evans (2007), Loss of relativistic electrons: Evidence for pitch angle scattering by electromagnetic ion cyclotron waves excited by unstable ring current protons, *J. Geophys. Res.*, *112*, A12213, doi:10.1029/2006JA012138.

Sandanger, M. I., F. Søraas, M. Sørbø, K. Aarsnes, K. Oksavik, and D. S. Evans (2009), Relativistic electron losses related to EMIC waves during CIR and CME storms, *J. Atmos. Sol. Terr. Phys.*, *71*, 1126–1144.

Seppälä, A., P. T. Verronen, V. F. Sofieva, J. Tamminen, E. Kyrölä, C. J. Rodger, and M. A. Clilverd (2006), Destruction of the tertiary ozone maximum during a solar proton event, *Geophys. Res. Lett.*, *33*, L07804, doi:10.1029/2005GL025571.

Søraas, F., K. Oksavik, K. Aarsnes, D. S. Evans, and M. S. Greer (2003), Storm time equatorial belt—An image of RC behavior, *Geophys. Res. Lett.*, *30*(2), 1052, doi:10.1029/2002GL015636.

Vernov, S. I., I. A. Savenko, P. I. Shavrin, and N. F. Pisarenko (1962), Detection of an inner radiation belt at the altitude of 320 km in the region of the South Atlantic magnetic anomaly, *Planet. Space Sci.*, *9*(11), 861–865.

Whittaker, I. C., C. J. Rodger, M. A. Clilverd, and J.-A. Sauvaud (2014), The effects and correction of the geometric factor for the POES/MEPED electron flux instrument using a multi-satellite comparison, *J. Geophys. Res. Space Physics*, *119*, 6386–6404, doi:10.1002/2014JA020021.

Yando, K., R. M. Millan, J. C. Green, and D. S. Evans (2011), A Monte Carlo simulation of the NOAA POES medium energy proton and electron detector instrument, *J. Geophys. Res.*, *116*, A10231, doi:10.1029/2011JA016671.

Paper II

Space Weather Impact on the Degradation of NOAA POES MEPED Proton Detectors

Ødegaard, L.-K. G., H. Nesse Tyssøy, M. I. Sandanger, J. Stadsnes, and F. Søraas

Journal of Space Weather and Space Climate, *6*, (2016). doi: 10.1051/swsc/201620

J. Space Weather Space Clim., **6**, A26 (2016)
DOI: 10.1051/swsc/2016020

SWSC

RESEARCH ARTICLE OPEN ACCESS

Space Weather impact on the degradation of NOAA POES MEPED proton detectors

Linn-Kristine Glesnes Ødegaard*, Hilde Nesse Tyssøy, Marit Irene Jakobsen Sandanger, Johan Stadsnes, and Finn Søraas

Birkeland Centre for Space Science (BCSS), Department of Physics and Technology, University of Bergen, Allégaten 55, N-5007 Bergen, Norway
*Corresponding author: linn-kristine.odegaard@uib.no

Received 20 December 2015 / Accepted 12 May 2016

ABSTRACT

The Medium Energy Proton and Electron Detector (MEPED) on board the National Oceanic and Atmospheric Administration Polar Orbiting Environmental Satellites (NOAA POES) is known to degrade with time. In recent years a lot of effort has been put into calibrating the degraded proton detectors. We make use of previous work and show that the degradation of the detectors can be attributed to the radiation dose of each individual instrument. However, the effectiveness of the radiation in degrading the detector is modulated when it is weighted by the mean *ap* index, increasing the degradation rate in periods with high geomagnetic activity, and decreasing it through periods of low activity. When taking *ap* and the radiation dose into account, we find that the degradation rate is independent of spacecraft and detector pointing direction. We have developed a model to estimate the correction factor for all the MEPED detectors as a function of accumulated corrected flux and the *ap* index. We apply the routine to NOAA POES spacecraft starting with NOAA-15, including the European satellites MetOp-02 and MetOp-01, and estimate correction factors.

Key words. Proton detector degradation – Space Weather – Calibration – MEPED – NOAA POES

1. Introduction

The space environment around the Earth is harsh, and instruments and satellites in orbit can be harmed if exposed to the strong radiation (see e.g. Horne et al. 2013). Here, we study the radiation damage experienced by the silicon solid state proton detectors, which are part of the Medium Energy Proton and Electron Detector (MEPED) on board the Polar Orbiting Environmental Satellites (POES) operated by the National Oceanic and Atmospheric Administration (NOAA).

NOAA POES are low Earth orbiting satellites with an approximate orbital altitude of 850 km. Fourteen spacecraft carry a designated detector suite to measure the flux of energetic charged particles at satellite altitude. The combined dataset from the MEPED detectors currently stretches over 37 years and is ideal for studies of long-term trends in space weather. However, Galand & Evans (2000) showed that the proton detector of the MEPED instrument suffered from degradation already after 1–2 years in operation. The degradation causes the instrument to seriously underestimate the incoming proton flux and makes the data unusable for quantitative studies. Lately, several studies have addressed the issue and estimated the degradation and how it evolves with time (Asikainen & Mursula 2011; Asikainen et al. 2012; Ødegaard 2013; Sandanger et al. 2015).

The goal of the studies by Asikainen & Mursula (2011), Asikainen et al. (2012) and Sandanger et al. (2015) is to extend the period of the quantitative applicability of the large MEPED dataset. The present study is driven by the same motivation, however, we aim to identify the controlling factors of the degradation. This is important because the detector correction from previous studies depends on new satellites being launched, and the last one is scheduled to launch in 2017.[1,2] We present a method to estimate the level of degradation of MEPED detectors which does not depend on the launch of new satellites.

In the following sections we will briefly present the NOAA POES satellites and the MEPED detectors. We will give some details on how the detectors degrade, and what has been done so far to correct the data. Finally, we will show how the degradation of the different energy channels of the detector can be related to the product of the accumulated corrected flux and the *ap* index for the individual detectors. We present a method to calibrate the detectors on yearly basis.

2. NOAA POES and MEPED

The NOAA POES are meteorological satellites that provide global forecasts for NOAA's National Weather Service (NWS) with space-based Earth remote sensing. Today they provide data used for (among others) applications related to the oceans, detection of forest fires and monitoring the ozone hole in the Antarctica (Davis 2007).

In addition to the remote sensing instruments aimed for weather and climate data, a Space Environment Monitor (SEM) is included on the NOAA POES, which measures charged particles at satellite altitude. The purpose of this instrument is to reveal the impact of energetic charged particles

[1] http://www.eumetsat.int/website/home/Satellites/CurrentSatellites/Metop/index.html
[2] http://poes.gsfc.nasa.gov/

on the upper atmosphere. The SEM instruments consist of several detectors, each designated to measure electrons or protons within a specific pointing direction and energy range. In this study we focus on the MEPED proton detector as this detector exhibits degradation over time. The MEPED electron detector is shielded by a foil preventing protons with energy below 200 keV from entering and does not suffer from significant degradation. The SEM instrument package was updated after the launch of NOAA-14, and for MEPED this included changes in the energy channels and the viewing direction of the 90° telescope. To distinguish between the two versions satellites up to and including NOAA-14 are referred to as SEM-1 satellites, and SEM-2 starting with NOAA-15.

The MEPED instrument has two proton telescopes viewing almost perpendicular to each other. One telescope is pointing radially outward and is called the 0° detector. At high latitudes this telescope views particles near the centre of the atmospheric bounce loss cone. At high latitudes the second telescope, called the 90° detector, views particles at the edge and outside the atmospheric bounce loss cone. We focus mainly on the SEM-2 satellites, although the results will be applicable to the SEM-1 satellites as well. For the SEM-2 MEPED proton detector, measured particles are sorted in five differential energy channels and one integral energy channel, and the nominal energy thresholds of P1–P6 are listed in Table 1 (Evans & Greer 2000). The detector was designed to measure the intensity of protons ranging from 30 keV to greater than 6.9 MeV. With this wide energy range, both auroral protons, radiation belt protons and solar proton events can be measured by MEPED (detailed descriptions of the instruments can be found in Raben et al. (1995) for SEM-1 and Evans & Greer (2000) for SEM-2).

The operational lifetimes of all the MEPED instruments are plotted in Figure 1. MetOp-02 and MetOp-01 are meteorological polar orbiting satellites launched by the European Organisation for the Exploitation of Meteorological Satellites (EUMETSAT), but carry the SEM-2 suit from NOAA. The yearly sunspot number is plotted in Figure 1 for reference to illustrate how the combined dataset covers more than three solar cycles.

3. Data

We use the proton measurements provided by the NOAA's National Geophysical Data Center.[3,4] The proton data is given within the six energy channels presented in Table 1. The data are accumulated for 1 s, but the 0° and 90° detectors share electronics and a full dataset takes 2 s to obtain (Evans & Greer 2000). We calculate the monthly mean integral proton flux spectrum without the P6 channel, which is disregarded due to contamination from relativistic electrons (Yando et al. 2011). When not contaminated by electrons, P6 has very low count rates, and can be safely dropped in this context. The *ap* index is downloaded from the OMNI database, and the sunspot number is obtained from the SIDC.

4. Previous correction for degradation

The MEPED proton detector degrades in two known ways. A dead layer is created on the front detector, which increases with time. In addition, atoms making up the silicon detector itself are shifted in their place (Evans & Greer 2000; Galand & Evans 2000; McFadden et al. 2007).

When the dead layer of the detector thickens, more of the particle's energy is deposited in the detector without being measured. Defects in the atom structure deeper in the detector will result in a trapping of the charge carriers released in the detector in the form of electron-hole pairs, thus less of the incoming particle's energy is collected. Throughout most of the satellites' orbits the measured proton spectra are usually decreasing power-law. The degradation would then cause the flux measured between the nominal energy thresholds to be underestimated, as only higher energy particles are able to trigger the thresholds. In the South Atlantic Anomaly, where the proton differential spectra have increasing fluxes across P1 and P2, the degraded detectors may actually be overestimating the fluxes between the nominal energy thresholds. Overall, since the most common situation is a decreasing power-law proton spectrum, the effective energy thresholds of the instrument increase with time. The degradation is more severe in the lower channels (P1–P3) compared to the higher (P4–P5) because higher energy protons penetrate deeper into the detector where the damage is less prominent (Galand & Evans 2000; McFadden et al. 2007; Asikainen et al. 2012).

An aluminium coating on the detector stops protons with energy $E \lesssim 9$ keV from entering the detector (Seale & Bushnell 1987). Protons with $E > 9$ keV pass through the aluminium layer depositing some energy there. With this energy loss accounted for by setting the detector pulse height logic to 21.4 keV, the lower energy threshold of P1 is 30 keV (Evans & Greer 2000). The proton population with energies from 9 to 30 keV, which is stopped inside of the detector but not counted, is expected to be considerable. This low energy proton population might be of importance for the degradation, especially in the front where the dead layer is created (Galand & Evans 2000). It is not possible to use the MEPED data alone to get a reliable estimate of the particle flux with $E < 30$ keV, and the damaging effect of these fluxes cannot be directly accounted for.

Figure 2 illustrates how severe the degradation can be. Figure 2a shows daily mean proton fluxes in P1 (nominally 30–80 keV) for the entire operational period of NOAA-15, both detectors. NOAA-15 was launched in 1998 and is still actively measuring protons with MEPED, which makes it the only SEM-2 satellite active through more than one whole solar cycle (as can be seen in the sunspot number, plotted in Fig. 2c).

Table 1. Energy thresholds of the MEPED proton detector (SEM-2).

Channel	Nominal energy range of protons (keV)
P1	30–80
P2	80–250[a]
P3	250[a]–800
P4	800–2500
P5	2500–6900
P6	>6900[b]

[a] We use 250 keV (Yando et al. 2011), as also used by Sandanger et al. (2015). The description of the instrument reports 240 keV (Evans & Greer 2000).
[b] According to simulations by Yando et al. (2011), P6 can measure protons with energy of at least 10 MeV. It is also sensitive to relativistic electrons.

[3] http://satdat.ngdc.noaa.gov/sem/poes/data/full/
[4] http://satdat.ngdc.noaa.gov/sem/poes/data/processed/ngdc/uncorrected/full/

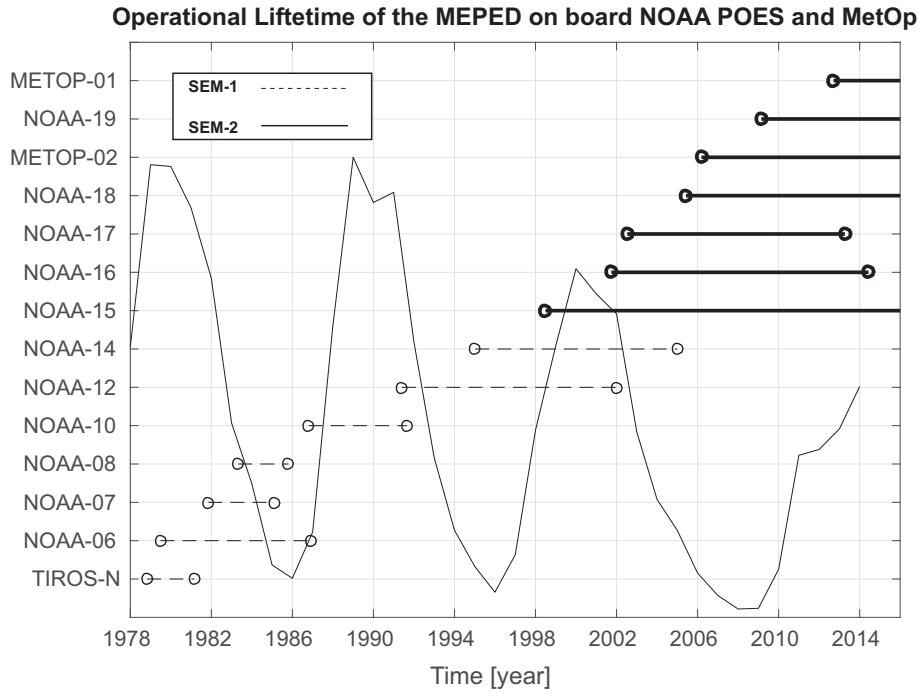

Fig. 1. The yearly sunspot number is shown as a solid black curve for reference. The operational lifetimes of the MEPED instrument on the SEM-1 satellites are plotted as dashed lines, and the SEM-2 satellites in thick solid lines.

Due to the general anisotropy in the proton flux the 90° detector is exposed to more radiation than the 0° detector throughout most of an orbit. The mean daily flux of the 90° detector is therefore initially higher than that of the 0° detector. However, the higher radiation dose will also degrade the 90° detector faster than the 0° detector, and, as seen in Figure 2b, the flux ratio between the two detectors becomes more and more unified until the 0° detector achieves a higher flux than the 90° detector in 2007.

The first extensive work of calibrating the entire MEPED proton dataset was done by Asikainen & Mursula (2011). An improved calibration was published the year after (Asikainen et al. 2012). Sandanger et al. (2015) used a different approach, utilizing a larger part of the available dataset, and accounting for alternating morning and evening orbits of the SEM-2 satellites (Magnetic Local Time effects).

Common for these studies is the technique used to quantify the degradation of a detector. When possible by criteria set by the authors, an integral energy spectrum from a newly launched satellite is compared to the integral energy spectrum from the degraded satellite. The detectors on the two satellites are assumed to measure the same particle population, and the new detector is expected to measure the real, non-degraded spectrum of particles. From this the increased energy thresholds of the degraded detector can be determined. The ratio of new energy threshold to the nominal energy threshold of a channel is called the α factor, or correction factor, for the energy channel in question. Details of comparing energy spectra and obtaining correction factors are described both in Asikainen & Mursula (2011) and Sandanger et al. (2015). The criteria for when a comparison between satellites can be made, which are the main distinctions between the methods, are summarized in Table 2.

The different criteria set by Asikainen & Mursula (2011) and Sandanger et al. (2015) provide different results. For example, NOAA-15 and NOAA-19 were excluded from calibration by the criteria set on separation in space by Sandanger et al. (2015), whereas Asikainen & Mursula (2011) were not able to calibrate the higher energy channels P4 and P5. Due to the small uncertainties in the α factors, and the consistent way of treating the time evolution of the factors, the results by Sandanger et al. (2015) are chosen for this study. The α factors calculated by comparing satellites from Sandanger et al. (2015) are presented here in Table 3. For each possible comparison, an α was calculated for each of the energy channels P1–P5, denoted as α_1–α_5 in the table.

Sandanger et al. (2015) proposed an iterative method to calculate the time evolution of the α factors from Table 3 with a monthly resolution. The α factors are calculated as a function of the accumulated *corrected* integral flux above a chosen energy threshold. We will make use of this method to get a reasonable estimation of the accumulated corrected fluxes, and show that there is a close relationship between the accumulated corrected fluxes and the α factors, as was also noted by Asikainen et al. (2012).

5. Predicting future degradation

The detectors will be degraded by the particles they measure. This implies that the degradation of the different detectors and the α factors will be dependent on the number of protons hitting the detectors. Assuming that the detectors are identical, the degradation process should influence all the detectors in the same way, independent of pointing direction and spacecraft. Therefore, if the correction factors found by Sandanger et al. (2015) are reliable, it should be possible to develop an analytical expression for the degradation valid for the MEPED proton detectors in both SEM-1 and SEM-2 satellites.

Sandanger et al. (2015) assume that the number of protons hitting the detector throughout its lifetime is responsible for raising the energy thresholds. Since the degradation raises

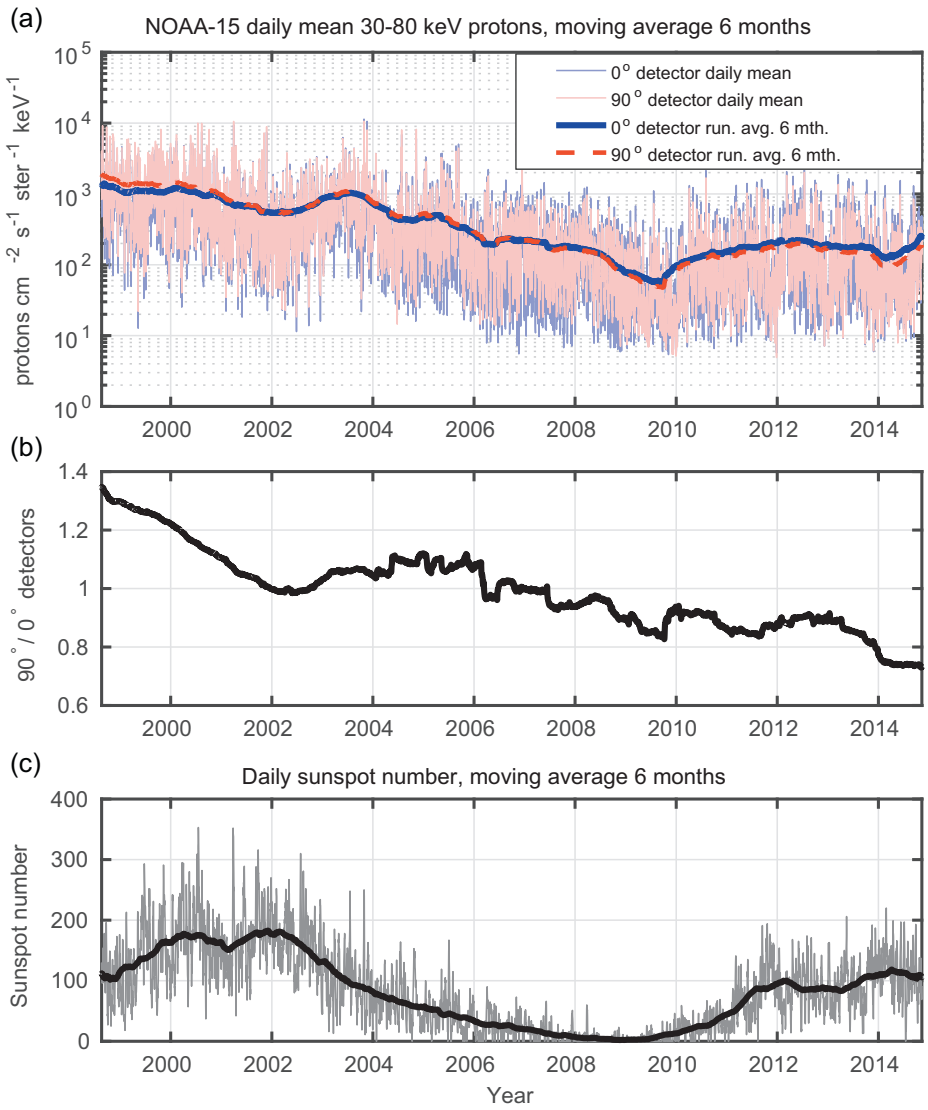

Fig. 2. (a) Daily mean uncorrected proton differential flux as measured by NOAA-15 P1 channel (30–80 keV) shaded in black. A running mean with a 6-month window is applied and plotted in solid and dashed lines on top. (b) 6-month running mean of 90° detector flux divided by that of the 0° detector. (c) The daily sunspot number shaded in grey. A moving average with a window of 6 months is applied to the data, and plotted in solid line on top. All panels show the period August 1998 to December 2014, each tick on the *x*-axis shows the 1st of January that year.

Table 2. Comparison of calibration methods and criteria.

	Asikainen & Mursula (2011) and Asikainen et al. (2012)	Sandanger et al. (2015)
α Factors provided for channels[a]	P1–P3	P1–P5
Separation in space between satellites	<1° magnetic latitude and longitude at fofl[b] and <10% relative difference in *L*-value	Only compare satellites with <1 h separation in MLT
Separation in time between comparable satellites	<30 s	–
Data used	Instantaneous measurements (2 s resolution)	Mean value of one month of data from whole orbit
Number of months data from new satellite is considered non-degraded	5	12
Method for obtaining time evolution	Linear, 2nd order, 3rd order, PCHIP[c] fit with α vs. time, or as a function of *ap* index	Iteration method using α vs. accumulated corrected integral flux

[a] P6 is excluded in all studies due to relativistic electrons contaminating the measurements.
[b] foot of field line (fofl) confining each satellite.
[c] Piecewise Cubic Hermite Interpolation Polynomial (PCHIP), shape preserving interpolation.

Table 3. The calibration α factors with standard deviations calculated by Sandanger et al. (2015).

Satellite	Year	Mean α (standard deviation)				
		α_1	α_2	α_3	α_4	α_5
				0° detector		
NOAA-16	2005 (Feb)	1.57 (0.08)	1.65 (0.08)	1.22 (0.05)	1.12 (0.06)	1.08 (0.08)
NOAA-17	2007 (Jul)	1.37 (0.06)	1.59 (0.07)	1.19 (0.02)	1.07 (0.01)	1.03 (0.01)
NOAA-17	2013 (Apr)	1.53 (0.05)	1.82 (0.10)	1.32 (0.07)	1.27 (0.09)	1.16 (0.08)
NOAA-18	2009 (Sep)	1.06 (0.04)	1.14 (0.05)	1.07 (0.01)	1.16 (0.01)	1.17 (0.01)
MetOp-02	2013 (Apr)	1.13 (0.07)	1.27 (0.10)	1.09 (0.07)	1.04 (0.06)	1.05 (0.06)
				90° detector		
NOAA-16	2005 (Feb)	1.89 (0.10)	1.86 (0.07)	1.31 (0.02)	1.08 (0.03)	1.03 (0.03)
NOAA-17	2007 (Jul)	1.65 (0.08)	1.94 (0.07)	1.46 (0.02)	1.25 0.01)	1.21 (0.01)
NOAA-17	2013 (Apr)	1.94 (0.06)	2.10 (0.10)	1.39 (0.09)	1.22 (0.06)	1.21 (0.05)
NOAA-18	2009 (Sep)	1.11 (0.05)	1.28 (0.06)	1.12 (0.01)	1.05 (0.01)	1.03 (0.01)
MetOp-02	2013 (Apr)	1.30 (0.09)	1.47 (0.10)	1.10 (0.06)	0.92 (0.05)	0.92 (0.05)

the energy thresholds, it will not be long before the detectors are unable to measure, for example, 30 keV protons in the P1 channel. Sandanger et al. (2015) chose to use a range of energies to represent the particle population responsible for the degradation which even the most degraded of the satellites they consider is able to measure; [60, 167, 360, 1050, 2300] keV. Each monthly integral proton spectrum is corrected by the appropriate α factor, and the fluxes are accumulated at the given thresholds. For a detailed description of the procedure we refer the reader to Sandanger et al. (2015) Section 6 and Figure 6.

We apply the method described by Sandanger et al. (2015). For every month in operation, we use all available data from the entire orbit and calculate a mean integral proton spectrum. Instead of using the energy thresholds as proposed by Sandanger et al. (2015) when accumulating the corrected fluxes, we performed a correlation analysis of their α factors versus the accumulated corrected fluxes for energies ranging from 90 keV to 2400 keV. The analysis resulted in maximum correlation for 90 keV independent of energy channel. A lower limit of 90 keV corresponds to an $\alpha = 3$ in the P1 channel. There is no physical limit for the maximum degradation at $\alpha = 3$, but we set the limit here as a tradeoff between allowing for a large degradation in the oldest detectors and keeping the energy threshold low to include the lower energy part of the spectrum in the accumulated flux. Sandanger et al. (2015) got a maximum $\alpha = 1.94$ for P1, while Asikainen et al. (2012) calculated a maximum $\alpha = 3.74$ for the NOAA-6 P1 channel. None of the other Asikainen et al. (2012) P1 factors were above 3 however, and we thus evaluate 90 keV as a suitable threshold. The resulting time evolutions of α as a function of accumulated corrected flux with $E > 90$ keV are plotted in Figure 3.

It might seem counterintuitive that also the α factors of the higher energy channels correlate best with the accumulated flux if the lower energy population is included. However, considering the high fluxes associated with low energy compared to high energy protons, it is likely that the main degradation in the silicone crystal occurs in the front end of the first detector. The low energy protons detected in P1–P3 ($E < 800$ keV) will deposit all their energy in the front end of the first silicon crystal. Going through this damaged region, the higher energy protons will also deposit a portion of their energy there. The change in the threshold for higher energy channels can therefore partly be ascribed to the damage caused by the lower energy protons. Together with considerable inter-correlation between the fluxes in the different energy channels, this might explain the strong correlation with the $E > 90$ keV proton fluxes for all the channels.

α factors from Table 3 are scattered versus the calculated accumulated corrected flux with $E > 90$ keV in Figure 4. The correlation coefficients for P1–P5 are $r = [0.84, 0.91, 0.86, 0.60, 0.55]$. For P4 and P5 we have removed the α factors of the MetOp-02 90° detector, which have $\alpha < 1$, when calculating the correlation. We do not believe that it is possible for the detectors to achieve lower energy thresholds than the nominal. The P1–P3 correlation coefficients are significant at the 5% level, while P4 at the 10% level. For P5, the *p*-value of the correlation coefficient is 0.12.

5.1. Linear regression

We want to express the degradation coefficient α as a linear function of the accumulated corrected flux with $E > 90$ keV (from here on abbreviated "*acf*"). We use the α factors from Table 3 and the calculated *acf* and do Ordinary Least Squares regression (OLS) on the data. We have removed all $\alpha < 1$ because of the non-physical implications of a negative degradation. The results of the OLS are summarized in Table 4.

The *p*-values for the estimated slopes and intercepts are calculated for a Student's *t*-test with $n - 2$ degrees of freedom, and *p*-value <0.05 indicates significant estimates for the parameters. The slopes are tested for significant difference from zero, while the intercepts are tested for significant difference from one. It would be impractical as well as non-physical to have $\alpha < 1$ for low accumulated fluxes as was found for the P1 channel, however, the intercepts were not found to be significantly different from one for any of the channels. Therefore, we instead perform a new regression where we set the intercept constant to $\alpha = 1$, which also reduces the degrees of freedom in the regression to $n - 1$. (In practice, we perform a Regression Through the Origin (RTO) after subtracting 1 from all α factors, see e.g. Eisenhauer 2003). The results from the RTO are given in Table 5.

We can compare the standard errors of the estimated slope in the two regressions, which is at least 50% lower in all channels for the RTO, indicating that this is the best of the two alternatives to fit a line to the data. Also, the *p*-values of the estimated slopes are smaller for the RTO, where all the estimated slopes were found to be significant to the 5% level. The regression lines found by RTO are shown in Figure 4

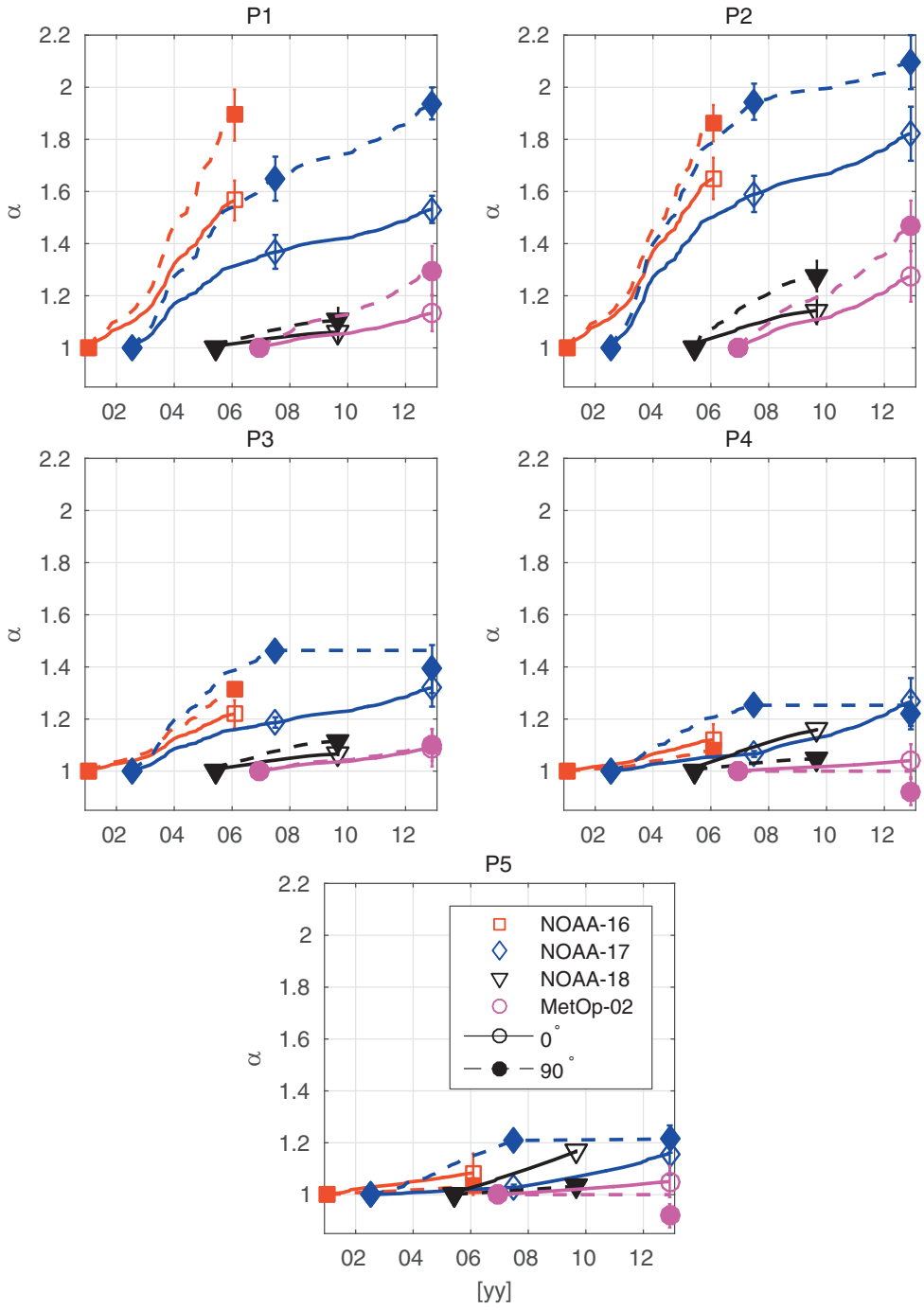

Fig. 3. α factors as a function of time for all satellites calibrated by Sandanger et al. (2015), both detectors. Upper row, left to right: P1 and P2 energy channels. Middle row, left to right: P3 and P4 energy channels. Bottom row: P5 energy channel. α is found as a function of the cumulative integral flux with $E > 90$ keV for all energy channels. The standard deviations of α are plotted as vertical lines.

together with the scatter plot of α versus *acf*. A 95% prediction interval is displayed for the regression, and we use a constant intercept = 1.

From the RTO (Table 5), we get the following equations for P1–P5:

$$\begin{aligned} \alpha_{P1} &= 1.1 \times 10^{-6} acf + 1 \\ \alpha_{P2} &= 1.4 \times 10^{-6} acf + 1 \\ \alpha_{P3} &= 5.3 \times 10^{-7} acf + 1\,, \\ \alpha_{P4} &= 3.0 \times 10^{-7} acf + 1 \\ \alpha_{P5} &= 2.3 \times 10^{-7} acf + 1 \end{aligned} \tag{1}$$

where *acf* is the accumulated corrected mean monthly integral flux with energy $E > 90$ keV.

The analytic expressions depend on the *acf* being a known parameter, which is not the case unless we already have a reliable estimate for the α factor of a detector. To achieve an estimated *acf*, we do a continuous month by month calculation as described in the next paragraph. This implies that we need to assume that the relationship found in Equation set (1) holds on time scales of a month, and not just on yearly basis.

The first step is to calculate the mean monthly integral flux from the uncorrected MEPED measurements for all months

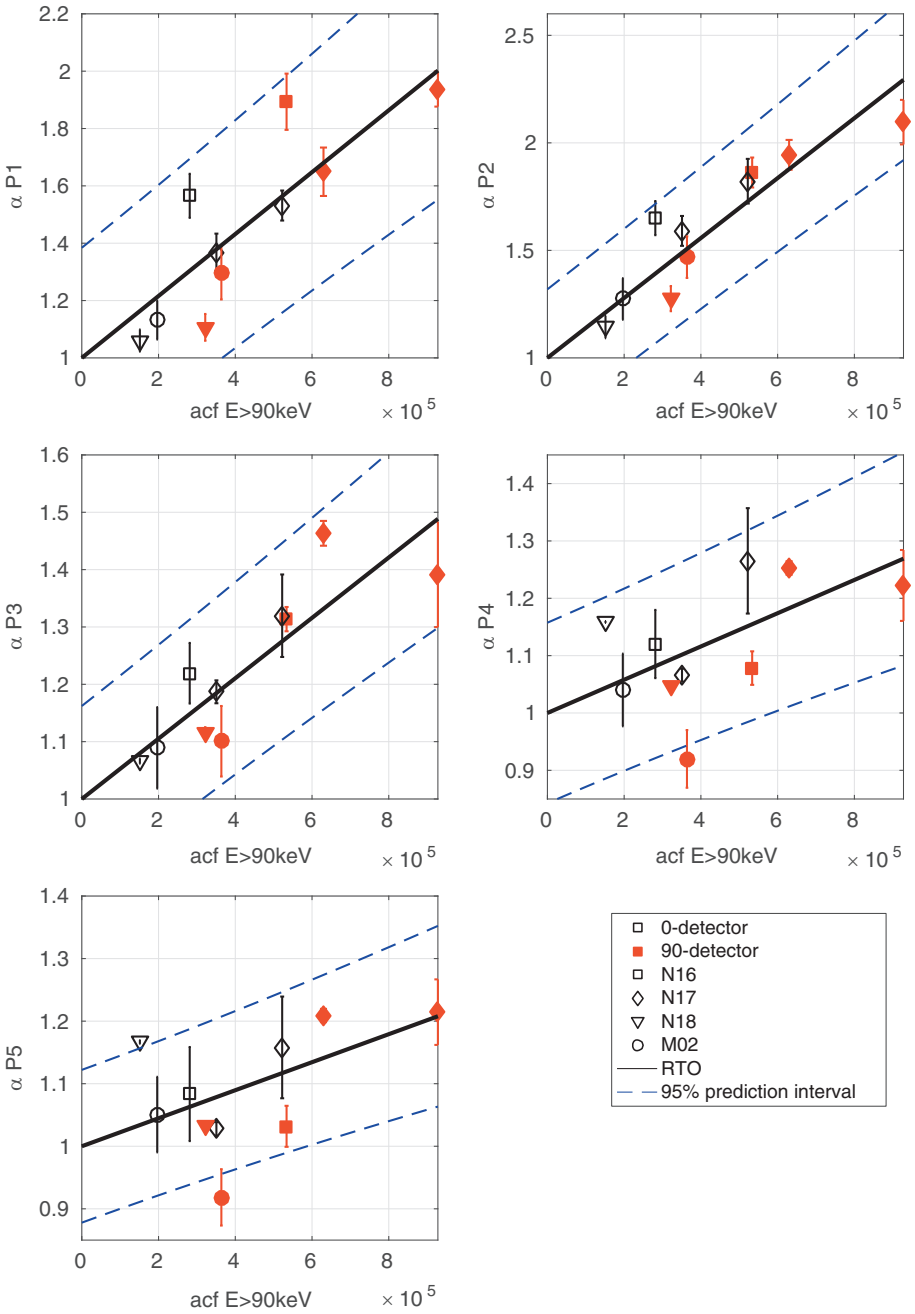

Fig. 4. α factors from Table 3 plotted versus the *acf* with energy $E > 90$ keV for all channels. The different satellites are plotted in different symbols, given in the legend. 0° and 90° detectors are distinguished by open black and solid red symbols, respectively. The NOAA-18 0° detector factors are removed from P4 and P5 in the regression. The best fit line found by regression is plotted in black, with accompanying 95% prediction intervals in dashed blue lines. The standard deviations of α are plotted as vertical lines.

Table 4. Ordinary least squares regression of α versus *acf*.

Channel	Parameter	Estimate	Standard error	*p*-value
P1	Intercept	0.96	0.12	0.61
	Slope	1.15×10^{-6}	2.6×10^{-7}	1.1×10^{-3}
P2	Intercept	1.08	0.1	0.23
	Slope	1.25×10^{-6}	2.1×10^{-7}	1.57×10^{-4}
P3	Intercept	1.00	0.05	0.45
	Slope	5.13×10^{-7}	1.1×10^{-7}	7.7×10^{-4}
P4	Intercept	1.04	0.05	0.23
	Slope	2.20×10^{-7}	1.1×10^{-7}	0.04
P5	Intercept	1.03	0.05	0.28
	Slope	1.78×10^{-7}	1.0×10^{-7}	0.06

Table 5. Regressionwith a constant intercept = 1, of α versus *acf*.

Channel	Parameter	Estimate	Standard error	*p*-value
P1	Slope	1.1×10^{-6}	1.1×10^{-7}	2.4×10^{-6}
P2	Slope	1.4×10^{-6}	9.3×10^{-8}	5.5×10^{-8}
P3	Slope	5.3×10^{-7}	4.7×10^{-8}	7.1×10^{-7}
P4	Slope	3.0×10^{-7}	5.0×10^{-8}	1.8×10^{-4}
P5	Slope	2.3×10^{-7}	4.6×10^{-8}	4.5×10^{-4}

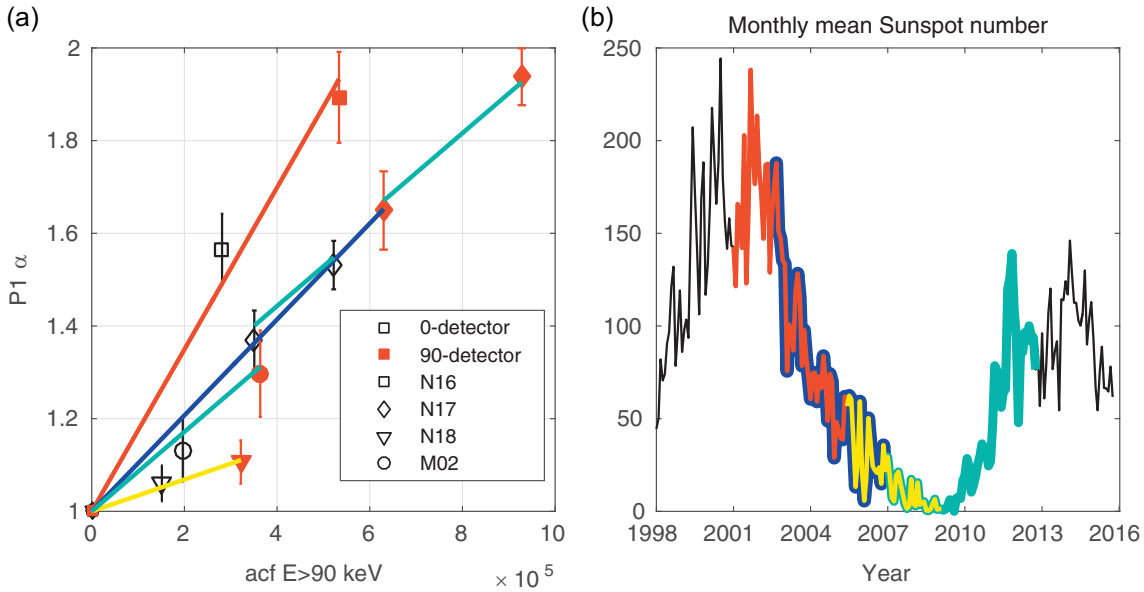

Fig. 5. (a) α factors for P1 plotted versus the *acf* ($E > 90$ keV). The standard deviations of α are plotted as vertical lines. (b) Monthly averaged sunspot number. Four calibration periods have been colour coded, and they are defined by the launch of new satellites. On the *x*-axis of the right panel each tick marks the 1st of January that year.

in operation. For the first month, we assume $\alpha = 1$ for all channels and make a continuous integral flux spectrum on the nominal energy thresholds with a Piecewise Cubic Hermite Interpolation Polynomial (PCHIP, a shape preserving interpolation routine) and numerically find the proton flux with $E > 90$ keV. The flux found is then applied in Equation set (1), and an α can be calculated for the next month. This calculated factor is used to correct the energy thresholds before constructing an integral flux spectrum for the next month, retrieving the flux with $E > 90$ keV and calculating the next α factor. The process is continued for as many months as there is data. For satellites previously corrected by Sandanger et al. (2015), we start by using the last provided factor in Table 3 and correcting the energy thresholds with these in the first step.

5.2. Introducing a dependence on *ap* index in the degradation

As a first approximation we have assumed that the degradation depends linearly on the accumulated corrected fluxes and proceeds similarly in all spacecraft. However, if we study the degradation of the satellites separately, we find that the degradation rate changes through the solar cycle, in particular for P1–P3. By degradation rate, we here mean $\Delta\alpha/\Delta acf$. That is, how much an α factor increases ($\Delta\alpha$) given a certain radiation dose (Δacf) over a given time, Δt. Galand & Evans (2000) noted that SEM-1 satellites launched near solar maximum seemed to degrade faster than those launched at the solar minimum, and that the solar history of the detectors was affecting the degradation rate of MEPED. We find the same effect in the SEM-2 MEPED instruments.

The effect is illustrated in Figure 5 for P1. Figure 5a shows the α factors versus *acf* for all the satellites calibrated by Sandanger et al. (2015), and the monthly sunspot number is plotted in Figure 5b. We have colour coded four periods which all correspond to the time between two α factors for one or more of the satellites as calculated by Sandanger et al. (2015). The slope between the *acf* and α for the different satellites changes through the solar cycle. The red period, which is closest to the solar maximum, has the steepest slope, while the yellow, which is closest to the solar minimum, has the gentlest slope. For example, approximately the same accumulated integral flux of $:3 \times 10^5$ [/cm^2 s ster] produces an $\alpha \approx 1.1$ in the NOAA-18 90° detector, and an $\alpha \approx 1.6$ in the NOAA-16 0° detector. $\Delta\alpha/\Delta acf$ is different through the solar cycle. We see the same feature in P2 and P3 as well (not shown). In addition, the two satellites MetOp-02 and NOAA-17, which have the turquoise period in common, have almost identical degradation rates during this period. This is an indication that there is some factor responsible for the different rates, and not just the detectors in the different satellites degrading in different manners. The definition of the red, blue, turquoise and yellow phases of the solar cycle is listed in Table 6.

Table 6. Definition of colour codes of solar cycle phases (see Fig. 5).

Colour	From	To	α factors used
Red	Launch NOAA-16 (2001)	Launch NOAA-18 + 6 months (2005)[a]	α_1 N16
Green	Launch NOAA-17 (2002)	Launch MetOp-02 + 6 months (2007)	α_1 N17
Yellow	Launch NOAA-18 (2005)	Launch NOAA-19 + 6 months (2009)	α_1 N18,
Turquoise	Launch MetOp-02 (2007)	Launch MetOp-01 + 6 months (2013)	α_1 M02, α_2 N17

[a] 6 months is added to the date of launch of the satellite defining the end of a period. This is because Sandanger et al. (2015) used one year of data from the new satellites to calibrate the old satellites and placed the calibration α factor in the middle of the respective 1-year period.

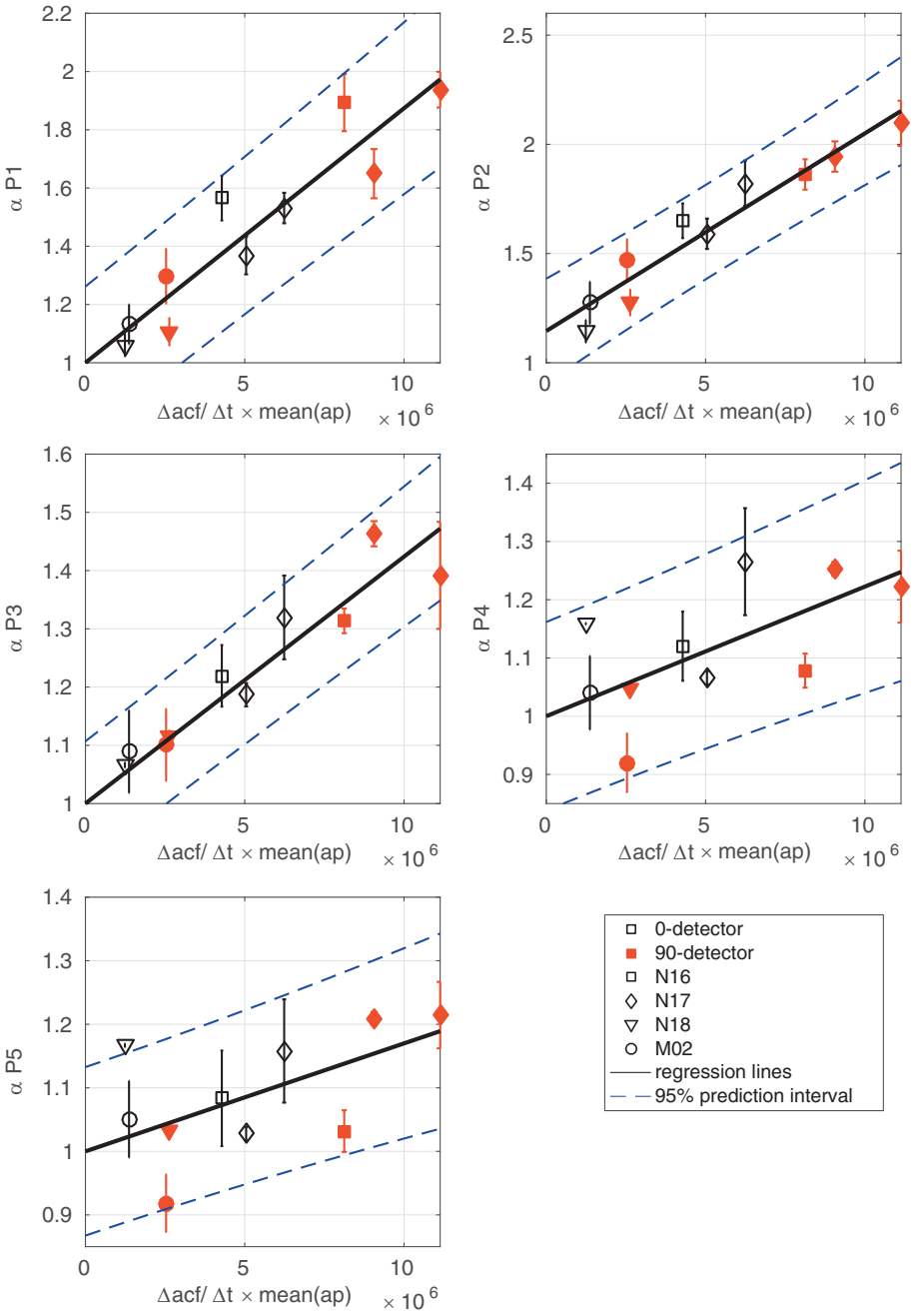

Fig. 6. α factors from Table 3 plotted versus the $\Delta acf/\Delta t$ ($E > 90$ keV) multiplied by the mean *ap* index in each period. $\alpha < 1$ are removed when calculating the best fit in the regression. The equations for the best fit lines are presented in Eq. (2). A 95% prediction interval for the regressions is plotted in dashed blue lines. The standard deviations of α are plotted as vertical lines.

Table 7. Ordinary least squares regression of α versus $\Delta acf/\Delta t \times \overline{ap}$.

Channel	Parameter	Estimate	Standard error	p-value
P1	Intercept	1.01	0.07	0.45
	Slope	8.6×10^{-8}	1.2×10^{-8}	4.7×10^{-5}
P2	Intercept	1.15	0.05	0.01
	Slope	9.0×10^{-8}	8.7×10^{-9}	3.3×10^{-6}
P3	Intercept	1.03	0.03	0.18
	Slope	3.9×10^{-8}	4.6×10^{-9}	1.6×10^{-5}
P4	Intercept	1.06	0.05	0.15
	Slope	1.5×10^{-8}	7.9×10^{-9}	0.05
P5	Intercept	1.05	0.05	0.17
	Slope	1.1×10^{-8}	7.5×10^{-9}	0.09

Table 8. Regression with a constant intercept = 1, of α versus $\Delta acf/\Delta t \times \overline{ap}$.

Channel	Parameter	Estimate	Standard error	p-value
P1	Slope	8.7×10^{-8}	6.0×10^{-9}	7.4×10^{-8}
P3	Slope	4.2×10^{-8}	2.5×10^{-9}	1.6×10^{-8}
P4	Slope	2.3×10^{-8}	4.1×10^{-9}	2.9×10^{-4}
P5	Slope	1.75×10^{-8}	3.8×10^{-9}	9.4×10^{-4}

One explanation of the observed variation in the degradation rate may be that it is caused by the proton population with energy $E < 90$ keV, which we have not included in our accumulated flux. To account for the variation, we weight the $\Delta acf/\Delta t$ by the mean ap index over the respective period (where Δt is the number of months in each of the coloured periods listed in Table 6). NOAA-17 is the only satellite calibrated over two periods. We calculate $\Delta acf/\Delta t$ separately for the two periods and multiply with the mean ap (abbreviated $\overline{ap}$) for each period. The $\Delta acf_2/\Delta t_2 \times \overline{ap}_2$, calculated for period 2, is added to the $\Delta acf_1/\Delta t_1 \times \overline{ap}_1$ for period 1.

All α factors versus $\sum(\Delta acf/\Delta t \times \overline{ap})$ are plotted in Figure 6. The summation symbol indicates that we have to add together results from the two periods for NOAA-17. Inclusion of the ap dependence improves the correlation coefficient in P1 from $r = 0.84$ to $r = 0.93$, in P2 from $r = 0.91$ to $r = 0.96$ and in P3 from $r = 0.86$ to $r = 0.95$. For P4 and P5 the correlation coefficients decrease slightly from $r = 0.60$ to $r = 0.58$ in P4, and from $r = 0.55$ to $r = 0.49$ in P5. P1–P3 and P5 correlations are significant to the 5% level, while P4 is significant to the 10% level. The fact that P4 and P5 are not much affected by the weighting with ap index can be interpreted as support for the theory that the lower energy proton population is influencing the degradation of the P1–P3 channels. As mentioned before, the lower energy protons will deposit their energy in the front part of the detector, and thus be of lesser importance for the P4 and P5 channels, which measure particles with energies that penetrate deep into the detector.

We performed an OLS with α versus $\sum(\Delta acf/\Delta t \times \overline{ap})$. The estimated parameters for P1–P5 are summarized in Table 7. The regression lines for P1, P3, P4 and P5 are not found to have intercepts significantly different from $\alpha = 1$. We therefore proceeded to a RTO for these channels, the results are presented in Table 8. Since the intercept is significant for P2 in the OLS, we select this as the best fit. For the four other channels, we use the fit found by RTO. The slopes of P1, P3, P4 and P5 have approximately 50% smaller standard error in the RTO compared to the OLS. The best fit lines are

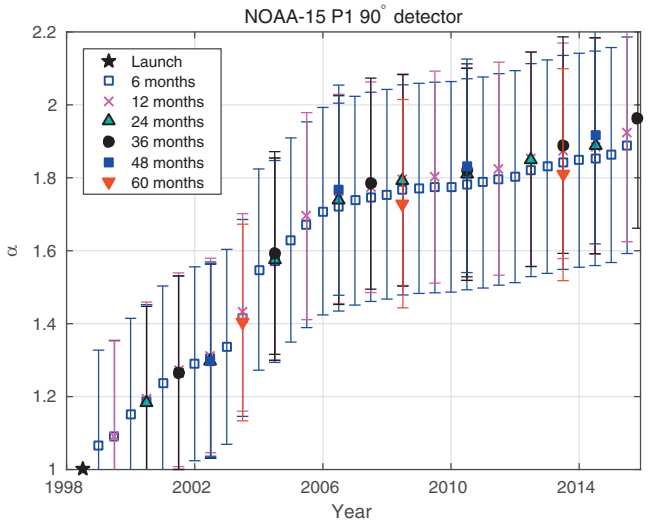

Fig. 7. α for the 90° detector of NOAA-15 calculated using different number of months between each factor. The 95% prediction interval is used to calculate errors.

summarized in Equation set (2) and plotted in Figure 6 together with a 95% prediction interval and the α factors by Sandanger et al. (2015). We can now express a refined degradation dependency:

$$\begin{aligned}
\alpha_{P1} &= 8.7 \times 10^{-8} \sum(\Delta acf/\Delta t \times \overline{ap}) + 1 \\
\alpha_{P2} &= 9.0 \times 10^{-8} \sum(\Delta acf/\Delta t \times \overline{ap}) + 1.15 \\
\alpha_{P3} &= 4.2 \times 10^{-8} \sum(\Delta acf/\Delta t \times \overline{ap}) + 1 \quad , \qquad (2) \\
\alpha_{P4} &= 2.2 \times 10^{-8} \sum(\Delta acf/\Delta t \times \overline{ap}) + 1 \\
\alpha_{P5} &= 1.7 \times 10^{-8} \sum(\Delta acf/\Delta t \times \overline{ap}) + 1
\end{aligned}$$

where the summation should be done over the number of periods chosen. That is, the α factor at the end of period 1 is $\alpha_1 : \Delta acf_1/\Delta t_1 \times \overline{ap}_1$, that after period 2 is $\alpha_2 : \Delta acf_1/\Delta t_1 \times \overline{ap}_1 + \Delta acf_2/\Delta t_2 \times \overline{ap}_2$, and so on.

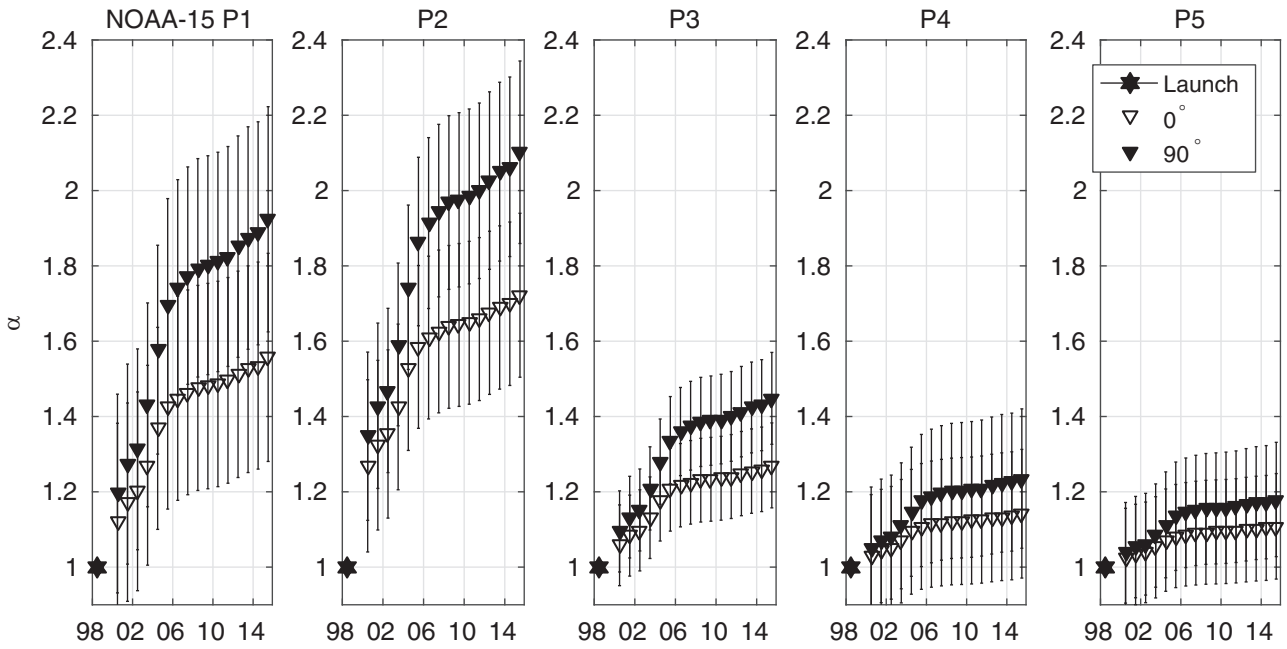

Fig. 8. α factors for NOAA-15 with 12 months in-between, calculated as described in Section 5.3. The 0° detector is shown as open triangles, and the 90° as filled triangles. The estimated error is calculated based on the 95% prediction interval.

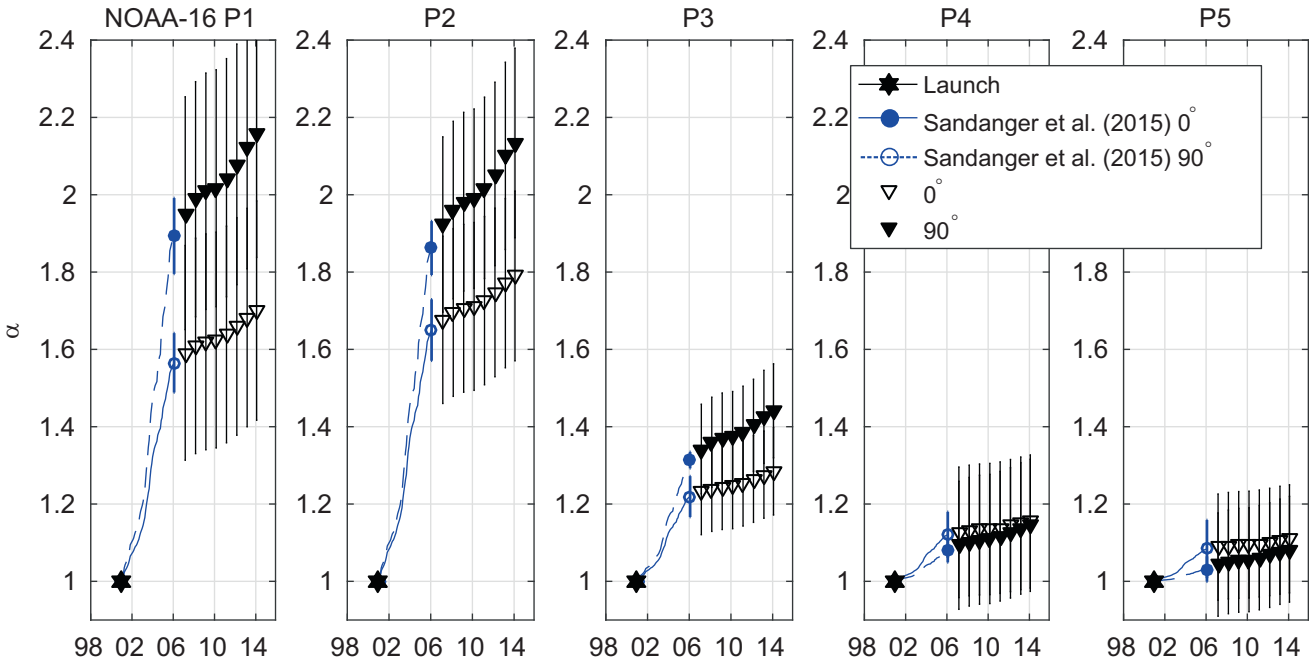

Fig. 9. α factors for NOAA-16 with 12 months in-between, calculated as described in Section 5.3. The 0° detector is shown as open triangles, and the 90° as filled triangles. The estimated error is calculated based on the 95% prediction interval. Factors from Sandanger et al. (2015) are shown as open (0°) and filled (90°) blue circles. Monthly α factors calculated with their method for $E > 90$ keV are displayed as blue solid (0°) and dashed (90°) lines.

Equation set (1) calculated α factors with a non-changing slope between α and *acf*. Equation set (2) weights the change in *acf*, that is Δacf, through a time period Δt with the mean *ap* index over the same time period. In this way we introduce an element which will increase the radiation dose efficiency in degrading the detectors (producing a $\Delta\alpha$) in periods where the geomagnetic activity is high.

5.3. Calibration of all satellites

We now have the tools needed to calculate calibration factors for all the degraded detectors. The first step is to calculate monthly mean integral fluxes from the degraded data for the satellite we want to calibrate. We assume that $\alpha = 1$ for all energy channels in the first month of operation, and thus the

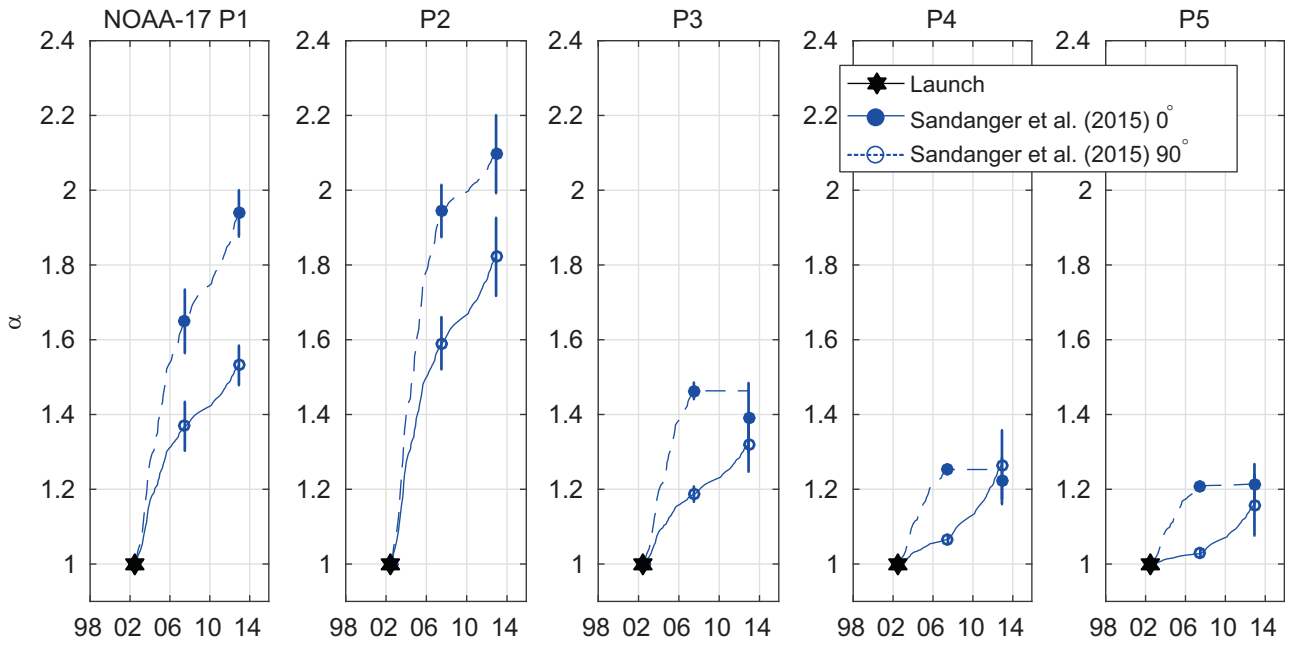

Fig. 10. NOAA-17 α factors from Sandanger et al. (2015) are shown as open (0°) and filled (90°) blue circles. Monthly α factors calculated with their method for $E > 90$ keV are displayed as blue solid (0°) and dashed (90°) lines.

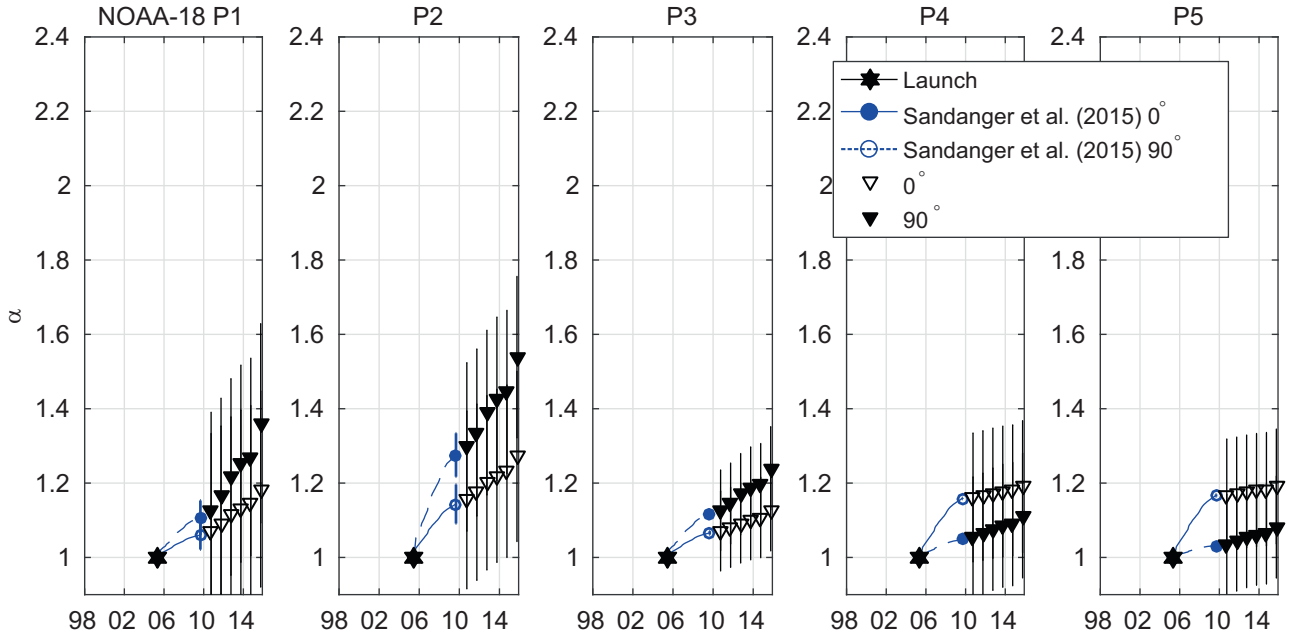

Fig. 11. α factors for NOAA-18 with 12 months in-between, calculated as described in Section 5.3. The 0° detector is shown as open triangles, and the 90° as filled triangles. The estimated error is calculated based on the 95% prediction interval. Factors from Sandanger et al. (2015) are shown as open (0°) and filled (90°) blue circles. Monthly α factors calculated with their method for $E > 90$ keV are displayed as blue solid (0°) and dashed (90°) lines.

corrected flux is equal to the uncorrected flux the first month. For the satellites already calibrated by Sandanger et al. (2015), we start the use of our method in the first month after their last calibration factor and use their α to correct the energy spectrum. We use Equation set (1) to calculate a first approximation of monthly α and correct the energy thresholds by these preliminary α factors. The integral flux of $E > 90$ keV is found numerically in each month and accumulated in the process, that is, we calculate the *acf*.

After we have achieved an estimate for the *acf* for all the months in operation, we choose an interval of appropriately many months (e.g. $\Delta t = 12$) and find the mean *ap* index in each of the intervals of length Δt. We multiply the $\Delta acf/\Delta t$ by the mean *ap* index in each interval and add the results together. Lastly, we use the sum of $\Delta acf/\Delta t \times \overline{ap}$ to calculate α by Eq. (2). We use the new estimation of α factors from Eq. (2) to go back and correct the uncorrected monthly energy spectra and calculate the *acf* again. We can use the new *acf* to

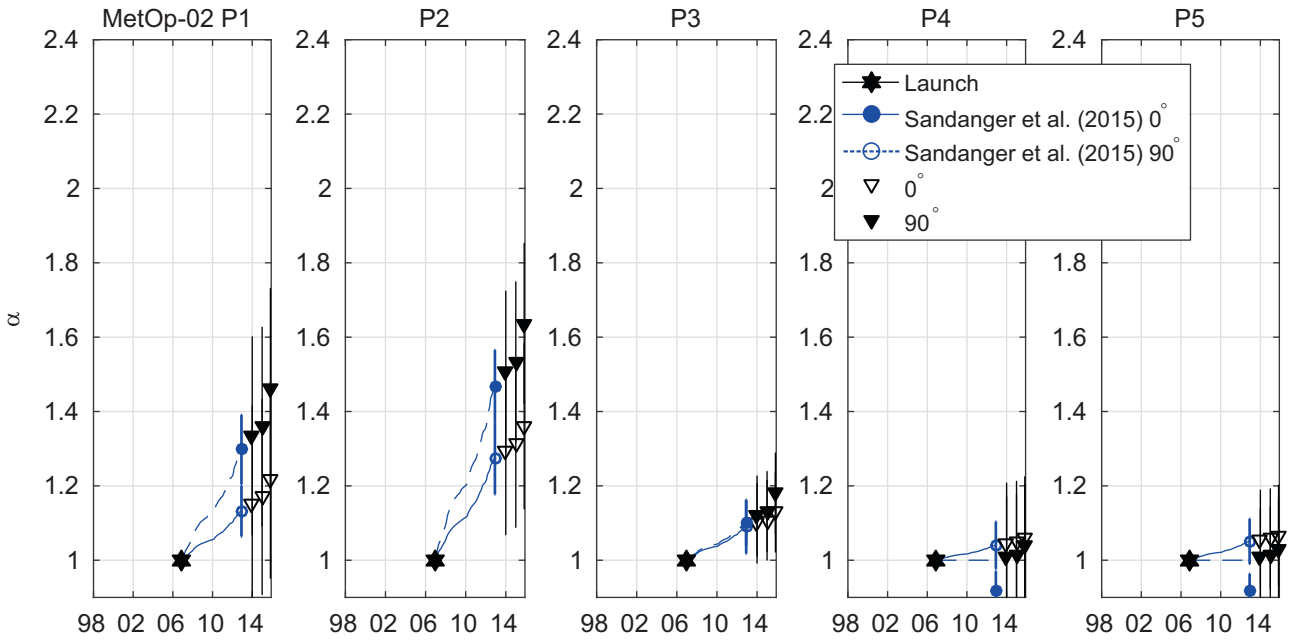

Fig. 12. α factors for MetOp-02 with 12 months in-between, calculated as described in Section 5.3. The 0° detector is shown as open triangles, and the 90° as filled triangles. The estimated error is calculated based on the 95% prediction interval. Factors from Sandanger et al. (2015) are shown as open (0°) and filled (90°) blue circles. Monthly α factors calculated with their method for $E > 90$ keV are displayed as blue solid (0°) and dashed (90°) lines.

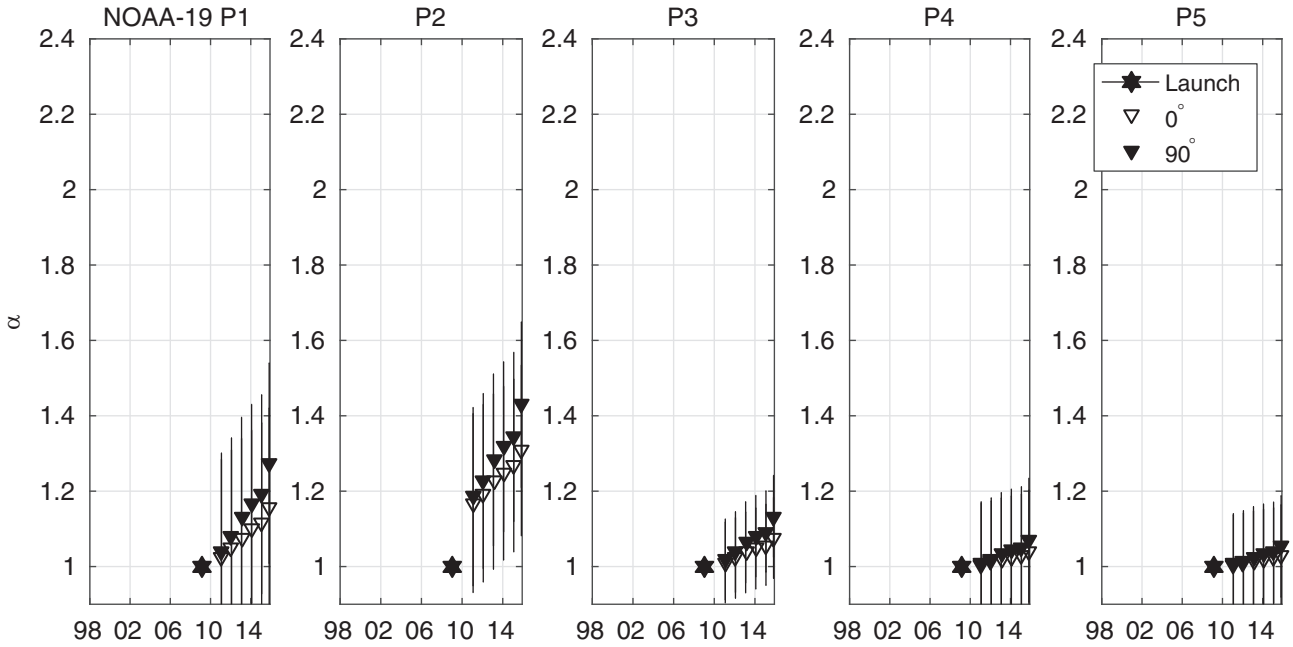

Fig. 13. α factors for NOAA-19 with 12 months in-between, calculated as described in Section 5.3. The 0° detector is shown as open triangles, and the 90° as filled triangles. The estimated error is calculated based on the 95% prediction interval.

calculate $\Delta acf/\Delta t \times \overline{ap}$ for the Δt = 12-month intervals, and from Equation set (2) estimate α again. The iteration process is repeated until the α factors calculated from Eq. (2) converge, which happens after 3–5 iterations.

It is not crucial to use a period of 12 months, as is illustrated in Figure 7 for NOAA-15's 90° detector. However, we encourage the use of intervals on the scale of years, rather than months. It seems that 6 months is a lower limit for the model to give consistent results. This is probably because the *ap* index varies in a more random fashion on the scale of one to a few months than on yearly basis. It is the trend of the *ap* index through the solar cycle rather than the monthly fluctuations that works as a weighting factor. In practice, by our method one can retrieve an estimated correction factor for a satellite in any chosen year directly (as shown in Fig. 7).

α factors for all satellites are calculated and plotted in Figures 8–14. The NOAA-17 MEPED lifetime ended in 2013, and we cannot extend the time series of α factors further

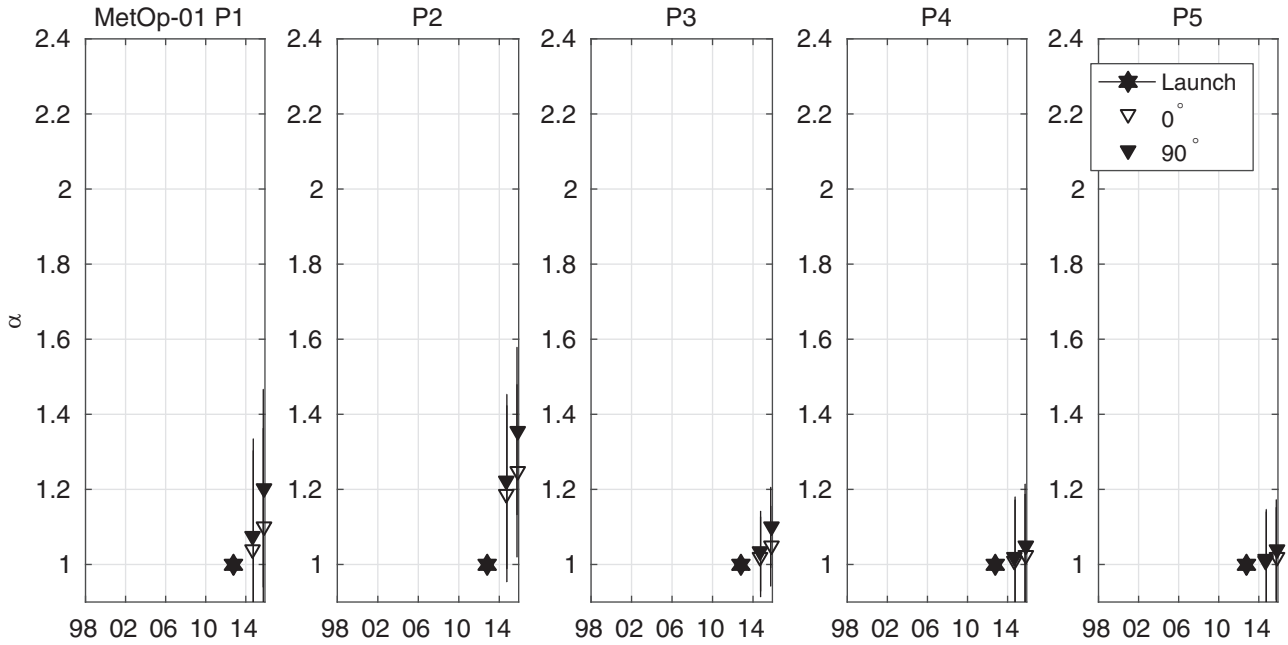

Fig. 14. α factors for MetOp-01 with 12 months in-between, calculated as described in Section 5.3. The 0° detector is shown as open triangles, and the 90° as filled triangles. The estimated error is calculated based on the 95% prediction interval.

than Sandanger et al. (2015). For NOAA-16, NOAA-18 and MetOp-02 we have plotted the α factors by Sandanger et al. (2015) on a monthly basis in blue (although, calculated as a function of *acf* with $E > 90$ keV for all channels, as opposed to their varying thresholds given here in Sect. 5). These are calculated using their method where each satellite and detector have an individually best fit slope between α and the corrected accumulated flux. In Figure 5 we showed how the degradation rate ($\Delta\alpha/\Delta acf$) varied for the satellites calibrated by Sandanger et al. (2015). The α factors presented in blue in Figures 9–12 thus have this variation included in them. α factors presented as black triangles are calculated using the method presented in this paper (filled triangles represent the 90° detector, open triangles the 0° detector). The error estimates were calculated from the 95% prediction intervals shown in Figure 6. The estimated errors are as large as ±0.27 in P1. The α factors estimated by satellite comparison in Sandanger et al. (2015) had smaller errors and are the preferred method to use when possible. We have here presented a model based on their results, and thus we expect the errors in our model estimated α factors to be larger. However, the correlations of 0.93, 0.96 and 0.95 in P1, P2 and P3 are encouraging in that the data our model is built on behaves consistently. The respective R^2 for the P1–P3 regressions (Eq. (2)) are 0.91, 0.93 and 0.93. For both P4 and P5, the regression R^2 is 0.85.

6. Summary

There is a significant relationship between the correction α factors of all the MEPED proton channels P1–P5 and the accumulated corrected proton fluxes with $E > 90$ keV independent of the pointing direction and spacecraft. However, there is a variation in the degradation rate ($\Delta\alpha/\Delta acf$) through the solar cycle which may be caused by the variation of the flux of lower energy protons not included in the accumulated corrected flux (*acf*). For P1–P3 the correlation improves when the accumulated flux is weighted by the mean *ap* index. The *ap* index measures geomagnetic activity and can be used as a measure of how the particle population in the magnetosphere varies over the course of a solar cycle. We exploit this to introduce a weighting factor to go from the non-varying relationship between α and *acf* presented in Equation set (1), to the refined Equation set (2). The consistent behaviour substantiates the degradation factors estimated by Sandanger et al. (2015). It further provides a method to determine the level of degradation for the satellites that they could not include in their analysis, NOAA-15, NOAA-19 and MetOp-01, as well as extend the α factors for NOAA-16, NOAA-18 and MetOp-02 beyond their last calibration point. In addition, it could enable us to estimate the level of degradation of the last satellite in the SEM-2 family, MetOp-C, which will be launched in 2017, and potentially the first generation SEM-1 MEPED detectors.

There are some limitations to the model. The severity of the NOAA-15 degradation indicated by Figure 9 in Sandanger et al. (2015) is not reflected in our estimated α factors. The underestimation is also clear if we compare our NOAA-15 estimates with the ones obtained by Asikainen & Mursula (2011). Our model is based on correction factors from the period 2005 to 2013. There may be larger uncertainties connected with the model when applying it in the inclining and maximum phase of the previous solar cycle, which was stronger than the current cycle. Also, our model is based on good statistics for the evolution of α for satellites up to approximately 6 years of age. For higher age and degradation, the model is based on only NOAA-17. When MetOp-C is launched additional correction factors for MetOp-02 and MetOp-01 can be calculated using the Sandanger et al. (2015) method. This will improve the model. Finally, other methods for calibrating NOAA-15 should be investigated. This would be helpful in describing degradation for a stronger solar maximum than observed in the current solar cycle.

Acknowledgements. The authors thank the reviewers for helpful suggestions and comments. This study was supported by the Research Council of Norway/CoE under Contract 223252/F50. The authors thank D. S. Evans and the NOAA's National

Geophysical Data Center (NGDS) for providing NOAA data. We acknowledge the use of NASA/GSFC's Space Physics Data Facility's OMNIWeb service and OMNI data. We thank the SIDC team, World Data Center for the Sunspot Index, Royal Observatory of Belgium, Monthly Report on the International Sunspot Number, online catalogue of the sunspot index: http://www.sidc.be/sunspot-data/. The editor thanks Timo Asikainen and an anonymous referee for their assistance in evaluating this paper.

References

Asikainen, T., and K. Mursula. Recalibration of the long-term NOAA/MEPED energetic proton measurements. *J. Atmos. Sol. Terr.Phys.*, **73**, 335–347, 2011, DOI: 10.1016/j.jastp.2009.12.011.

Asikainen, T., K. Mursula, and V. Maliniemi. Correction of detector noise and recalibration of NOAA/MEPED energetic proton fluxes. *J. Geophys. Res.*, **117 (A9)**, A09204, 2012, DOI: 10.1029/2012JA017593.

Davis, G. History of the NOAA satellite program. *J. Appl. Remote Sens.*, **1 (1)**, 2007, DOI: 10.1117/1.2642347.

Eisenhauer, J.G. Regression through the Origin. *Teaching Statistics*, **25 (3)**, 76–80, 2003, DOI: 10.1111/1467-9639.00136.

Evans, D.S., and M.S. Greer. *Polar Orbiting Environmental Satellite Space Environment Monitor – 2 Instrument Descriptions and Archive Data Documentation*, Natl. Atmos. and Oceanic Admin., Space Environ. Cent, Boulder, Colorado, NOAA Technical Memorandum OAR SEC 93, version 1.4, January 2004, 2000.

Galand, M., and D.S. Evans. *Radiation Damage of the Proton MEPED Detector on POES (TIROS/NOAA) Satellites*, Space Environment Center, Boulder, Colorado, NOAA Technical Memorandum OAR 456-SEC, 2000.

Horne, R.B., S.A. Glauert, N.P. Meredith, D. Boscher, V. Maget, D. Heynderickx, and D.Pitchford. Space weather impacts on satellites and forecasting the Earth's electron radiation belts with SPACECAST. *Space Weather*, **11**, 169–186, 2013, DOI: 10.1002/swe.20023.

McFadden, J.P., D.S. Evans, W.T. Kasprzak, L.H. Brace, D.J. Chornay, et al. *In-Flight Instrument Calibration and Performance Verification*, ESA Publications Division, 277–385, 2007.

Ødegaard, L.-K.G. Recalibration of the MEPED Proton Detectors Onboard NOAA POES Satellites, *Masters degree*, University of Bergen, 2013.

Raben, V.J., D.S. Evans, H.H. Sauer, S.R. Sahm, and M. Huynh. *TIROS/NOAA Satellite Space Environment Monitor Data Archive Documentation: 1995 Update. NOAA Technical Memorandum ERL SEL-86*, National Oceanic and Atmospheric Administration, 1995.

Sandanger, M.I., L.-K.G. Ødegaard, H. Nesse Tyssøy, J. Stadsnes, F. Søraas, K. Oksavik, and K. Aarsnes. In-flight calibration of NOAA POES proton detectors – derivation of the MEPED correction factors. *J. Geophys. Res. [Space Phys.]*, **120**, 9578–9593, 2015, DOI: 10.1002/2015JA021388.

Seale, R., and R.-H. Bushnell. *The TIROS-N/NOAA A-J Space Environment Monitor Subsystem. NOAA Technical Memorandum ERL SEL-75*, Space Environment Laboratory, Boulder, Colorado, 1987.

Yando, K., R.M. Millan, J.C. Green, and D.S. Evans. A Monte Carlo simulation of the NOAA POES medium energy proton and electron detector instrument. *J. Geophys. Res. [Space Phys.]*, **116 (A10231)**, 2011, DOI: 10.1029/2011JA016671.

Cite this article as: Ødegaard L.-K.G., Tyssøy H.N., Sandanger M.I.J., Stadsnes J., & Søraas F. Space Weather impact on the degradation of NOAA POES meped proton detectors. *J. Space Weather Space Clim.*, **6**, A26, 2016, DOI: 10.1051/swsc/2016020.

Paper III

Energetic electron precipitation into the middle atmosphere - Constructing the loss cone fluxes from MEPED POES

Nesse Tyssøy, H., M. I. Sandanger, L.-K. G. Ødegaard, J. Stadsnes, A. Aasnes, and A. E. Zawedde

Journal of Geophysical Research: Space Physics, *21* (2016). doi: 1002/2016JA022752

AGU PUBLICATIONS

JGR

Journal of Geophysical Research: Space Physics

RESEARCH ARTICLE
10.1002/2016JA022752

Special Section:
Energetic Electron Loss and its Impacts on the Atmosphere

Energetic electron precipitation into the middle atmosphere—Constructing the loss cone fluxes from MEPED POES

H. Nesse Tyssøy[1], M. I. Sandanger[1], L.-K. G. Ødegaard[1], J. Stadsnes[1], A. Aasnes[1], and A. E. Zawedde[1]

[1]Birkeland Centre for Space Science, Department of Physics and Technology, University of Bergen, Bergen, Norway

Key Points:
- Precipitating energetic electrons are often highly anisotropic; neither of the MEPED telescopes gives a good measure of the loss cone flux
- Electron fluxes measured by the MEPED telescopes are matched with pitch angle profiles derived from the theory of wave-particle interaction
- Complete bounce loss cone fluxes are constructed, and the electron energy deposition into the mesosphere is calculated

Correspondence to:
H. Nesse Tyssøy,
hilde.tyssoy@uib.no

Citation:
Nesse Tyssøy, H., M. I. Sandanger, L.-K. G. Ødegaard, J. Stadsnes, A. Aasnes, and A. E. Zawedde (2016), Energetic electron precipitation into the middle atmosphere—Constructing the loss cone fluxes from MEPED POES, *J. Geophys. Res. Space Physics*, *121*, doi:10.1002/2016JA022752.

Received 28 MAR 2016
Accepted 24 MAY 2016
Accepted article online 27 MAY 2016

Abstract The impact of energetic electron precipitation (EEP) on the chemistry of the middle atmosphere (50–90 km) is still an outstanding question as accurate quantification of EEP is lacking due to instrumental challenges and insufficient pitch angle coverage of current particle detectors. The Medium Energy Proton and Electron Detectors (MEPED) instrument on board the NOAA/Polar Orbiting Environmental Satellites (POES) and MetOp spacecraft has two sets of electron and proton telescopes pointing close to zenith (0°) and in the horizontal plane (90°). Using measurements from either the 0° or 90° telescope will underestimate or overestimate the bounce loss cone flux, respectively, as the energetic electron fluxes are often strongly anisotropic with decreasing fluxes toward the center of the loss cone. By combining the measurements from both telescopes with electron pitch angle distributions from theory of wave-particle interactions in the magnetosphere, a complete bounce loss cone flux is constructed for each of the electron energy channels >50 keV, >100 keV, and >300 keV. We apply a correction method to remove proton contamination in the electron counts. We also account for the relativistic (>1000 keV) electrons contaminating the proton detector at subauroral latitudes. This gives us full range coverage of electron energies that will be deposited in the middle atmosphere. Finally, we demonstrate the method's applicability on strongly anisotropic pitch angle distributions during a weak geomagnetic storm in February 2008. We compare the electron fluxes and subsequent energy deposition estimates to OH observations from the Microwave Limb Sounder on the Aura satellite substantiating that the estimated fluxes are representative for the true precipitating fluxes impacting the atmosphere.

1. Introduction

The almost continuous precipitation of low-energy auroral electrons (<30 keV) from the magnetospheric plasmasheet deposit their energy above 90 km in the auroral oval. The auroral electrons are often isotropic, and a positive correlation between geomagnetic activity or particle precipitation and the NO_x composition is fairly well established [*Baker et al.*, 2001; *Barth et al.*, 2003; *Sætre et al.*, 2004, 2006; *Hendrickx et al.*, 2015]. The role of the more energetic electron precipitation (EEP) in changing the chemistry of the middle atmosphere (50–100 km) is, on the other hand, still an outstanding question [*Rozanov et al.*, 2012; *Sinnhuber et al.*, 2012]. These often highly anisotropic electrons originate from the outer radiation belts, and their precipitation to the atmosphere is related to complex wave-particle interactions mostly confined to subauroral latitudes. The relation of EEP events to geomagnetic activity is not well defined yet, but it is known to be associated with both enhanced solar wind pressure caused by coronal mass ejections and high-speed solar wind streams (HSSWS) [*Turunen et al.*, 2009; *Meredith et al.*, 2011]. As the different events might have quite different geomagnetic signatures, recent studies apply energetic electron measurements to indicate the coexistence of electron precipitation and atmospheric chemical changes. For example, *Newnham et al.* [2011], *Daae et al.* [2012], and *Andersson et al.* [2012, 2014a, 2014b] suggest that electron precipitation during moderate but frequently occurring geomagnetic storms may have a significant impact on the HO_x and NO_x production rate and subsequently the catalytic destruction of ozone.

Accurate quantification of the effect of energetic electron precipitation, however, remains due to instrumental challenges. Most of the current particle detectors in space are unsuitable for determining the amount of particles precipitating into the atmosphere. The majority measures only the trapped particle fluxes because of inadequate pitch angle resolution [*Rodger et al.*, 2013]. In this respect, the Medium Energy Proton and Electron Detectors (MEPED) on board the Polar Orbiting Environmental Satellites (POES) and European Organisation for the Exploitation of Meteorological Satellites (EUMETSAT) MetOp has an expedient design.

MEPED consist of two electron and two proton telescopes, pointed in two directions, approximately 0° and 90° to the local vertical. At middle and high latitudes the 0° telescope measures particle fluxes that will be lost to the atmosphere, whereas the 90° telescope might detect precipitating particle fluxes and/or trapped particles in the radiation belts [*Rodger et al.*, 2010]. The long measurement time series and multiple local time coverage make the POES/MEPED and MetOp/MEPED data set valuable in respect to estimating the medium- to high-energy particle loss to the atmosphere.

The pitch angle, α, of a charged particle trapped in the magnetosphere is defined as the angle between its velocity vector and the magnetic field line it gyrates around. While the pitch angle changes as the particle moves along the magnetic field, the equatorial pitch angle, α_{eq}, is often used as a reference. Here the particles may have a range of different pitch angle distributions (PADs). The level of anisotropy varies significantly with particle energy, location, and geomagnetic activity. This implies that the 0° and 90° telescopes cannot alone be used to determine the level of precipitating particle fluxes. Only in a rare case of strong pitch angle diffusion and an isotropic distribution will the 0° or 90° telescope give a realistic precipitating flux estimate. In case of an anisotropic distribution, the 0° detector will underestimate, while the 90° detector will overestimate the flux of precipitating electrons.

To overcome this challenge, *Rodger et al.* [2013] applied a geometric mean between the fluxes measured by the 0° and 90° detectors to determine the true precipitating electron fluxes. They examined the EEP measurement during ~250 satellite overflights of the Kilpisjärvi riometer in Finland ($L = 6.13$). As the riometer responds to the precipitating fluxes, an estimate of the energy deposition and its subsequent ionization and the expected riometer absorption can be used to compare the different measurements. At high flux levels ($> 10^6\,cm^{-2}\,s^{-1}\,sr^{-1}$ for >30 keV) there was found a relatively good agreement between the absorption estimated from the geometric mean of the flux measurement and the riometer absorption. At lower flux levels, however, the space-based measurements significantly underestimate the absorption by ~7–9 times. In fact, the level of agreement between a geometric mean of the space based electron fluxes and the riometer absorption appears to be strongly dependent upon the level of diffusion and hence the level of isotropy in the PADs. Considering that the Kilpisjärvi riometer is located in the auroral zone where isotropy is more common compared to the subauroral latitudes where the medium energy (100–300 keV) and relativistic (>300 keV) electron precipitation usually occur, the geometric mean will not provide sufficient accuracy in determining the particle energy deposition.

The level of diffusion itself has previously been determined from the MEPED POES observations [*Kirkwood and Osepian*, 2001; *Li et al.*, 2013, 2014a, 2014b] with the purpose of identifying the sources for pitch angle scattering such as chorus, hiss, and whistler mode waves. The 0° and 90° fluxes were fitted onto the solution of the Fokker-Planck equation for wave-particle diffusion [*Kennel and Petschek*, 1966]. Although, the Fokker-Planck equation requires steady state conditions where the particles being lost will be replenished so that the pitch angle distribution is in diffusion equilibrium, *Li et al.* [2013] and multiple follow-up papers have shown that without any strict criteria the diffusion coefficient estimated from the MEPED instrument was consistent with independent observations of chorus waves by the Van Allen Probes.

Estimating the diffusion strength from the POES/MEPED 0° and 90° detector forms the base of our study. After accounting for proton degradation [*Sandanger et al.*, 2015; *Ødegaard et al.*, 2016] and electron contamination [*Evans and Greer*, 2000; *Yando et al.*, 2011], we identify the level of diffusion and hence the angular distribution within the loss cone. We take into account the detector sensitivity when the directional flux varies over the field of view solid angle of the telescope. In addition, we estimate the flux of relativistic electrons (>1000 keV) which contaminate the highest MEPED proton channel [*Yando et al.*, 2011]. In total, these steps make up a complete tool box for overcoming the known challenges in regard to proton contamination, degradation, and insufficient loss cone information for the MEPED electron data, giving us a unique estimate of the precipitating electron fluxes in the mesosphere. Finally, we use the observed fluxes during a HSSWS demonstrating its applicability. Comparing the estimated fluxes and subsequent energy deposition to the OH density as measured by the Microwave Limb Sounder (MLS) on board the Aura satellite, we substantiate that our method gives a realistic estimate of precipitating energetic electron fluxes. To our knowledge, this is the first time direct satellite electron measurements are used to quantitatively determine its impact on HO_x during a weak geomagnetic storm.

2. The MEPED Instrument and Data

MEPED is part of the Space Environment Monitor 2 (SEM-2) instrument package on board the POES and MetOp satellites, which are polar orbiting Sun-synchronous satellites at an altitude of ~850 km with an orbital

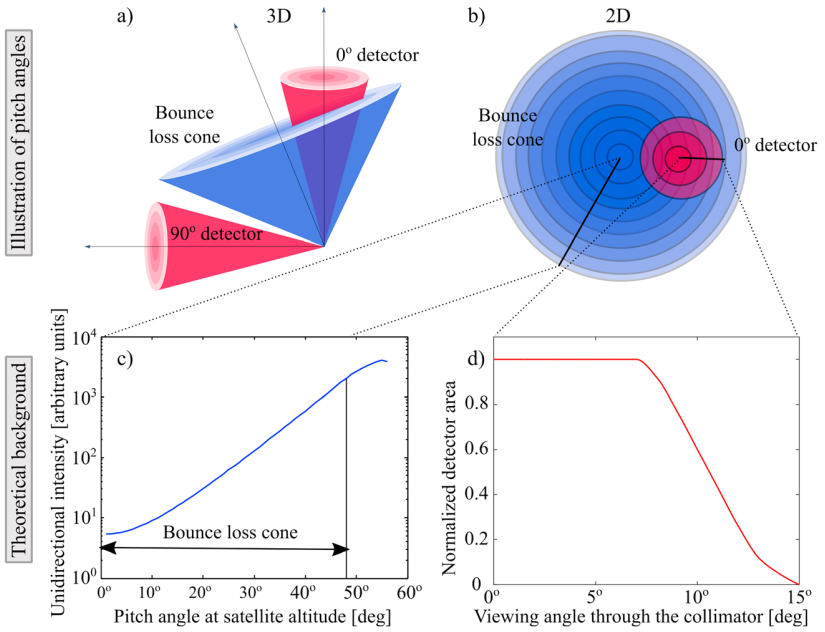

Figure 1. (a and b) The MEPED telescope viewing angles in respect to the loss cone exemplified for one case at high latitudes. (c) A theoretical pitch angle distribution profile based on a selected solution of the Fokker-Planck equation for particles. (d) The detector response-function for different viewing angles through the detector collimator.

period of ~100 min. MEPED includes an omnidirectional detector system that detects protons of higher energies than 16 MeV, but our focus is the four solid-state directional telescopes that measures electron fluxes in three energy ranges >50 keV, >100 keV, and >300 keV, and proton fluxes in five differential channels from 30 to 6900 keV and one integral channel >6900 keV.

The field of view of both the telescopes is 30° full width, with a higher detector response at the center angles as illustrated in Figure 1. The MEPED raw data are sampled every other second with 1 s integration period [*Evans and Greer*, 2000]. We average the fluxes over a 16 s interval, which corresponds to about 100 km along the satellite track or approximately 1° latitude similar to *Codrescu et al*. [1997]. The MEPED data files also list the pitch angle estimated from the International Geomagnetic Reference Field (IGRF) model, a parameter necessary to determine where the telescopes are pointing relative to the loss cone.

3. Proton Correction of the Electron Fluxes

The MEPED electron data are not straight forward to use. The electron telescopes are known to exhibit a spurious response to protons [*Evans and Greer*, 2000; *Yando et al*., 2011] as listed in Table 1. In order to correct for the false counts, we can use the proton flux measurement from the proton telescopes.

It has, however, been well documented that the solid state detectors will degrade over time as a result of radiation damage [*Galand and Evans*, 2000; *Asikainen and Mursula*, 2011; *Asikainen et al*., 2012; *Sandanger et al*., 2015]. This impact is significant after 2–3 years of operation, changing the energy ranges of the proton detector. The

Table 1. Summary of Electron Energy Channels and Their Sensitivity to Electron and Proton Fluxes

Energy Channel	Electron Energy Range	Contaminating Protons
E1	>50 keV[a]	210–2600 keV
E2	>100 keV	280–2600 keV
E3	>300 keV	440–2600 keV
P6	>1000 keV[a]	

[a]Effective energy range derived from Geant-4 geometric factors [*Yando et al*., 2011].

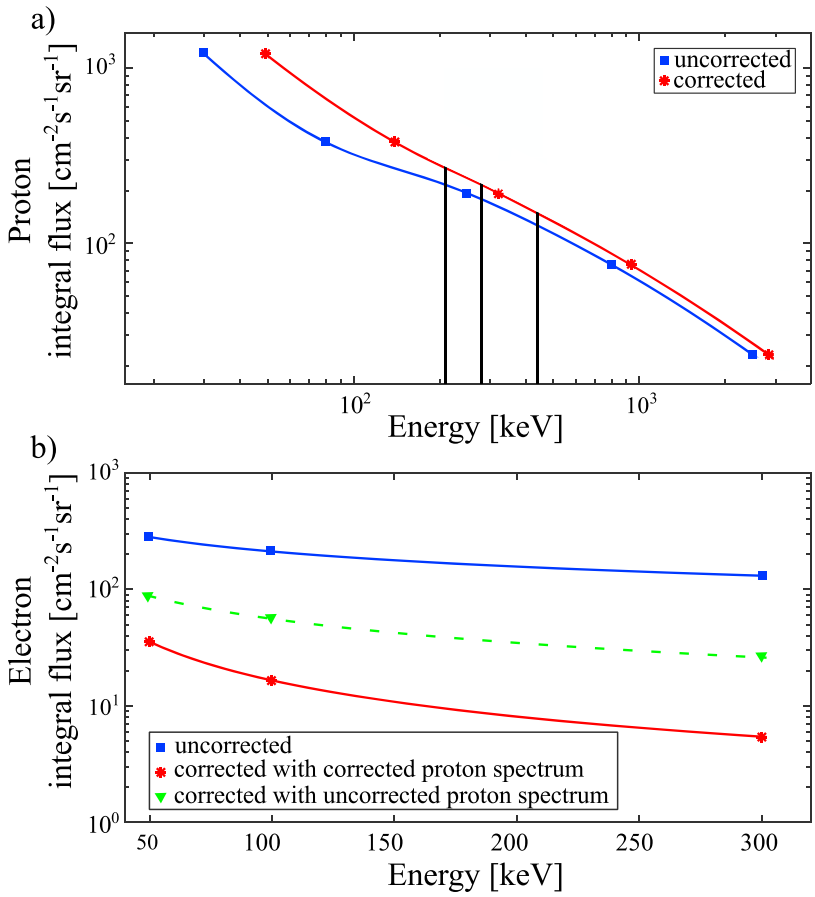

Figure 2. An illustration of proton and electron flux correction exemplified by NOAA/POES 15 in March 2013 at high latitudes in Northern Hemisphere. (a) The uncorrected integral spectrum (blue line) has the nominal energy thresholds: 30, 80, 250, 800, and 2500 keV. In the corrected spectrum (red line) the energy thresholds has changed according to the correction factors found by *Sandanger et al.* [2015]. The proton fluxes in the energy range from 210, 270, and 440 keV (marked as black vertical lines) to 2600 keV are subtracted from the original measured electron fluxes (blue line) in Figure 2b. The resulting fluxes represent the true electron fluxes in the respective energy bands (red line). The electron fluxes resulting from subtracting the uncorrected proton fluxes are also marked (green line).

degradation needs to be taken into account in a quantitative assessment of the data. The first effort to derive correction factors for the new energy ranges for the proton telescopes on board the different satellites was carried out by *Asikainen and Mursula* [2011] and followed up by *Asikainen et al.* [2012] and *Ødegaard* [2013]. Recently, a new study by *Sandanger et al.* [2015] uses a larger statistical database showing consistent result, indicating a robust calibration procedure. A follow-up study by *Ødegaard et al.* [2016] shows that all detectors degrade in the same manner in the same phase of a solar cycle. This knowledge is applied to determine correction factors to create a complete set of correction factors for the SEM-2 package up to present time.

The correction factors are applied to an integral flux spectrum to determine the pertinent energy ranges of the protons measured by the telescope used as described in *Sandanger et al.* [2015]. This is also illustrated in Figure 2a for a measurement by POES 15 in March 2012. The uncorrected integral flux spectrum (blue line, Figure 2a) has the nominal energy thresholds: 30, 80, 250, 800, and 2500 keV. In the corrected spectrum the energy thresholds have changed according to the correction factors, α_x found by *Sandanger et al.* [2015], $30\alpha_1$, $80\alpha_2$, $250\alpha_3$, $800\alpha_4$, and $2500\alpha_5$ keV (red line, Figure 2a). Subsequently, a monotonic Piecewise Cubic Hermite Interpolating Polynomial (PCHIP) is applied to the measured fluxes, and the proton fluxes in the energy ranges known to impact the respective electron channels are then retrieved and subtracted from the original measured electron fluxes (blue line, Figure 2b). The resulting fluxes represent the true electron fluxes in the respective energy bands (red line, Figure 2b). The importance of the correction of the proton flux

spectrum is demonstrated in Figures 9 and 10 in *Sandanger et al.* [2015]. It is also demonstrated in Figure 2b. The uncorrected proton fluxes will cause a systematic overestimation of the electron fluxes (green line). The PCHIP routine is similar to the interpolating method presented by *Asikainen and Mursula* [2011], but we use different correction factors for the proton degradation. Other studies attempting to remove the proton contamination have used slightly different approaches in terms of creating a differential proton spectrum. *Lam et al.* [2010] estimated the proton energy spectrum by fitting a series of piecewise exponential functions across each measured proton energy channel range combined with the bow tie method [*Selesnick and Blake,* 2000]. *Peck et al.* [2015] performed various fits to the spectral distribution: exponential, power law, single Maxwellian, and double Maxwellian. *Lam et al.* [2010] and *Peck et al.* [2015], however, did not account for the proton detector degradation. They will subsequently overestimate the resulting electron fluxes in the cases when the proton contamination is present. The degree of overestimation will depend on the degradation of the proton detectors and the proton fluxes measured.

4. Capturing the Relativistic Electrons >1 MeV With the MEPED Proton Telescopes

There is also contamination from relativistic electrons in the proton fluxes. The collimator magnets sweep aside the electrons less than ~1 MeV. Higher-energy electrons, however, will hit the detector and possibly be detected as protons in P1, P2, P3, or P6, while P4 and P5 have a small responsivity to relativistic electrons. At electron energies >1 MeV the P6 is highly sensitive to electrons and parity with the proton response is reached at ~2 MeV [*Yando et al*., 2011].

Previously, this feature has been applied in qualitative studies of relativistic electrons [*Miyoshi and Kataoka*, 2008; *Sandanger et al*., 2007, 2009; *Rodger et al*., 2010]. The geometric factors provided by *Yando et al.* [2011] enable a quantitative assessment of the fluxes. *Peck et al.* [2015] utilize the estimated geometric factors in a sophisticated proton correction routine and apply the geometric factors of differential energies consistent with Appendix B in *Yando et al.* [2011]. The differential energy spectra are estimated by fitting the measurements of P1–P5 to energy exponential, power law, single and double relativistic Maxwellian distributions, or a weighted combination of these. The respective spectral shapes are then extrapolated to higher energies. The discrepancies between the extrapolated fits and the fluxes measured in P6 are then assumed to be primarily relativistic electrons >1 MeV. The resulting MEPED electron fluxes are further applied in an in-flight comparison with electron fluxes measured by the IDP (Instrument for Detecting Particles) on DEMETER (Detection of Electromagnetic Emissions Transmitted from Earthquake Regions) spacecraft [*Sauvaud et al*., 2006]. The comparison shows that electron fluxes measured by MEPED are greater than electron fluxes measured by IDP, which *Peck et al.* [2015] attribute partially to differences in pitch angle range for the measurement on the two spacecraft. As previously mentioned, using uncalibrated proton spectra might also contribute to an overestimate of the electron fluxes measured by MEPED.

The routine by *Peck et al.* [2015] offers an estimate of >1 MeV fluxes continuously, only disrupted by solar proton events and the South Atlantic anomaly (SAA). We apply a somewhat simpler approach to avoid an overestimate of the relativistic electron fluxes. We use the fluxes reported in the P6 channel only when there are little or no protons detected in the P5 channel. We require the count rate in P5 to be less than 10% of the count rate in P6. This automatically excludes regions impacted by SPEs, geomagnetic storms accelerating protons to high energies, and the SAA. Further, we demand that the P6 channel fluxes are lower than the proton corrected E3 channel fluxes. The count rate in P6 is then assumed to be solely due to >1 MeV electrons.

Figure 3 shows the differential proton fluxes for P4 (800–2500 keV) and P5 (2500–6900 keV), the mixed proton and electron flux response in P6 (>6900 keV protons/> 1000 keV electrons), and the estimated pure relativistic electron response in P6 in a year of solar maximum (2003) and a year of solar minimum (2008). The P5 channel has in general low or no counts. This implies that we will have a reasonable continuous coverage of the >1000 keV radiation belt electrons throughout the solar cycle as shown in Figure 3 (fourth and eight panels). It is therefore possible to investigate their general impact upon the atmosphere. The extensive time coverage of the POES and MetOp satellites will enable a quantitative long-term study of the behavior of these high-energy electrons. For the year 2003 there are, however, multiple time periods of enhanced fluxes in the P5 channel. It is clear from Figure 3 (fourth panel) that these periods are efficiently eliminated by the applied criteria. Although radiation belt electrons generally will be accelerated in these geomagnetic storms, the intensity level cannot be retrieved from MEPED during periods of high fluxes of protons hitting the detectors.

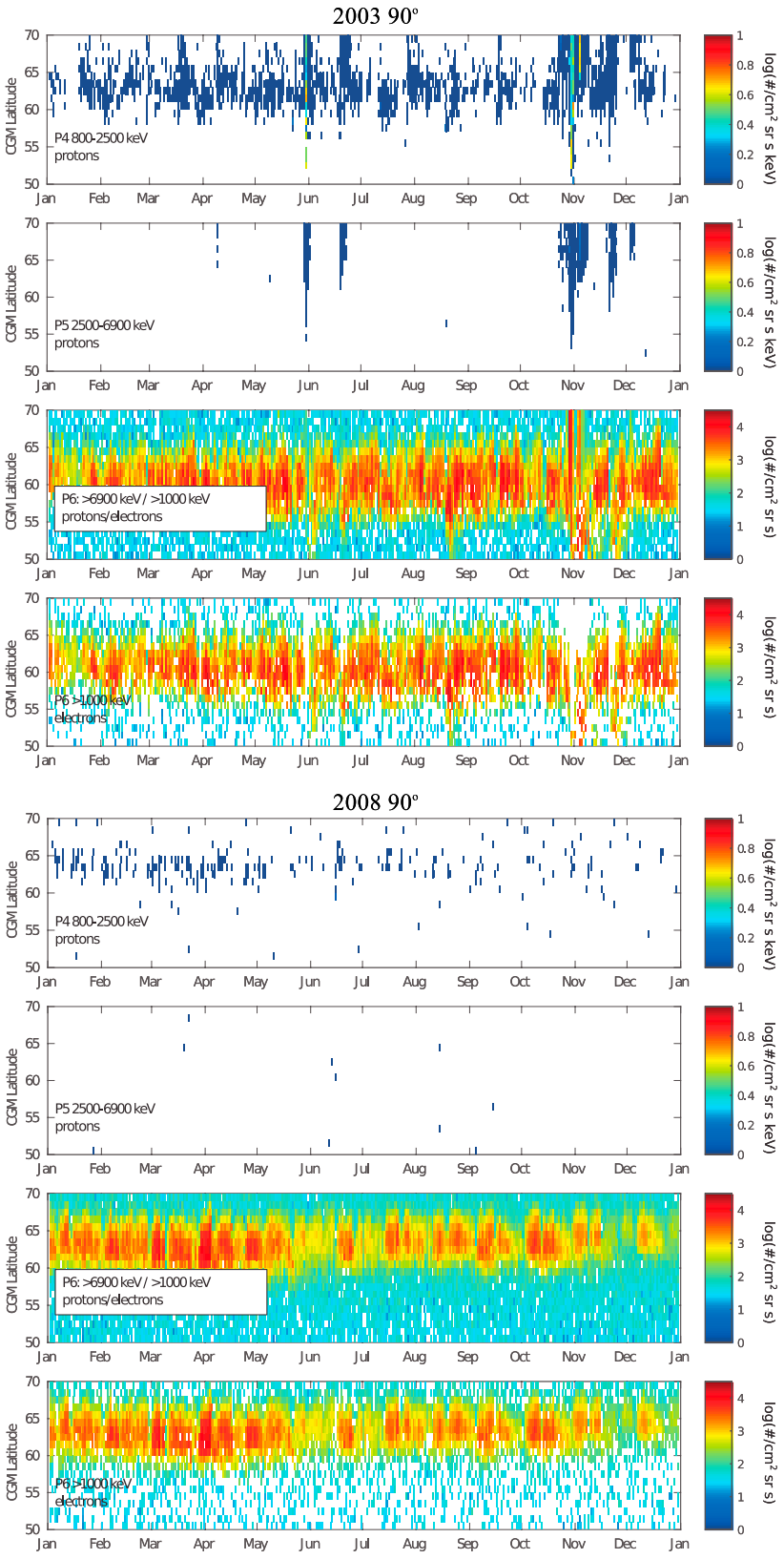
2003 90°
P4 800-2500 keV protons
P5 2500-6900 keV protons
P6: >6900 keV / >1000 keV protons/electrons
P6 >1000 keV electrons
2008 90°
P4 800-2500 keV protons
P5 2500-6900 keV protons
P6: >6900 keV / >1000 keV protons/electrons
P6 >1000 keV electrons
CGM Latitude
log(#/cm² sr s keV)
log(#/cm² sr s)
Jan Feb Mar Apr May Jun Jul Aug Sep Oct Nov Dec Jan

Figure 3

On the other hand, due to the nature of the electron acceleration processes, it is expected that they will be delayed in respect to the onset of the geomagnetic storms. It will therefore be possible to study their potential impact upon the atmosphere in the aftermath of even strong SPEs where high-energy electrons are clearly evident at latitudes down to about 50° (Corrected Geomagnetic) latitudes.

5. Determining the Level of Diffusion and the Loss Cone Pitch Angle Distribution

With the corrected and extended electron spectra, we can now determine the level of electron pitch angle anisotropy and diffusion using measurements from both the 0° and 90° telescopes in a combination with theoretically determined PADs. Taking into account the detector response for different PADs, the 0° and 90° fluxes are fitted onto the solution of the Fokker-Planck equation for wave-particle interactions [*Kennel and Petschek*, 1966]. Finally, we estimate the equivalent isotropic flux level over the bounce loss cone in order to give a more precise estimate of the energy deposition in the upper atmosphere.

5.1. Accounting for the Detector Geometry

Yando et al. [2011] provide geometric factors for the entire detector area given the simplifying assumption that the incident flux is isotropic. In most cases, except for very strong diffusion, the electron fluxes are anisotropic. This implies that the directional flux varies over the acceptance solid angle of the detector, see Figures 1a–1c for one case at high latitudes. The effective detector area also varies with the viewing angle through the collimator, see Figure 1d. The resulting detector count rate is derived by integrating the product over the solid angle of the detectors field of view. This is analogous to Figure 1b shown in *Li et al.* [2013] illustrating the geometry for calculating counting rates of the detector.

The offset between the direction of the telescopes and the magnetic field line where the PAD is centered varies over the orbit of the satellite. Hence, the detector sensitivity needs to be taken into account for different PADs and different pointing directions for the telescopes.

5.2. Quasi-Linear Theory of Wave-Particle Interaction

Pitch angle scattering by wave-particle interaction has received considerable attention from the very early stages of studying the dynamics of the radiation belt from both theoretical and experimental points of view. This effort resulted in the solution of the Fokker-Planck equation for particle diffusion and yields the following equilibrium equatorial PAD [*Kennel and Petschek*, 1966; *Theodoridis and Paolini*, 1967]:

$$j\left(E,\ D,\ \alpha_{\mathrm{eq}},\ B_{\mathrm{eq}},\ L\right) = N{\cdot}S(E)D^{-1}h\left(\alpha_{\mathrm{eq}}\right) \tag{1a}$$

$$j\left(E,\ D,\ \alpha_{\mathrm{eq}},\ B_{\mathrm{eq}},\ L\right) = N{\cdot}S(E)D^{-1}\left[h(\alpha_0) + \ln\left(\frac{\sin\alpha_{\mathrm{eq}}}{\sin\alpha_0}\right)\right] \tag{1b}$$

inside ($\alpha_{eq} \le \alpha_0$) and outside $\left(\alpha_0 \le \alpha_{eq} \le \frac{\pi}{2}\right)$ the loss cone, respectively, where

$$h\left(\alpha_{\mathrm{eq}}\right) \equiv \frac{\sqrt{DT}}{\alpha_0}\left[\frac{I_0\left(\frac{\alpha_{eq}}{\sqrt{DT}}\right)}{I_1\left(\frac{\alpha_0}{\sqrt{DT}}\right)}\right]$$

$j(E, D, \alpha_{\mathrm{eq}}, B_{\mathrm{eq}}, L)$ is the equatorial distribution for electrons of energy, E, diffusion coefficient D, and pitch angle, α_{eq}, at the equatorial point, B_{eq}. N is a normalizing constant. $S(E)$ is the particle injection source, assumed to be nonzero only at $\alpha_{\mathrm{eq}} = \frac{\pi}{2}$. The α_0 is the equatorial loss cone angle. T is the escape time of a particle that is inside the bounce loss cone. I_0 and I_1 are the modified Bessel functions of first kind. The diffusion coefficient is defined as

$$D \equiv \left|\cos\alpha_{\mathrm{eq}}\right| \frac{\Delta\alpha_{\mathrm{eq}}^2}{\delta t}$$

The above equations do not depend on the specific mechanism responsible for the pitch angle diffusion [*Theodoridis and Paolini*, 1967]. Their validity is, however, limited to steady state diffusion. Nevertheless, recent results by, e.g., *Li et al.* [2013, 2014a, 2014b] have validated the application of the Fokker-Planck

Figure 3. Pass-by-pass MEPED 90° detector P4, P5, and P6 fluxes binned in a uniform grid of CGM latitude and date of 1° and 1 day for 18–24 MLT for the years 2003 and 2008. Panels 1,2, 5 and 6 show P4 (800–2500 keV) and P5 (2500–6900 keV) differential fluxes multiplied with the respective energy band width. Panels 3 and 7 give the uncorrected P6 integral fluxes (>6900 keV protons/>1000 keV electron fluxes). Panels 4 and 8 give the estimated >1000 keV electron fluxes.

equations by analyzing conjunction events between the POES/MEPED electron observations and the chorus wave amplitudes measured by the Van Allen Probes during multiple geomagnetic storms with strong electron flux variation. *Kennel and Petschek* [1966] also pointed out that the shape of the PAD outside the loss cone is essentially independent of the magnitude of the diffusion coefficients as long as it is nonzero. At high latitudes the loss cone constitutes just a marginal part of the fluxes, so it is therefore not likely to affect the general PADs at short timescales.

Taking advantage of the relatively large loss cone at ~850 km compared to the equator, we transform the entire PAD from the equator to the satellite altitude and thereafter to the top of the atmosphere (~120 km) presuming that the pitch angles are redefined in terms of the magnetic field at any location by the first adiabatic invariant:

$$\frac{|v|\sin^2\alpha}{B} = \text{constant} \tag{2}$$

and assuming that $|v|$ is constant along the path. This assumption will not hold for low-energy electrons where the acceleration by parallel electric field needs to be taken into account, but it is approximately valid for the MEPED energy ranges > 50 keV. We then get

$$\sin^2\alpha = \sqrt{\frac{B}{B_{eq}}}$$

where B_{eq} is the magnetic flux density at the equator.

All the transformations of the PADs for different levels of diffusion strength, $\sqrt{DT} = \frac{1}{\chi}$, have been done in advance, creating an extensive library of look-up tables where the denominator changes in steps of 1 from 1 to 400 and thereafter in steps of 10 from 400 to 4000. They apply to all possible loss cone sizes and their respective PADs. All sets of PAD are made at equator, at satellite altitude, and at the top of the atmosphere (~120 km).

We estimate the loss cone size at the equator for all possible latitude and longitude positions of the satellite, by tracking along the magnetic field lines using the IGRF model. The result is an additional look-up table. When applying the routine to electron flux measurement at a specific location of the satellite (at one specific data point), we use this look-up table to find the specific loss cone size, which then is used to find the correct set of PADs in the library. When comparing the theoretical PADs with the measured particle fluxes the procedure is as follows:

1. Determine the pitch angles of center look directions of the 0° and 90° telescopes.
2. Calculate the ratio, $R_{O,}$ between of the fluxes detected by the 0° and 90° detector.
3. Calculate the ratio, R_T, between the fluxes of the two detectors for theoretical PADs using the procedure described in section 5.1. This is done for a dense set of PADs corresponding to different values of the diffusion strength, DT, using the relevant look-up table.
4. Determine which PAD gives the same ratio R_T as the observed ratio, R_O. This gives us the right diffusion level and the specific PAD of the observed particle fluxes is determined.

Finally, from the PAD at 120 km, we calculate the number of particles that crosses a unit horizontal area per second. We then find the equivalent isotropic flux which gives the same number of particles per second through the unit horizontal area, which we refer to as the equivalent isotropic flux level over the bounce loss cone. Each energy interval is treated separately as the level of diffusion will depend on the particle energy. A simplified summary of the steps of the procedure are illustrated in Figure 4.

6. The Electron Precipitating Fluxes During the HSSWS of February 2008

In order to check if our procedure leads to a realistic estimate of the precipitating electron fluxes, we investigate the OH response to a weak geomagnetic active period driven by HSSWS in the beginning of February 2008. The solar wind starts to increase around 12 UT of 31 January reaching 600 km/s around 15 UT on 1 February as shown in Figure 5. The elevated solar wind speed is sustained for almost 3 days accompanied with moderate *Ap* values of 17–19. The *AE* index does also show moderate deflection reaching a maximum level of approximately 900 nT. Based on the classification of geomagnetic storms by *Loewe and Prölss* [1997], this event qualifies as a weak geomagnetic storm as the *Dst* reaches two minimum values about −30 and −50 nT. The double structure is most likely due to the plateau seen in the solar wind speed in the same period.

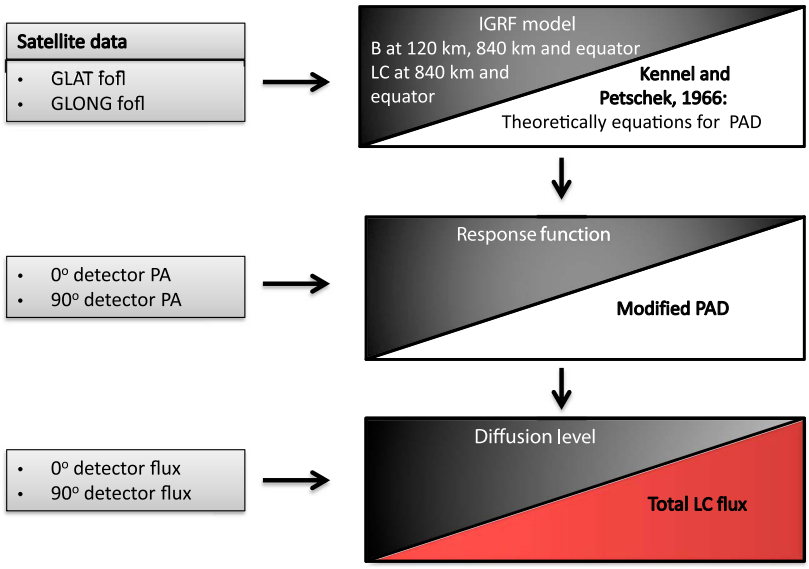

Figure 4. An overview of the procedure demonstrating the use of satellite data together with the IGRF model, theory of wave-particle interactions in the magnetosphere, and the angular response function of the detectors. The result is an estimate of the diffusion level and subsequently the total loss cone fluxes.

Figure 6 shows that the >50 keV trapped electron fluxes for 62°–64° CGM latitude measured by the 90° detector increases as the *Dst* decreases. The fluxes are still elevated at the end of the storm indicating that the storm causes enhancement of the radiation belt fluxes. A similar, but delayed response, is seen in the >100 keV, >300 keV, and >1000 keV trapped fluxes. This is in line with current theory suggesting that the acceleration processes associated with potential relativistic electrons in the radiation belt requires both a seed population and time [e.g., *Summers et al.*, 1998; *Horne et al.*, 2009]. The electron fluxes measured by the 0° detector, on the other hand, show an elevated, but more variable behavior more in line with the *AE* index. For the >50 keV fluxes the maxima reach almost the level of the trapped fluxes indicating strong pitch angle diffusion, but in general, the fluxes appear strongly anisotropic. At higher energies the ratios between the 90° and 0° fluxes indicate weaker pitch angle diffusion.

In the cases of strong anisotropy it is necessary to require a lower limit for the 0° electron fluxes. If the 0° detector report fluxes close to the noise level, we cannot determine its real value. This will overestimate the pitch angle diffusion strength and hence lead to an overestimation of the loss cone flux. Thus, we only infer the loss cone flux where the >50 keV and >100 keV fluxes measured by both 0° and 90° are sufficiently larger than the background level (~300 $cm^{-2}s^{-1}sr^{-1}$) and assume zero fluxes otherwise. This is more prudent compared to *Rodger et al.* [2013] which uses fluxes of 100 $cm^{-2}s^{-1}sr^{-1}$ as the lower limit, but weaker than the limit 500 $cm^{-2}s^{-1}sr^{-1}$ applied by *Li et al.* [2013]. In practice, this implies that our routine will be unfit to determine the medium electron energy drizzle into the atmosphere at the current spatial and temporal resolution. Assuming zero fluxes in these cases will therefore potentially underestimate of the precipitating fluxes prior to and after an event.

In 2008 NOAA/POES 18 share the same local time coverage as the Aura satellite which measures the OH density. This means that we can determine the precipitating fluxes close in both time and space to the Sun-synchronous polar orbiting Aura satellite. We utilize the OH observations measured by the Aura/MLS instrument. The data are version 3.3, level 2 nighttime (solar zenith angle $>100°$) and are screened according to the selection criteria by *Livesey et al.* [2013]. The OH concentration is given as parts per billion which we convert to number density by also utilizing the MLS temperature measurements.

The potential impact of particles on the OH production will be oriented in geomagnetic coordinates. Evaluating OH in a geomagnetic coordinate system will, however, impose a daily variation in OH. This is due to the offset between the two coordinate systems as several processes such as tides, planetary waves, photolysis, and other species interacting with OH, are better lined up in geographic coordinates. To avoid this diurnal variation in CGM coordinates, we use a daily running mean at the specific CGM latitude. The result is

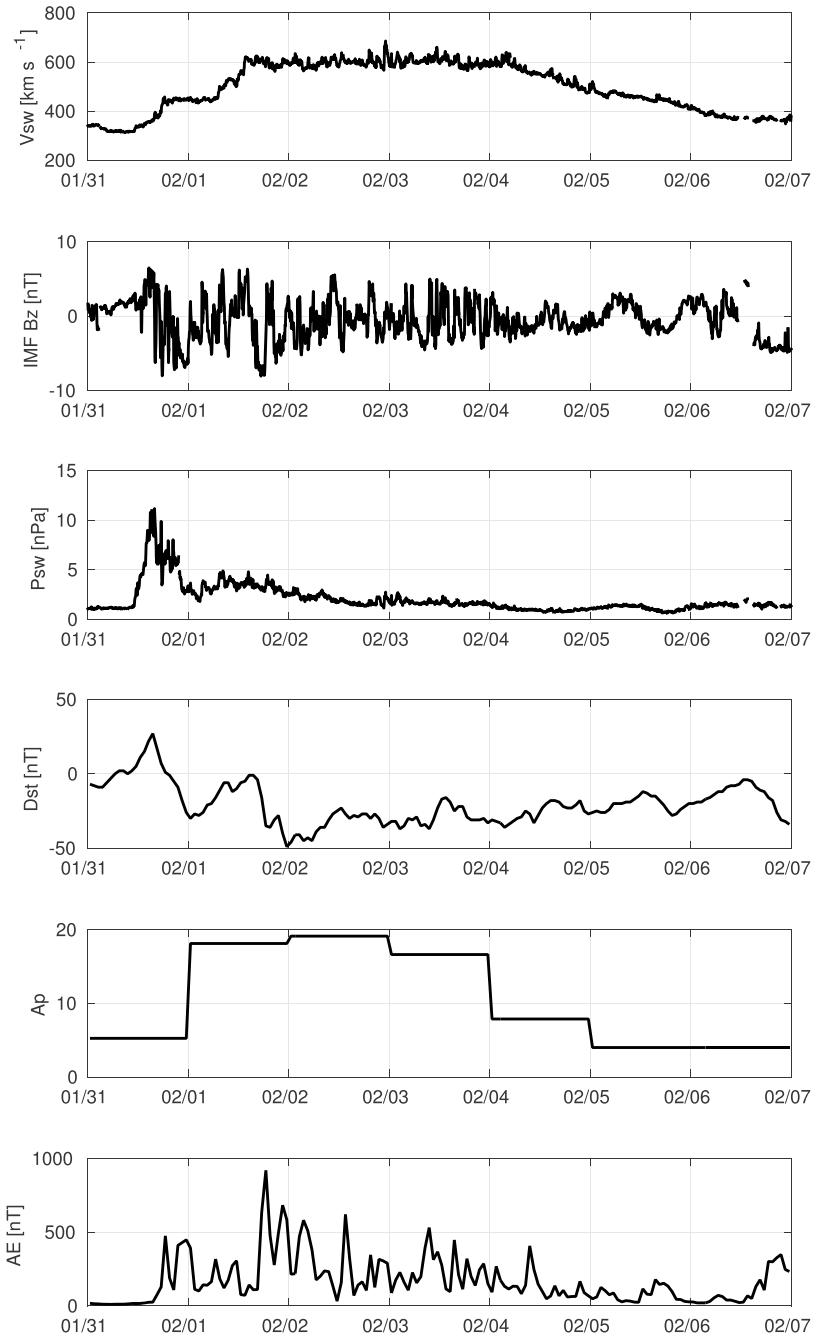

Figure 5. Solar wind conditions and geomagnetic indices on 31 January to 6 February 2008.

shown in Figure 7a for the altitude range 64–78 km. The altitude range is chosen based on the energy deposition during this event (see Figure 7b). Above 80 km there is not sufficient pressure to form water cluster ions needed in the EEP-HO_x production [*Solomon et al.*, 1981; *Sinnhuber et al.*, 2012].

The first geomagnetic quiet days illustrate a strong altitude gradient in the OH density. One of its key features of nighttime OH is the presence of an enhancement of OH in a narrow layer around 82 km [*Pickett et al.*, 2006]. It is linked to collisional quenching of vibrational excited OH that is caused by the reaction of ozone with atomic hydrogen [*Damiani et al.*, 2010]. In Figure 7a the OH density gradually decreases toward a local minimum around 75 km. Here the main source of OH is photolysis of water vapor by Lyman alpha. During winter

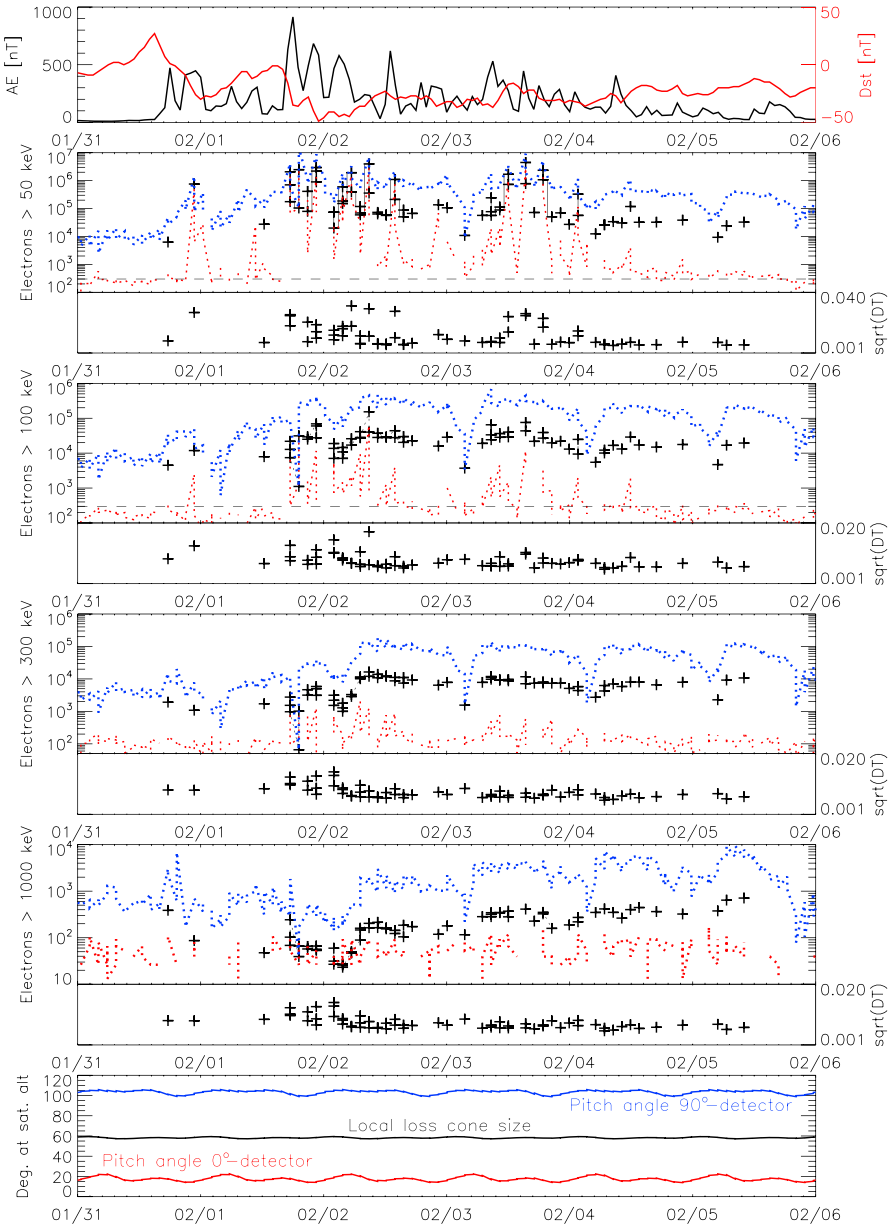

Figure 6. (first panel) *AE* (black) and *Dst* (red) from 31 January to 6 February 2008. (second to fifth panels) Electron fluxes >50, >100, >300, and >1000 keV measured by the 0° (red dotted line) and 90° (blue dotted line) detector on NOAA/POES 18 from 31 January to 6 February 2008 at 62–64 CGM latitude for nighttime conditions. The estimated equivalent isotropic fluxes in the loss cone and the associated diffusion strength, $\sqrt{DT}$, are marked as black crosses. The black dashed lines in the two uppermost electron flux panels illustrate the criteria applied for estimating the loss cone fluxes. (sixth panel) Loss cone size variability (black) and pitch angle pointing direction of the 0° (red) and 90° (blue) telescopes.

at high latitudes (~60°N/S) in the altitude range of 66–77 km, near the polar night terminator, however, the nearly grazing incidence of solar radiation makes the atmosphere optically thick leading to attenuation of this radiation. This will result in low background HOx production and a minimum in the background OH in this altitude range [*Marsh et al.*, 2001; *Sonnemann et al.*, 2006]. Similar features of a local OH minimum are also found by, e.g., *Damiani et al.* [2010].

Using the estimate of the equivalent isotropic flux level over the bounce loss cone, we can utilize the cosine-dependent IDH (Isotropic over the Downward Hemisphere) model of *Rees* [1989] to calculate the subsequent energy deposition as a function of altitude. This is based on a standard reference atmosphere (Committee on

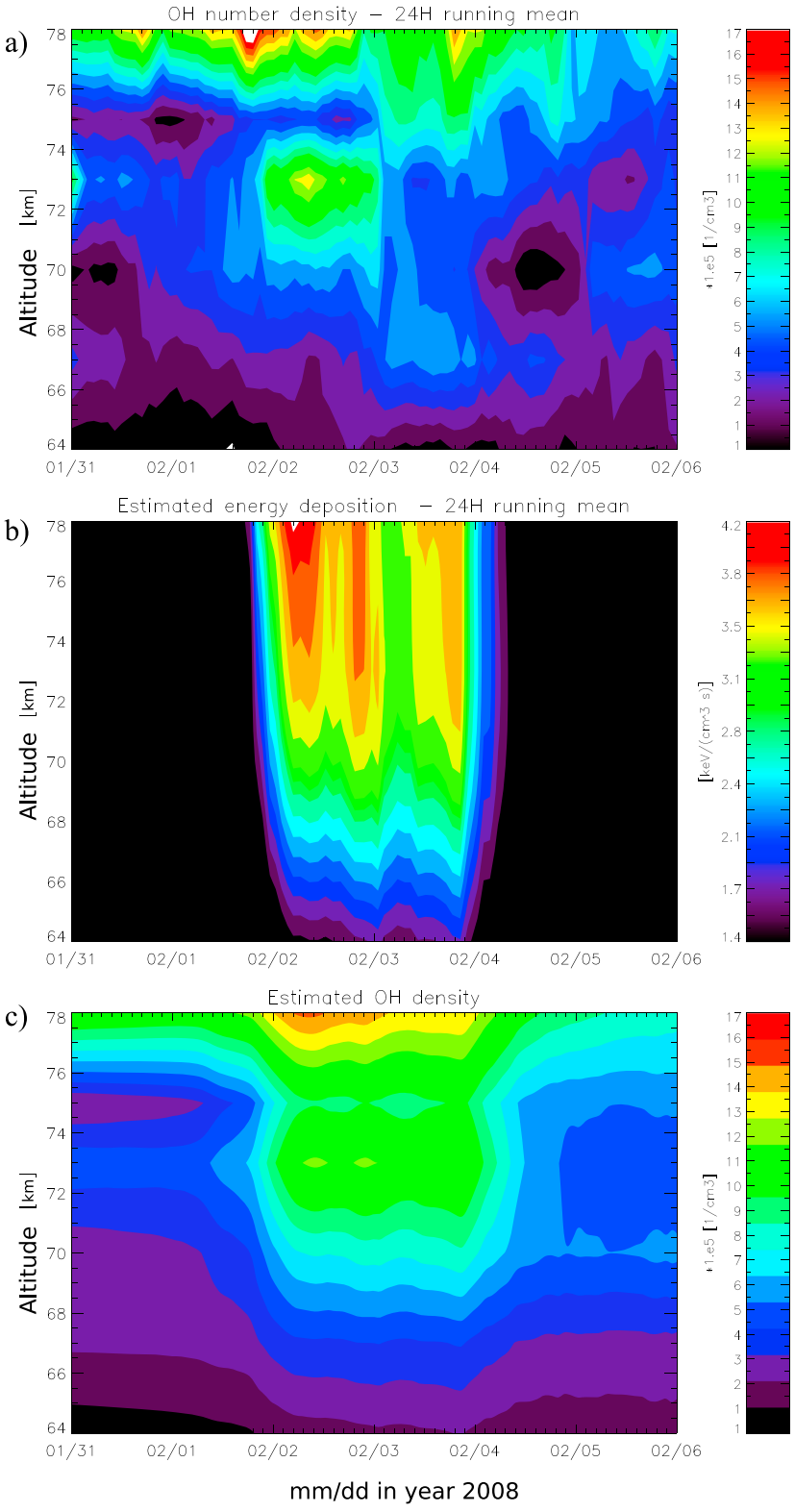

Figure 7. (a) The 24 h running mean of the nighttime OH measured by MLS AURA at 62°–64° CGM latitude at the Northern Hemisphere from 31 January to February 2008. For the same period, (b) the estimated energy deposition based on the loss cone flux method for MEPED electron measurement from NOAA/POES 18. (c) The energy deposition estimate is then used in a simple model to predict the expected OH density.

Space Research International Reference Atmosphere 1986). The result is shown in Figure 7b for a 24 h running mean. In Figure 7a we see that the OH density increase significantly beyond the background at all altitudes from 67 to 78 km around 12 UT on 1 February, maximizing around 10 UT on 2 February. At this point of time the OH density is elevated in the entire altitude interval from 64 km to 78 km. Both the time and altitude change are well aligned with the increased fluxes and the estimated energy deposition as function of altitude. The local extremes seen in the background OH are still visible, but the local minimum at 75 km altitude is less pronounced. The energy deposition also clearly displays a secondary maximum during 3 February. This is weaker but still distinctly evident also in OH. The elevated OH density between 64 and 68 km appears to have a stronger response to the energy deposition compared to the response above 70 km. Qualitatively, it is clear that the electron precipitation even during a weak geomagnetic storm can cause a measurable increase in OH also in the lower mesosphere, here down to about 64 km.

To quantitatively evaluate the impact of the electron fluxes, we apply a simple model making a rough approximation of the OH production and loss. We assume that the electron fluxes and the subsequent energy deposition are linearly changing between each passage (~100 min) with step size of 5 min. We adopt a height-dependent OH production rate based on the model results from the University of Bremen Ion Chemistry model (UBIC) shown in Figure 6 in *Sinnhuber et al.* [2012]. At 70 km and below we assume a production rate of 0.9 OH molecules per ion pair, while at 73, 75, and 78 km the production efficiency is reduced to 0.75, 0.65, and 0.4 OH per ion pair, respectively. We assume a height-dependent lifetime monotonously varying from 0.5 to 3 h in the altitude interval 64–78 km. The OH production from EEP and the subsequent loss is treated separately from the background OH. We assume a background OH concentration based on an average of 1 day prior and 1 day after the elevated electron fluxes requiring a smooth linear transition throughout the event. The result is shown in Figure 7c. It is evident that the estimated OH density is in the same order of size as the observed OH density. In particular, the first part of the event appears to be well in line with the OH estimate on all height levels. The later part of the event appears to overestimate the level of OH in the altitude region between 70 and 75 km. Considering the OH increase found below 70 km appear to be related to the energy deposition, we speculate if the lack of agreement between 70 and 75 km can be related to short-time changes in background level of OH such as gravity wave activity. The EEP-OH production efficiency may also depend on the level of atomic oxygen and water vapor [*Solomon et al.*, 1981], which will vary with the dynamics of the background atmosphere. All in all, considering a highly varying atmospheric background and the simplicity of our OH production model, we find it to be probable that our loss cone fluxes give a realistic estimate of the true precipitating electron fluxes. In contrast, applying just the 0° or the 90° detector fluxes will underestimate or overestimate the OH production by an order of magnitude (not shown).

7. Conclusion and Future Work

In order to achieve a realistic estimate of the precipitating electron fluxes, we apply the measurement from both the 0° and 90° telescopes on the MEPED detector. We correct for proton contamination in the electron counts, where the proton spectra have already been corrected due to detector degradation. We also account for the relativistic ($>$1000 keV) electrons contaminating the proton detector. This gives us full range coverage of electron energies that will be deposited in the middle atmosphere from 60 to 80 km. By combining the measurements from both telescopes with electron pitch angle distributions from theory of wave-particle interactions in the magnetosphere, a complete bounce loss cone flux is constructed for each of the electron energy channels $>$ 50 keV, $>$ 100 keV, $>$ 300 keV, and $>$ 1000 keV. The result should be considered with some caution as there will be times when the PADs deviates considerably from steady state diffusion.

Comparing the estimated fluxes and subsequent energy deposition to the OH density as measured by the MLS on board the Aura satellite during a weak geomagnetic storm, we substantiate that our method gives a realistic estimate of precipitating energetic electron fluxes. We find that the estimated fluxes both qualitatively and quantitatively are in line with the observed increase of HO_x during a weak geomagnetic storm. It should, however, be noted that this is not an infallible validation considering the assumptions of time variations, OH background, etc. Further validation of the method could be achieved with, for example, comparison with indirect measurements of the particle precipitation such as cosmic radio noise absorption measured by riometers. More work should also be done to achieve also a good estimate of the potential electron drizzle when the 0° detector measures close to the noise floor. In addition, assessment of the limitation and subsequent errors associated with the use of the IGRF model should be made for varying levels of geomagnetic activity.

Quantifying of the level of precipitating energetic electrons is essential in order to determine the level of EEP production of OH and NO in the middle atmospheric chemistry and hence its potential impact upon ozone, temperature, and dynamics. The presented method can be applied to all NOAA/POES and MetOp satellites and with their wide local time coverage the measurements could be combined to achieve a global estimate of the electron energy input in the atmosphere during periods of enhanced geomagnetic activity.

Acknowledgments
This study was supported by the Research Council of Norway under contracts 184701 and 223252/F50. The authors thank the NOAA's National Geophysical Data Center (NGDS) for providing NOAA data (http://satdat.ngdc.noaa.gov/) and WDC Geomagnetism, Kyoto, Japan, for *AE* and *Dst* indices (http://wdc.kugi.kyoto-u.ac.jp/wdc/Sec3.html); SPDF Goddard Space Flight Center for solar wind parameters (http://omniweb.gsfc.nasa.gov/); and NASA Goddard Earth Science Data and Information Services Center (GES DISC) for providing Aura/MLS data (http://mls.jpl.nasa.gov/).

References

Andersson, M. E., P. T. Verronen, S. Wang, C. J. Rodger, M. A. Clilverd, and B. R. Carson (2012), Precipitating radiation belt electrons and enhancements of mesospheric hydroxyl during 2004–2009, *J. Geophys. Res.*, *117*, D09304, doi:10.1029/2011JD017246.

Andersson, M. E., P. T. Verronen, C. J. Rodger, M. A. Clilverd, and A. Seppälä (2014a), Missing driver in the Sun–Earth connection from energetic electron precipitation impacts mesospheric ozone, *Nat. Commun.*, *5*(5197).

Andersson, M. E., P. T. Verronen, C. J. Rodger, M. A. Clilverd, and S. Wang (2014b), Longitudinal hotspots in the mesospheric OH variations due to energetic electron precipitation, *Atmos. Chem. Phys.*, *14*(2), 1095–1105.

Asikainen, T., and K. Mursula (2011), Recalibration of the long-term NOAA/MEPED energetic proton measurements, *J. Atmos. Sol. Terr. Phys.*, *73*, 335–347.

Asikainen, T., K. Mursula, and V. Maliniemi (2012), Correction of detector noise and recalibration of NOAA/MEPED energetic proton fluxes, *J. Geophys. Res.*, *117*, A09204, doi:10.1029/2012JA017593.

Baker, D. N., C. A. Barth, K. E. Mankoff, S. G. Kanekal, S. M. Bailey, G. M. Mason, and J. E. Mazur (2001), Relationships between precipitating auroral zone electrons and lower thermospheric nitric oxide densities: 1998–2000, *J. Geophys. Res.*, *106*(A11), 24,465–24,480, doi:10.1029/2001JA000078.

Barth, C. A., K. D. Mankoff, S. M. Bailey, and S. C. Solomon (2003), Global observations of nitric oxide in the thermosphere, *J. Geophys. Res.*, *108*(A1), 1027, doi:10.1029/2002JA009458.

Codrescu, M. V., T. J. Fuller-Rowell, R. G. Roble, and D. S. Evans (1997), Medium energy particle precipitation influences on the mesosphere and lower thermosphere, *J. Geophys. Res.*, *102*(A9), 19,977–19,987, doi:10.1029/97JA01728.

Daae, M., P. J. Espy, H. Nesse Tyssøy, D. Newnham, J. Stadsnes, and F. Søraas (2012), The effect of energetic electron precipitation on middle mesospheric night-time ozone during and after a moderate geomagnetic storm, *Geophys. Res. Lett.*, *39*, L21811, doi:10.1020/2012GL053787.

Damiani, A., M. Storini, M. L. Santee, and S. Wang (2010), Variability of the nighttime oh layer and mesospheric ozone at high latitudes during northern winter: Influence of meteorology, *Atmos. Chem. Phys.*, *10*(21), 10,291–10,303.

Evans, D. S., and M. S. Greer (2000), Polar orbiting environmental satellite space environment monitor-2: Instrument descriptions and archive data documentation, NOAA Tech. Memo., OAR SEC 93, 93, version 1.4, Boulder, Colo., 2004 Jan.

Galand, M., and D. S. Evans (2000), Radiation damage of the proton MEPED detector on POES (TIROS/NOAA) satellites, *NOAA Tech. Memo., OAR 456-SEC. 42*, Boulder, Colo.

Hendrickx, K., L. Megner, J. Gumbel, D. E. Siskind, Y. J. Orsolini, H. Nesse Tyssøy, and M. Hervig (2015), Observation of 27 day solar cycles in the production and mesospheric descent of EPP-produced NO, *J. Geophys. Res. Space Physics*, *120*, 8978–8988, doi:10.1002/2015JA021441.

Horne, R. B., M. M. Lam, and J. C. Green (2009), Energetic electron precipitation from the outer radiation belt during geomagnetic storms, *Geophys. Res. Lett.*, *36*, L19104, doi:10.1029/2009GL040236.

Kennel, C. F., and H. E. Petschek (1966), Limit on stably trapped particle fluxes, *J. Geophys. Res.*, *71*(1), 1–28, doi:10.1029/JZ071i001p00001.

Kirkwood, S., and A. Osepian (2001), Pitch angle diffusion coefficients and precipitating electron fluxes inferred from EISCAT radar measurements at auroral latitudes, *J. Geophys. Res.*, *106*(A4), 5565–5578, doi:10.1029/2000JA900143.

Lam, M. M., R. B. Horne, N. P. Meredith, S. A. Glauert, T. Moffat-Griffin, and J. C. Green (2010), Origin of energetic electron precipitation >30 keV into the atmosphere, *J. Geophys. Res.*, *115*, A00F08, doi:10.1029/2009JA014619.

Li, W., B. Ni, R. M. Thorne, J. Bortnik, J. C. Green, C. A. Kletzing, W. S. Kurth, and G. B. Hospodarsky (2013), Constructing the global distribution of chorus wave intensity using measurements of electrons by POES satellites and waves by the Van Allen Probes, *Geophys. Res. Lett.*, *40*, 4526–4532, doi:10.1002/grl.50920.

Li, W., et al. (2014a), Evidence of stronger pitch angle scattering loss caused by oblique whistler-mode waves as compared with quasi-parallel waves, *Geophys. Res. Lett.*, *41*, 6063–6070, doi:10.1002/2014GL061260.

Li, W., et al. (2014b), Quantifying hiss-driven energetic electron precipitation: A detailed conjunction event analysis, *Geophys. Res. Lett.*, *41*, 1085–1092, doi:10.1002/2013GL059132.

Livesey, N. J., et al. (2013), Earth Observing System (EOS) Aura Microwave Limb Sounder (MLS) version 3.3 and 3.4 level 2 data quality and description document, Jet Propul. Lab., Calif. Inst. of Technol., Pasadena, Calif.

Loewe, C. A., and G. W. Prölss (1997), Classification and mean behavior of magnetic storms, *J. Geophys. Res.*, *102*(A7), 14,209–14,213, doi:10.1029/96JA04020.

Marsh, D., A. K. Smith, G. Brasseur, M. Kaufmann, and K. Grossmann (2001), The existence of a tertiary ozone maximum in the high-latitude middle mesosphere, *Geophys. Res. Lett.*, *28*, 4531–4534, doi:10.1029/2001GL013791.

Meredith, N. P., R. B. Horne, M. M. Lam, M. H. Denton, J. E. Borovsky, and J. C. Green (2011), Energetic electron precipitation during high-speed solar wind stream driven storms, *J. Geophys. Res.*, *116*, A05223, doi:10.1029/2010JA016293.

Miyoshi, Y., and R. Kataoka (2008), Flux enhancement of the outer radiation belt electrons after the arrival of stream interaction regions, *J. Geophys. Res.*, *113*, A03S09, doi:10.1029/2007JA012506.

Newnham, D. A., P. J. Espy, M. A. Clilverd, C. J. Rogder, A. Seppälä, D. J. Maxfield, P. Hartogh, K. Holmen, and R. B. Horne (2011), Direct observations of nitric oxide produced by energetic electron precipitation in the Antarctic middle atmosphere, *Geophys. Res. Lett.*, *38*, L20104, doi:10.1029/2011GL049199.

Ødegaard, L.-K. G. (2013), Recalibration of the MEPED proton detectors onboard NOAA POES satellites, Master thesis in Space Physics, Department of Physics and Technology, Univ. of Bergen, Norway.

Ødegaard, L.-K., G. H. Nesse Tyssøy, M. I. Sandanger, J. Stadsnes, and F. Søraas (2016), Space Weather impact on the degradation of energetic proton detectors, *J. Space Weather Space Clim.*, doi:10.1051/swsc/2016020.

Peck, E. D., C. E. Randall, J. C. Green, J. V. Rodriguez, and C. J. Rodger (2015), POES MEPED differential flux retrievals and electron channel contamination correction, *J. Geophys. Res. Space Physics*, *120*, 4596–4612, doi:10.1002/2014JA020817.

Pickett, H. M., W. G. Read, K. K. Lee, and Y. L. Yung (2006), Observation of night OH in the mesosphere, *Geophys. Res. Lett.*, *33*, L19808, doi:10.1029/2006GL026910.

Rees, M. H. (1989), *Physics and Chemistry of the Upper Atmosphere*, Cambridge Univ. Press, Cambridge, U. K.

Rodger, C. J., M. A. Clilverd, J. C. Green, and M. M. Lam (2010), Use of POES SEM-2 observations to examine radiation belt dynamics and energetic electron precipitation into the atmosphere, *J. Geophys. Res.*, *115*, A04202, doi:10.1029/2008JA014023.

Rodger, C. J., A. J. Kavanagh, M. A. Clilverd, and S. R. Marple (2013), Comparison between POES energetic electron precipitation observations and riometer absorptions: Implications for determining true precipitation fluxes, *J. Geophys. Res. Space Physics*, *118*, 7810–7821, doi:10.1002/2013JA019439.

Rozanov, E., M. Calisto, T. Egorova, T. Peter, and W. Schmutz (2012), Influence of the precipitating energetic particles on atmospheric chemistry and climate, *Surv. Geophys.*, *33*, 483–501, doi:10.1007/s10712-012-9192-0.

Sætre, C., J. Stadsnes, H. Nesse, A. Aksnes, S. M. Petrinec, C. A. Barth, D. N. Baker, R. R. Vondrak, and N. Østgaard (2004), Energetic electron precipitation and the NO abundance in the upper atmosphere: A direct comparison during a geomagnetic storm, *J. Geophys. Res.*, *109*, A09302, doi:10.1029/2004JA010485.

Sætre, C., C. A. Barth, J. Stadsnes, N. Østgaard, S. M. Bailey, D. N. Baker, and J. W. Gjerloev (2006), Comparisons of electron energy deposition derived from observations of lower thermospheric nitric oxide and from X-ray bremsstrahlung measurements, *J. Geophys. Res.*, *111*, A04302, doi:10.1029/2005JA011391.

Sandanger, M. I., F. Søraas, M. Sørbø, K. Aarsnes, K. Oksavik, and D. S. Evans (2009), Relativistic electron losses related to EMIC waves during CIR and CME storms, *J. Atmos. Sol. Terr. Phys.*, *71*, 1126–1144.

Sandanger, M. I., L.-K. G. Ødegaard, H. Nesse Tyssøy, J. Stadsnes, F. Søraas, K. Oksavik, and K. Aarsnes (2015), In-flight calibration of NOAA POES proton detectors—Derivation of the MEPED correction factors, *J. Geophys. Res. Space Physics*, *120*, 9578–9593, doi:10.1002/2015JA021388.

Sandanger, M., F. Søraas, K. Aarsnes, K. Oksavik, and D. S. Evans (2007), Loss of relativistic electrons: Evidence for pitch angle scattering by electromagnetic ion cyclotron waves excited by unstable ring current protons, *J. Geophys. Res.*, *112*, A12213, doi:10.1029/2006JA012138.

Sauvaud, J., A. T. Moreau, R. Maggiolo, J.-P. Treilhou, C. Jacquey, A. Cros, J. Coutelier, J. Rouzaud, E. Penou, and M. Gangloff (2006), High-energy electron detection onboard DEMETER: The IDP spectrometer, description and first results on the inner belt, *Planet. Space Sci.*, *54*(5), 502–511, doi:10.1016/j.pss.2005.10.019.

Selesnick, R. S., and J. B. Blake (2000), On the source location of radiation belt relativistic electrons, *J. Geophys. Res.*, *105*(A2), 2607–2624, doi:10.1029/1999JA900445.

Sinnhuber, M., H. Nieder, and N. Wieters (2012), Energetic particle precipitation and the chemistry of the mesosphere/lower thermosphere, *Surv. Geophys.*, *33*, doi:10.1007/s10712-012-9201-3.

Solomon, S., D. Rusch, J. Gérard, G. Reid, and P. Crutzen (1981), The effect of particle precipitation events on the neutral and ion chemistry of the middle atmosphere: II. Odd hydrogen, *Planet. Space Sci.*, *29*(8), 885–893, doi:10.1016/0032-0633(81)90078-7.

Sonnemann, G. R., M. Grygalashvyly, P. Hartogh, and C. Jarchow (2006), Behavior of mesospheric ozone under nearly polar night conditions, *Adv. Space Res.*, *38*, 2402–2407, doi:10.1016/j.asr.2006.09.011.

Summers, D., R. M. Thorne, and F. Xiao (1998), Relativistic theory of wave-particle resonant diffusion with application to electron acceleration in the magnetosphere, *J. Geophys. Res.*, *103*(A9), 20,487–20,500, doi:10.1029/98JA01740.

Theodoridis, G. C., and F. R. Paolini (1967), Pitch angle diffusion of relativistic outer belt electrons, *Ann. Geophys.*, *23*, 375–381.

Turunen, E., P. T. Verronen, A. Seppälä, C. J. Rodger, M. A. Clilverd, J. Tamminen, C.-F. Enell, and T. Ulich (2009), Impact of different energies of precipitating particles on NO_x generation in the middle and upper atmosphere during geomagnetic storms, *JASTP*, *71*, 1176–1189, doi:10.1016/j.jastp.2008.07.005.

Yando, K., R. M. Millan, J. C. Green, and D. S. Evans (2011), A Monte Carlo simulation of the NOAA POES Medium Energy Proton and Electron Detector instrument, *J. Geophys. Res.*, *116*, A10231, doi:10.1029/2011JA016671.

Paper IV

Energetic electron precipitation in weak to moderate corotating interaction region-driven storms

Ødegaard, L.-K. G., H. Nesse Tyssøy, F. Søraas, J. Stadsnes, and M. I. Sandanger

Journal of Geophysical Research: Space Physics, *122* (2017). doi:10.1002/2016JA023096.

AGU PUBLICATIONS

JGR

Journal of Geophysical Research: Space Physics

RESEARCH ARTICLE
10.1002/2016JA023096

Key Points:
- Use a new and better estimation of loss cone flux to study energetic electron precipitation driven by CIRs
- A linear relationship is found between the energy input into the magnetosphere and precipitation of relativistic electrons
- Precipitation patterns vary in MLT and latitude, attributed to different wave-particle interactions and energy dependent drift periods

Correspondence to:
L.-K. G. Ødegaard,
linnkglesnes@gmail.com

Citation:
Ødegaard, L.-K. G., H. N. Tyssøy, F. Søraas, J. Stadsnes, and M. I. Sandanger (2017), Energetic electron precipitation in weak to moderate corotating interaction region-driven storms, *J. Geophys. Res. Space Physics*, *122*, 2900–2921, doi:10.1002/2016JA023096.

Received 21 JUN 2016
Accepted 14 FEB 2017
Accepted article online 18 FEB 2017
Published online 3 MAR 2017
Corrected 22 MAR 2017

This article was corrected on 22 MAR 2017. See the end of the full text for details.

Energetic electron precipitation in weak to moderate corotating interaction region-driven storms

Linn-Kristine Glesnes Ødegaard[1], Hilde Nesse Tyssøy[1], Finn Søraas[1], Johan Stadsnes[1], and Marit Irene Sandanger[1]

[1] Birkeland Centre for Space Science, Department of Physics and Technology, University of Bergen, Bergen, Norway

Abstract High-energy electron precipitation from the radiation belts can penetrate deep into the mesosphere and increase the production rate of NO_x and HO_x, which in turn will reduce ozone in catalytic processes. The mechanisms for acceleration and loss of electrons in the radiation belts are not fully understood, and most of the measurements of the precipitating flux into the atmosphere have been insufficient for estimating the loss cone flux. In the present study the electron flux measured by the NOAA POES Medium Energy Proton and Electron Detectors 0° and 90° detectors is combined together with theory of pitch angle diffusion by wave-particle interaction to quantify the electron flux lost below 120 km altitude. Using this method, 41 weak and moderate geomagnetic storms caused by corotating interaction regions during 2006–2010 are studied. The dependence of the energetic electron precipitation fluxes upon solar wind parameters and geomagnetic indices is investigated. Nine storms give increased precipitation of $> \sim 750$ keV electrons. Nineteen storms increase the precipitation of $> \sim 300$ keV electrons, but not the $> \sim 750$ keV population. Thirteen storms either do not change or deplete the fluxes at those energies. Storms that have an increase in the flux of electrons with energy $> \sim 300$ keV are characterized by an elevated solar wind velocity for a longer period compared to the storms that do not. Storms with increased precipitation of $> \sim 750$ keV flux are distinguished by higher-energy input from the solar wind quantified by the ε parameter and corresponding higher geomagnetic activity.

1. Introduction

Understanding acceleration and loss processes of the energetic electrons in the radiation belts has been a hot topic in recent years (see reviews by *Friedel et al.* [2002], *Millan and Thorne* [2007], *Millan and Baker* [2012], and references therein). The electron energies observed in the radiation belts are much higher than in the solar wind, which means that acceleration takes place inside the magnetosphere. There have been two main theories on how the acceleration to relativistic energies occurs. These are inward radial diffusion (Betatron acceleration) and local wave-particle acceleration [*Friedel et al.*, 2002]. Local wave-particle acceleration, with chorus mode electron cyclotron waves as the most important, has now been commonly accepted as the mechanism responsible for the acceleration to relativistic energies [*Kessel*, 2016]. Studies applying data from the Van Allen Radiation Belt Storm Probes have recently shed light on the question of where in the magnetosphere electrons are accelerated. *Reeves et al.* [2013] investigated a large geomagnetic storm where the Van Allen Probes data show strong evidence of local acceleration at $L \approx 4$ in the equatorial plane.

The electron flux in the outer radiation belt is highly variable and thought to be a result of the competition between acceleration and loss. Geomagnetic storms can both enhance and deplete the energetic electron flux in the radiation belts [*Reeves et al.*, 2003]. Fluxes are commonly seen to be depleted during the main phase of a storm (known as flux "dropout" or the "*Dst* effect"), and in the recovery phase fluxes can recover to prestorm levels, stay depleted or build up to exceed prestorm levels [*Reeves et al.*, 2003; *Meredith et al.*, 2011]. The flux dropout can be a combination of adiabatic and nonadiabatic effects as losses through the magnetopause and atmospheric precipitation [*Millan and Thorne*, 2007]. The drivers of the radiation belt response have not been fully revealed. Many have noted that higher solar wind velocity increases the probability of energetic electron buildup after a storm [e.g, *Kilpua et al.*, 2015], although *Reeves et al.* [2011] pointed out that the relationship is not a linear one.

Storms caused by coronal mass ejections (CMEs) and corotating interaction regions (CIRs) can both produce enhanced radiation belt fluxes. Occurrence rate of CMEs closely follow the solar cycle sunspot number,

while CIRs/high-speed solar wind streams (HSSWS) are more prominent in the declining and minimum phase [*Tsurutani et al.*, 2006a]. *Asikainen and Ruopsa* [2016] found that HSSWSs are more efficient in producing electron precipitation in the declining phase compared to the minimum phase, even though the occurrence of HSSWS is almost equally large in both time periods. CMEs were also, maybe surprisingly, found to be most efficient in producing energetic electron precipitation during the declining phase.

Radiation belt electrons can be scattered in pitch angle by plasma waves and consequently be lost to the atmosphere [e.g., *Tsurutani and Lakhina*, 1997; *Millan and Thorne*, 2007, and references therein]. Plasma waves are generated when there is an instability in the plasma, which redistributes free energy in the system, often associated with, e.g., a density gradient, temperature gradient, magnetic fluctuations, or pitch angle anisotropy in the plasma population. Plasma wave generation is naturally enhanced during disturbed geomagnetic conditions when energy is transferred from the solar wind into the magnetosphere, which strengthen convection of plasma and intensity of currents. During geomagnetic storm time particle precipitation is increased.

Precipitation of radiation belt energetic electrons is of interest to the atmospheric community [e.g., *Andersson et al.*, 2012, 2014a, 2014b; *Rodger et al.*, 2010a; *Rozanov et al.*, 2012; *Sinnhuber et al.*, 2012; *Seppälä et al.*, 2009, 2013; *Seppälä and Clilverd*, 2014; *Seppäla et al.*, 2015; *Turunen et al.*, 2009; *Zawedde et al.*, 2016]. Radiation belt electrons are energetic enough to penetrate deep into the mesosphere where their energy deposition increases the production rate of NO_x and HO_x, which in turn will reduce the ozone density in catalytic processes [*Sinnhuber et al.*, 2012]. During polar winter the precipitation effects can be long lived and potentially influence temperature and winds, causing dynamical signatures that can propagate all the way down to the surface [*Seppälä et al.*, 2009; *Sinnhuber et al.*, 2012]. Quantifying the energetic electron precipitation (EEP) fluxes and the subsequent atmospheric effects still remains an unsolved, important question. *Anderson et al.* [2015] show that small geomagnetic storms affect the radiation belt acceleration and loss in much the same way as large storms, comparing their results with the larger storms studied by *Reeves et al.* [2003]. Several studies indicate that also small and frequently occurring storms associated with HSSWS significantly impact NO_x and HO_x production rates in the mesosphere [*Andersson et al.*, 2012; *Daae et al.*, 2012; *Andersson et al.*, 2014a, 2014b; *Zawedde et al.*, 2016].

EEP in relation to geomagnetic storms has been the focus of many recent studies [e.g., *Asikainen and Ruopsa*, 2016; *Blum et al.*, 2015; *Clilverd et al.*, 2010; *Kavanagh et al.*, 2012; *Meredith et al.*, 2011; *Rodger et al.*, 2010a, 2010b, 2015]. However, all studies have different approaches to quantifying the precipitated electron flux. An electron is precipitated when it is lost to the atmosphere by collisions with atmospheric particles. This process takes place over a range of altitudes as the atmosphere gets denser, but it is custom to use 100–120 km as a boundary below which most particles are considered to give up their energy.

Currently, the best alternative for measuring particles in the atmospheric loss cone is the National Oceanic and Atmospheric Administration (NOAA) Polar Orbiting Environmental Satellites (POES), covering a large range of magnetic local times (MLT) at 800–850 km. The almost identical Medium Energy Proton and Electron Detectors (MEPED) flown on POES constitutes probably the longest running continuous measurements of energetic electrons and protons to date, with a wide range of energies sampled. The two electron telescopes flown on each satellite see only a limited range of pitch angles as they go along the satellite track [*Evans and Greer*, 2000]. At high latitudes, the 0° detector, which points radially outward, will measure mostly particles near the center of the atmospheric loss cone, while the 90° detector (mounted approximately 90° away from the first detector) measures a mix of trapped and precipitating particles [*Rodger et al.*, 2010a, 2010c; *Nesse Tyssøy et al.*, 2016]. Studies utilizing only one of the telescopes [e.g., *Meredith et al.*, 2011] will underestimate (0°) or overestimate (90°) the total precipitated flux in any given location. *Rodger et al.* [2013] and *Asikainen and Ruopsa* [2016] used the geometric mean between the count rates of the two telescopes. *Rodger et al.* [2013] found that the geometric mean of > 30 keV electron fluxes was in agreement with riometer absorption observations when the flux was $> 10^6$ (cm^{-2} s^{-1} sr^{-1}), but that the geometric mean fluxes underestimated absorption when fluxes were $< 10^6$. Using only riometer observations gives no energy resolution, only the integral flux of electrons with energy $E > 30$ keV assuming a specific spectral form [e.g., *Kavanagh et al.*, 2012]. Other satellites in low polar orbit (e.g., Solar Anomalous and Magnetospheric Particle Explorer, or SAMPEX) have a poor coverage of the loss cone [*Blum et al.*, 2015].

In the present study we utilize a physics-based technique which quantifies the electron flux lost below 120 km altitude from the two NOAA POES MEPED detectors [*Nesse Tyssøy et al.*, 2016]. The method estimates the

atmospheric loss cone size for all locations on Earth (above ±40° latitude) and combines the measurements from MEPED 0° and 90° detectors together with theoretical pitch angle distributions from wave-particle interactions [*Kennel and Petschek*, 1966; *Theodoridis and Paolini*, 1967] to determine the total precipitated flux at 120 km. This offers a new and optimized method to study radiation belt losses to the atmosphere, especially in geomagnetic disturbances caused by HSSWS/CIRs, which are known to have a weak geomagnetic signature [*Tsurutani et al.*, 2006a], and often weaker diffusion. In these cases, the MEPED 0° detector may register only a few counts near the center of the loss cone, whereas there may still be significant fluxes if the whole bounce loss cone is considered.

We identify 41 isolated events and perform a superposed epoch analysis. The events are sorted into groups according to their increase or decrease in precipitating fluxes with energy larger than approximately 300 keV and 750 keV poststorm compared to prestorm. We examine their relationship to geomagnetic indices and solar wind parameters. Last, we investigate one of the features that appears to stand out in the group of enhanced high-energy fluxes, namely the flux dependence on the energy input to the magnetosphere from the solar wind, quantified using the *Akasofu* [1981] epsilon parameter (ϵ) (given in SI units by *Koskinen* [2002]). The goal is to be able to determine which storms are likely to cause increased precipitation of high-energy electrons and to single out the potential parameters to be used in a future parametrization of EEP.

2. Data and Methods

The MEPED electron detectors suffer from contamination from protons [*Evans and Greer*, 2000; *Yando et al.*, 2011; *Green*, 2013]. In addition, the geometric factor for the detectors varies with energy [*Yando et al.*, 2011; *Green*, 2013]. The nominal energy boundary of the lowest electron channel (E1) is 30 keV. *Yando et al.* [2011] found that the geometric factor for 30 keV was 2×10^{-3} cm^2 sr, only 20% of the 1×10^{-2} cm^2 sr given in the Instrument Description [*Evans and Greer*, 2000; *Green*, 2013]. *Green* [2013] used a wide range of input spectrum shapes to deduce the appropriate geometric factor, energy value, and flux conversion that works best regardless of the spectrum. However, the energy values they provided were different if a power law spectrum or an exponential spectrum was used. We have done an analysis which is somewhat similar to *Green* [2013], giving a more consistent result independent of the spectrum shape. The method is outlined in Appendix A. The new geometric factors are given in Table A1, together with the new, optimized lower energy threshold for each of the electron channels.

The proton measurements from MEPED are corrected for degradation using results obtained by *Sandanger et al.* [2015], *Ødegaard et al.* [2016], and *Ødegaard* [2016], before being used to remove the proton contamination from the electron measurements. The contaminating proton energies for E1, E2, and E3 are > 210 keV, > 280 keV, and > 440 keV, respectively [*Evans and Greer*, 2000; *Yando et al.*, 2011]. From the corrected and interpolated proton spectrum, the flux of protons at these energies can be retrieved and subsequently subtracted from the electron flux.

The method of using the proton telescope to estimate the contaminating fluxes in the electron telescope is an approximation, since there will be statistical differences of the actual proton flux in the two telescopes. However, in most of our storms the proton flux is orders of magnitude smaller than the electron flux. When the estimated contaminating flux is larger than 50% of the total (uncorrected) flux measured in the electron detector, we discard the data. On average, 2–3% of the data is removed in each channel from the 90° detector and 4–7% from the 0° detector in each storm. Most of the data removed are between 60 and 70° geomagnetic latitude, and more data are removed in the dusk sector than the rest of the hemisphere. There is generally more proton contamination in E1 and E2 than in E3, especially in the 0° detector. Care should always be taken when using the MEPED electron data, especially during periods of high proton fluxes (e.g., during CMEs).

Due to the response of relativistic electrons in the highest proton channel (P6) of the MEPED instrument, we are able to construct a fourth electron channel measuring higher-energy electrons, as described in *Nesse Tyssøy et al.* [2016]. Together with the P6 electron measurements, we have an integral spectrum of electron fluxes at energies > 43 keV, > 114 keV, > 292 keV, and > 756 keV (see Table A1). For simplicity, we refer to the MEPED channels as E1, E2, E3, and P6, which is common when using the MEPED data. In this work, we study the fluxes in each energy channel separately.

Lastly, we use the technique described in *Nesse Tyssøy et al.* [2016] to construct the local atmospheric Bounce Loss Cone (BLC) fluxes from the electron fluxes measured by the 0° and 90° detectors, in all four energy

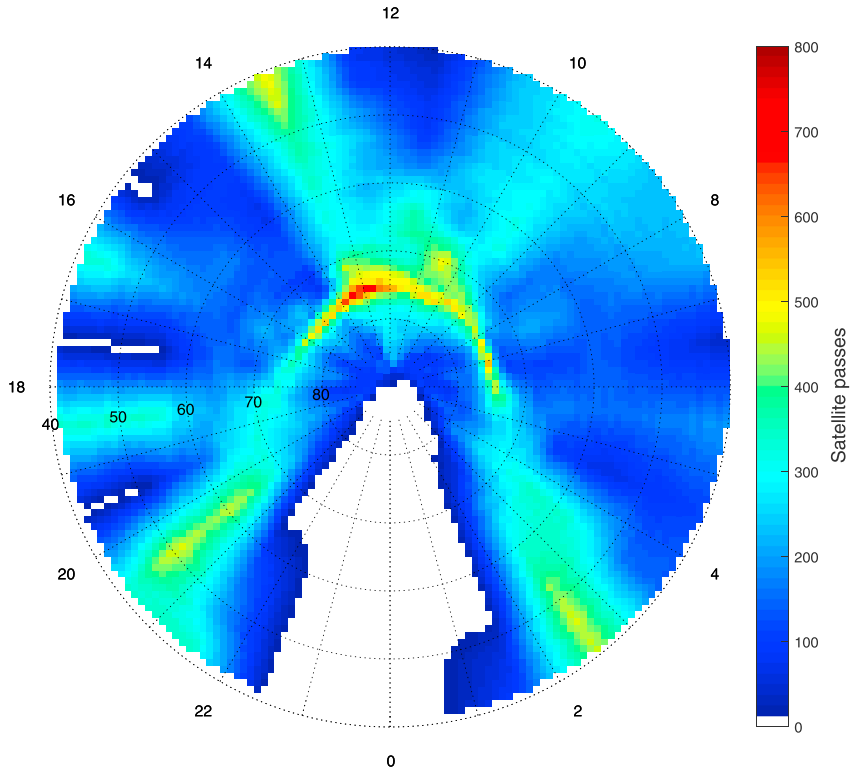

Figure 1. The total number of times a satellite entered a box of size 1 h MLT and 1° corrected geomagnetic latitude during 41 storms.

channels. For full details concerning the method of obtaining BLC fluxes, we refer the reader to *Nesse Tyssøy et al.* [2016]. When the 0° detector is measuring fluxes close to the noise level of the instrument, the uncertainty in the estimated BLC fluxes will increase. *Nesse Tyssøy et al.* [2016] therefore caution against using the estimated BLC fluxes during very quiet times. In this study we have not applied any filter on low fluxes but keep in mind this advice when we interpret our findings.

We use all available POES satellites throughout a storm and data from the Northern Hemisphere. The data are binned in 1 h MLT versus 1° corrected geomagnetic (CGM) latitude boxes and averaged in 2 h intervals. The hemispheric coverage varies from storm to storm, depending on year and how many NOAA POES satellites are in operation at the time. None of the satellites' orbits cross near 24 MLT in the Northern Hemisphere, which results in limited coverage between 22 MLT and 2 MLT. The remaining MLTs are well represented, as shown in Figure 1. For the epoch analyses we split the hemisphere into four MLT sectors and study the time evolution of the average flux in each sector. These are 2–6, 6–12, 12–18, and 18–22 MLT.

The field of view of the 90° telescope relative to the BLC varies over the satellite orbit. At 55°–68° invariant latitude the 90° telescope will mainly measure not only trapped particles but also particles inside the Drift Loss Cone. Most of the time the trapped population is orders of magnitude higher than the precipitated one [*Rodger et al.*, 2010c]. For a given L shell in this region, when averaged over all geographic longitudes, the stably trapped particle fluxes will tend to dominate the average fluxes. We henceforth consider these average fluxes (measured by the 90° telescope) as the trapped fluxes. With this precaution, we will therefore use, similar to, e.g., *Horne et al.* [2009] and *Meredith et al.* [2011], the 90° flux as a qualitative proxy for how the trapped fluxes in the radiation belts behave and contrast these with the precipitating BLC fluxes.

We focus on geomagnetic disturbances created by HSSWS and typical CIR signatures which originate from solar coronal holes. A CIR can be identified in the solar wind velocity as a change from a slow speed (approximately 300–400 km/s) to a high speed (approximately 600–800 km/s) over the course of 1–2 days. Ahead of the solar wind velocity increase there is a region with compressed magnetic field, where the corotating high-speed solar wind interacts with the preceding slow solar wind [*Richardson*, 2006]. The compression

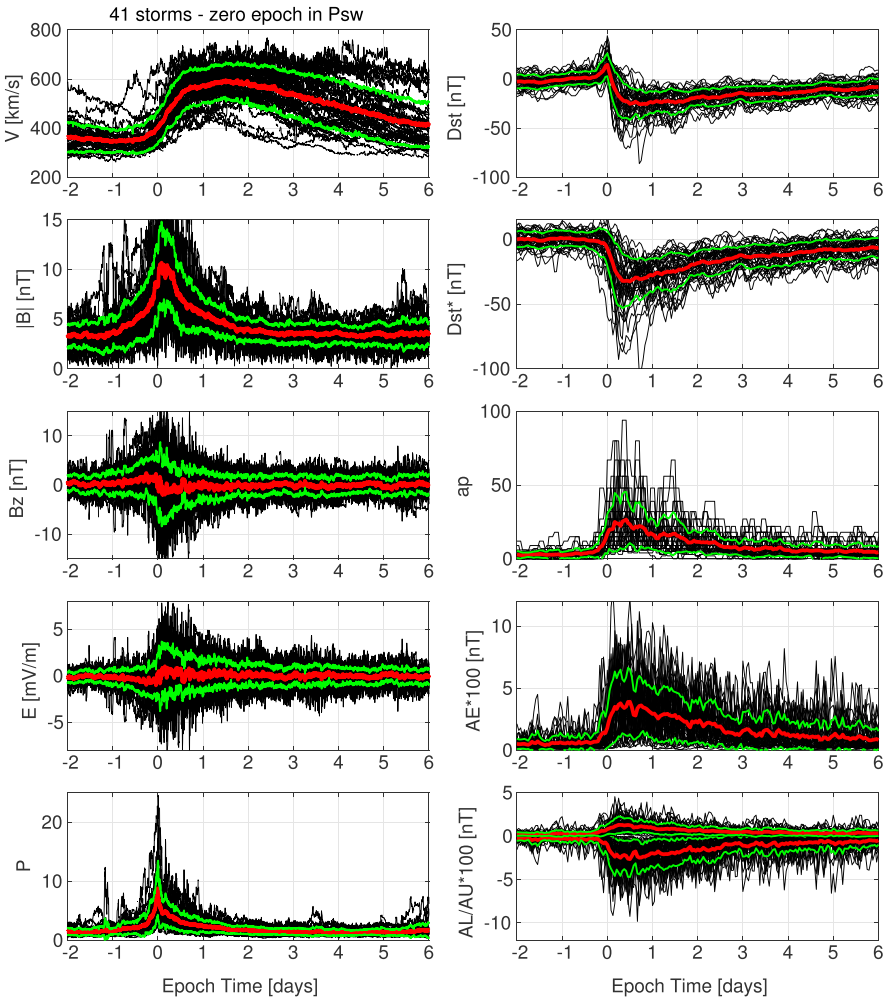

Figure 2. Superposed epoch analysis of 41 CIR/HSSWS storms from 2006 to 2010. (left column) Five-minute OMNI data are plotted for the solar wind measurements. (right column) One-hour resolution geomagnetic indices are plotted (3 h for *ap*). The mean is plotted in thick red lines, with the standard deviation of the data given as green lines. The timing of zero is described in the text in section 2 and listed in Table B1.

is also seen in the solar wind plasma density and pressure [*Tsurutani et al.*, 2006b]. Due to the pressure enhancement, CIR storms will often display a positive gradient in the *Dst* index before the start of the storm, although not as abrupt as the CME storm sudden commencement [*Borovsky and Denton*, 2006; *Tsurutani et al.*, 2006b].

To ensure that an identified CIR was geoeffective, we visually inspected the 1-hourly *Dst* index for typical storm signatures and checked it against a published online catalogue of coronal holes (http://www.solen.info/solar/coronal_holes.html). No criterion was put on the size of the storms with respect to the *Dst* index, but the conditions 2 days prior to the main phase of the event should be quiet (average $Dst > -20$ nT). We focus on the years 2006–2010 which are in the declining and minimum phase of the solar cycle, where CIRs dominate the geomagnetic activity. When we excluded the few periods of coronal mass ejections [*Richardson and Cane*, 2010], we were left with a selection of 41 weak to moderate events, listed in Table B1. Many would not be classified as geomagnetic storms by usual criteria [e.g., *Gonzalez et al.*, 1994]; 12 events have -20 nT $\geq$ minimum $Dst > -30$ nT, 21 events have -30 nT $\geq$ minimum $Dst \geq -50$ nT, and 8 have minimum $Dst < -50$ nT.

We use the solar wind pressure pulse arrival at the bow shock nose (from the OMNI database) as the zero epoch in our analyses, characterized by the maximum pressure. We use solar wind data with a 5 min cadence. When the solar wind pressure data are ambiguous, we select the time when the main phase of the storm starts

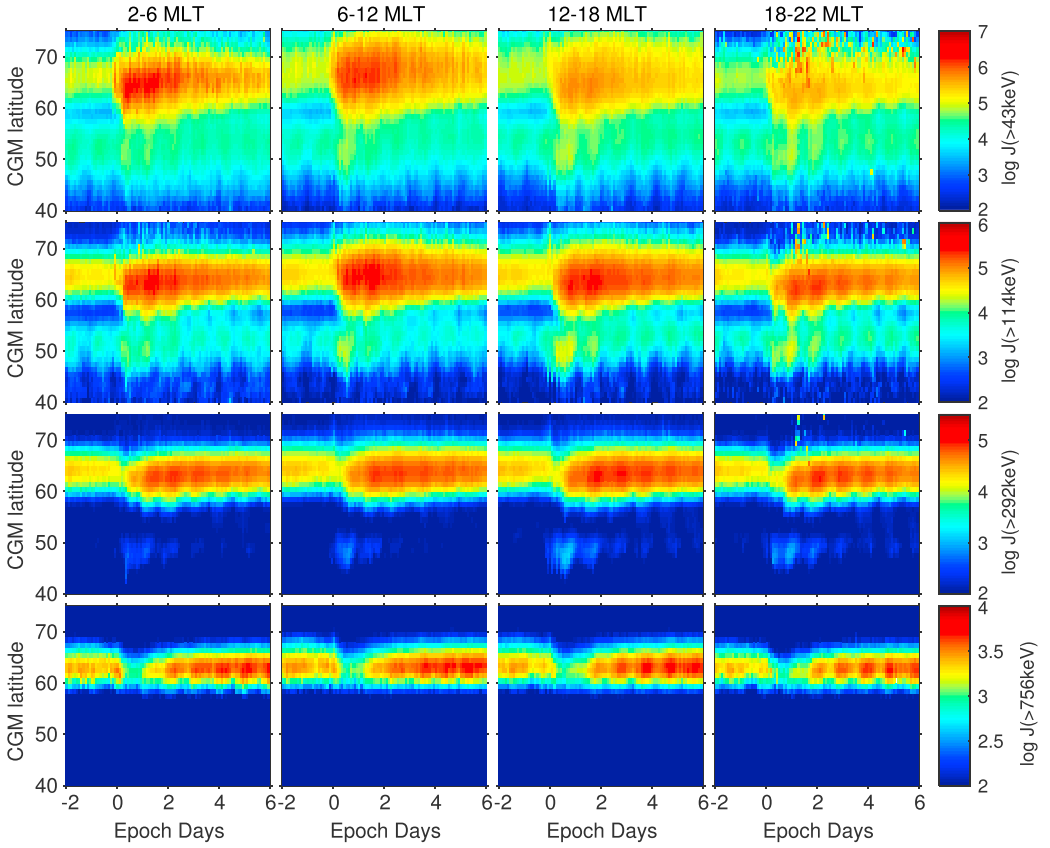

Figure 3. Superposed epoch analysis of 41 CIR/HSSWS storms from 2006 to 2010, measurements from the 90° detector of the MEPED instrument. All available NOAA POES satellites were used, and the data were binned in a 1° CGM latitude versus 2 h grid. The fluxes are plotted in logarithmic color scale (in units of integral flux [cm^{-2} s^{-1} sr^{-1}]) and the data are divided into the four sectors (from left to right) 0–6 MLT, 6–12 MLT, 12–18 MLT, and 18–24 MLT. (top to bottom) E1, E2, E3, and P6 flux are shown. Note that the range of the colorbar is different for the four channels.

in the *Dst* index. This is found by identifying the timing of the maximum value in the *Dst* index preceding the *Dst* minimum reached at the peak of the storm.

For the total epoch length we use 2 days prior to zero epoch and 6 days after the zero epoch, 8 days in total. The exact timing used for zero epoch in each storm is listed in Table B1.

3. Superposed Epoch Analysis

The solar wind data for all 41 events are plotted in Figure 2 with a 5 min resolution and the geomagnetic indices with an hourly resolution (except for *ap*, which has a 3 h resolution). The mean of all events is plotted in red with the standard deviation of the data given in green. Individual storms are plotted in black. The pressure corrected *Dst* index, *Dst**, is calculated as

$$Dst^* = Dst - (15.8 * P^{0.5}) + 20 \quad (1)$$

where P is the solar wind pressure with a 1 h resolution [*Burton et al.*, 1975].

The average event is small with a minimum *Dst* of −25 nT in the main phase, which is reached about 12 h after zero epoch. The average prestorm conditions are quiet with northward interplanetary magnetic field (IMF $B_Z > 0$) and slow solar wind velocity $V_{SW} \sim 350$ km/s. The solar wind velocity starts to increase about 6 h before zero epoch and reaches a plateau of maximum ~ 600 km/s at 18–48 h. The IMF B_Z turns southward right before zero epoch and is predominantly southward for approximately 12 h. IMF B_Z oscillates rapidly, seen as a widening of the envelope of B_Z in Figure 2. There is an increase in the IMF |B| from about −1 day to about 2 days after zero, which is typical for CIR storms. The *AL* index is stronger than the *AU* index, also a typical feature of CIR or HSSWS storms [*Tsurutani et al.*, 2006a]. The mean *Dst* and *Dst** indices do not recover fully in

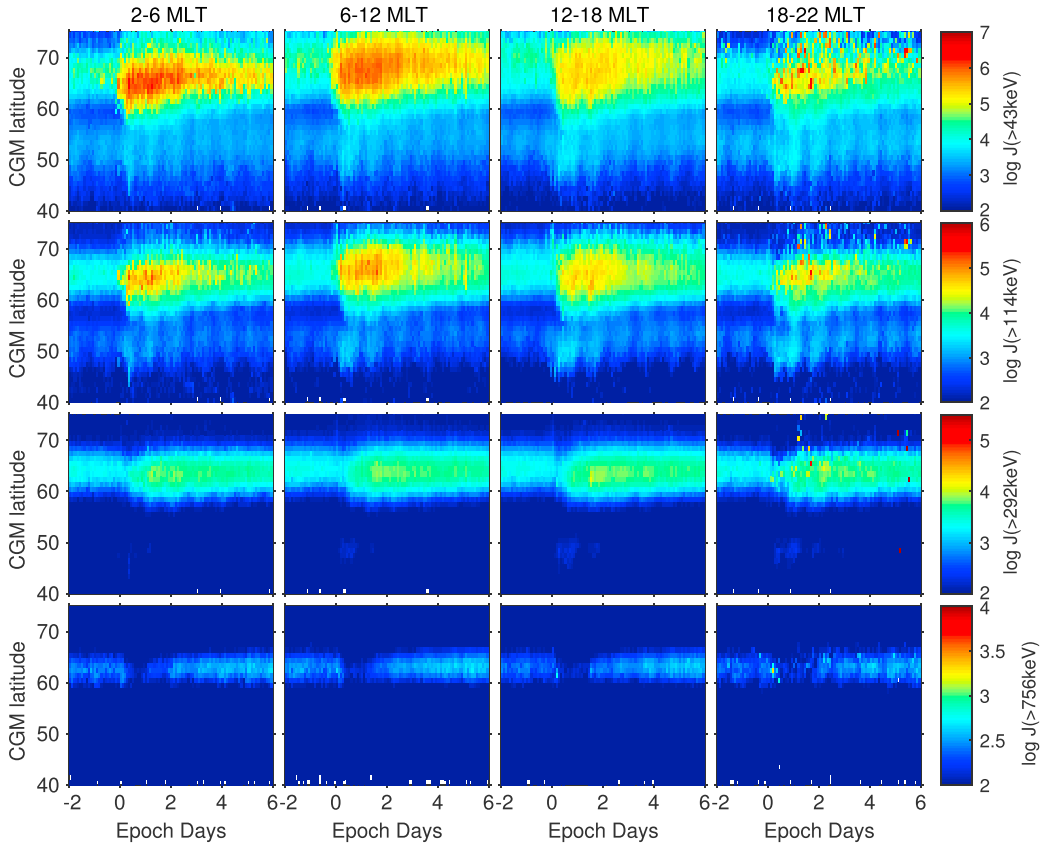

Figure 4. Same as Figure 3 but for the BLC fluxes. The color scale is logarithmic in units of integral flux (cm^{-2} s^{-1} sr^{-1}).

the 6 days after zero epoch. Recovery phases for CIR storms can last from days to many weeks [*Tsurutani et al.*, 2006a]. This is because new particles are injected in the ring current and also in the recovery phase of such storms [*Søraas et al.*, 2004].

Figure 3 shows the mean behavior of the trapped radiation belt fluxes in the 41 events as a function of time and geomagnetic latitude. The four MLT sectors are plotted from left to right, and the four energy channels from top to bottom in ascending order. The color scale is logarithmic and different for each energy channel. The standard deviation of the mean is found to be around 1 order of magnitude smaller than the mean (not shown). The specific value of the standard deviation varies with latitude and is generally largest at the latitudinal boundaries of the region of enhanced flux and smallest at latitudes near the maximum flux (CGM latitude ~60°–70°). The standard deviation of the mean is also higher in the 18–22 MLT sector high-latitude region, due to the poorer satellite coverage as well as a smaller data set due to proton contamination.

We see both the inner (~45°–55° CGM) and outer radiation belt (~60°–75°) in the two lowest energy channels. The inner belt is present also before the storm. There is a hint of electrons in the E3 channel during the main phase of the storm in the inner belt, but generally the high-energy electrons are concentrated in the outer belt.

The E1 trapped fluxes are enhanced abruptly around zero epoch, first seen at CGM latitudes near 65° in the 2–6 and 18–22 MLT sectors, and somewhat higher latitudes in the 6–12 and 12–18 MLT sectors. In the 12–18 and 18–22 MLT sectors, the maximum flux is lower compared to the 2–6 and 6–12 MLT sectors. Most probably, this feature is created by the direction of electron drift path around the Earth, causing some of the particles to be lost before they can complete the full drift path. *Lam et al.* [2010] show that precipitation measured in the E1 channel of the electron MEPED detector is correlated with chorus waves, causing a higher loss of particles between 22 and 12 MLT compared to between 12 and 22 MLT. *Summers et al.* [2007] give a detailed overview of how each wave mode (chorus, hiss, and electromagnetic ion cyclotron (EMIC)) contribute to the total electron loss rate depending on MLT, energy, and L shell of the electron.

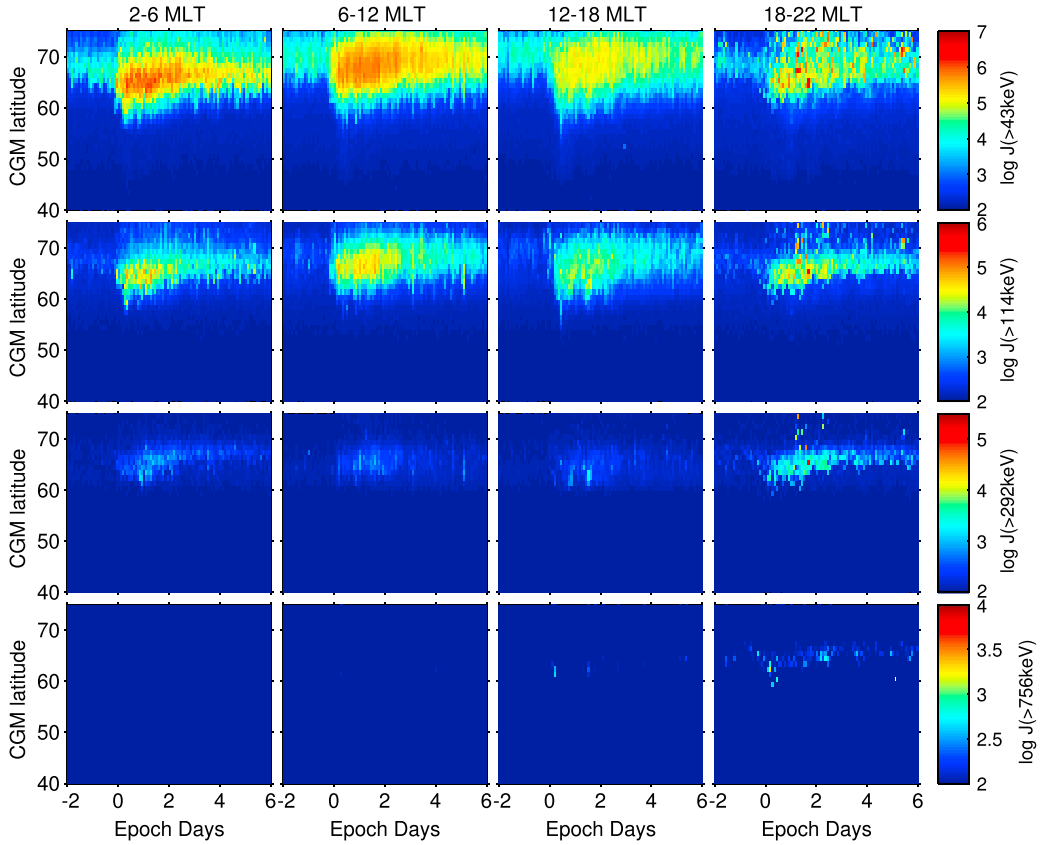

Figure 5. Same as Figure 3 but for the 0° detector. The color scale is logarithmic in units of integral flux (cm^{-2} s^{-1} sr^{-1}).

In the 6–12 and 12–18 MLT sectors, the enhancement is seen in a broader CGM latitude band compared to the two other sectors. The flux cutoff is also seen at higher latitudes in the 6–12 and 12–18 MLT sectors compared to the 18–22 and 2–6 MLT sectors, a feature of the radiation belts that was early shown to exist [*Frank et al.*, 1964; *Williams and Palmer*, 1965]. There is clearly a difference between the sectors in both onset latitude, the maximum flux, and how broad the latitude range of precipitation is. The irregular fluxes seen at high latitudes in the E1 and to some degree the E2 channels in the 18–22 MLT sector is, as already mentioned, caused by a combination of limited satellite coverage at these latitudes (see Figure 1) and the larger proton contamination in this sector compared to the rest of the sectors. The amount of data removed due to contamination in this sector is higher than in the other sectors for all of the storms. This means that the remaining data set is smaller than in the other three sectors, and thus, the electron flux in the 18–22 MLT sector is connected with a larger uncertainty.

The enhancement of E2 flux is delayed by a few hours compared to the E1 flux, both at onset and maximum. In E2, the magnitude of the maximum flux is more similar in all MLT sectors than in E1, consistent with a faster drift of higher-energy electrons. We still see that the dayside fluxes cover a wider range in CGM latitude than the nightside fluxes. The E3 and P6 fluxes are even more delayed with respect to the E1 fluxes and display a clear flux dropout for some time after zero epoch. There is also a daily modulation of the fluxes (most easily seen in the P6 channel) which may be due to variations in the magnetic field with geographic longitude (and thus with UT time, when sampled at a constant MLT sector) and also loss of particles in the Southern Hemisphere.

The BLC fluxes are plotted in Figure 4 in the same manner as the trapped fluxes, and the color scale of each channel is the same in the two figures for easier comparison. Also, for this data, the standard deviation of the mean is found to be around an order of magnitude smaller than the mean (not shown). The largest precipitation occurs in the outer belt, but there also appears to be precipitation from the inner belt in the two lower energy channels which would be completely missed if only the 0° detector was used, as shown in Figure 5. This should, however, be interpreted with some caution as the 0° fluxes are close to the detector background of

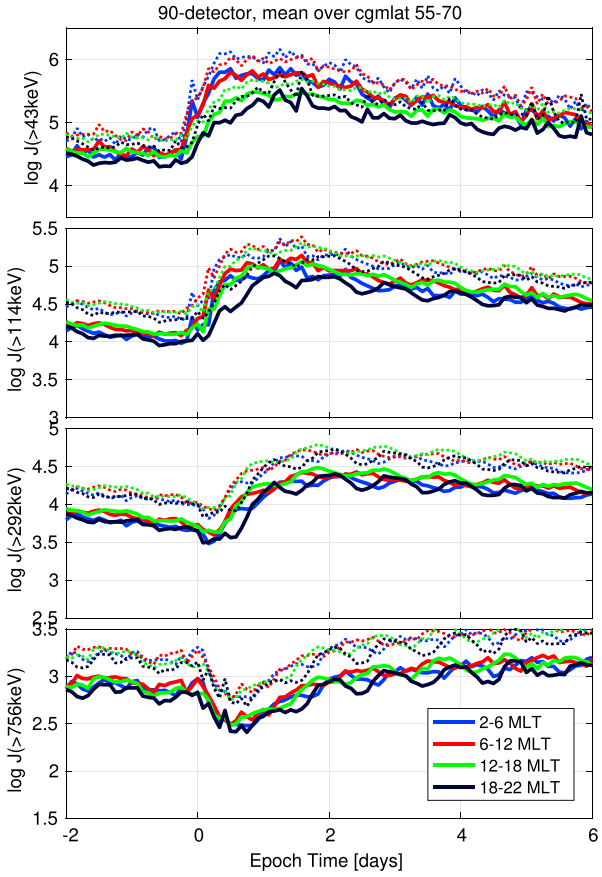

Figure 6. Superposed epoch analysis of 41 CIR/HSSWS storms from 2006 to 2010, measurements from the 90° detector of the MEPED instrument. All available NOAA POES satellites were used, and for each of the sectors 0–6 MLT, 6–12 MLT, 12–18 MLT, and 18–24 MLT the flux was averaged between CGM latitudes 55 and 70°. (top to bottom) E1, E2, E3, and P6 flux are shown. Note that the range on the *y* scale is different for the four channels, and logarithmic is in units of integral flux (cm^{-2} s^{-1} sr^{-1}). The sum of mean flux and the positive standard deviation of the mean flux for each storm is plotted as dotted line.

the MEPED instrument. *Nesse Tyssøy et al.* [2016] pointed out that the BLC fluxes might be associated with large errors in these cases. We note that the E1 and E2 BLC fluxes are higher in the 2–6 and 6–12 MLT sectors, consistent with a higher loss in this region due to chorus waves [*Lam et al.*, 2010]. This fits with our interpretation of the E1 and E2 trapped fluxes in Figure 3.

To determine how much the trapped and precipitated fluxes increase, we take the average flux over 55°–70° CGM latitude and compare the maximum flux after zero epoch to the mean flux 48 to 36 h before zero epoch. The time series of the mean fluxes are plotted in Figures 6 and 7 for the trapped and BLC fluxes, respectively. The trapped flux (BLC flux) in the E1 channel increases by a factor of 9–18 (17–44), depending on sector. The maximum flux in the dayside sectors is higher than the nightside sector, and the maximum is reached approximately 0.5 days earlier. The smallest increase is found in the 12–18 MLT and 18–22 MLT sectors in both the trapped and BLC fluxes. In the E2 channels, the trapped flux (BLC flux) increases by a factor of 8–11 (9–15), with the highest increase in the 6–12 MLT sector. The 18–22 MLT maximum is the smallest of the four sectors and also delayed with respect to the other sectors. The MLT dependence of the increase is less prominent in the E3 and P6 channels, where the trapped flux (BLC flux) increases by factors of ~6 (~3) and ~3 (~1.5) in the two channels, respectively.

There is a seemingly interesting feature in the E3 and P6 channels in the 18–22 MLT sector. The average BLC fluxes increase near zero epoch when the average of the trapped fluxes is decreasing. This may be evidence of a process of strong pitch angle scattering, since a simultaneous flux increase in the 18–22 MLT sector is found in the 0° fluxes, shown in Figure 5. However, closer inspection of the behavior of each single storm reveals that

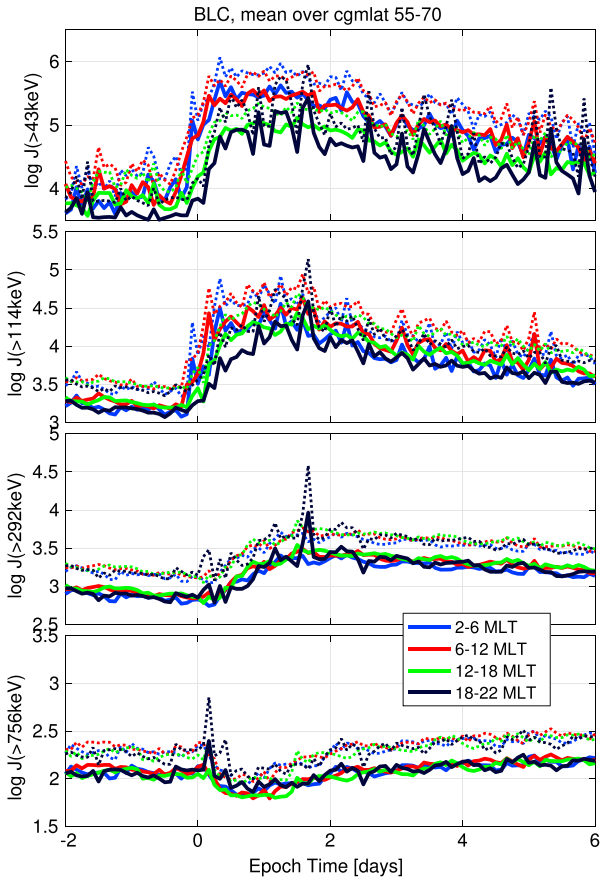

Figure 7. Same as Figure 6 but for the BLC fluxes. Note that the range on the *y* scale is different for the four channels, and logarithmic is in units of integral flux (cm^{-2} s^{-1} sr^{-1}).

the enhancement is not a general feature for all storms but caused by a few storms with high precipitation of high-energy electrons in the early recovery phase. The P6 channel is only used for electron measurements when the flux of high-energy protons in P4 and P5 of the MEPED proton detector is significantly lower than the flux in the P6 channel, and this feature is therefore not caused by protons.

The timing of the precipitation, the MLT dependence, and the limited latitude distribution (which can be seen in Figure 4) are consistent with pitch angle scattering by EMIC waves. EMIC waves usually occur at the duskside in the storm main phase as they are generated by ring current injections. Their confinement in latitude is related to the location of the plasmapause, which is close to $L = 4$ and acts as a wave guiding boundary for the EMIC waves. Around $L = 4$ the hot ring current particles overlap with the cold plasmasphere and allow generation and propagation of EMIC waves.

4. Sorting Events by Increase/Decrease in High-Energy BLC Flux

Still an unsolved question is what separates storms that enhance the flux of relativistic electrons in the magnetosphere and the storms that do not. From the perspective of the atmospheric modeling community, we are interested in knowing whether a storm will produce enhanced *precipitation* of relativistic electrons, which penetrate deep into the atmosphere. We therefore divide our events into groups according to whether the poststorm BLC fluxes of P6 and E3 are greater than the prestorm fluxes. We compare the mean BLC flux of the 2 days before zero epoch to the mean of days 4 and 5 after zero. The average BLC flux over all MLT sectors between CGM latitudes 55° – 70° is compared in the two time intervals. The events are divided into three groups: (1) post-P6 flux > 2× pre-P6 flux; (2) post-E3 flux > 2× pre-E3 flux and post-P6 flux ≤ 2×pre-P6 flux; and (3) post-E3 flux ≤ 2× pre-E3 flux and post-P6 flux ≤ 2×pre-P6 flux, where flux here is the BLC flux specifically. We refer to the groups as 1, 2, and 3, respectively.

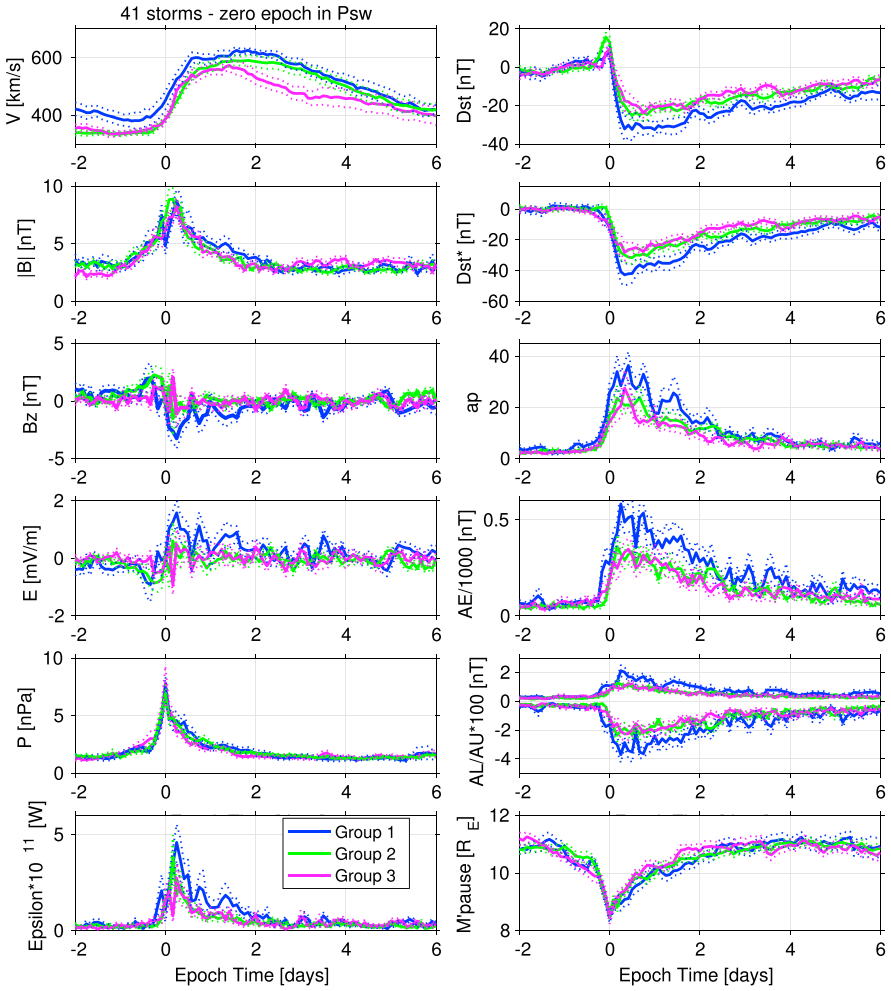

Figure 8. Superposed epoch analysis of 41 CIR/HSSWS storms from 2006 to 2010. Here we have averaged all the data in Figure 2 with a 2 h epoch resolution as was used on the flux data. We have divided all the storms into three groups (see text for description). The mean ± the standard deviation of the mean of each group is plotted as dotted lines.

The criteria of postflux being more than twice the preflux level are in line with previous studies of radiation belt enhancement or depletion [*Reeves et al.*, 2003; *Anderson et al.*, 2015]. Applying the criteria, 9 of 41 events (22%) belong in group 1. Of the remaining 32 events, 19 belong in group 2 (46%), whereas the last 13 events belong in group 3 (32%). Of the group 3 events, 10 decrease in P6 flux, while the remaining 3 have a ratio between 1 and 2.

Figure 8 shows the superposed epoch analysis of the solar wind parameters and geomagnetic indices for the different groups. The mean of group 1 is plotted in blue, group 2 in green, and group 3 in magenta. The sum of mean and its respective standard deviation of each group is plotted in dotted line with the same color as the mean. The maximum solar wind pressure is similar in all three groups ($P_{SW} \sim 7.5$), although group 3 has the largest maximum. Group 1 is separated by having the largest positive solar wind electric field, sustained higher than groups 2 and 3 for approximately 2 days following zero epoch. This indicates a larger energy input to the magnetosphere from the solar wind and also causes these storms to have a larger geomagnetic signature, seen in all the indices. Solar wind electric field is calculated as

$$E = -V \times B_Z \tag{2}$$

and we see that it is mainly the B_Z component that separates groups 1 and 2 from each other, since the solar wind velocity measurements for these two groups are very similar. Even though the solar wind velocities of groups 1 and 2 are very similar, group 2 starts from a lower mean speed, more similar to group 3 events

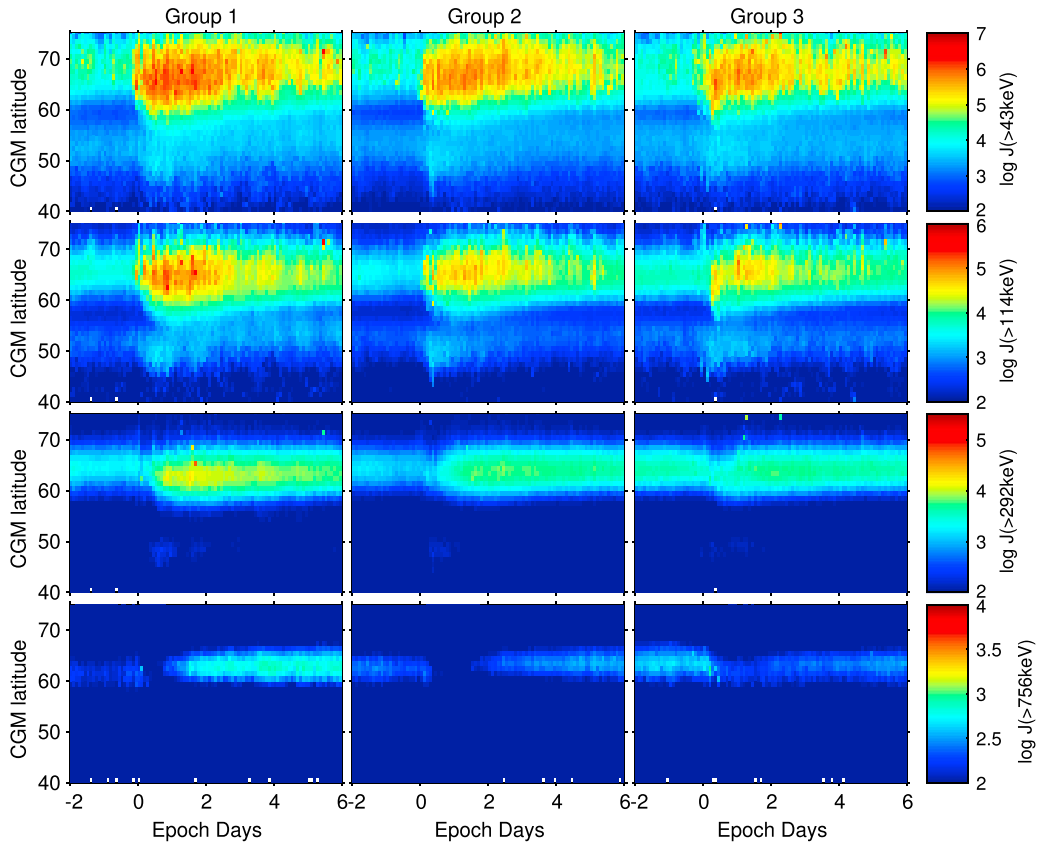

Figure 9. Superposed epoch analysis of 41 CIR/HSSWS storms from 2006 to 2010, divided into groups defined based on increase in P6 flux and E3 flux in the BLC precipitating fluxes. The mean flux between 55° and 70° CGM latitude and all MLT sectors of the two first days in the epoch is compared to the two last days in the epoch. The BLC fluxes are plotted in logarithmic color scale (in units of integral flux [cm^{-2} s^{-1} sr^{-1}]), and the data shown here are the mean over all MLT sectors. (top to bottom) E1, E2, E3, and P6 flux are shown. (left column) Events that have an increased flux in the P6 channel (group 1). (middle column) Events that have increased flux in the E3 channel but not the P6 channel are shown (group 2). (right column) Events that do not display increased fluxes in E3 or P6 (group 3). Note that the range of the colorbar is different for the four channels.

(in fact, they are so similar that it can be hard to see group 2 on the figure, because it is overplotted by group 3). Focusing on only the solar wind velocity after zero epoch, one would not tell groups 1 and 2 apart. Group 3 does not reach a maximum speed quite as high and also decreases faster after the maximum. The plateau of maximum speed is sustained for approximately 3 days in groups 1 and 2, but only little over 1.5 days in group 3.

The superposed epoch analysis of the BLC flux (mean over all MLT sectors) divided into groups is plotted in Figure 9, the trapped fluxes in Figure 10. Also for these plots, the standard deviation was found to be at least 1 order of magnitude smaller than the mean (not shown).

Group 1 events are characterized by the largest poststorm fluxes in all channels, both trapped and BLC flux. E3 trapped (BLC) flux increase by a factor of 11 (5), and for P6 by a factor of 7 (3). Group 2 events have the smallest prestorm E1 and E2 fluxes, both trapped and BLC flux. Group 3 events have the highest prestorm E3 and P6 fluxes, both trapped and BLC flux. In group 3 the total level of P6 flux decrease poststorm compared to prestorm.

4.1. The Energy Input From the Solar Wind to the Magnetosphere

Relating the findings from the superposed epoch analysis of fluxes to the superposed epoch analysis of solar wind measurements and geomagnetic indices, we investigate the relationship between fluxes and solar wind energy input to the magnetosphere closer. The simplest form of energy coupling function from the solar wind to the magnetosphere is the electric field [e.g., *Burton et al.*, 1975]. Interpreting the integrated electric field as a proxy for energy input, this suggests that group 1 consists of storms with a larger energy transfer.

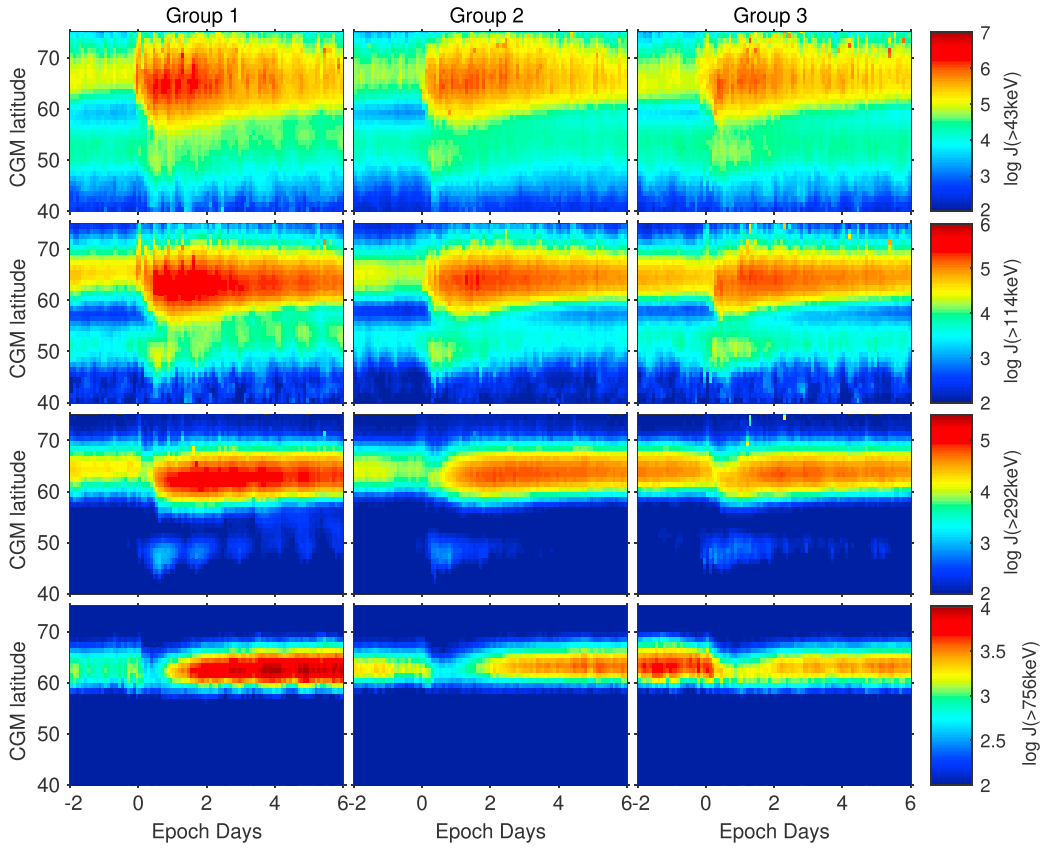

Figure 10. The same as in Figure 9 but here we plot 90° fluxes for the same groups. The range of the colorbar is identical to the BLC fluxes within each channel (and in units of integral flux [cm^{-2} s^{-1} sr^{-1}]). Groups are defined based on the BLC fluxes, see the text for a detailed description.

To investigate this closer, we instead calculate the energy input using the *Akasofu* [1981] epsilon parameter, given in SI units by *Koskinen* [2002]:

$$\varepsilon = \frac{4\pi}{\mu_0} VB^2 \sin^4\left(\frac{\theta}{2}\right) l_0^2 \tag{3}$$

where $\frac{4\pi}{\mu_0} = 10^7$, V is the solar wind velocity, B is the total solar wind magnetic field, θ is the clock angle (angle between the IMF vector and the Z axis, projected into the GSM Y-Z plane, $\tan\theta = \frac{B_y}{B_z}$), and $l_0 = 7R_E$. ε have the units of Watts. The mean ε for the three groups is also plotted in Figure 8.

If we integrate the epsilon parameter from zero epoch until the end of epoch for each group, we get 3.3×10^{18} J for group 1, 2.1×10^{18} J for group 2, and 2.2×10^{18} J for group 3. It is clear that the energy input is larger for group 1 after zero epoch. It does not, however, separate group 2 from group 3. When we study the fluxes in E3 of groups 2 and 3 more closely (Figures 9 and 10), we see that it is the prestorm level that separates these groups. When considering the poststorm flux in E3, there is little difference between the two groups.

To investigate the relationship between the precipitating fluxes and energy input more closely, we calculate the daily mean BLC flux over all MLT and CGM latitudes 55°–70° starting from zero epoch. From the daily means we subtract the mean BLC flux from −2 days to zero epoch. This leaves us with a daily net change in flux compared to the prestorm flux. We compare the daily change in flux with the integrated ε from zero epoch to, and including, the day in question.

For the E3 fluxes, we find the highest correlation on the third day after zero epoch. The results are shown in Figure 11 (left). In this figure, each storm is color coded according to which group it belongs to. The mean energy input for each group is plotted as dashed, vertical lines. The mean energy input for group 1 is a factor of 1.65 larger than for group 2 on days 3 and 4, and a factor of 1.82 larger than group 3. For the P6 fluxes,

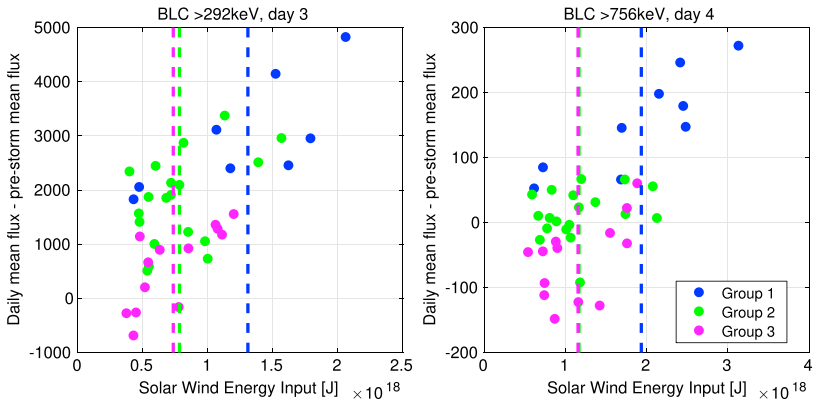

Figure 11. Prestorm flux calculated as mean over epoch hours −48 to 0, CGM latitude 55°−70°, and all MLT. Daily mean BLC flux (starting with day 1 from zero epoch) is calculated over the same geomagnetic coordinates. We subtract prestorm flux from daily mean flux and plot versus the integrated ϵ parameter. The best correlation for E3 (P6) daily mean BLC flux is found on day 3 (4) versus energy input in Joules (integrated ϵ from zero epoch up to, and including, day 3 (4)). Correlation coefficient irrespective of group: E3, $r = 0.70$ and P6, $r = 0.68$. The mean energy input for each group is plotted as dashed vertical lines in the same color as the dots ((right) the green vertical dashed line is overplotted by the magenta line).

we find the best correlation on day 4. The results are shown in Figure 11 (right). The mean energy input for group 1 is a factor of 1.7 larger than for group 2, which is the same as found for E3 on the third day. The mean of group 1 is a factor of 1.8 larger than group 3 in P6 and 1.7 in E3.

There seems to be a limit of about 2.1×10^{18} J in the course of 4 days which has to be exceeded before electrons are accelerated to energies measured by the P6 channel and scattered into the loss cone. After this, the flux added to the loss cone (change from previous flux level) increases linearly. Below this limit, the change in flux appears more or less random for the P6 flux.

Disregarding the group the events belong to and correlating all 41 data points on the third (fourth) day, we find a correlation coefficient of 0.70 (0.68) for the E3 (P6) fluxes with the integrated ϵ. Looking only at group 1, the correlation coefficient is 0.72 (0.86). However, keep in mind that this is based on only nine events. A significant correlation of 0.75 is also found for group 3, E3 channel. The P6 fluxes show no significant correlation (to the 5% level) for group 2 and group 3.

4.2. The Dependence of the Precipitating Fluxes on the Radiation Belt Fluxes

The relationships between the ratio of poststorm to prestorm fluxes in the BLC and the 90° detector fluxes are shown for E3 and P6 in Figure 12. There are strong relationships between the trapped and BLC flux

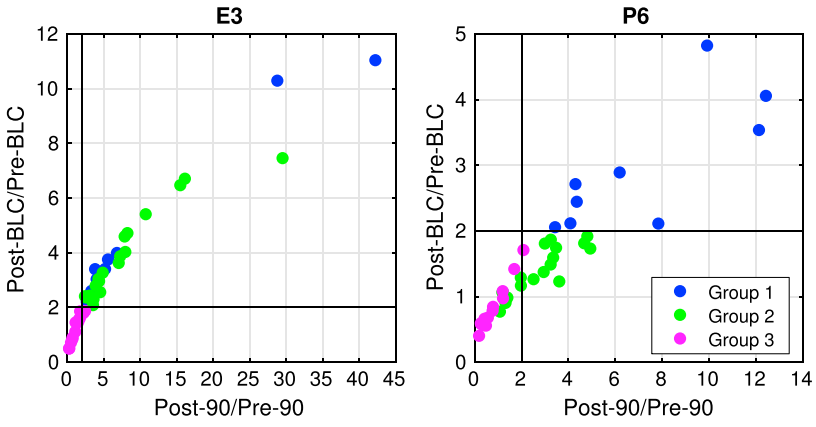

Figure 12. The ratios of postfluxes to prefluxes in BLC and 90° fluxes are scattered for all 41 storms ((left) E3, > 292 keV; (right) P6, > 756 keV). The color indicates which group the event belongs to, as defined based on the increase seen in BLC flux (see text for full description). Some of the blue dots are overplotted by green dots in Figure12 (left) (E3).

ratios both for the E3 and P6 fluxes; however, the relationships are not linear but better fit a power law of the form

$$y = ax^b \tag{4}$$

where y is the ratio post-BLC/pre-BLC flux, x is the ratio post-90/pre-90 flux, and the constants $a = 1.2$ (0.8) and $b = 0.6$ (0.6) for E3 (P6).

This implies that defining flux increase or decrease based on BLC or trapped fluxes will give different event selection into the groups. In this study we used the P6 BLC flux ratio (poststorm flux to prestorm flux) > 2 to define group 1 (blue circles). In Figure 12 (right), we see that all points above the horizontal line at BLC ratio = 2 are colored blue. Using the vertical line (ratio of trapped fluxes = 2) would produce a different set of storms belonging to group 1. The same is true for group 2, which is defined in the same way using the E3 fluxes (and subtracting the storms already sorted into group 1). This would also alter the superposed epoch analysis of solar wind parameters and geomagnetic indices, removing the characteristics of group 1 that were shown in Figure 8. This illustrates the added value and importance of studying precipitation from the radiation belts in itself, especially when considering the atmospheric effects. Using the BLC flux we get a new perspective on the processes important for the loss, and there exist a nonlinear dependence between the precipitation and the growth in the radiation belt for the CIR storms.

5. Discussion

The main focus of this work is to study weak to moderate geomagnetic disturbances caused by CIRs and to determine if they lead to precipitation of high-energy electrons from the radiation belts. The radiation belt is known to be highly dynamic during geomagnetic storms, and the competition between acceleration and loss processes determines the final response of the electron population. To have increased precipitation from the radiation belts in the recovery phase the total population has to increase, as confirmed by Figure 12. The relationship between geomagnetic storms and energization and acceleration of electrons is not fully understood [*Kessel*, 2016], and the response of the electron population to a storm does not necessarily scale with the size of the storm [*Anderson et al.*, 2015].

Higher-solar wind velocity has been noted by many to play a significant role in flux enhancements, but the relationship is not one-to-one [*Asikainen and Ruopsa*, 2016; *Kilpua et al.*, 2015; *Reeves et al.*, 2011]. As shown in Figure 8, we find a higher solar wind velocity sustained for a longer period in the groups of storms with enhanced precipitation of $> \sim 750$ keV (P6) and $> \sim 300$ keV (E3) (groups 1 and 2) compared to the group where flux increase is limited below a factor of 2 (group 3). As illustrated in the envelope of the solar wind B_Z component (Figure 2), magnetic field fluctuations are associated with CIR storms. This will cause intermittent intervals of enhanced magnetospheric convection and substorm activity [*Meredith et al.*, 2011] and subsequently acceleration and pitch angle scattering by associated wave activity.

The storms that caused increased precipitation of $> \sim 750$ keV electrons (group 1) showed a stronger mean signature in the *Dst*, *Dst**, *ap*, *AE*, *AU*, and *AL* indices (see Figure 8). The clearest parameter for separating the storms that caused the highest increase in $> \sim 750$ keV precipitation was an energy input $> 2.1 \times 10^{18}$ J over 4 days after zero epoch, as estimated by the integrated ε parameter. We also observed that the group of events with decreased or unchanged fluxes of $> \sim 300$ keV and $> \sim 750$ keV fluxes (group 3) has the highest average prestorm flux of the three groups (see Figure 9). In this group, it seems that a significant prestorm flux in the radiation belts are effectively lost when the storm onsets. However, the weak solar wind energy input later in the storm is not strong enough to fill the radiation belts and cause significant precipitation. Since the prestorm flux in these storms is higher compared to the two other groups, a strong solar wind driver would be needed to cause the flux to build up to the same or higher levels as before the storm started.

The energy input could not separate the storms in group 2 and group 3. In the solar wind parameters, groups 1 and 2 are mainly separated by group 1 having a more negative B_Z, which indicates a stronger energy transfer from the solar wind to the magnetosphere in the case of $> \sim 750$ keV precipitating fluxes. This was confirmed by the integrated ε parameter, showing a larger estimated energy input for group 1. This might be applied to improve the current energetic electron parametrizations which are usually based solely on geomagnetic indices. In particular, recent studies/review papers highlight the importance of a more accurate parametrization of energetic electron precipitation in order to correctly simulate the polar winter stratosphere-mesosphere region [e.g., *Rozanov et al.*, 2012; *Sinnhuber et al.*, 2012; *Randall et al.*, 2015].

The geomagnetic indices have strong limitations in this context. While the lower energy part of the electron precipitation spectrum is known to be closely correlated with geomagnetic indices [e.g., *Hendrickx et al.*, 2015], the higher electron energies are more ambiguous [*Turunen et al.*, 2009].

In summary, our findings suggest the solar wind speed and the electric field to be possible candidates for a parametrization of EEP. Elevated solar wind velocity for 3 days increases the likelihood of $> \sim 300$ keV precipitation, while the addition of a more negative B_Z increases the likelihood of $> \sim 750$ keV precipitation.

Additionally, a parametrization should also consider the local time variations and the time evolution of the events. The superposed epoch analysis of all 41 events divided into MLT sectors (Figures 3 and 4) showed that the trapped and BLC fluxes behaved in much the same manner, but with the trapped fluxes having larger intensities in all energy channels. Expected dropouts were seen in the $> \sim 300$ keV and $> \sim 750$ keV fluxes following main phase of the storm. Increasing delay in flux buildup with energy was also found. Both the trapped and the BLC fluxes decreased during main phase, implying that the disappearing flux was not mainly precipitated but lost to the magnetopause or influenced by adiabatic effects. These findings are in accordance with previous studies [*Reeves et al.*, 2003; *Millan and Thorne*, 2007; *Meredith et al.*, 2011; *Anderson et al.*, 2015]. As shown in Figure 8, the magnetopause (modeled as by *Shue et al.* [1998]) only moves into 8 R_E during the pressure enhancement associated with the CIR. Therefore, if magnetopause shadowing plays a role in the flux decrease from the trapped population, there needs to be significant outward radial transport. Electrons are known to move radially outward during the main phase to conserve their third invariant. *Turner et al.* [2012] point out that both enhanced dawn-dusk electric fields and diamagnetic effects from a partial ring current during the storm's main phase can result in violation of the third invariant and rapid outward radial transport, resulting in losses to the magnetopause in only a few hours. Also, a phase space density (PSD) that is decreasing with respect to increasing radial distance can result in outward radial diffusion as diffusion always acts to transport particles in the opposite direction to the PSD gradient. Finally, ultralow-frequency (ULF) waves can violate the third adiabatic invariant and allow for electron radial diffusion. Exemplified by a CIR event with *Dst* minimum > -50 nT, *Turner et al.* [2012] confirm that this mechanisms can indeed deplete the outer radiation belt above $L \sim 4R_E$ in only a few hours.

Using the trapped fluxes to define the three groups of events would provide different superposed epoch analyses, as opposed to using the BLC fluxes. This was shown in Figure 12. There is a strong relationship between the enhancement a storm produces in trapped and precipitated fluxes, but it is not a one-to-one, linear relationship. This may be important to keep in mind when atmospheric EEP effects are studied in relation to the radiation belt dynamics.

6. Conclusions

We have presented trapped and precipitating electron fluxes for 41 small to moderate storms associated with CIRs. We performed a superposed epoch analysis of the events divided into groups according to whether the storm increased precipitation of $> \sim 300$ keV or $> \sim 750$ keV electrons, when the 2 days before zero epoch were compared with the two last days in the epoch interval, over all MLTs and CGM latitude 55–70°. Nine storms that had post-P6 flux > 2×pre-P6 flux were sorted into group 1. From the remaining storms, 19 had post-E3 flux > 2×pre-E3flux and were sorted into group 2. The last 13 storms, where the fluxes of $> \sim 300$ keV and $> \sim 750$ keV were limited below an increase of a factor 2, were sorted into group 3.

A superposed epoch analysis of solar wind parameters divided into the three groups showed that the solar wind electric field was larger for group 1, as a result of a more negative B_Z component. We showed that the energy input from the solar wind to the magnetosphere was larger for group 1 compared to the two other groups. Together with the longer duration of enhanced solar wind velocity, the solar wind electric field stand out as possible parameters to predict whether a storm will cause enhanced precipitation with relativistic energy in the recovery phase. To accelerate and precipitate $> \sim 300$ keV electrons, elevated solar wind velocity over longer periods appears to be vital. We also illustrate the importance of an MLT consideration. For example, we find a localized loss to the atmosphere in the main phase in the MLT 18–22 sector at CGM latitudes around 60°.

Appendix A: Optimized Electron Energy Limits and Associated Geometric Factors

The nominal electron energy limits for the MEPED electron telescope were given as >30, >100, and >300 keV [*Evans and Greer*, 2000]. *Yando et al.* [2011] performed a Monte Carlo simulation of the response functions

Table A1. The Optimized Integral Energy Limit for Channels E1, E2, E3, and P6 and the Associated Geometric Factors

	E1	E2	E3	P6
Integral energy limit (keV)	43	114	292	756
Geometric factor[a]	1.01×10^{-2}	1.12×10^{-2}	8.08×10^{-3}	7.39×10^{-3}
Maximum positive deviation[b]	26	7	7	30
Maximum negative deviation[b]	20	6	11	17

[a]Given in units of cm^{-2} sr.
[b]Given in percent (%).

using the Geant4 code. The simulation reveals a fairly slant response function near the lower energy limit, in particular for the first electron energy channel. They found the effective range for E1 to be 50 keV. Effective range was defined as the energy limit which corresponds to a geometric factor half of the total instrument geometric value [*Yando et al.*, 2011, Table 3]. When in operation the true energy limits and the corresponding geometric factors will, however, depend on the incoming electron energy spectrum. Hence, *Green* [2013] calculated new energy limits and associated geometric factors based on a range of exponential spectra and power law spectra, optimized by using the Bowtie method. In respect to the three electron channels the derived, optimized center energies are associated with fairly large uncertainties. We also note that there generally is a large distance between the energy limit giving the minimum spread in geometric factor for power law spectra and exponential spectra. Therefore, based on the response functions given by *Yando et al.* [2011], we revisit the electron energy limits of the electron detector, as well as the electron response in the P6 channel. We aim to determine an optimized effective integral energy limit for the MEPED electron measurements.

Similar to *Green* [2013] we assume both power law and exponential spectra to give a reasonable representation of the incoming electron energies:

$$n_i = \int_{E=0}^{2.5\ \mathrm{MeV}} \mathrm{G}_i(E) E^{-\gamma} \mathrm{d}E,\ i = 1, 2, 3 \tag{A1}$$

$$n_i = \int_{E=0}^{2.5\ \mathrm{MeV}} \mathrm{G}_i(E) E^{\frac{-E}{E_0}} \mathrm{d}E,\ i = 1, 2, 3 \tag{A2}$$

where n_i is the normalized count rate for the three electron channels E1, E2, and E3. For practical reasons we have put an upper limit on the different energy channels. This limit is so high that it will not have a large effect on the flux of the integral spectrum for realistic spectral shapes. The geometric factors $\mathrm{G}_i(E)$ are taken from Table B4 in the supplemented with readings from Figure 5c in *Yando et al.* [2011] to obtain better energy resolution of the geometric factors near the lower energy thresholds of the three energy channels.

A similar procedure is used to calculate the count rate of electrons in the P6 channel, when P5 ≪ P6. Here we assume only a power spectrum:

$$n_{P6} = \int_{E=0}^{7\ \mathrm{MeV}} \mathrm{G}_{P6}(E) E^{-\gamma} \mathrm{d}E \tag{A3}$$

The geometric factors $\mathrm{G}_{P6}(E)$ are taken from Table B2 and Figure 8 in *Yando et al.* [2011]. The ranges of γ and E_0 used in equations (A1)–(A3) are given in Table A2.

Table A2. The Range of γ and E_0 Included in Equations (A1)–(A3)

	γ		E_0 keV	
Channel	Range	Step Size	Range	Step Size
E1	0.25–4.5	0.25	10–300	10
E2	0.25–4.5	0.25	20–400	10
E3	0.25–4.5	0.25	40–900	20
P6	0.25–4.5	0.25		

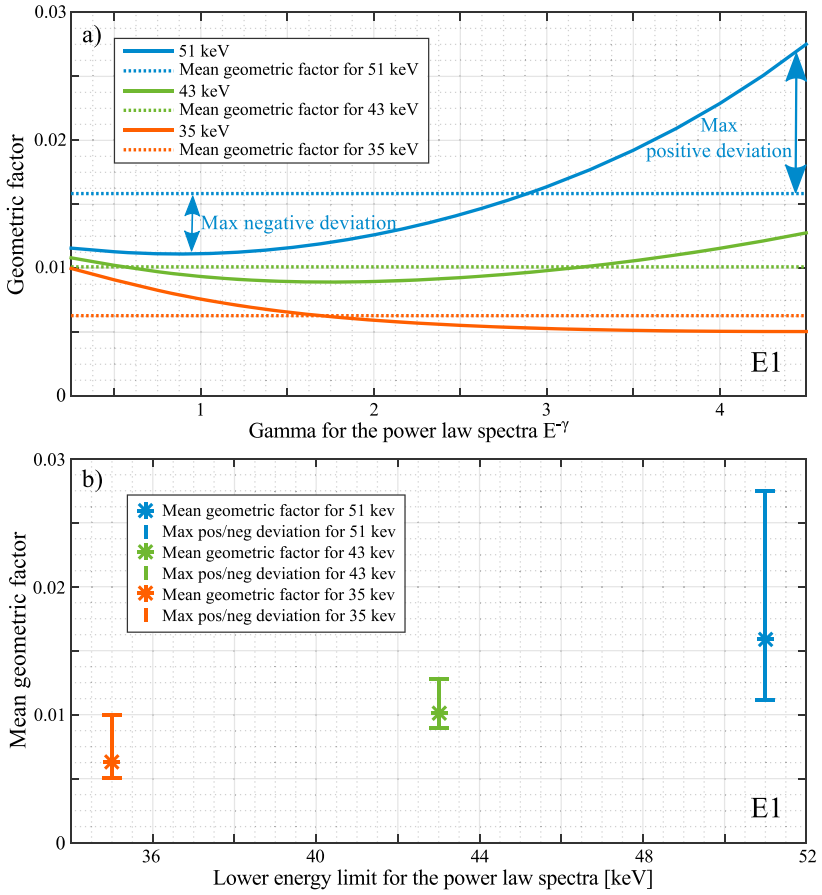

Figure A1. The Figure illustrates two steps of the method toward finding the optimized geometric factor for the E1 energy channel. (a) The geometric factor is plotted for different γ of the power law spectra. The three solid lines represent spectra where 35 keV (orange), 43 keV (green), or 51 keV (blue) are taken as the lower energy limit of the spectra. Each curve's mean geometric value is shown as dotted line. (b) The three mean geometric factors (shown as dotted lines in Figure A1a) are now plotted (as asterisk) versus the lower energy limit for the power law spectra. The vertical error bars in Figure A1b are the maximum positive and negative deviations shown as arrows in Figure A1a.

Afterward we calculate average geometric factors, $\bar{G}_i$ and $\bar{G}_{P6}$, for a dense set of γ and E_0 values for different values of the lower energy threshold, E_i and E_{P6}:

$$\bar{G}_i = \frac{n_i}{J_i(> E_i) - J_i(> 2.5\ \text{MeV})} \tag{A4}$$

for E1, E2, and E3, and

$$\bar{G}_{P6} = \frac{n_{P6}}{J_{P6}(> E_{P6}) - J_{P6}(> 7\ \text{MeV})} \tag{A5}$$

for P6.

Figure A1 illustrates different steps in the method of determining an optimized geometric factor, with the E1 channel used as an example. The Figure displays how the mean geometric factor is calculated for different values for the lower energy limit. To make the figure readable, we only show three examples here, 35 keV, 43 keV, and 51 keV. The example shown is for power law spectra, but the procedure is the same for the exponential spectra. In Figure A1a, the geometric factors are plotted as functions of γ for the three example lower energy limits. The mean of each curve is plotted as horizontal dotted lines in Figure A1a and asterisk in Figure A1b. The vertical error bars in Figure A1b are the maximum positive and negative deviations shown with arrows in Figure A1a.

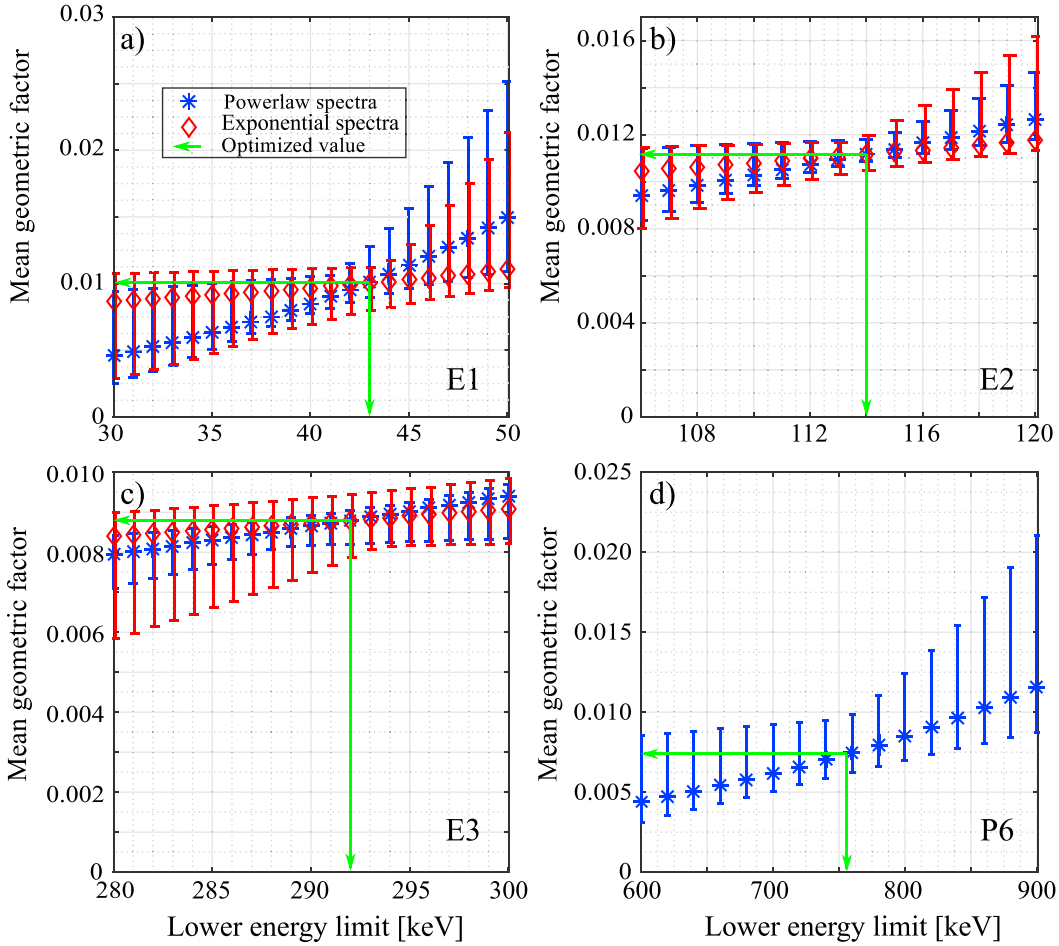

Figure A2. (a and b) The mean geometric factor as a function of the lower integral energy limit for channels E1 and E2 over the given range of γ and E_0 for power law (blue asterisk) and exponential spectra (red diamond), respectively. (c and d) The same for E3 and P6 (only power law). The associated maximum positive and negative percentage deviations are shown as vertical bars. The optimized integral energy limit and associated mean geometric factors from Table A1 are marked in all four panels as green vertical and horizontal lines.

Figure A2 show the derived results for (a) E1, (b) E2, (c) E3, and (d) P6, with power law spectra given in blue and exponential spectra in red. The aforementioned positive and negative deviations are also shown in each panel, as error bars. The optimized lower energy limit and associated geometric factor will be somewhat different for the power law spectra and exponential spectra. For example, in Figure A2a, we find, focusing on the power law spectra, that 41 keV and a geometric factor of 0.9×10^{-2} (cm^{-2} sr) gives the minimum deviation for the geometric factor over the range of γ values. For the exponential spectra, the energy and associated geometric factor is 43 keV and 1.01×10^{-2} (cm^{-2} sr). The optimized energy limit giving minimum deviation for all γ and E_0 is the energy of 43 keV and 1.01×10^{-2} (cm^{-2} sr). The optimized energy limits and associated geometric factor for E1, E2, E3, and P6 are given in Table A1.

In contrast to *Green* [2013] we find the optimized energy limits for power law and exponential spectra to be only a few keV apart. For example, for E2 the optimized energy for the power law spectra and exponential spectra is 113 and 115 keV, respectively. According to Figure 3-3 in *Green* [2013] the optimized energies are $\sim$ 122 and 160 keV. In general, we get a smaller maximum deviation for the geometric factor compared to *Green* [2013]. We base the range of γ and E_0 on the flux measurements from a 10 day period, 17–27 August 2005. It includes both low and high geomagnetic activity (*Kp* range: 0–9).

Appendix B: List of Storms Used in the Study

A list of storms used in this study is presented in Table B1.

Table B1. Date and Time of Zero Epoch of Identified Storms

Storm nr	Date	Time (UT)
1	18 May 2006	05:55
2	6 Jun 2006	10:35
3	14 Jun 2006	20:40
4	4 Jul 2006	12:35
5	7 Aug 2006	02:50
6	24 Sep 2006	01:25
7	12 Oct 2006	12:30
8	27 Oct 2006	22:35
9	9 Nov 2006	18:25
10	29 Jan 2007	06:20
11	27 Feb 2007	07:25
12	1 Apr 2007	00:05
13	22 May 2007	14:55
14	17 Dec 2007	05:40
15	31 Jan 2008	14:50
16	10 Feb 2008	05:40
17	8 Mar 2008	12:50
18	26 Mar 2008	09:20
19	4 Apr 2008	16:15
20	23 Apr 2008	05:00
21	14 Jun 2008	17:15
22	11 Jul 2008	23:20
23	22 Jul 2008	08:45
24	9 Aug 2008	04:40
25	4 Sep 2008	00:45
26	2 Oct 2008	09:10
27	11 Oct 2008	07:45
28	28 Oct 2008	10:30
29	7 Nov 2008	14:00
30	15 Nov 2008	17:30
31	14 Feb 2009	04:30
32	12 Mar 2009	20:20
33	21 Mar 2009	04:30
34	8 Apr 2009	18:10
35	19 Aug 2009	11:15
36	20 Jan 2010	16:35
37	10 Mar 2010	11:55
38	2 May 2010	08:15
39	15 Jun 2010	08:30
40	23 Aug 2010	22:20
41	23 Oct 2010	03:30

Acknowledgments
This study was supported by the Research Council of Norway/CoE under contract 223252/F50. The authors thank the NOAA's National Geophysical Data Center (NGDS) for providing NOAA data. The OMNI data were obtained from the GSFC/SPDF OMNIWeb interface at http://omniweb.gsfc.nasa.gov. The processed data used in this study are available upon request.

References

Akasofu, S.-I. (1981), Energy coupling between the solar wind and the magnetosphere, *Space Sci. Rev.*, *28*(1963), 121–190.

Anderson, B. R., R. M. Millan, G. D. Reeves, and R. H. W. Friedel (2015), Acceleration and loss of relativistic electrons during small geomagnetic storms, *Geophys. Res. Lett.*, *42*, 10,113–10,119, doi:10.1002/2015GL066376.

Andersson, M. E., P. T. Verronen, S. Wang, C. J. Rodger, M. A. Clilverd, and B. R. Carson (2012), Precipitating radiation belt electrons and enhancements of mesospheric hydroxyl during 2004–2009, *J. Geophys. Res.*, *117*, D09304, doi:10.1029/2011JD017246.

Andersson, M. E., P. T. Verronen, C. J. Rodger, M. A. Clilverd, and S. Wang (2014a), Longitudinal hotspots in the mesospheric OH variations due to energetic electron precipitation, *Atmos. Chem. Phys.*, *14*(2), 1095–1105, doi:10.5194/acp-14-1095-2014.

Andersson, M. E., P. T. Verronen, C. J. Rodger, M. A. Clilverd, and A. Seppälä (2014b), Missing driver in the Sun-Earth connection from energetic electron precipitation impacts mesospheric ozone, *Nat. Commun.*, *5*, 5197, doi:10.1038/ncomms6197.

Asikainen, T., and M. Ruopsa (2016), Solar wind drivers of energetic electron precipitation, *J. Geophys. Res. Space Physics*, *121*, 1–50, doi:10.1002/2015JA022215.

Blum, L., X. Li, and M. Denton (2015), Rapid MeV electron precipitation as observed by SAMPEX/HILT during high-speed stream-driven storms, *J. Geophys. Res. Space Physics*, *120*, 3783–3794, doi:10.1002/2014JA020633.

Borovsky, J. E., and M. H. Denton (2006), Differences between CME-driven storms and CIR-driven storms, *J. Geophys. Res.*, *111*, A07S08, doi:10.1029/2005JA011447.

Burton, R. K., R. L. McPherron, and C. T. Russell (1975), An empirical relationship between interplanetary conditions and *Dst*, *J. Geophys. Res.*, *80*(31), 4204–4214.

Clilverd, M. A., C. J. Rodger, T. Moffat-Griffin, E. Spanswick, P. Breen, F. W. Menk, R. S. Grew, K. Hayashi, and I. R. Mann (2010), Energetic outer radiation belt electron precipitation during recurrent solar activity, *J. Geophys. Res.*, *115*, 1–15, doi:10.1029/2009JA015204.

Daae, M., P. Espy, H. Nesse Tyssøy, D. Newnham, J. Stadsnes, and F. Søraas (2012), The effect of energetic electron precipitation on middle mesospheric night-time ozone during and after a moderate geomagnetic storm, *Geophys. Res. Lett.*, *39*, L21811, doi:10.1029/2012GL053787.

Evans, D. S., and M. S. Greer (2000), *Polar Orbiting Environmental Satellite Space Environment Monitor—2 Instrument Descriptions and Archive Data Documentation*, NOAA Technical Memorandum OAR SEC 93, version 1.4, Natl. Atmos. and Oceanic Admin., Space Environ. Cent., Boulder, Colo.

Frank, L. A., J. A. Van Allen, and J. D. Craven (1964), Large diurnal variations of geomagnetically trapped and of precipitated electrons observed at low altitudes, *J. Geophys. Res.*, *69*(15), 3155–3167, doi:10.1029/JZ069i015p03155.

Friedel, R. H. W., E. G. D. Reeves, and T. Obara (2002), Relativistic electron dynamics in the inner magnetosphere—A review, *J. Atmos. Sol. Terr. Phys.*, *64*(2), 265–282, doi:10.1016/S1364-6826(01)00088-8.

Gonzalez, W. D., J. A. Joselyn, Y. Kamide, H. W. Kroehl, G. Rostoker, B. T. Tsurutani, and V. M. Vasyliunas (1994), What is a geomagnetic storm?, *J. Geophys. Res.*, *99*(A4), 5771, doi:10.1029/93JA02867.

Green, J. (2013), MEPED telescope data processing theoretical basis document version 1.0, NOAA Technical Memorandum, version 1.0. [Available at http://www.ngdc.noaa.gov/stp/satellite/poes/documentation.html.]

Hendrickx, K., L. Megner, J. Gumbel, D. E. Siskind, Y. J. Orsolini, H. Nesse Tyssøy, and M. Hevig (2015), Observation of 27 day solar cycles in the production and mesospheric descent of EPP-produced NO, *J. Geophys. Res. Space Physics*, *120*, 8978–8988, doi:10.1002/2015JA021441.

Horne, R. B., M. M. Lam, and J. C. Green (2009), Energetic electron precipitation from the outer radiation belt during geomagnetic storms, *Geophys. Res. Lett.*, *36*, L19104, doi:10.1029/2009GL040236.

Kavanagh, A. J., F. Honary, E. F. Donovan, T. Ulich, and M. H. Denton (2012), Key features of $>$ 30 keV electron precipitation during high speed solar wind streams: A superposed epoch analysis, *J. Geophys. Res.*, *117*, 1–13, doi:10.1029/2011JA017320.

Kennel, C. F., and H. E. Petschek (1966), Limit on stably trapped particle fluxes, *J. Geophys. Res.*, *71*(1), 1–28.

Kessel, M. (2016), Things we don't yet understand about solar driving of the radiation belts, *J. Geophys. Res. Space Physics*, *121*(6), 5549–5552, doi:10.1002/2016JA022472.

Kilpua, E., H. Hietala, D. L. Turner, H. E. J. Koskinen, T. I. Pulkkinen, J. V. Rodriguez, E. G. D. Reeves, S. G. Claudepierre, and H. E. Spence (2015), Unraveling the drivers of the storm-time radiation belt response, *Geophys. Res. Lett.*, *42*, 3076–3084, doi:10.1002/2015GL063542.

Koskinen, H. E. J. (2002), Magnetospheric energy budget and the epsilon parameter, *J. Geophys. Res.*, *107*(A11), 1415, doi:10.1029/2002JA009283.

Lam, M. M., R. Horne, N. P. Meredith, S. A. Glauert, T. Moffat-Griffin, and J. C. Green (2010), Origin of energetic electron precipitation $>$30 keV into the atmosphere, *J. Geophys. Res.*, *115*, A00F08, doi:10.1029/2009JA014619.

Meredith, N. P., R. B. Horne, M. M. Lam, M. H. Denton, J. E. Borovsky, and J. C. Green (2011), Energetic electron precipitation during high-speed solar wind stream driven storms, *J. Geophys. Res.*, *116*, 1–16, doi:10.1029/2010JA016293.

Millan, R. M., and D. N. Baker (2012), Acceleration of particles to high energies in Earth's radiation belts, *Space Sci. Rev.*, *173*(1–4), 103–131, doi:10.1007/s11214-012-9941-x.

Millan, R. M., and R. M. Thorne (2007), Review of radiation belt relativistic electron losses, *J. Atmos. Sol. Terr. Phys.*, *69*(3), 362–377, doi:10.1016/j.jastp.2006.06.019.

Nesse Tyssøy, H., M. I. Sandanger, L.-K. G. Ødegaard, J. Stadsnes, A. Aasnes, and A. E. Zawedde (2016), Energetic electron precipitation into the middle atmosphere—Constructing the loss cone fluxes from MEPED POES, *121*, 5693–5707, doi:10.1002/2016JA022752.

Ødegaard, L.-K. G., H. Nesse Tyssøy, M. I. Jakobsen, J. Stadsnes, and F. Søraas (2016), Space weather impact on the degradation of NOAA POES MEPED proton detectors, *J. Space Weather Space Clim.*, *6*(A26), doi:10.1051/swsc/2016020.

Ødegaard, L.-K. G. (2016), Energetic particle precipitation into the middle atmosphere—Optimization and applications of the NOAA POES MEPED data, PhD. thesis, Univ. of Bergen, Bergen, Norway.

Randall, C. E., V. L. Harvey, L. A. Holt, D. R. Marsh, D. Kinnison, B. Funke, and P. F. Bernath (2015), Simulation of energetic particle precipitation effects during the 2003–2004 Arctic winter, *Geophys. Res. Lett.*, *120*, 5035–5048, doi:10.1002/2015JA021196.

Reeves, E. G. D., K. L. McAdams, R. H. W. Friedel, and T. P. O'Brien (2003), Acceleration and loss of relativistic electrons during geomagnetic storms, *Geophys. Res. Lett.*, *30*(10), 1529, doi:10.1029/2002GL016513.

Reeves, E. G. D., S. K. Morley, R. H. W. Friedel, M. G. Henderson, T. E. Cayton, G. Cunningham, J. B. Blake, R. a. Christensen, and D. Thomsen (2011), On the relationship between relativistic electron flux and solar wind velocity: Paulikas and Blake revisited, *J. Geophys. Res.*, *116*, A02213, doi:10.1029/2010JA015735.

Reeves, E. G. D., et al. (2013), Electron acceleration in the heart of the Van Allen radiation belts, *Science*, *341*.

Richardson, I. (2006), The formation of CIRs at stream-stream interfaces and resultant geomagnetic activity, in *Recurrent Magnetic Storms: Corotating Solar Wind Streams, Geophys. Monogr. Ser.*, vol. 167, pp. 45–58, AGU, Washington, D. C., doi:10.1029/167GM06.

Richardson, I. G., and H. V. Cane (2010), Near-Earth interplanetary coronal mass ejections during solar cycle 23 (1996–2009): Catalog and summary of properties, *Sol. Phys.*, *264*(1), 189–237, doi:10.1007/s11207-010-9568-6.

Rodger, C. J., M. A. Clilverd, J. C. Green, and M. M. Lam (2010a), Use of POES SEM-2 observations to examine radiation belt dynamics and energetic electron precipitation into the atmosphere, *J. Geophys. Res.*, *115*, A04202, doi:10.1029/2008JA014023.

Rodger, C. J., M. A. Clilverd, A. Seppälä, N. R. Thomson, R. J. Gamble, M. Parrot, J. A. Sauvaud, and T. Ulich (2010b), Radiation belt electron precipitation due to geomagnetic storms: Significance to middle atmosphere ozone chemistry, *J. Geophys. Res.*, *115*, 1–12, doi:10.1029/2010JA015599.

Rodger, C. J., B. R. Carson, S. A. Cummer, R. J. Gamble, M. A. Clilverd, J. C. Green, J. A. Sauvaud, M. Parrot, and J. J. Berthelier (2010c), Contrasting the efficiency of radiation belt losses caused by ducted and nonducted whistler-mode waves from ground-based transmitters, *J. Geophys. Res.*, *115*, 1–13, doi:10.1029/2010JA015880.

Rodger, C. J., A. J. Kavanagh, M. A. Clilverd, and S. R. Marple (2013), Comparison between POES energetic electron precipitation observations and riometer absorptions: Implications for determining true precipitation fluxes, *J. Geophys. Res. Space Physics*, *118*, 7810–7821, doi:10.1002/2013JA019439.

Rodger, C. J., A. T. Hendry, M. A. Clilverd, C. A. Kletzing, J. B. Brundell, and E. G. D. Reeves (2015), High-resolution in situ observations of electron precipitation-causing EMIC waves, *Geophys. Res. Lett.*, *42*, 9633–9641, doi:10.1002/2015GL066581.

Rozanov, E., M. Calisto, T. Egorova, T. Peter, and W. Schmutz (2012), Influence of the precipitating energetic particles on atmospheric chemistry and climate, *Surv. Geophys.*, *33*(3–4), 483–501, doi:10.1007/s10712-012-9192-0.

Sandanger, M. I., L.-K. G. Ødegaard, H. Nesse Tyssøy, J. Stadsnes, F. Søraas, K. Oksavik, and K. Aarsnes (2015), In-flight calibration of NOAA POES proton detectors—Derivation of the MEPED correction factors, *J. Geophys. Res. Space Physics*, *120*, 9578–9593, doi:10.1002/2015JA021388.

Seppälä, A., and M. A. Clilverd (2014), Energetic particle forcing of the Northern Hemisphere winter stratosphere: Comparison to solar irradiance forcing, *Front Phys.*, *2*, 1–6, doi:10.3389/fphy.2014.00025.

Seppälä, A., C. E. Randall, M. A. Clilverd, E. Rozanov, and C. J. Rodger (2009), Geomagnetic activity and polar surface air temperature variability, *J. Geophys. Res.*, *114*, 1–10, doi:10.1029/2008JA014029.

Seppälä, A., H. Lu, M. A. Clilverd, and C. J. Rodger (2013), Geomagnetic activity signatures in wintertime stratosphere wind, temperature, and wave response, *J. Geophys. Res. Atmos.*, *118*, 2169–2183, doi:10.1002/jgrd.50236.

Seppäla, A., M. A. Clilverd, M. J. Beharrell, C. J. Rodger, P. T. Verronen, M. E. Andersson, and D. Newnham (2015), Substorm-induced energetic electron precipitation: Impact on atmospheric chemistry, *Geophys. Res. Lett.*, *42*, 8172–8176, doi:10.1002/2015GL065523.

Shue, J. H., et al. (1998), Magnetopause location under extreme solar wind conditions, *J. Geophys. Res.*, *103*(A8), 1281–1334, doi:10.1029/98JA01103.

Sinnhuber, M., H. Nieder, and N. Wieters (2012), Energetic particle precipitation and the chemistry of the mesosphere/lower thermosphere, *Surv. Geophys.*, *33*(6), 1281–1334, doi:10.1007/s10712-012-9201-3.

Søraas, F., K. Aarsnes, K. Oksavik, M. I. Sandanger, D. S. Evans, and M. S. Greer (2004), Evidence for particle injection as the cause of *Dst* reduction during HILDCAA events, *J. Atmos. Sol. Terr. Phys.*, *66*(2), 177–186, doi:10.1016/j.jastp.2003.05.001.

Summers, D., N. Binbin, and N. P. Meredith (2007), Timescales for radiation belt electron acceleration and loss due to resonant wave-particle interactions: 2. Evaluation for VLF chorus, ELF hiss, and electromagnetic ion cyclotron waves, *J. Geophys. Res.*, *112*, 1–21, doi:10.1029/2006JA011993.

Theodoridis, G. C., and F. R. Paolini (1967), Pitch angle diffusion of relativistic outer belt electrons, *Ann. Geophys.*, *23*, 375–380.

Tsurutani, B. T., and G. S. Lakhina (1997), Some basic concepts of wave-particle interactions in collisionless plasmas, *Rev. Geophys.*, *35*(4), 491–502.

Tsurutani, B. T., et al. (2006a), Corotating solar wind streams and recurrent geomagnetic activity: A review, *J. Geophys. Res.*, *111*, A07S01, doi:10.1029/2005JA011273.

Tsurutani, B. T., R. L. McPherron, W. D. Gonzalez, G. Lu, N. Gopalswamy, and F. L. Guarnieri (2006b), Magnetic storms caused by corotating solar wind streams, in *Recurrent Magnetic Storms: Corotating Solar Wind Streams, Geophys. Monogr. Ser.*, vol. 167, edited by B. T. Tsurutani et al., pp. 1–17, AGU, Washington, D. C., doi:10.1029/167GM03.

Turner, D. L., Y. Shprits, M. Hartinger, and V. Angelopoulos (2012), Explaining sudden loss of outer radiation belt electrons during geomagnetic storms, *Nat. Phys.*, *8*, 202–212, doi:10.1038/nphys2185.

Turunen, E., P. T. Verronen, A. Seppälä, C. J. Rodger, M. A. Clilverd, J. Tamminen, C.-F. Enell, and T. Ulich (2009), Impact of different energies of precipitating particles on NO_x generation in the middle and upper atmosphere during geomagnetic storms, *J. Atmos. Sol. Terr. Phys.*, *71*(10–11), 1176–1189, doi:10.1016/j.jastp.2008.07.005.

Williams, D. J., and W. F. Palmer (1965), Distortions in the radiation cavity as measured by an 1100-kilometer polar orbiting satellite, *J. Geophys. Res.*, *70*(3), 557–567.

Yando, K. B., R. M. Millan, J. C. Green, and D. S. Evans (2011), A Monte Carlo simulation of the NOAA POES Medium Energy Proton and Electron Detector instrument, *J. Geophys. Res.*, *116*, A10231, doi:10.1029/2011JA016671.

Zawedde, A. E., H. N. Tyssøy, J. Stadsnes, L.-K. Ødegaard, M. I. Sandanger, P. J. Espy, and R. Hibbins (2016), The impact of energetic electron precipitation on mesospheric hydroxyl during a year of solar minimum, *J. Geophys. Res.*, *121*, 5914–5929, doi:10.1002/2016JA022371.

Erratum

In the originally published version of this article, two errors were detected. The units specified in footnote "a" of Table A1 have been corrected to read "cm^{-2} sr". Also, in the next to last paragraph of Appendix A, all instances of "$(cm^2\ s\ str)^{-1}$" have been corrected to read "$(cm^{-2}$ sr)." The current version may be considered the authoritative version of record.